Superthermal Electrons at Mars: Photoelectrons, Solar Wind Electrons, and Dust Storm Influences

by

Shaosui Xu

A dissertation submitted in partial fulfillment
of the requirements for the degree of
Doctor of Philosophy
(Atmospheric, Oceanic, and Space Sciences and Scientific Computing)
in The University of Michigan
2015

Doctoral Committee:

Professor Michael W. Liemohn, Chair
Research Professor Stephen W. Bougher
Professor Iain D. Boyd
Research Professor Michael R. Combi

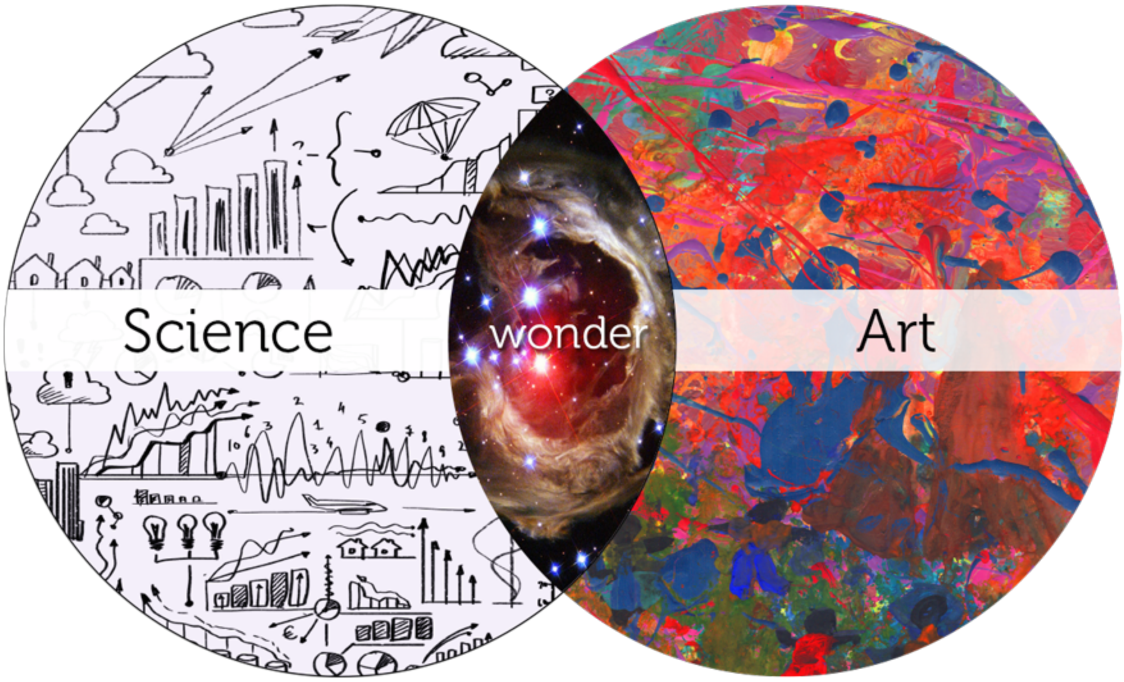

Every science begins as philosophy and ends as art. - Will Durant

Photo from website: *http://www.brainpickings.org/2012/04/25/e-o-wilson-on-art/*

For all the people that help me understand myself and the world better.

ACKNOWLEDGEMENTS

The past few years have been quite a journey for me. I have grown both intellectually and as an independent individual who is trying to find her stance in this limitless world. Certainly this is not the end of such a journey but it does afford me a chance for a moment of introspection. In this pause, I would like to thank a long list of people for their guidance and support.

First and foremost, I would like to express my gratitude towards my academic advisor and dissertation committee chair, Professor Mike Liemohn. I am very fortunate to have an advisor with such a broad range of knowledge of different fields and it has always been a pleasure to learn from and discuss with him about my own research and far beyond. He has been very patient with my frequent visits to his offices and would spend hours answering my all sorts of questions despite his busy schedule. He is also the type of advisor who has students' best interests in heart, and his guidance for my long-term success has been invaluable. My thanks to his kindness, encouragement, and support are beyond words. I will be forever in debt to his mentorship that ranges from grammar corrections to help me finding my passion for space science.

I would also like to thank my dissertation committee, Prof. Stephen Bougher, Prof. Michael Combi, and Prof. Iain Boyd, who have provided their generous guidance and valuable suggestions for my research of and beyond this dissertation. I am also grateful for comments and advices from the Mithras group throughout the past few years, including Prof. Andy Nagy, Dr. Natasha Ganushkina, Dr. Dan Welling, Dr. Raluca Ilie, Prof. Shasha Zou, Dr. Chris Parkinson, Dr. Roxanne Katus, Dr. Darren

De Zeeuw, and many more. I would like to express my gratitude to Prof. Mark Moldwin, Prof. Paul Drake, Prof. Sue Lepri, Prof. Sushil Atreya, Prof. Aaron Ridley, Prof. Xianglei Huang, Prof. Philip Roe, Prof. Anna Gilbert, Prof. Divakar Viswanath, and Prof. Smadar Kani for their excellent instruction and enlightening discussions outside of classes. In addition to being my instructor, I would like to thank Prof. James Slavin for numerous insightful conversations all these years. I have also learned a lot from discussions in the journal clubs and am thankful to people who participated and shared their wisdom, such as Prof. Xianzhe Jia, Dr. Jim Raines, etc.

Outside of Michigan, I have also learned from many others. This summer, I spent four weeks in Space Science Laboratory (SSL) of University of California, Berkeley. I am very grateful to Dr. David Mitchell who agreed to host me and provided tremendous help for my research there, from writing specific programs for me (plus lots of debugging) to hours and hours of scientific discussions, not to mention patiently sitting the whole day to help me set up the computer and helping my entire thesis research. I would like to thank Dr. Jim McFadden for helping me with Mars Atmosphere and Volatile EvolutioN (MAVEN) ion data, Dr. Robert Lillis for scientific discussions during meetings, Dr. Matthew Fillingim for help on Martian nightside ionosphere and being a good poster-mate. I would also like to express my thankfulness to Dr. Shannon Curry, who not only was very kind to me when she was still at Michigan, but she also helped me with graduating, finding a postdoc position and for also giving advices on my future career. I am also very thankful for many more people at SSL who treated me with such hospitality and generosity.

Naturally, my research would not be possible without observational data, hence kudos to the amazing mission teams. I would like to thank the whole Mars Global Surveyor team for providing such an amazing dataset. Much thanks to Dr. Michael Smith in particular, who helped me learn more about the Martian lower atmosphere and dust storms. I would also like to thank Prof. Bruce Jakosky for fearlessly leading the MAVEN mission and the whole MAVEN team for their efforts in producing a comprehensive set of data. In particular, I would like to thank Prof. Bill Peterson for involving me to a study with MAVEN data and also Ed Thiemann for providing data and also for an excellent hiking trip in Boulder. I also thank David Brain for offering to help me find a postdoc position and patiently answering my emails. On that note, I would also like to thank many collaborators have given me insightful comments and suggestions, including Dr. Juan Fontenla, Dr. Phillip Chamberlin, Dr. Qiuhua Zheng, and Dr. Mei-Ching Fok. Special thanks also to Alex Shane, who collaborated with us on a study on superthermal electrons on the Martian nightside.

There are many people that I am so thankful for to make my research in Michigan possible. Some of them provide administrative support, including Laura Hopkins, Eidilia Thomas, Jan Beltran, Sandra Pytlinski, Sandee Hicks, Rachel Long, who have shown such patience and kindness to students. Some of them make everything computer related work, which is essential for me to do any research, including Faye Ogasawara, Darren Britten-Bozzone, Bryan White, and Melissa Terwilliger, etc. Also a big round of applause to Jason Gilbert for making the AOSS LaTeX template.

To get through the grad school, it would have been miserable to say the least without friends and peers in Michigan. My life here would have never been the same without the company of Xiangyun Zhang, Jie Zhu, Yuanfeng Liu, Yuxi Chen and Xiaojian Liu. They are the kind of friends that make Ann Arbor home. Because of them, I have a life beyond work and internet; traveling, Friday dining out, weekend movies, playing cards, hot pots, potlucks, shopping, teaching me how to drive, discussing science, chatting meaningful or meaningless topics, and countless precious moments that I will treasure for life. I am also very grateful that we have a large Chinese group in AOSS, including Meng Jin, Chunpeng Wang, Xianjing Liu, and many more, who have helped with my work and life for years.

I owe a debt of gratitude to Xing Meng and Fang Fang who taught me coding with the terminals and the basics of the Space Weather Frame Work, especially the Radiation Belt Environment. I also thank Zhengguang Huang, Chuanfei Dong, and Judit Szente for teaching me Tecplot. These experiences laid the basis for my current and future research. I have learned from Blake Johnson to always keep a curious mind and dialectical eyes about everything. I have also learned from Lois Smith what driven really is, which inspires me to be more motivated and productive. She has also been a great friend to me; often encouraging me to step outside of my comfort zones, and giving me so many wonderful experiences and memories. I also would like to thank Doga Can Su Ozturk for teaching me to enjoy life more. Thank you to all my Michigan peers that have made this department such a positive and enjoyable environment to work at.

Lastly but most importantly, I would like to express my love and thankfulness for my family, who agreed with my selfish decision of choosing a place so far away from home. Without your understanding and endless support, I could have never been able to chase my dreams. But my dreams (literally) always have you to star in, even though I could not spend much time with you physically. I would like to borrow a metaphor, which goes: I am a kite but you always held the line that leads me home. Without you, I will lose my direction.

One final note, I would like to thank whoever invented music and those who write genius/wonderful/cheesy/down right bad music, which keeps me focused on my work. While it is gradually damaging my hearing, it helps me producing good stuff (hopefully).

TABLE OF CONTENTS

CHAPTER

LIST OF FIGURES

Figure

ABSTRACT

Superthermal Electrons at Mars

by

Shaosui Xu

Chair: Michael Liemohn

Mars is unique in the solar system in terms of its interaction with solar wind because it lacks of a significant intrinsic global magnetic field but possesses localized strong crustal fields. This interaction results in a very complex magnetic topology at Mars so that superthermal electrons, mainly including photoelectrons and solar wind electrons, can be distinctively important for such a complicated planetary space environment. These energetic electrons ($\sim 1-1000$ electron volts) can carry and rapidly redistribute energy along the magnetic field lines. They are also a reliable tool to deduce the Martian magnetic topology, which is critical to understand the electromagnetic dynamics of the Martian space environment.

The investigation methodology involves both data analysis and modeling. The observational data are mainly from the magnetometer/electron reflectometer (MAG/ER) and Thermal Emission Spectrometer (TES) instruments onboard Mars Global Surveyor (MGS). The methods to reduce spacecraft electron contamination and also to separate photoelectron and solar wind electron samples are explained here. The modeling work mainly relies on the SuperThermal Electron Transport (STET) model. The detailed model description and validation are given. In addition, this dissertation also discusses the update to the STET model, i.e. incorporating two new solar irradiance models: the Flare Irradiance Spectral Model (FISM) and the Heliospheric Environment Solar Spectral Radiation (HESSR) model.

This dissertation mainly investigates three topics of superthermal electrons at Mars. (1) This dissertation confirms that the long-lived influence of Martian low-altitude dust storms on high-altitude photoelectron fluxes is common for a wide range of energy and pitch angles and determines that this effect originates from the thermosphere-ionosphere source region of the photoelectrons, rather than at exospheric altitudes at or above MGS. Through simulations, the results suggest that the global dust storm altered the photoelectron fluxes by causing CO_2 to be the dominant species at a much larger altitude range than usual. (2) Because the integral of the production rate above the superthermal electron exobase is about the same for all solar zenith angles, quite counterintuitively, it is found, observationally and numerically/theoretically, that the high-altitude photoelectron fluxes are quite independent of solar zenith angle. (3) Based on the energy spectral (flux against energy) difference between photoelectrons and solar wind electrons, a statistical approach is taken to distinguish the two populations and also allows us to quantify the occurrence rate of solar wind electron precipitation and also these electrons' energy deposition. The broad impact and future work of this dissertation is also briefly discussed, especially with the comprehensive neutral and plasma measurements from the Mars Atmosphere and Volatile EvolutioN (MAVEN) mission to further our understanding of the Martian space environment.

CHAPTER I

Introduction

1.1 Mars

Mars garners people's interest because of how similar this planet is to Earth, and because of its potential habitability. Pictures and measurements from spacecraft have suggested that Mars might once have had streams, rivers, or even an ocean, alluding to the possible existence of life in the past. Yet how the planet lost its water remains mysterious, deduced to be directly related to the loss of its thick atmosphere. One of the most popular theories of Mars' inability of sustaining its atmosphere, as well as liquid water, is due to its lack of a significant intrinsic global magnetic field like Earth so that this planet's upper atmosphere is exposed to solar wind that continuously streams away from the Sun. Solar wind consists of solar plasma and also magnetic fields, called the interplanetary magnetic fields (IMFs).

Albeit thin, the Martian upper atmosphere is photoionized by solar photons on the dayside, which forms an ionosphere. For the first order consideration, because of the lack of a significant intrinsic global magnetic field, the solar wind mainly interacts with the Martian ionosphere. This interaction results in several distinct structures. Because the solar wind is supersonic, i.e. the bulk velocity exceeds the fast magnetosonic wave speed, there is a bow shock formed as the Mars ionosphere acts as an effective obstacle to the solar wind. Between the bow shock and the effective

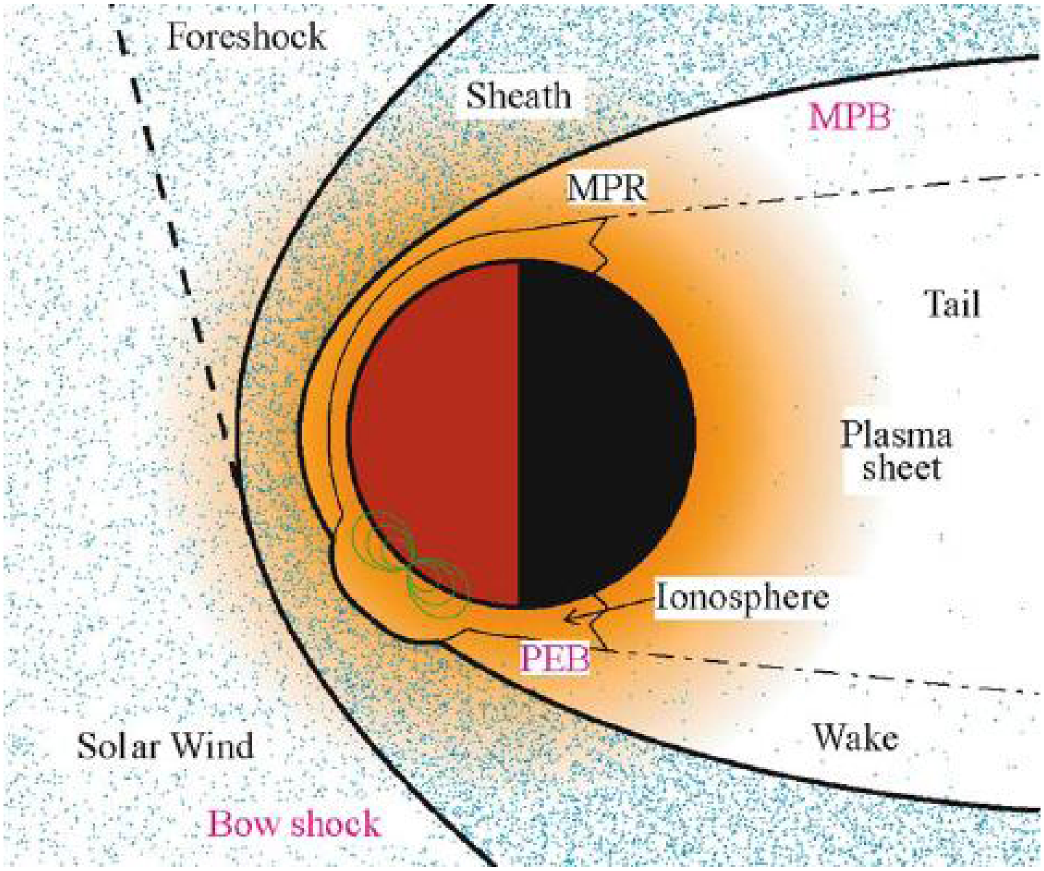

Figure 1.1: A sketch of major boundaries and regions of the Martian plasma environment. Photo courtesy: *http://www.setterfield.org/Astronomy/Mars.html*.

obstacle is the region called the magnetosheath (*Nagy et al.*, 2004), inside of which significant mass-loading takes place. The Martian ionosphere behaves like a conductor and generates currents within it to largely prevent IMF and solar plasma penetrating deep to the atmosphere. As a result, IMF piles up and drapes around the planet, forming the magnetic pile-up region and boundary (MPR and MPB, respectively). This is a typical picture, as shown in the Figure 1.1, for the interaction between solar wind and an unmagnetized object with an atmosphere, such as comets, Venus and Mars.

However, Mars is unique in the solar system in terms of interaction with solar wind. Martian crustal magnetic anomalies have been discovered by the magnetometer/electron reflectometer (MAG/ER) on board the Mars Global Surveyor (MGS) spacecraft (*Acuña et al.*, 1998), and their interaction with IMF results in complex magnetic field topology (e.g. *Brain et al.*, 2003, 2007; *Harnett and Winglee*, 2005; *Liemohn et al.*, 2007a,b; *Ma et al.*, 2014), including closed (connected both ends to the planet), open (connected at one end to the planet and at one end to the IMF), and unconnected or draped (connected both ends to the IMF) magnetic field lines. Studies have been conducted on how the crustal magnetic fields affect localized plasma processes (e.g. *Withers et al.*, 2005; *Nielsen et al.*, 2007; *Krymskii et al.*, 2003; *Brain et al.*, 2010).

1.2 Superthermal Electrons

Superthermal electrons (a very small fraction of the total population with energies far exceeding the average thermal energy (*Gombosi*, 1998)) on Mars mainly consist of two parts: photoelectrons and solar wind/magnetosheath electrons. When photoionization happens, because of an electron's small mass, they carry away the excessive energy of photons. These energetic electrons (∼1 electron volts−1 kilo-electron volts), i.e. photoelectrons, then transfer energy to thermal electrons through Coulomb collisions. Thermal electrons then collide with ions, which consequentially heat up the neutral atmosphere through friction with neutral particles. This process is a significant pathway for solar energy transfer to the upper atmosphere.

As mentioned above, the magnetic topology is rather complicated at Mars. Superthermal electrons with energies lower than a few tens of kilo-electron volts (keV) are usually considered to be bounded to and move along the magnetic field lines, which leads to energy redistribution. The closed magnetic field isolates ionospheric originated photoelectrons from solar wind particles and allows them to move energy from one end of the loop and be deposited at the other end. The open magnetic field lines allow solar wind electrons (from the IMF end of an open field line) to enter the Martian upper atmosphere and deposit their energy through collisions. Especially, dayside to nightside electron transport and also solar wind electron precipitation are considered the main energy source at Martian nightside, causing heating (e.g. *Krymskii et al.*, 2002, 2004), excitation (especially aurora on the nightside (e.g. *Bertaux et al.*, 2005; *Brain et al.*, 2006a; *Leblanc et al.*, 2008)) and dissociation and ionization (*Schunk and Nagy*, 2000). On the other hand, for Mars, it is difficult to infer if the magnetic field is closed, open, or draped from just instantaneous magnetic field measurements, which is critical information to analyze dynamical processes. Rather, electron angular distribution is used to deduce Martian magnetic topology (*Liemohn et al.*, 2006; *Brain et al.*, 2007).

1.3 Specific Topics and Motivations

Now that we have established the importance of superthermal electrons at Mars, this dissertation mainly investigates three topics of dayside superthermal electron physics: photoelectrons and dust storms, photoelectrons and solar zenith angle, and solar wind electron precipitation.

1.3.1 Photoelectrons and Dust Storms

Trantham et al. (2011) analyzed the dayside photoelectron observations from the magnetometer/electron reflectometer instruments onboard Mars Global Surveyor (*Acuña et al.*, 1992; *Mitchell et al.*, 2001) over the strong crustal field regions and quantitatively determined that, among all possible candidates, the local solar extreme-ultraviolet (EUV) proxy was the main controlling factor of photoelectron fluxes. In spite of the normal linear dependence between these two, a second linear trend is, however, found with the primary contribution being the much higher photoelectron fluxes from late 2001 to early 2002.

This time period corresponds to a global-scale dust storm at late 2001 or Mars Year (MY) 25 (e.g. *Smith et al.*, 2002; *Clancy et al.*, 2010). Most of Mars' large dust storms occur in southern hemisphere springs and summers, when Mars is near perihelion. Dust suspended in the dry Martian atmosphere is known to play an important role in the Martian atmospheric dynamics; when dust opacity is high enough, its absorption of solar radiation is comparable to CO_2 gas, thus contributing to the variability of the circulation and weather on Mars (e.g. *Gierasch and Goody*, 1972; *Haberle et al.*, 1982; *Medvedev et al.*, 2011).

Even though the dust primarily remains below 60 km, its influence extends to higher altitudes as it absorbs solar radiation and heats the atmosphere, causing an elevated atmospheric density at higher altitudes due to the increased scale height. Many studies have been conducted on dust storm influences on the Martian upper atmosphere (e.g. *Keating et al.*, 1998; *Bougher et al.*, 1999, 2004, 2006; *Baird et al.*, 2007; *Lillis et al.*, 2008, 2010a; *England and Lillis*, 2012; *Withers and Pratt*, 2013; *Medvedev et al.*, 2013). The change in neutral atmosphere, especially the increase of neutral density due to a heated atmosphere caused by dust storms, leads to the variability of the ionosphere. On one hand, observations of MGS, both during aerobraking (*Keating et al.*, 1998) and during the science phasing orbits (*Tracadas et al.*, 2001), have shown a factor of 3 increase in the mass density at 130 km altitude and a factor of 2 increase at 180 km a few days after the start of dust storms, respectively. By examining a few different dust storm events, *Withers and Pratt* (2013) found the increases of upper atmospheric density were usually a factor of a few responding to moderate regional storms and of an order of magnitude during the large storms. On the other hand, modeling results of *Bougher et al.* (1997) on a 20-sol dust storm also showed a 5-10 times increase of thermospheric density at 110 km; furthermore, *Bell et al.* (2007) conducted a sensitivity study of the vertical depth of the dust layer and found, when the 9-micron dust optical depth $\tau = 0.3$, a 100% increase in atmospheric density at the equatorial height of 110 km and a 650% increase at the winter pole. In fact, the study of *Bell et al.* (2007) implies that the Hadley circulation transmits changes in the lower atmosphere caused by dust loading into the upper atmosphere, which is supported by the study of *Withers and Pratt* (2013). Neutral density is one of the dominant controlling factors of the ionosphere electron density profile (with similar effects expected on ionospheric photoelectrons). Increased altitudes of the ionospheric peak electron density due to the expanded atmosphere during dust storms have been observed (*Hantsch and Bauer*, 1990; *Wang and Nielsen*, 2003). In fact, the height of the electron peak can also be used to study the physical state of the Mars lower and upper atmosphere (e.g. *Bougher et al.*, 2004; *Zou et al.*, 2011).

MGS was operated at altitudes around 400 km, well above the electron peak altitude. Using drag data from this satellite, *Forbes et al.* (2008) concluded that the dust storm at MY 25 seemed to not influence exospheric temperature or density but the authors only addressed the relationship between the instantaneous dust opacity within ±30° latitude and the exosphere. *Liemohn et al.* (2012), however, conducted the time-history influence of dust storms on dayside photoelectrons observed by MGS above the strong crustal fields. The inclusion of 7-Earth-month time-history dust opacity not only successfully merged two linear EUV dependence trends into one but also significantly increased the correlation of photoelectron fluxes and the new controlling function, the EUV proxy multiplied by the time-history dust opacity. This modification to the controlling function, sometimes corrected by an order of magnitude, can be considered as a change to the photoelectron production rate and/or to high-altitude scattering effects, which can be caused by the change in the neutral density at ionospheric altitudes and/or at exospheric altitudes, respectively.

Since both *Trantham et al.* (2011) and *Liemohn et al.* (2012) only investigated one single velocity space bin, 27 electron volts (eV) at pitch angle 80°-90°, the question remains: **how does the full energy and pitch angle distribution of high-altitude photoelectrons respond to low-altitude dust storms?** Similarly, **what is the physics governing this connection?** Hence, it is necessary to examine dust storms' effects on all the available energy channels and pitch angles. This examination allows us to investigate the physical processes behind the dust storms, which the former two studies barely addressed. Differences in the response of different energy photoelectrons may be an indicator of physical processes that have an energy preference, such as scattering and/or collisions. The pitch angle can give information on where photoelectrons reside, for example, photoelectrons near 90° pitch angle are mostly located and bouncing at or beyond the MGS orbit. The examination of pitch angle bins might uncover where those dust-related physical processes most likely happen. Furthermore, we use the SuperThermal Electron Transport (STET) model (*Liemohn et al.*, 2003) to investigate what characteristics of the atmosphere can lead to such photoelectron flux enhancements.

1.3.2 Photoelectrons and Solar Zenith Angle

Solar zenith angle (SZA) is known to have effects on the Martian upper atmosphere, both the thermosphere and the ionosphere (e.g. *Withers*, 2009; *Haider et al.*, 2011). The dayside Martian ionosphere is relatively well described by Chapman theory (*Chapman*, 1931a,b), especially in terms of electron peak values. Particularly, for an ionosphere in photochemical equilibrium, the peak density is roughly proportional to the square root of the cosine of solar zenith angle (SZA), as well as that the peak altitude rises with increasing SZA. Such studies include occultation profiles from early missions (e.g. *Hantsch and Bauer*, 1990; *Zhang et al.*, 1990), Mars Global Surveyor (MGS) Radio Science profiles of electron density (e.g. *Withers and Mendillo*, 2005; *Fox and Yeager*, 2006, 2009), and measurements from the Mars Advanced Radar for Subsurface and Ionospheric Sounding (MARSIS) (*Gurnett et al.*, 2005) instrument on board Mars Express (e.g *Nielsen et al.*, 2007; *Morgan et al.*, 2008; *Gurnett et al.*, 2008; *Němec et al.*, 2011). Similarly, the Martian total electron content (TEC), derived from echoes of MARSIS, is also found to approximately match the Chapman theory (e.g. *Safaeinili et al.*, 2007; *Lillis et al.*, 2010b). However, not all the quantities have obvious dependence on SZA. Based on the power k=0.5, *Withers et al.* (2014) concluded that the electron temperature at the main peak is in fact independent of SZA.

The main local source of photoelectrons are photoionization and secondary ionization while the main scattering and energy loss process is collisions with other species, especially neutral particles at lower altitudes (e.g. *Nagy and Banks*, 1970; *Banks and Nagy*, 1970). The photoionization production rate is controlled by the local solar irradiance, which should vary significantly with SZA due to a slant path at high SZAs and different atmospheric density profiles. On the other hand hand, transport is also very important to photoelectrons. When semi-vertical (as opposed to purely horizontal) magnetic fields are present, such as at Earth and at Martian strong crustal field regions, photoelectrons can gyrate around magnetic fields and transport from low altitudes to high altitudes. Then, the high-altitude electron flux is the integral of photoelectrons transported from the ionospheric production peak region to higher altitudes. Because the production rate decreases exponentially with increasing altitude, the photoelectron fluxes measured at high altitudes are supposedly dominated by the production region at lower altitudes, where it is Chapman-like and has a strong SZA dependence. At Mars, photoelectron fluxes over the crustal field regions were presumed to be SZA dependent (e.g. *Liemohn et al.*, 2012). For example, *Trantham et al.* (2011) investigated the main controlling factors of photoelectrons observed by MGS and included the effects of SZA in their local EUV proxy, which is claimed to be the best organizer of photoelectron fluxes.

However, **do the observed high-altitude photoelectron fluxes really depend on solar zenith angle?** The answer concerns energy redistribution at Mars. Mars' complicated magnetic topology (e.g. *Brain et al.*, 2007; *Liemohn et al.*, 2007a) allows photoelectrons, therefore energy, transport from one location to another, especially important to the nightside atmosphere through cross-terminator transport. In addition, the escaping photoelectrons could set up ambipolar electric fields that facilitate ion escape. In this dissertation, we examine the relationship of high-altitude photoelectrons and SZA by analyzing the measured photoelectron fluxes from the magnetometer/electron reflectometer (MAG/ER) instrument onboard Mars Global Surveyor (*Acuña et al.*, 1998; *Mitchell et al.*, 2001), accompanied by further exploration with a superthermal electron transport model.

1.3.3 Solar Wind Electron Precipitation

Open magnetic field lines, resulting from the connection between the IMF and crustal fields, have been discovered and confirmed by several studies via identifying solar-wind/magnetosheath electron precipitation (e.g. *Mitchell et al.*, 2001; *Liemohn et al.*, 2003; *Brain et al.*, 2005; *Dubinin et al.*, 2008a,b). Futhermore, *Brain et al.* (2007) discussed how often the fields above different geographic regions were open/closed by analyzing electron pitch angle distributions. These open field lines allow ionospheric photoelectrons to escape into space (e.g. *Frahm et al.*, 2006a,b; *Liemohn et al.*, 2006, 2007b) and solar-wind/magnetosheath electrons to precipitate into the Martian upper atmosphere. The precipitation of superthermal electrons into the Martian atmosphere can cause heating (e.g. *Krymskii et al.*, 2002, 2004), excitation (especially aurora on the nightside (e.g. *Bertaux et al.*, 2005; *Brain et al.*, 2006a; *Leblanc et al.*, 2008)) and dissociation and ionization (*Schunk and Nagy*, 2000).

Mitchell et al. (2001) identified solar-wind/magnetosheath electron precipitation through open magnetic field lines on the nightside, resulting in the spikes of high electron fluxes in between plasma voids (whose energy spectra are near instrument background level flux, a feature of closed magnetic fields). Also, *Dubinin et al.* (2008a) observed spatially organized narrow spikes in regions of strong crustal field on the Martian nightside by the Analyzer of Space Plasma and Energetic Atoms (ASPERA-

3) experiment (*Barabash et al.*, 2006) onboard the Mars Express spacecraft. Furthermore, a systematic study of the nightside electron precipitation's geographic pattern and dependence on solar wind conditions was conducted by *Lillis and Brain* (2013). On the day side, *Brain et al.* (2005) studied how often solar wind/magnetosheath electrons penetrate below 400 km by analyzing the omni-directional electron fluxes measured by MGS and then concluded the hemispherical asymmetry and the seasonal variation of the altitude of the magnetic pileup boundary (MPB), also its dependence on the IMF directions. In particular, a higher probability of magnetosheath plasma intrusion was observed in some patches surrounded by closed strong crustal fields, where field lines more likely connect to the IMF.

Martian strong crustal fields should be oppositely directed with IMF most of the time, which most likely leads to reconnections and consequently open magnetic fields. Then one might ask: **what is the occurrence rate of dayside solar wind/magnetosheath electron precipitation over strong crustal fields** Also, open magnetic fields allow particle and energy exchange between the solar wind and the Martian atmosphere. So, **what is solar wind electrons' energy deposition into the Martian atmosphere?** For this part of the dissertation, we take a statistical approach to identify solar wind/magnetosheath electrons and ionospheric photoelectrons and determine the occurrence rate of solar wind electron precipitation. Furthermore, although solar photon absorption is certainly the largest source of energy input to the dayside Martian upper atmosphere, quantification of how superthermal electrons' energy input compares to solar input has not been done. This new approach also allows us to quantify the energy flux deposition of solar-wind/magnetosheath electrons into the dayside Martian upper atmosphere and compare it with solar flux input.

1.4 Overview of Dissertation

This dissertation mainly investigates the following three topics of superthermal electrons at Mars:

- Understanding the underlying physics of the connection between photoelectrons and dust storms;
- Determining the relation between high-altitude photoelectrons and solar zenith angle;
- Quantifying the occurrence rate and energy deposition of solar wind electron precipitation into Martian dayside atmosphere through cusps over the strong crustal field regions.

The investigation methodology involves both data analysis and modeling. Chapter II introduces the instruments, such as MAG/ER and Thermal Emission Spectrometer (TES) onboard MGS, and the selection procedures of photoelectrons and solar wind electrons, followed by the description, validation, and development of the SuperThermal Electron Transport (STET) model in Chapter III. Then, in Chapters IV and V, we investigate how dust storms and solar zenith angle, respectively, affect high-altitude photoelectrons through analyzing MGS data as well as simulations with the STET model. Chapter VI switches to another population, solar wind electrons, and studies the dayside precipitation occurrence rate and the energy deposition of these electrons via a statistical approach to MGS data. A similar study on the nightside is also briefly described. A preliminary work with observations from the Mars Atmosphere and Volatile EvolutioN (MAVEN) mission is briefly discussed in Chapter VII. This dissertation finally closes with conclusions and future work in Chapter VIII.

CHAPTER II

Methodology: Data

Part of this dissertation involves analyzing electron data and dust opacity data mainly from instruments onboard Mars Global Surveyor (MGS). In this chapter, a brief description of the instruments is given. Then, the selection procedures of photoelectrons and solar wind electrons are described in detailed.

2.1 Instrumentation

Mars Global Surveyor was a global mapping mission that aimed to examine the entire planet, from the ionosphere down through the atmosphere to the surface, and deep into Mars' interior. MGS arrived at Mars on September 12, 1997, and was initially operated in a highly elliptical polar orbit. On February 4, 1999, the spacecraft concluded aerobraking into a circular mapping orbit at 405±36 km altitude and locked to 0200/1400 local time (LT) during its mapping phase. The instruments onboard the spacecraft had been making measurements for over nine years until late 2006 when the spacecraft lost contact with Earth.

Together with vector magnetic field data measured by the magnetometer(MAG), the electron reflectometer (ER) onboard MGS measured superthermal electron angular distributions with an energy range of 10 eV-20 keV (*Acuña et al.*, 1992; *Mitchell et al.*, 2001). Every 2-8 seconds, the ER recorded electron fluxes in sixteen $22.5^\circ \times 14^\circ$

sectors, which spanned the entire 360° × 14° field of view (FOV). With both the vector magnetic field and the electron angular distribution measured, the FOV can be converted into pitch angles (Eq. 1 in *Mitchell et al.* (2001)). As the MGS spacecraft did not spin, the ER can only provide 2-D pitch angle distributions (PADs) rather than a full 3-D velocity space distribution; the sampled width of the PAD also varies according to the orientation of the ambient field with respect to the ER detection plane. In other words, if the magnetic field was in the plane of the instrument field of view all 180° were sampled, but if the magnetic field was perpendicular to this plane, only pitch angles near 90° were sampled (see Figure 9 of *Liemohn et al.* (2006)). It is important to notice this possible bias in the number of samples for the different pitch angles.

The Thermal Emission Spectrometer (TES) instrument on MGS is fully described by *Christensen et al.* (1992, 2001) and the details of extracting dust opacity values from these observations are given by *Smith* (2004). The dust opacity record shows a clear seasonal variation, with higher values caused by dust storms occurring each southern hemisphere spring and summer, as shown in Figure 2.1. Since even local dust events can cause a global response of the upper atmosphere (e.g. *England and Lillis*, 2012; *Withers and Pratt*, 2013), this study is based on the globally averaged dust opacity values. The dust opacities at MGS' latitude were presented by *Liemohn et al.* (2012) and other studies.

2.2 Data Processing

Superthemal electrons consist of photoelectrons and solar wind electrons. How to distinguish these two populations is described in detail. Also, contamination from spacecraft photoelectrons can be significant to low energy measurements, so a method to reduce this contamination is provided here.

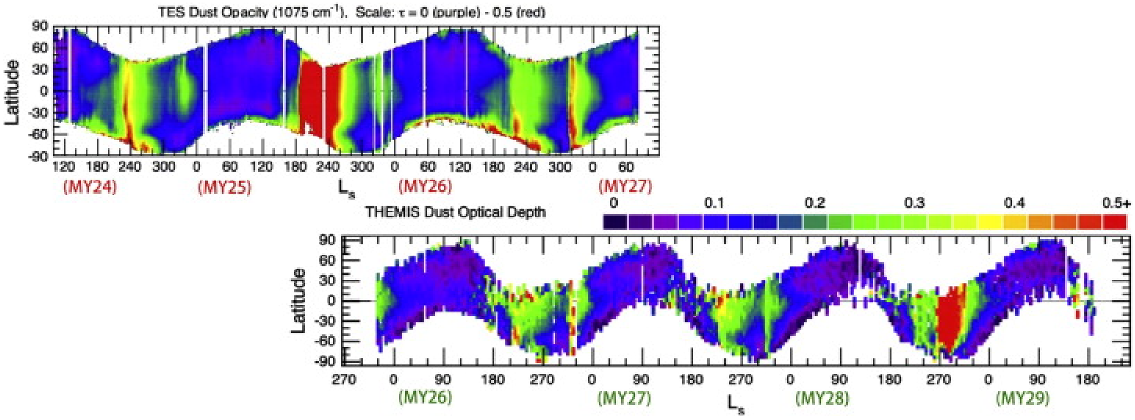

Figure 2.1: Zonal-averaged column dust opacity: (top panel) MGS-TES observations (*Smith*, 2006) from $L_s = 120°$ of Mars Year (MY) 24 to $L_s = 80°$ of MY27; (bottom panel) observations from Thermal Emission Imaging System onboard Mars Odyssey from $L_s = 330°$ of MY25 to $L_s = 190°$ of MY29 (*Smith*, 2009), also Figure 1 of *Medvedev et al.* (2011).

2.2.1 Photoelectron Selection

To select dayside photoelectrons, the methodology is similar to that of *Trantham et al.* (2011). Photoelectrons observed at an altitude of 400 km by MGS on closed magnetic field lines are most likely originated from the ionosphere lower down on that same field line. On Mars, a region consisting of closed magnetic loops is mostly within longitudes of 160° and 200° and north latitudes of $-30°$ and $-70°$, as shown in Figure 2.2, and this spatial constraint is applied to our data selection, along with a magnetic field magnitude minimum constraint (35 nT). In addition, to avoid cusps between loops where solar wind electron precipitation could happen, only elevation angles within ±45° of horizontal are selected. All energies were intended to be examined but the photoelectron fluxes in energy channels higher than 746 eV are at or near the 1-count instrument threshold. Hence only 12 out of the 19 energy channels are examined, from 11.4 to 746 eV (lower bound of the lowest channel and upper bound of the highest channel, respectively). Also, a pitch angle bin size of 10° is used, mapping the ER anode sectors into these 18 identically sized pitch angle bins.

However, our full examination of all available energy and pitch angle bins found

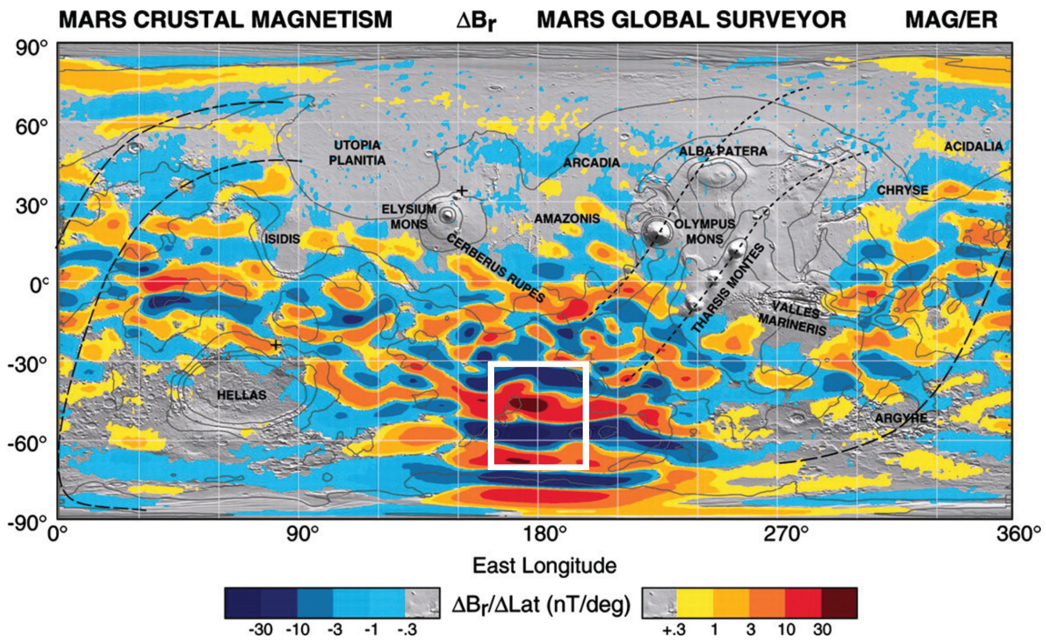

Connerney J E P et al. (2005) Proc. Nati. Acad. Sci. USA;vol. 102, no. 42:14970-14975

Figure 2.2: Radial B field of Mars (*Connerney et al.*, 2005), with the white box representing the geographic selection boundaries of this study, also Figure 1 of *Trantham et al.* (2011). Copyright (2005) National Academy of Sciences, U.S.A.

that the aforementioned method is insufficient. Figure 2.3 shows an example of one selected orbit, Earth year 2000 Day 288, 14:29:01. The top two panels show how the magnetic elevation angles and latitudes change within this 490 s interval, respectively. The latitude is from $-60°$ to $-35°$, crossing most of the entire spatial box of strong crustal fields, while the B elevation angle increases from $-35°$ to $45°$, decreases to $-45°$ and then increases to $45°$ again. The smooth change of B elevation angle indicates the loop structure of the magnetic field. The data absent from 120 s to 200 s are due to the elevation angle criteria described above. Other large gaps are caused by the unsuccessful conversion from anode bins into pitch angles. The eight contour plots in Figure 2.3 show fluxes of two energy channels, 515 eV (b-e) and 36 eV (g-j). Figure (2.3b, 2.3g) are the differential electron fluxes recorded in the 16 anode sectors against time for two energies, respectively, while the color is normalized electron flux (relative to the maximum value, also given in each plot) for all eight contour plots.

Here, since the time for each measurement from MAG/ER is different, a 6 second time interval is used in the contour plots, causing the small gaps in between data points. The ER has a 360° × 14° field of view (FOV) and measures each pitch angle (PA) twice, once for each 180-degree span of instrument azimuth around the FOV. Pitch angles are determined by the magnetic field's azimuthal and elevation angles and also the azimuth of the incident electron, i.e. the angle of each sector in the FOV plane (*Mitchell et al.*, 2001). Figure 2.3g shows constant high fluxes across sectors 5-12, regardless of the elevation angle of the magnetic field and the latitude of the measurement. In fact, this feature is found in energies lower than 53 eV for almost the entire 7-year data. Given the fact that these 8 sectors look towards and along the spacecraft bus, the systematically higher flux values of these sectors at lower energies throughout this interval of changing magnetic field direction strongly suggest contamination by spacecraft photoelectrons and secondary electrons.

Originally, simply averaging the fluxes of two bins of the same pitch angle for all energies is used, shown in Figure (2.3c-d, 2.3h-i). Because of this new discovery of contamination at low energies, while the same method is used for energies higher than 53 eV, only the rest of the 8 sectors other than sectors 5-12 are taken into account to calculate the electron fluxes of lower energy channels, shown in Figures 2.3e and 2.3j. Notice that for the lower 4 panels in Figure 2.3, with time along the x-axis, the y-axis is now denoted as "Modified PA." Aside from converting fluxes of 16 sectors into pitch angle distributions (PADs), the pitch angle is also flipped when the B field points downward (data points below the dashed line in 2.3a). For example, if B points towards the planet, the original pitch angle of 10° would now be 170°. In other words, electrons at pitch angle $0° - 90°$ ($90° - 180°$) always have a velocity component away from (towards) the planet. Figures 2.3c and 2.3d (also 2.3h and 2.3i) show a comparison between the normal PA and "Modified PA." In this case, we can separate pitch angles into three parts. For PA near 90°, it's the so-called trapped

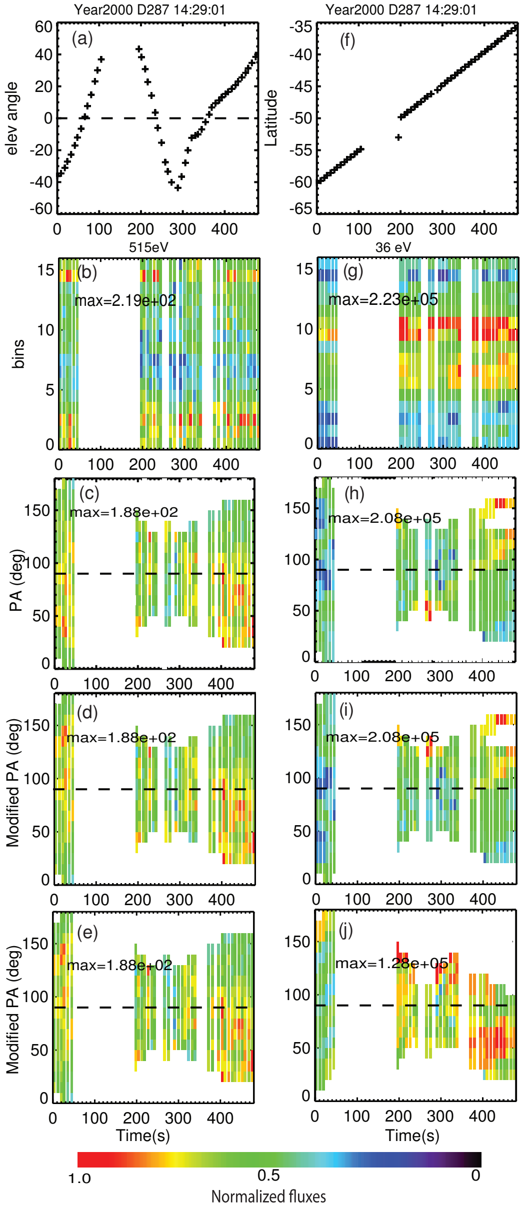

Figure 2.3: An example of one selected orbit, Earth year 2000 Day 288, 14:29:01. The top two (a, f) show how the magnetic elevation angles and latitudes change within 490 s, respectively. The left four color plots (b-e) correspond to energy channel 515 eV while the right four (g-j) correspond to 36 eV. The color is normalized electron flux (relative to the maximum value $[cm^{-2}s^{-1}ster^{-1}eV^{-1}]$ of each plot). Panels (b) and (g) are the differential electron fluxes recorded in the 16 anode sectors against time while panels (c) and (h) are the fluxes converted into pitch angle distributions (PADs). The lower four (d, e, i, j) are fluxes converted into PADs but with Modified PA bins as the y-axis. The dash line in (a) marks 0 magnetic elevation angle, below which the pitch angle is flipped. The dash line in (c, d, e, h, i, j) marks 90° pitch angle.

zone since electrons are mostly scattered into these pitch angles due to their source (ionosphere) being located at altitudes of strong magnetic field and then bounce at MGS altitudes or above. As magnetic loops of strong crustal fields are relatively short, photoelectrons basically come from the ionosphere at one end of the loop, then move along the field line, and are lost to the ionosphere at the conjugate end of the field line, if they are not scattered. As a result, upward electrons, especially PA near 0°, can be considered as fresh photoelectrons coming from the ionosphere while downward electrons (PA near 180°) are those moving along the field lines and towards the sink, far away from their source region.

After applying the contamination filter, the unfiltered Figure 2.3d is identical to the filtered Figure 2.3e since the filter has no effect on energy channels higher than 53 eV. However, for 36 eV, Figure 2.3i has fewer bins than Figure 2.3j because the contamination filter removes some of the data in the pitch angle space. Pitch angles greater than 120° after 350 s, where fluxes are especially high, are absent because fewer sectors are used to determine PADs for low energy channels. In the meantime, the maximum of Figure 2.3j now is 60% of Figure 2.3i with the removal of those high fluxes. As a result, PADs are now more isotropic.

To further confirm that the method above is valid, example energy spectra are shown in Figure 2.4. The three plots correspond to three pitch angle bins, $0^\circ - 10^\circ$, $80^\circ - 90^\circ$, $170^\circ - 180^\circ$, respectively, at the same time period as Figure 2.3. The energy spectrum of every single time is over-plotted, highlighted in different colors, black for 0 s and then green and then red for the latest time, 490 s. Because ER only provides 2D samples of electron fluxes, 90° pitch angle is constantly measured while more field-aligned pitch angles are sampled only part of the time. As a result, only 3-5 spectra are seen in Figure 2.4a and 2.4c while more are seen in Figure 2.4b. Nevertheless, clear photoelectron energy spectrum features, such as the knee at 60-70 eV, the sharp drop at around 500 eV and the cut-off at 800 eV (e.g. *Mitchell et al.*, 2001; *Liemohn* *et al.*, 2003), are seen in Figure 2.4. The absence of the low energy part in Figure 2.4a is due to the spacecraft photoelectron contamination issue described above, resulting in fewer sectors used to calculate low-energy photoelectron fluxes.

2.2.2 Solar Wind Electron Selection

To select the solar-wind/magnetosphere electron precipitation through cusps, where the magnetic topology changes from one closed loop arch to the next, over the strong crustal fields, the same geographic constraints are applied. The cusps are located between the closed magnetic field loops, and are more likely found when the field line is more vertical. Therefore any open magnetic field within the cusp region is more likely to be seen at large magnetic elevation angle at the MGS altitude. Hence, an absolute magnitude elevation angle observed by MGS MAG greater than 45°, is applied, complementary to the magnetic elevation angle criterion for photoelectron selection, because the chance to observe solar-wind/magnetosheath electrons at smaller angles is very low (*Liemohn et al.*, 2003; *Trantham et al.*, 2011). A minimum magnetic field strength of 35 nT to ensure strong crustal fields and a maximum SZA of 90° to select dayside data are also applied.

2.2.2.1 Identifying Solar Wind Electrons

Solar-wind/magnetosheath electrons have been previously identified on the dayside by studies (e.g. *Liemohn et al.*, 2003) of MGS observations. Figure 2.5 shows the measurements of one orbit of MGS on January 15, 2004, starting at universal time (UT) 10:50:00. From around UT 10:54 to UT 11:11, MGS flew through the strong crustal fields (east longitude 190° to 170°, south latitude 80° to 30°) on the dayside (SZA 75° to 30°). The strong crustal fields can usually be identified by the large variation of the elevation angles of the magnetic field, shown in Figure 2.5d, and the large magnitude (a few tens of nT to over 200 nT seen in Figure 2.5e). Figure 2.5f shows

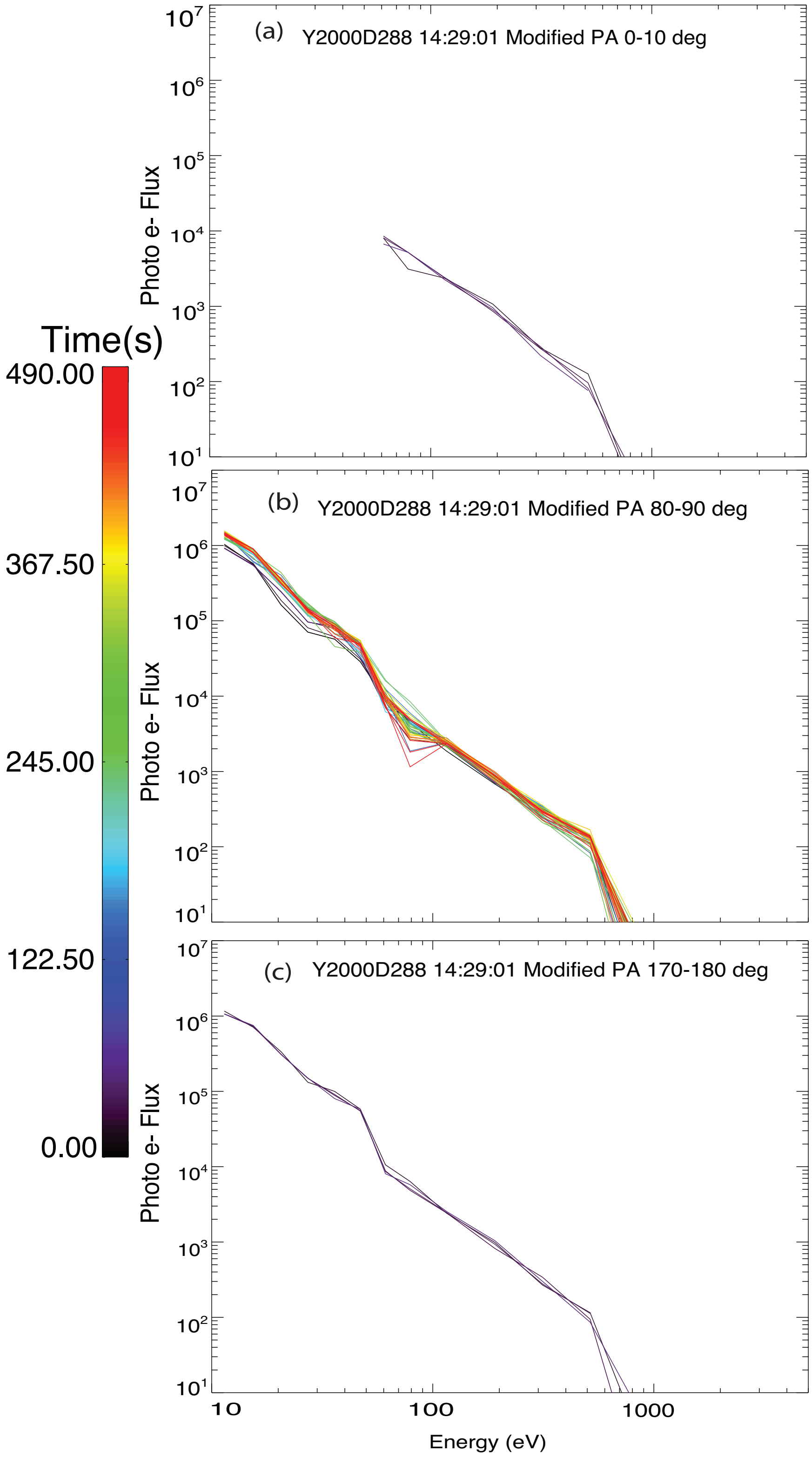

Figure 2.4: Energy spectra of differential number fluxes ($cm^{-2}s^{-1}ster^{-1}eV^{-1}$) at three different pitch angles, $0° - 10°$, $80° - 90°$, $170° - 180°$, a, b, c, respectively. Colors highlight different data points within the same time period as Figure 2.3.

the differential number flux (# $eV^{-1}cm^{-2}s^{-1}sr^{-1}$) for 36 eV and 115 eV two energy channels at pitch angle (PA) $150° - 160°$. Within the first minute, MGS was around the terminator (SZA $\sim 90°$) and the fluxes for both channels are relatively high and then drop significantly when the satellite flew through the crustal fields as the electron population switched from solar-wind/magnetosheath electrons, with higher fluxes, to the ionospheric originated photoelectrons, with lower fluxes. The flux drop for the two channels are different, a factor of ~ 2 decrease for the 36 eV channel and a much larger (over an order of magnitude) decrease for the 115 eV channel. This different amount of flux drop is due to one of the photoelectrons' features: the sharp drop of photoelectron fluxes around 60 eV, the so-called "knee" in the energy spectra (due to the sharp drop in solar photons below 15 nm) while for solar-wind/magnetosheath electron spectra, the decrease of electron fluxes is much slower (e.g. *Fox and Dalgarno*, 1979; *Mantas and Hanson*, 1979; *Crider et al.*, 2000; *Mitchell et al.*, 2001; *Liemohn et al.*, 2003). In other words, the flux ratio of the 36 eV and 115 eV channels is much higher for photoelectrons than solar-wind/magnetosheath electrons, as shown in Figure 2.5g.

However, the fluxes jump back to their original high values occasionally during the flight over the strong crustal fields (Figure 2.5f), such as at UT 10:58 and UT 11:04. Magnetic fields with near 90° elevation angles are more likely to be connected to the IMF, thus a higher possibility of solar-wind/magnetosheath electrons entering the Martian atmosphere. These spikes seem to correspond to high elevation angles by comparing Figure 2.5 d and f, thus considered as solar-wind/magnetosheath electron precipitation through the magnetic field lines inside the cusps on the dayside. Furthermore, data points with flux ratios below the dashed line in Figure 2.5g (ratio=27) are marked with black dots in Figure 2.5d, marked as T1 and T2. Over the strong crustal fields (UT 10:54 - 11:11), the low flux ratios are seen at elevation angles near 90°, as expected.

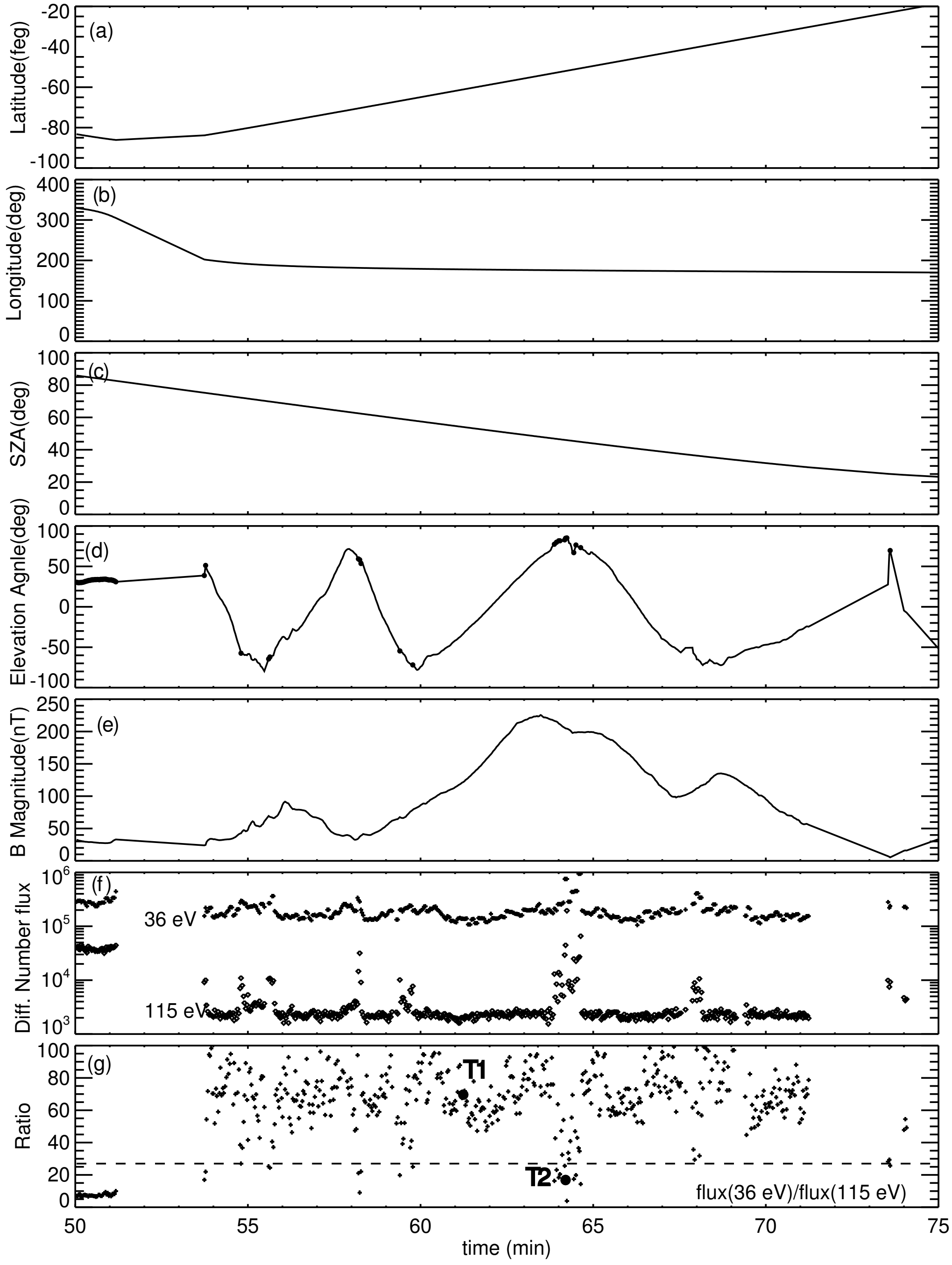

Figure 2.5: One orbit example: MGS data for January 15, 2004, the x-axis is the time in minuets, starting from UT 10:00:00. Shown are (a) MGS location over Mars in latitude; (b) MGS location over Mars in east longitude; (c) MGS solar zenith angle; (d) The elevation angle of the magnetic fields; (e) The magnitude of the magnetic fields; (f) Differential number flux (# $eV^{-1}cm^{-2}s^{-1}sr^{-1}$) for 36 eV and 115 eV two energy channels at PA $150° - 160°$; (g) The flux ratio of the two energy channels shown in (f). The dashed line in (g) is a ratio of 27. The black dots in (d) are when the flux ratios are below this dashed line. The two black dots in (g) are two points used for Figure 2.6.

The basic idea is to separate solar-wind/magnetosheath electrons and ionospheric photoelectrons by utilizing the different flux ratios of the two populations, with one energy channel smaller than the energy of this knee, e.g. 36 eV, and one channel larger, e.g. 115 eV. To further validate this idea, the energy spectra (differential number flux at PA 150° $\sim$ 160° against energy in eV) of two data points with a high and low flux ratio (T1 and 2 in Figure 2.5g, respectively) are shown in Figure 2.6. The solid line is for the higher ratio ($\sim$ 70, T1) while the dashed line is for the lower ratio ($\sim$ 20, T2), with the dotted line showing the instrument background flux. The energy spectrum for T1 shows some ionospheric photoelectron features: the knee around 60 eV and also the sharp decrease of fluxes around 500 eV due to the extremely small source term for energies above. However, for T2, none of these features are seen. This characteristic difference in energy spectra for high and low flux ratios holds for all the examples that we individually examined. Hence, it is reasonable to distinguish the two populations by analyzing the statistical results of their flux ratios over the whole mapping phase of MGS, from Earth year 1999 to 2007.

The left column of Figure 2.7 is the ratio of electron fluxes at 36 eV and at 115 eV against time while the right column is the histogram of the left plots. Each row is for different "modified pitch angles", from top to bottom: $0°-10°$, $40°-50°$, $80°-90°$, and $170°-180°$. As shown in the first row of Figure 2.7, when the pitch angle is $0°-10°$, the ratio is centered at a few tens and the distribution over 7 years is an approximately Gaussian distribution, peaked at a flux ratio $\sim$ 50. Since this peak flux ratio is closer to that of T1 ($\sim$ 70), i.e. the photoelectron sample, these electrons are likely fresh ionospheric photoelectrons, propagating upward. As the pitch angle increases, especially for the downward pitch angle bins, such as $170° - 180°$, ratios extend below 20 while the histogram starts to show a bimodal distribution. A Gaussian-like distribution centers at a ratio of around 60, which resembles the population seen above at upward field-aligned pitch angles as ionospheric photoelectrons. In

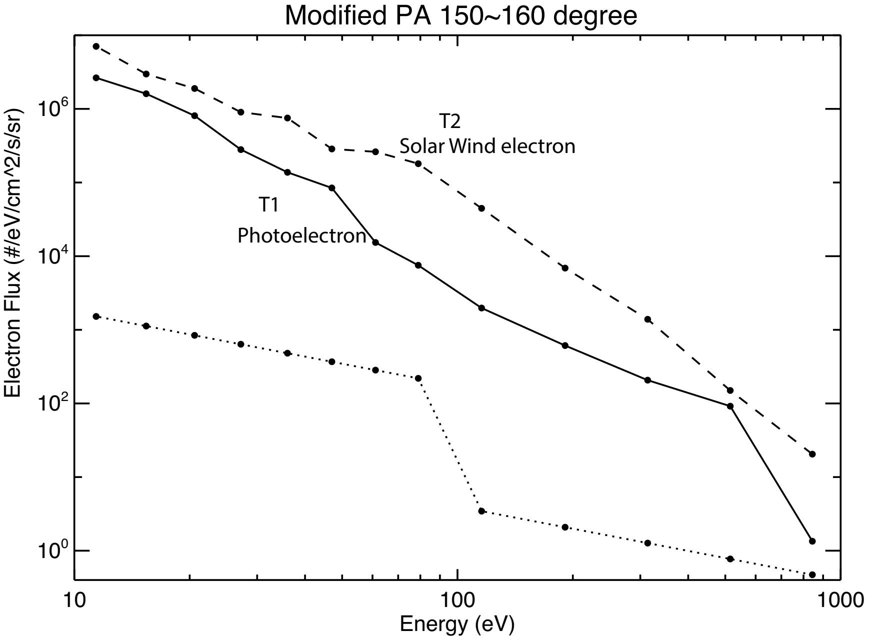

Figure 2.6: Energy spectra (differential number flux at PA 150° − 160° against energy in eV) of the two black dots in Figure 2.6. The solid line is for the higher ratio (T1) while the dashed line is for the lower ratio (T2). The dotted line is the instrumental background flux.

addition, another peak of a lower ratio, around 10, is also shown, indicating another population of electrons. i.e. solar-wind/magnetosheath electrons. This population change at different pitch angles (PAs) can be explained as follows. Over the strong crustal field, electrons that move along the magnetic field line away from the planet (PA $< 90°$) most likely originated in the ionosphere. For pitch angles greater than 90°, electrons either originated in the ionosphere in the conjugate leg of the same magnetic field loop or originated in the solar wind/magnetosheath, precipitating into the atmosphere through an open magnetic field line (most likely inside the cusps). The second population, as shown in PA $40° - 50°$ of panels in the second row, is possibly reflected solar-wind/magnetosheath electrons due either to the collisional scattering with the neutral atmosphere and/or charged particles or to the magnetic mirroring effect as the magnetic field strength increases when closer to the planet above the strong crustal field regions. The existence of these reflected electrons suggests a loss cone of $< 40^\circ$. Notice that the y ranges of the histogram plots in Figure 2.7 are different. There are fewer data samples at more field-aligned pitch angles ($\sim 0^\circ$ or 180°) than more perpendicular pitch angles ($\sim 90^\circ$), due to the 2D FOV (field of view) of the instrument.

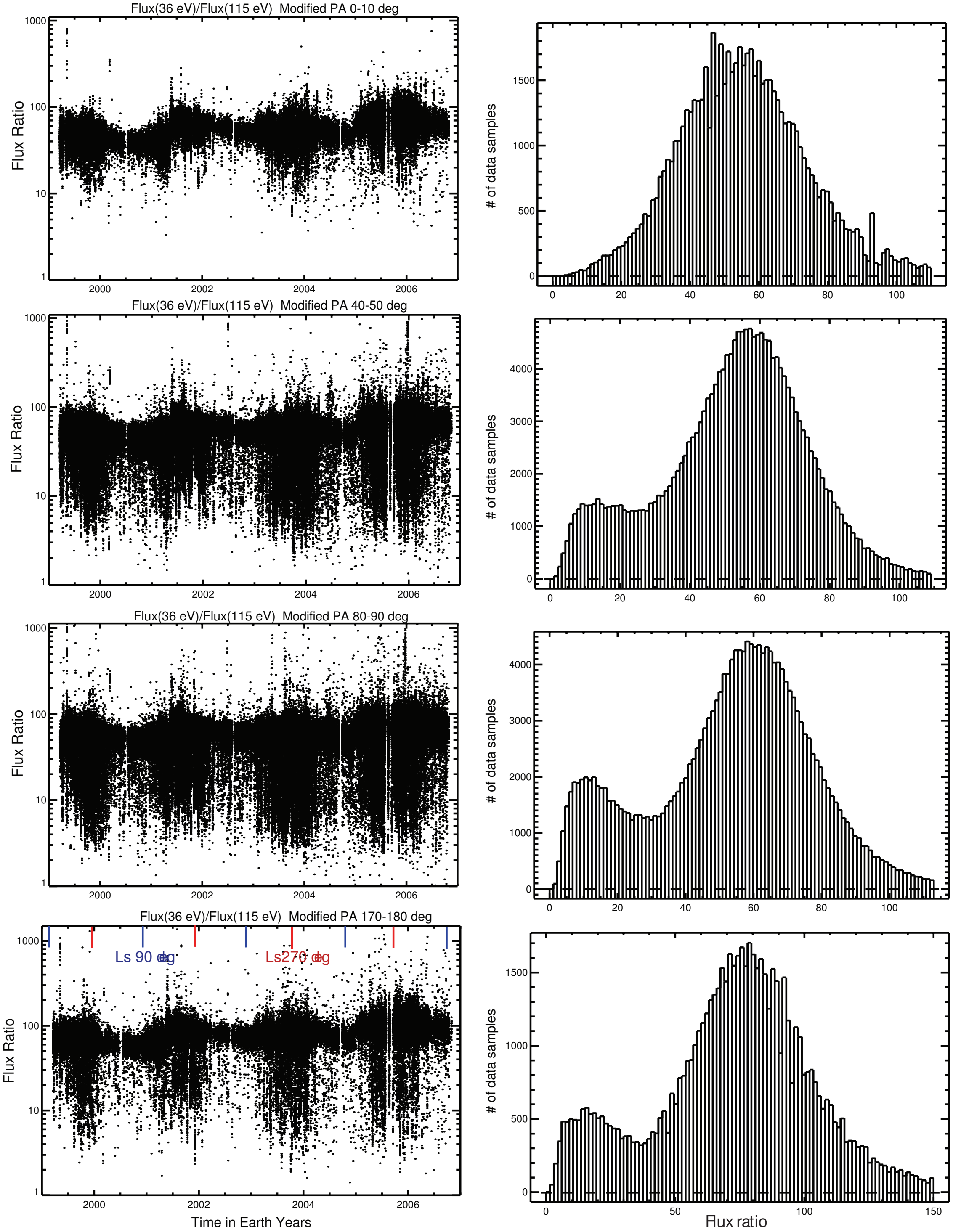

Figure 2.7: The left column is the ratio of electron fluxes at 36 eV and at 115 eV against time; the right column is the histogram of the left plots. Each row is for different "modified pitch angles", from top to bottom: $0° - 10°$, $40° - 50°$, $80° - 90°$, and $170° - 180°$. The blue and red ticks in the lowest left panel mark solar longitude (Ls) of 90° and 270°, i.e. Martian southern winters and summers, respectively

CHAPTER III

Methodology: Modeling

Another means to conduct this thesis study is through simulations with a superthermal electron transport model. Unlike Earth, the magnitude of the magnetic fields at Mars can change rapidly within a few hundred kilometers in altitude. Hence the model tool of the Martian environment requires a sophisticated theoretical description and the ability to modulate arbitrary magnetic fields. The superthermal electron transport (STET) model is a multi-stream model that calculates the superthermal electron distribution function from the gyration-averaged Boltzmann kinetic equation and simulates the superthermal electron transport along a flux tube (*Liemohn et al.*, 2003). It was initially developed for the Earth environment (*Korablev et al.*, 1993; *Khazanov and Liemohn*, 1995; *Liemohn et al.*, 1997) and has then been modified for the Martian upper atmosphere (*Liemohn et al.*, 2003, 2006). This model not only satisfies the aforementioned requirements to simulate electron transport in the Martian environment but also has the potential to model time-dependent processes. In this chapter, the description of the model is first given, followed by the validation of the model. Finally, some development, incorporating two new solar irradiance models into STET, has been done.

3.1 STET Model Description

Starting with the Bolzmann kinetic equation (also equation 1 of *Khazanov et al.* (1994)), assuming that the electron Larmor radius of superthermal electrons is small compared to the gradient of the local magnetic field (*Liemohn et al.*, 2003), the guiding center approximated version in the coordinate system [t, E, μ, s] is expressed as

$$\frac{\beta}{\sqrt{E}}\frac{\partial\psi}{\partial t} + \mu\frac{\partial\psi}{\partial s} - \frac{1-\mu^2}{2}\left(-\frac{F}{E} + \frac{1}{B}\frac{\partial B}{\partial s}\right)\frac{\partial\psi}{\partial\mu} + EF\mu\frac{\partial}{\partial E}\left(\frac{\psi}{E}\right) = \\ Q + S_{ee} + \sum_{\alpha}\left(S_{e\alpha} + S^{*}_{e\alpha} + S^{+}_{e\alpha}\right) + \sum_{i}\left(S_{ei} + S^{*}_{ei} + S^{-}_{ei}\right) \tag{3.1}$$

where E is the electron energy in eV, s is the coordinate along the local magnetic field line, and θ is the electron pitch angle (PA), the constant $\beta = 1.7 \times 10^{-8} eV^{1/2} cm^{-1} s$, $\mu = \cos\theta$. The force due to a parallel electric field is $F = eE_{\|}$, in units of eV cm^{-1}. S_{ee} describes collisions with Maxwellian/thermal electrons, $S_{e\alpha}$ and S_{ei} elastic collisions with neutral and ion species, $S^{*}_{e\alpha}$ and S^{*}_{ei} account for excitation of neutral and ion species, $S^{+}_{e\alpha}$ and S^{-}_{ei} ionization and recombination, and Q the electron production rate due to photoionization of neutral species. $\psi(t,\, E,\, \mu,\, s)$ is the differential flux of electrons and $\psi dEd\Omega$ is the flux of electrons with energy from E to $E + dE$ inside a solid angle $d\Omega$ at a point s along the field.

Note that the use of a guiding center approximation for these calculations is justified because the gyroradius of the simulated electrons is always less than the radius of curvature of the field lines as well as less than the spatial grid step. For instance, the lowest magnetic field values used in the calculations below is 10 nT, which results in a gyroradius of 1 km and 3.4 km for 10 and 100 eV electrons, respectively. The magnetic field radius of curvature, for the fields applied in this study, are at a minimum 50 km and usually much larger than this. In addition, the step size used in these regions of low magnetic field will always be larger than the electron gyroradius within our simulation energy range.

Due to the much larger densities of neutral species than ions and the small cross section of dissociative recombination for superthermal electrons, the terms S_{ei}^{*} and S_{ei}^{-} are generally neglected. The rest of the collision terms can be expressed as:

$$S_{ee} + S_{ei} = An_e \left\{ \frac{\partial}{\partial E}\left(\frac{\psi}{E}\right) + \frac{1}{2E^2}\frac{\partial}{\partial \mu}\left[\left(1-\mu^2\right)\frac{\partial \psi}{\partial \mu}\right] \right\} \tag{3.2}$$

$$S_{e\alpha} = \frac{n_\alpha \sigma_\alpha^{(1)}}{2}\frac{\partial}{\partial \mu}\left[\left(1-\mu^2\right)\frac{\partial \psi}{\partial \mu}\right] \tag{3.3}$$

$$S_{e\alpha}^{*} = n_\alpha \sum_j \left[\sigma_{\alpha j}^{*}(E+E_{\alpha j}^{*})\psi(E+E_{\alpha j}^{*},\mu) - \sigma_{\alpha j}^{*}(E)\psi(E,\mu)\right] \tag{3.4}$$

$$S_{e\alpha}^{+} = n_\alpha \int\limits_{E+E_\alpha^+}^{2E+E_\alpha^+} I_\alpha^+(E', E'-E-E_\alpha^+)\psi(E',\mu)\mathrm{d}E'$$
$$+\frac{n_\alpha}{2\pi}\int\limits_{2E+E_\alpha^+}^{\infty} I_\alpha^+(E',E)\int\limits_0^{2\pi}\psi(E',\sqrt{1-\mu^2}\cos\eta)\mathrm{d}\eta\mathrm{d}E' - n_\alpha\sigma_\alpha^+(E)\psi(E,\mu) \tag{3.5}$$

where $A = 2\pi e^4 ln\Lambda = 2.6 \times 10^{-12}$ eV^{2}cm^2, and $ln\Lambda$ is the Coulomb logarithm, n_α is the density of neutral species α, $\sigma_\alpha^{(1)}(E) = \int I_\alpha(E,\chi)(1-\cos\chi)\mathrm{d}\Omega$ is the transport cross section, χ is the scattering angle, and $I_\alpha(E,\chi)$ the differential elastic cross section, $\sigma_{\alpha j}^{*}$ is the total cross section of scattering to excite a neutral particle with a threshold energy $E_{\alpha j}^{*}$, and the ionization energy is E_α^+. The total cross section of ionization by an electron with an energy E is

$$\sigma_\alpha^+(E) = \int\limits_0^{(E-E_\alpha^+)/2} I_\alpha^+(E,E_2)\mathrm{d}E_2 \tag{3.6}$$

where $I_\alpha^+(E, E_2)$ is the appropriate differential cross section, and E_2 is the energy of a secondary electron.

The detailed simplification of these collision terms are described in *Khazanov et al.* (1994). In addition, terms of order of m_e/m_i, where m_e and m_i are the mass of electron and ions, respectively, and second derivatives with respect to energy are also omitted from the calculation (*Khazanov et al.*, 1994).

As said in the Introduction, the magnetic field magnitude on Mars can change by a factor of ten within a few hundred kilometers, which means a larger variation of the local pitch angle than found at Earth. To avoid a non-Cartesian grid, which may increase the approximation errors of the derivatives $\partial/\partial s$ and $\partial/\partial\mu$, the kinetic equation is rewritten in s-μ_0 space, instead of s-μ space. Here $\mu_0 = \cos(\theta_0)$ and θ_0 is the pitch angle at the location of minimum B, also referred to as minimum-B pitch angle. The transformation from the local pitch angle μ to the minimum-B pitch angle μ_0 is

$$\mu_0 = \frac{\mu}{|\mu|}\sqrt{1 - \frac{B_0}{B}(1 - \mu^2)} \tag{3.7}$$

where B_0 is the minimum B strength along the field line. Figure 3.1 (Figure 7 of *Liemohn et al.* (2003)) shows the corresponding s-μ_0 space to s-μ space, and a Cartesian grid is applicable with the removal of the $\partial B/\partial s$ term. With this new space, only slow collisional processes redistribute the electrons in μ_0.

The code was designed to well resolve the "slow" process of pitch angle scattering. Hence equation (1) is rewritten as a diffusion equation in s-μ_0 space,

$$\left(\sqrt{\frac{m}{2E}}\frac{\partial\psi}{\partial t} + \mu\frac{\partial\psi}{\partial s} + C_1\frac{\partial\psi}{\partial E}\right) + C_2\frac{\partial}{\partial\mu_0}\left(C_3\frac{\partial\psi}{\partial\mu_0}\right) = Q \tag{3.8}$$

In equation 3.8, the coefficients C_1, C_2 and C_3 include summations over various neutral and plasma species in the Martian upper atmosphere. In equation 3.8, the

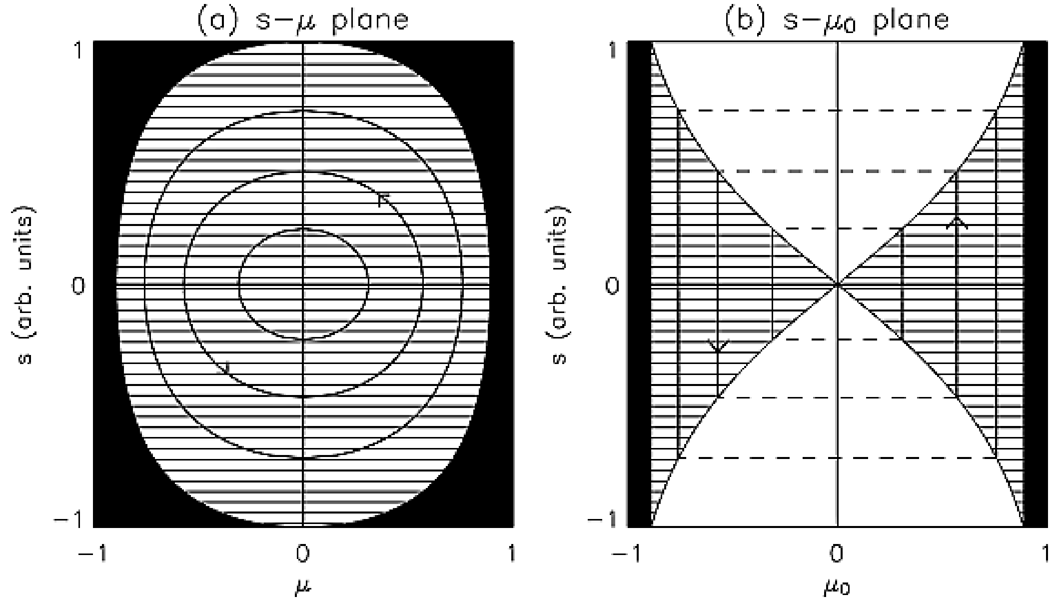

Figure 3.1: Schematics of superthermal electron trajectories as a function of spatial distance along the field line and pitch angle from the left-hand side of equation 3.1, showing the trajectory dependence on (a) local pitch angle (s-μ space) and (b) equatorial pitch angle (s-μ_0 space). Also Figure 7 of *Liemohn et al.* (2003).

spatial transport derivative (the second term) and the energy degradation derivative (the third term) are treated analogously as the time derivative in a standard diffusion equation, a numerical technique developed by *Khazanov* (1979). By using a finite-difference approximation for these real/pseudo- time derivatives,

$$\frac{\partial \psi}{\partial t} = \frac{\psi - \psi^{t-\Delta t}}{\Delta t} \tag{3.9}$$

$$\frac{\partial \psi}{\partial s} = \begin{cases} \frac{\psi - \psi^{-s}}{\Delta s} & \mu_0 > 0 \\ \frac{\psi - \psi^{+s}}{\Delta s} & \mu_0 < 0 \end{cases} \tag{3.10}$$

$$\frac{\partial \psi}{\partial E} = \frac{\psi^{E} - \psi}{\Delta E} \tag{3.11}$$

equation 3.8 can be reduced to

$$\frac{\partial^2\psi}{\partial\mu_0^2} + D_1\frac{\partial\psi}{\partial\mu_0} - D_2\psi = D_3. \tag{3.12}$$

where $\psi^{t-\Delta t}$ is ψ at the previous time step; ψ^{+s} and ψ^{-s} are ψ at the next upper and lower s step; ψ^E is the ψ at the next higher energy step; Δt, ΔE, and Δs are the step lengths in t, E, and s. Coefficients D_1, D_2 and D_3 are functions of the variables t, s, μ_0 and E. More details of the derivation can be found in *Khazanov* (1979) and *Gefan and Khazanov* (1990).

The analogy of the spatial transport derivative and energy degradation derivative to the time derivative disadvantages the resultant scheme in resolving propagation fronts along the field line but well suits for resolving the long-term development, evolution, and interplay between the source cones and trapped zone (*Liemohn et al.*, 2003).

The last PA grid of each spatial location requires a special formula for the calculation of the flux at this grid point, denoted as k_{end} (*Liemohn*, 1997):

$$\psi_{k_{end}} = \left[\frac{\beta\psi^{t-\Delta t}}{\sqrt{E}\Delta t} + \frac{\mu\psi^{s-\Delta s}}{\Delta s} + \frac{\xi\psi^{E-\Delta E}}{\Delta E} + Q + S + \frac{p_{end}}{2}\left(\psi^{+}_{k_{end}-1} + \psi^{-}_{k_{end}-1}\right)\right] / \left(p_{end} + \frac{\beta}{\sqrt{E}\Delta t} + \frac{\mu}{\Delta s} + \frac{\xi}{\Delta E} + L\right) \tag{3.13}$$

where p_{end} stands for the fraction of the electron flux scattered from the pitch angle $k_{end} - 1$, and “+” and “-” superscripts indicate upward and downward flowing flux, respectively. S here is the source due to cascading and L represents the energy degradation due to collisions. Finally, $\xi = An_e/E$, related to the Coulomb collision. At very low altitudes, the scattering terms with p_{end} dominate the numerator and denominator of this equation, resulting in a nearly isotropic distribution. At higher altitudes, either the Δt or Δs terms will dominate this equation. However, in our set up for these simulations with a very large Δt (i.e., jump to steady state), there is one exception. At the spatial location of minimum B, the local μ value for k_{end} is $\mu = 0$, and therefore the transport terms drop to zero. This allows other, usually negligible, source terms to dominate the equation, which can result in an anomalously large flux value in this one point of the $s - \mu_0$ grid. To correct this issue, we add some small transport to PA = 90°, as would be the case if some small perturbations were present. The specific implementation of this small transport effect is defined such that $\mu(k_{end}, i) = (\mu(k_{end} - 1, i) + \mu(k_{end} - 1, i + 1))/8$, where i indicates the spatial grid points.

The boundary conditions applied to STET are as follows. For the energy grid, it is assumed that the flux above the highest energy step is zero. For the spatial grid, it is assumed that there is no source below the lowest altitude step and that any downward-directed flux at this location is lost. If the field line is "open" and connected to the solar wind at either or both ends, then the highest altitude spatial step will have an imposed downward-directed electron flux and the upward fluxes are assumed to be lost.

The cross-section information of photoionization and excitation for Mars environment used in the model is from *Fox* (1991), with an updated electron impact cross-section from *Sung and Fox* (2000). The neutral and ionospheric density profiles for Mars upper atmosphere are linearly interpolated from the Mars Thermospheric General Circulation Model (MTGCM) (*Bougher et al.*, 1988, 1994, 2001) within MTGCM's calculation domain from 100 km to 240 km. Above this altitude, both the neutral and electron densities are linearly extrapolated from the logarithm of the two topmost values from MTGCM. For now, the STET model uses the Hinteregger-81 model (*Hinteregger et al.*, 1981) as solar irradiance input, scaled by $F_{10.7}$, with the additional correction from *Solomon et al.* (2001), i.e. multiplying the flux of photons for wavelengths below 25 nm by a factor of 4. The modeled photon flux, actually Earth values, is then scaled to Mars values by accounting for the relative distance of both planets from the Sun.

3.2 STET Model Validation

Even though this superthermal electron transport (STET) model has already been used to simulate the Martian environment (*Liemohn et al.*, 2003, 2006), this section provides rigorous numerical convergence tests on the STET model. In addition, three physical parameters, $F_{10.7}$ values, thermal electron/plasma density and neutral densities, are examined. These tests not only demonstrate the STET model's ability to handle a large range of inputs but also verify the performance of the model. The final validation of the model is through the comparison between the model and the observations from the magnetometer/electron reflectometer instrument on board Mars Global Surveyor.

3.2.1 Convergence Tests

Firstly, convergence tests for the pitch angle (PA) grid, spatial grid and energy grid have been conducted. Figure 3.2 shows the neutral density profiles of O, O_2, N_2, CO_2, CO, thermal electron density and also neutral temperature against altitude from MTGCM for the superthermal transport code. The MTGCM run was at an Ls of 90 degree with an Earth F10.7 of 100 sfu.

If it is not specified, then the standard setup for this model validation section is an Earth F10.7 value of 100 sfu, 1.57 astronaut unit (AU) as the Sun-Mars distance to scale the modeled Earth EUV fluxes, which is about the average distance, and a constant energy step of 1 eV for the range 0.5-200.5 eV. Also, the solar zenith angle is set as 10°. Symmetric closed B field lines, as shown in Figure 3.3, and the same background atmosphere and illumination for the two legs of the B fields, are given. Because of the symmetry, only results of photoelectrons flowing in the "+s" direction (i.e. from s=0 km to maximum s) are shown in the following sections. That is, the

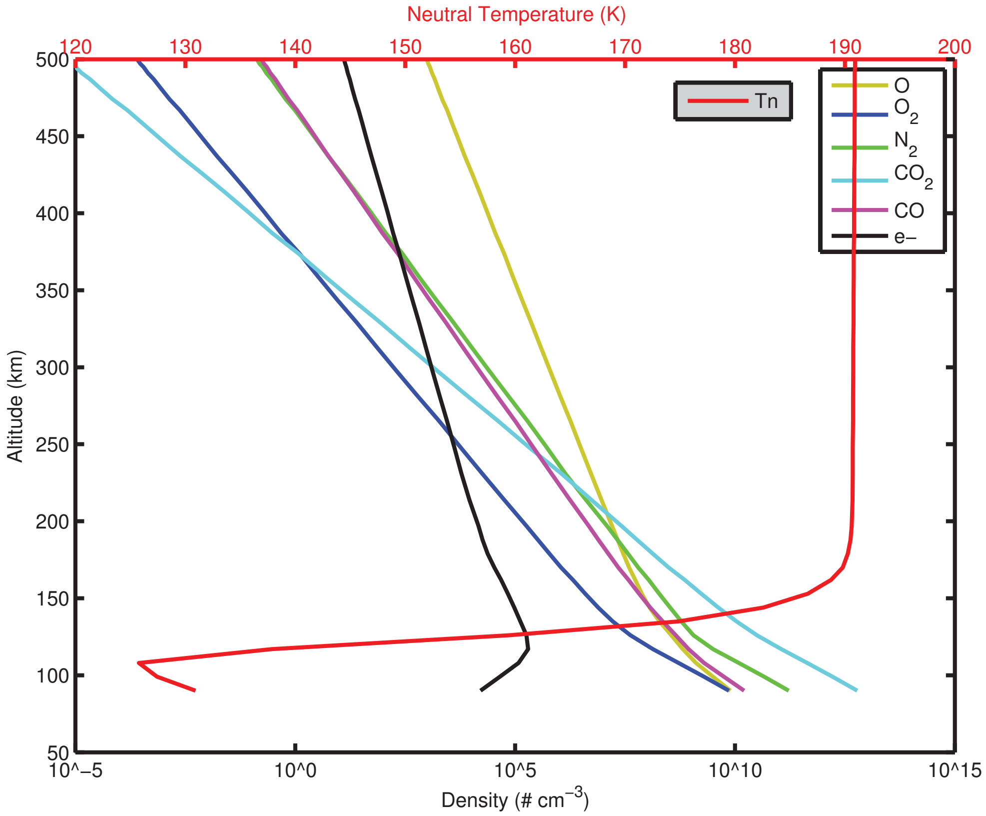

Figure 3.2: Neutral densities, thermal electron density and neutral temperature of Mars to be used in the calculations that follow, from MTGCM against altitude near solar minimum, $L_s = 90^\circ$ condition.

electron fluxes in the +s direction look identical to those in the -s direction at an equivalent distance from the source region. While the distance variable s starts at z=0, the calculation does not start at the surface of the planet, rather it starts at z=90 km in the simulations presented below. Furthermore, for the case of precipitating electrons along an open field line, the calculation can start at the top of the simulation domain where the source of the particles is applied. Note that there are other "standard" field line configurations at Mars, namely open lines connected to both Mars and the solar wind and draped solar wind field lines. They will not be examined here because the primary difference is the boundary condition.

These runs are steady-state with a time step set to be 10^5 s, approximately one day, so large that the $\partial/\partial t$ term is mostly negligible. The convergence criteria is $|\psi - \psi_{last}|/\psi < 0.01$, where ψ and ψ_{last} are the electron flux at the current time step and the last time step. However, the STET model is capable of simulating time-dependence cases, simply setting the time step to an appropriately small value so that the $\partial/\partial t$ term plays a role, and has been applied to Earth space environment (e.g. *Liemohn*, 1997). The time-dependent simulations for Mars environment are planned as future work.

3.2.1.1 Pitch Angle Grid

Two different field line configurations, a short B field line (green) and a long B field line (red), are shown in Figure 3.3; Figure 3.3a - 3.3b for distance s, and B strength against altitude and Figure 3.3c for B strength against distance s. For the pitch angle grid convergence test, the short B field line will be used. The distance step size ds is 5 km below 200 km to well resolve the ionosphere and 10 km above this altitude. Also, the dotted line in Figure 3.3a marks the relationship for a vertical B field line for comparison.

As said in section 3.1, the calculation is in '$\mu_0 - s$' space instead of 'pitch angle-s'

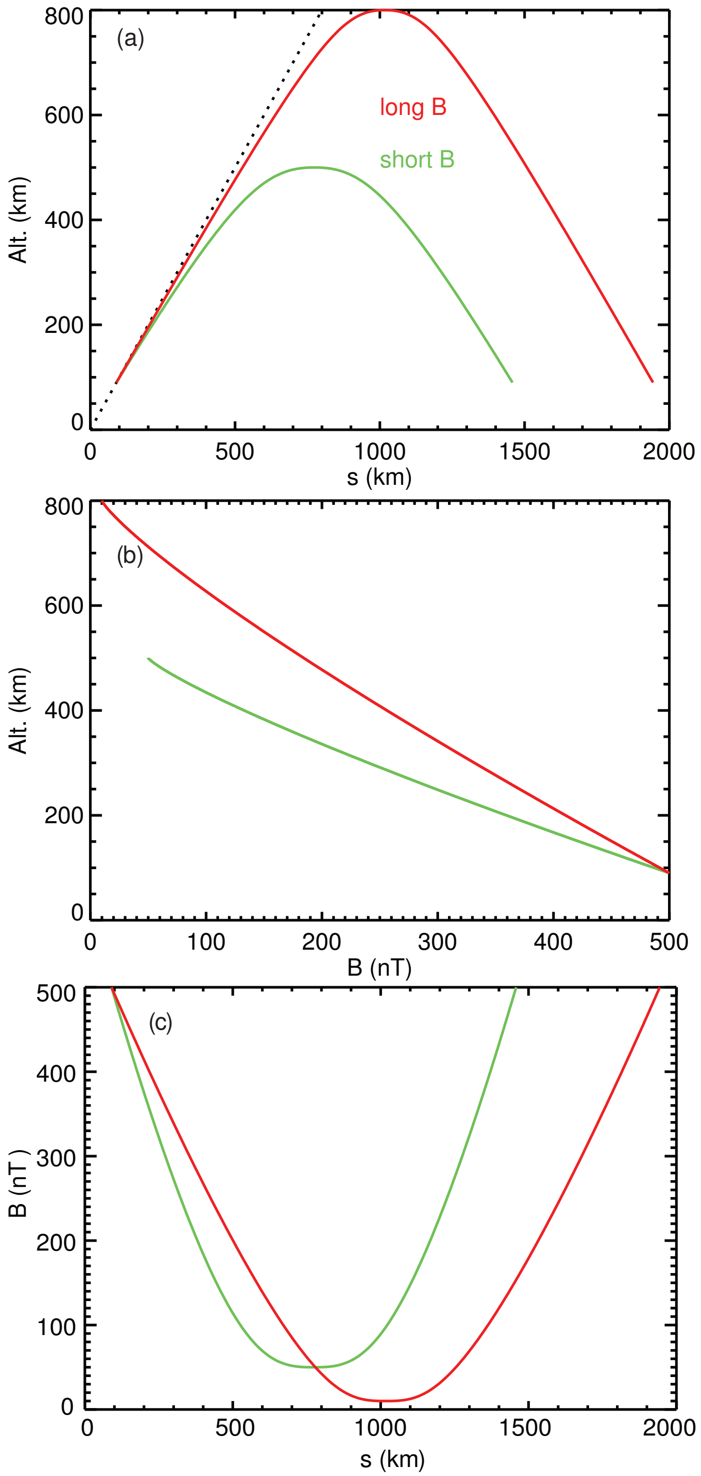

Figure 3.3: Two magnetic field configurations used in this study, the short B field line highlighted in green and the long B field line in red. (a) B field lines' altitude against distance s, and the dotted line sketches a perfect vertical B field line; (b) B field strength against altitude; (c) B field strength against distance s.

space, the transformation from pitch angles to μ_0 is not only as a function of cosine but also determined by the local magnetic strength relative to the minimum magnetic field strength. This non-linear transformation, although providing advantages described in the section 3.1, makes the pitch angle grid setup not so straight forward. A constant μ_0 grid was tested but yields very large θ_0 spacing in the high-B-field ionospheric source region of the photoelectrons. To ensure several pitch angle grid steps in the ionosphere, therefore, a different approach was used. The pitch angle (PA) grid is set up as follows: a uniform minimum-B pitch angle θ_0 for all grid points except for the last pitch angle step size. The last PA step size is calculated as $\Delta\theta_0(top) = 90° - \sin^{-1}(\sqrt{B(s_{top})/B(s_{top-1})})$, i.e. the difference of 90° and θ_0 at the second-to-top location ($\theta_0(s_{top} - 1) = \sin^{-1}(\sqrt{B(s_{top})/B(s_{top-1})})$). The exception of the last pitch angle step size is to ensure the grid number K increase is no larger than 1 for the top s grid, which otherwise not only is a waste of grids but also can cause numerical issues. To calculate the pitch angle step sizes, take a total of 10 grid points as an example, it is $x * (10 - 1) + 1° = 90°$, where 1° is the last step size. In this case, x=9.9°. Four different total pitch angle grid numbers, 6, 10, 20, and 40, are tested. For this particular B field line, it is translated into the uniform minimum-B pitch angle step size of θ_0 of 17.8°, 9.9°, 4.7°, 2.3°, respectively, and also 1.0° for the last step size.

The results are shown in Figure 3.4. The three rows are for three energies: 21 eV, 111 eV, and 196 eV. The left and middle columns are the differential number flux at local PA = 0° and 90°, respectively, against distance s. For the left column, the differential number fluxes are almost the same, unaffected by the different total pitch angle grid numbers. The fluxes firstly increase rapidly, mostly because of the source production by photoionization in the neutral atmosphere, then decrease slightly at $s \sim 200$ km due to the decreased source and loss processes, such as scattering, and slightly increase again at $s \sim 1300$ km caused by the source production in the other ionosphere. For the middle column (local PA=90°), the fluxes are now influenced by the pitch angle grid size and converge as the grid step size is reduced. The right column shows the differential number flux against pitch angle at the top of the B field line. The pitch angle distributions are the typical source-cone distribution (high fluxes at PAs near 0° and low fluxes at PAs near 90°). The left and right columns show that, with decreased pitch angle grid size, the flux distribution is more smooth and that a grid number of 10 is needed to resolve the pitch angle grid.

The example of a pitch angle distribution at each distance step with a total pitch angle grid of 20 is shown in Figure 3.5. Three rows are for three energies: 21 eV, 111 eV, and 196 eV. The left column is the minimum-B pitch angle distribution, also an example of how the grid is actually setup in the calculation domain, while the right column shows the local pitch angle distribution. The white lines in the right column mark the same minimum-B pitch angles for different local pitch angles at each s location. The pitch angle distribution is quite isotropic for altitudes lower than 350 km, corresponding to s $<$ 400 km and $>$ 1150 km, and rapid drop of fluxes at PA near 90° happens at higher altitudes due to the conservation of the first adiabatic invariant.

3.2.1.2 s Grid

With the knowledge of an appropriate pitch angle step size, the next step is to test the s grid of the short B field line with a total PA grid number of 20, although the pitch angle grid size changes slightly according to the last s grid step, which determines the last pitch angle grid step size. To ensure the ionosphere is well resolved, the s grid step size under altitude of 200 km is half of that above 200 km. The results of the four combinations of s grid step size, (20, 40), (10, 20), (5, 10), and (2.5, 5) (in km), are shown in Figure 3.6. The corresponding PA grid step sizes are, (4.47°, 5.1°), (4.62°, 2.2°), (4.68°, 1.0°), (4.72°, 0.3°), the former number for 19 uniform PA

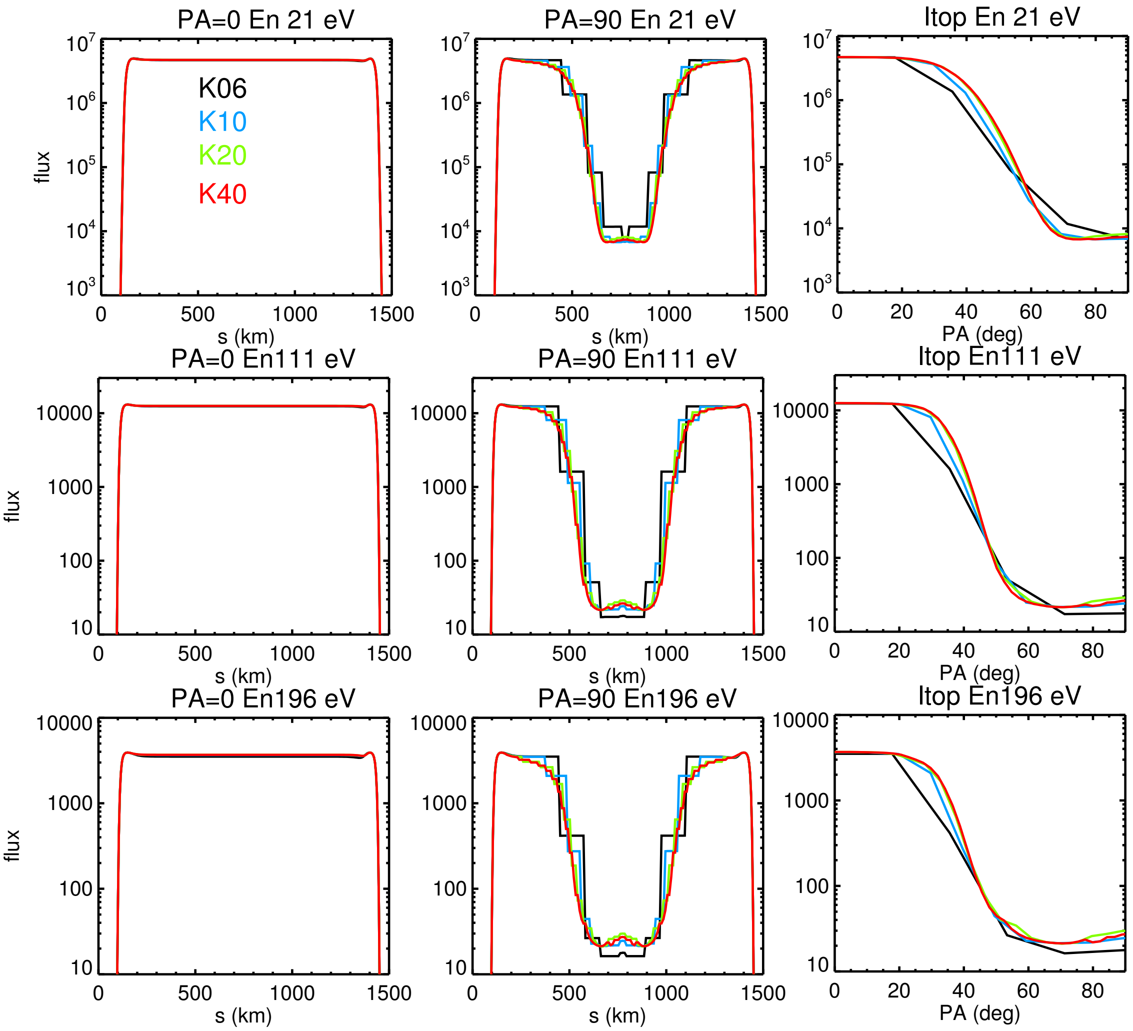

Figure 3.4: Results of different total pitch angle grid number, 6, 10, 20, and 40, highlighted in black, light blue, green, and red, respectively, in each plot. Three rows are for three energies: 21 eV, 111 eV, and 196 eV. The left and middle columns are the differential number flux (cm^{-2} s^{-1} eV^{-1} sr^{-1}) at PA = 0° and 90°, respectively, against distance s. The right column shows the differential number flux (cm^{-2} s^{-1} eV^{-1} sr^{-1}) against pitch angle at the top of the B field line.

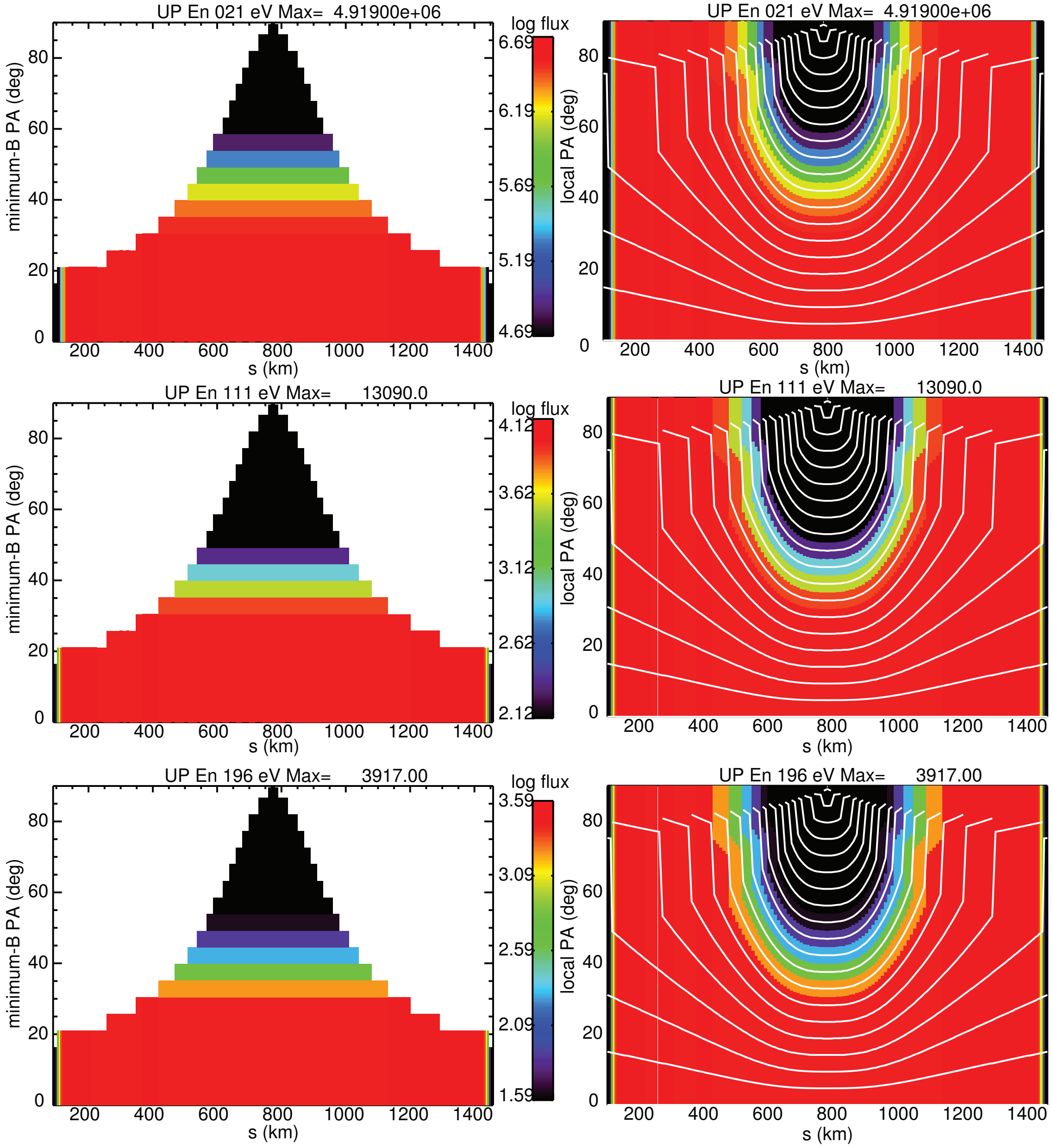

Figure 3.5: Pitch angle distributions along the whole B field for the run with a total pitch angle grid number of 20. Three rows again are for three energies: 21 eV, 111 eV, and 196 eV. The left column is the minimum-B pitch angle distribution while the right column shows the local pitch angle distribution. The color shows the differential number flux in log scale, with a range from the maximum flux to 2 orders of magnitude smaller, and the white lines in the right column mark the same minimum-B PA.

step size and the latter for the last step size. Similar to Figure 3.4, the three rows of Figure 3.6 are for three energies: 21 eV, 111 eV, and 196 eV.

The left and middle columns are the differential number flux at local PA = 0° and 90°, respectively, against distance s. These are not pitch angle distributions at a given altitude but rather flux values at a constant local pitch angle value as a function of altitude. In the middle column, which shows the altitude profile of fluxes for the locally-mirroring pitch angle, note that the finer spatial resolution results have a stair-step profile at high altitudes while the coarser spatial resolution results appear to be smoother at these altitudes (e.g., compare the red and black curves). This is because of the relationship between the spatial and pitch angle grids due to the changing magnetic field strength along the field line. Because these simulations were conducted with a fixed configuration for the minimum-B pitch angle steps, the addition of more spatial grid points along the field line results in several spatial locations with the same Ko(i) (i.e., number of minimum-B pitch angle steps for that i_{th} spatial location). Because transport dominates at the higher altitudes, the lowest altitude for a particular Ko(i) value will dominate the flux level, as seen by the nearly constant flux values for each K increment in the left column of Figure 3.5. This results in a stair-step profile for the PA = 90° flux values. For coarser spatial step sizes at high altitudes, Ko(i) will increment more often, perhaps with every spatial step, resulting in a smoother altitude profile for the locally mirroring fluxes. The right column shows the differential number flux against pitch angle at the top of the B field line. While all the lines are mostly on top of each other, the smaller s step size leads to a smoother pitch angle distribution at the top of the B field lines for trapped pitch angles (PA$\sim$ 90°). Overall, the results suggest that the fluxes are not very sensitive to the s grid step sizes. However it does make sense to have s grid step size smaller than local scale heights of the neutral species at Mars.

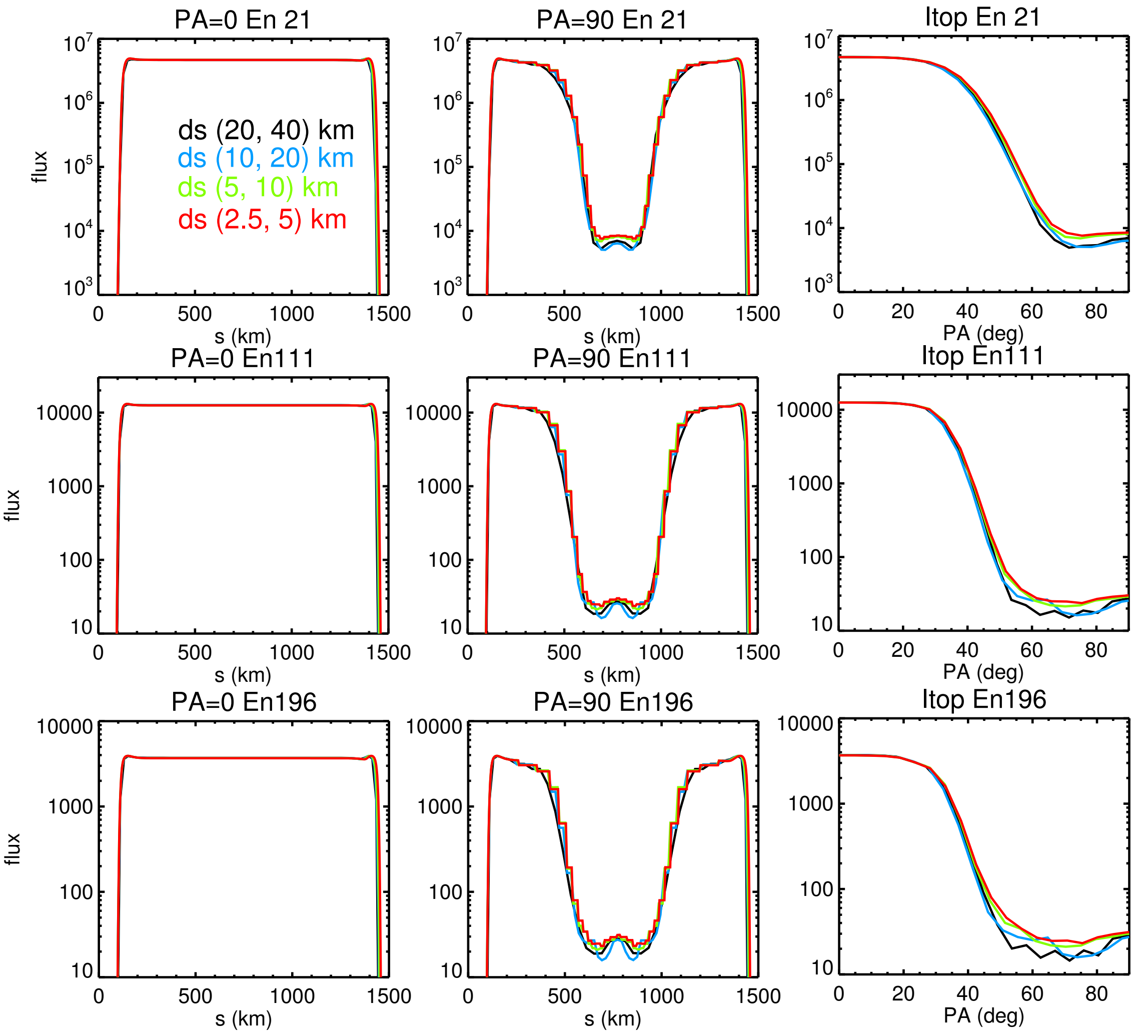

Figure 3.6: Results of different s grid size combinations, (20, 40), (10, 20), (5, 10), and (2.5, 5) (in km), highlighted in black, light blue, green, and red, respectively, in each panel. Three rows are for three energies: 21 eV, 111 eV, and 196 eV. The left and middle columns are the differential number flux ($\mathrm{cm}^{-2}\ \mathrm{s}^{-1}\ \mathrm{eV}^{-1}\ \mathrm{sr}^{-1}$) at local PA $= 0^\circ$ and 90°, respectively, against distance s. The right column shows the differential number flux ($\mathrm{cm}^{-2}\ \mathrm{s}^{-1}\ \mathrm{eV}^{-1}\ \mathrm{sr}^{-1}$) against pitch angle at the top of the B field line.

3.2.1.3 Different Magnetic Field Configurations

The tested magnetic field in sections 3.2.1.1 and 3.2.1.2 belongs to the relatively short field lines among the Martian strong crustal fields. Hence, another B field with a more extended altitude and a larger ratio of B strength maximum and minimum is also tested, as shown in red in Figure 3.3. The s step size is 10 km below 200 km and 20 km above. Because of this larger B maximum and minimum ratio, the uniform pitch angle step size setup described in section 3.1 has its disadvantages because of the complicated transformation from pitch angles to μ_0. The number of PA grid points at each altitude for this PA setup is shown in Figure 3.7a, black for a total PA grid points of 20, light blue for 50. It is easy to see that, for $s < 600$ km (altitude below 570 km), only less than 1/3 of the total PA grid points are utilized, resulting in rather coarse pitch angle resolutions in these altitudes.

Hence, the code is provided with another pitch angle grid setup. If $\theta_0(200)$ is the minimum-B pitch angle at 200 km, then from the minimum altitude to 200 km, K_1 of pitch angle grid points is assigned to this region and the pitch angle step size is $\theta_0(200)/K_1$. The second region is set up as such, from $\theta_0(200)$ to $2 * \theta_0(200)$ with K_2, so that the pitch angle step size is $\theta_0(200)/K_2$. Given K_4 is 1 for the last pitch angle step size with the same setting as the shorter B field line. K_3 is $K_{total} - (K_1 + K_2 + K_4)$, accounting for minimum-B pitch angles from $2 * \theta_0(200)$ to $\theta_0(s_{top} - 1)$, where $\theta_0(s_{top} - 1)$ is θ_0 at the second-to-top location. Here, denote this method as the "non-uniform" PA grid setup. Two pitch angle grids of this non-uniform setup are shown in Figure 3.7a, green for a total pitch angle grid points of 20 and red for 25, with (2.24° , 1.1° , 9.1° , 7.9°) & (4,8,7,1) and (2.24° , 1.1° , 5.4° , 7.9°) & (4,8,12,1) for $\Delta\theta_0(1-4)$ & K_{1-4}, respectively. The only difference between the two is the K_3.

The results of two uniform PA grid setup and two non-uniform PA grid setup are shown in Figure 3.7b - 3.7d, energy 111 eV as an example. Figure 3.7b - 3.7d are

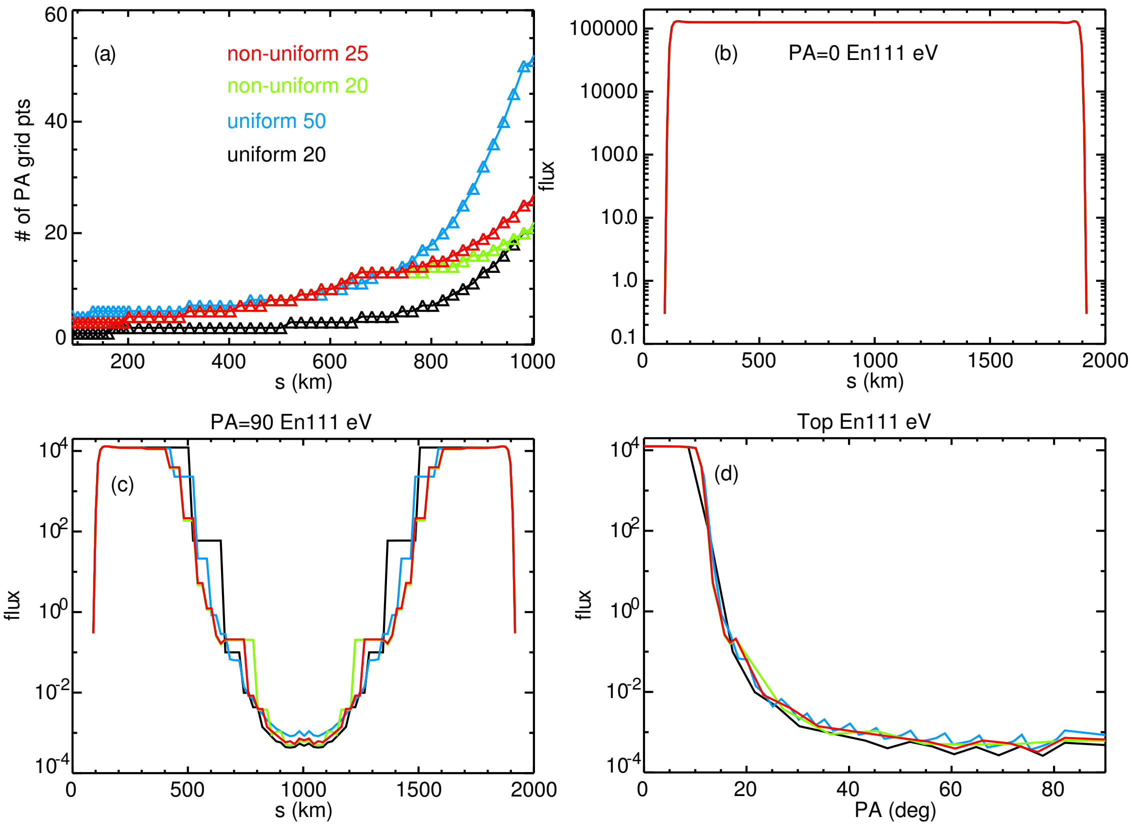

Figure 3.7: (a) Number of pitch angle grid points at each altitude. Black and blue lines are for uniform pitch angle grid setup with a total grid number of 20 and 50, respectively. The green and red lines are for non-uniform pitch angle grid setup with a total grid number of 20 and 25, respectively. (b) and (c) show the differential number flux (cm^{-2} s^{-1} eV^{-1} sr^{-1}) at PA = local 0° and 90°, respectively, against distance s. (d) shows the differential number flux (cm^{-2} s^{-1} eV^{-1} sr^{-1}) against pitch angle at the top of the B field.

the differential number flux at PA 0° and 90° against distance s, and the differential number flux at the top of the B field against pitch angle, respectively. In Figure 3.7c, two runs (black and light blue) with uniform PA grid setup are chunky between s 300-600 km while both runs (green and red lines) with the non-uniform setup are of a much finer resolution, even better than uniform PA grid setup with 50 grid points. For $600 < s < 1000$ km, the non-uniform setup provides the same as or slightly coarser resolution than the uniform setup. At the maximum altitude, the pitch angle distribution (Figure 3.7d) of all the runs are about the same. In all, this non-uniform pitch angle grid setup not only provides a good resolution with much fewer grid points but also some freedom to obtain the desired grid resolution at some particular regions according to the specific configuration of a magnetic field line.

Since section 3.2.1.2 already shows that the results are somehow insensitive to s grid step size, the test of s grid is skipped here.

3.2.1.4 Energy Grid

The last grid that needs to be tested is the energy grid, which is independent of B field configuration. Hence the short B field, shown in green in Figure 3.3, is chosen to carry out the convergence test, with a PA grid setup the same as the case of a total PA grid number of 20 in section 3.1 and s grid setup of (10, 20) km. Four uniform energy grid sizes of 1eV, 2 eV, 4 eV, and 10 eV are used, with the results shown in Figure 3.8a - 3.8d, respectively. Typical features of photoelectron energy spectra, such as the large flux drop near 60 eV due to the sharp drop in solar photons below 15 nm, the spikes near 270 eV and 500 eV due to Auger (inner shell) electron production by soft X rays, and the abrupt cutoff around 500 eV as the extreme small source term beyond the last Auger peak, are seen in Figure 3.8a - 3.8d (e.g. *Nagy and Banks*, 1970; *Mantas and Hanson*, 1979; *Liemohn et al.*, 2003). The flux spikes in the 20-30 eV range due to the intense He II 30.4 nm solar line and also Auger peaks near 360 eV can only be identified in finer resolutions, below 4 eV, i.e. Figure 3.8a - 3.8c.

The results above suggest that the determination at whether an energy grid size is sufficient highly depends on the question being asked and the energy range or feature being investigated. More than occasionally, especially for data-model comparisons, finer resolution in low energy range is required and a relatively coarse resolution in high energy range is acceptable. It is possible to set up the energy grid such that dE/E=constant. However, in order to have 1 eV grid resolution at 25 eV, it puts a lot of grid points in the 1-10 eV energy range. This makes a dE/E based energy grid impractical. Hence, we designed and tested a non-constant energy grid size as follows: 1 eV for energy below 40 eV, 2 eV for 40-200 eV, and 4 eV for energy above 200 eV, with the results shown in Figure 3.8e. Flux spikes in the 20-30 eV range, Auger peaks near 270 eV and 360 eV and other features are easily identified. This energy grid setup also speeds up calculation due to fewer energy grid steps.

To more clearly show the structures in the low energy range for different energy grid sizes, the energy spectra in the energy range of 0-50 eV for the five energy grid setups at an altitude of 150 km are shown in Figure 3.8f. Results of the four uniform energy grid sizes of 1eV, 2 eV, 4 eV, 10 eV and the non-constant energy grid size are colored in blue, light blue, green, yellow and red, respectively. In addition, a run with energy grid size of 0.5 eV, with a energy range of 0.25-200.25 eV, is also carried out to illustrate the finer structures of the photoelectrons in 0-50 eV range for comparison, highlighted in black in Figure 3.8f. Especially, in the 20-25 eV range, this black line shows three flux spikes, which smears into two with a step size of 1 eV. When the step size becomes coarser, the energy spectra is smeared further. In Figure 3.8f, the downside with the uneven energy grid size, however, is seen in the red line. Small oscillations occur just below the energy where the grid size changes, for example near 30-40 eV, making the red line more spiky than the black line. With the technique

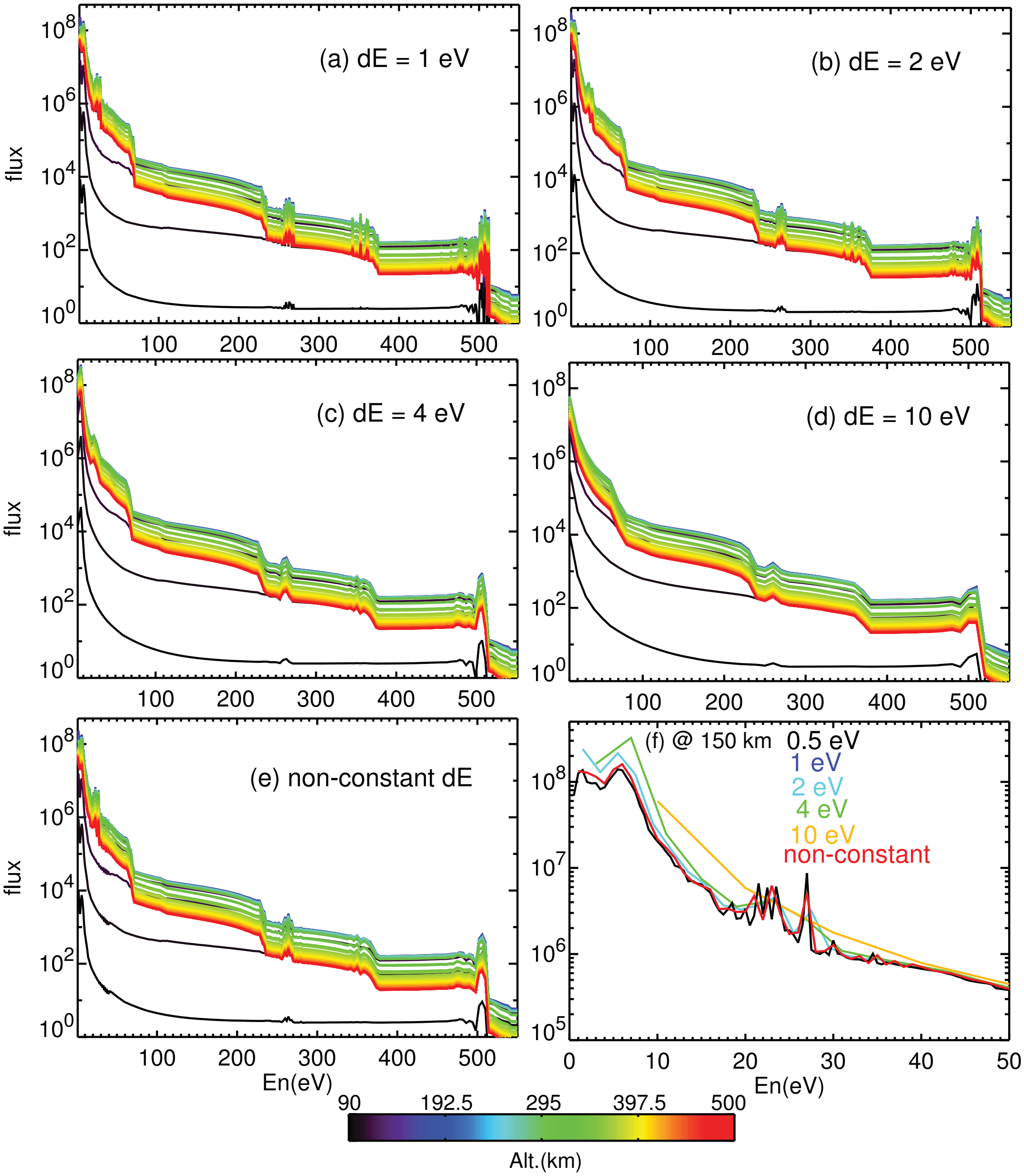

Figure 3.8: Panels (a-d) show the omni-directional differential number flux against energy for a constant energy grid size with grid sizes of 1eV, 2 eV, 4 eV, and 10 eV, respectively. Different colors highlight the energy spectra at different altitudes, as shown in the color bar. Panel (e) is for the results of a non-constant energy grid size. Panel (f) shows the energy spectra at the altitude of 150 km from 0 eV to 50 eV. Results of the four uniform energy grid sizes of 1eV, 2 eV, 4 eV, 10 eV and the non-constant energy grid size are colored in blue, light blue, green, yellow and red, respectively. In addition, the result of a run with energy grid size of 0.5 eV is highlighted in black.

used in *Swartz et al.* (1975) and a grid size change under a factor of 2, the oscillations are relatively small.

3.2.2 Physical Parameter Tests

With the appropriate PA, s and energy grid setups determined, to further verify the model, the next step is to examine the performance of the transport code with different physical parameters, specially $F_{10.7}$ values (section 3.2.2.1), thermal electron/plasma density (section 3.2.2.2), and neutral densities (section 3.2.2.3). The short B field line is used in this section, with s step size of (10, 20) km. The pitch angle grid setup is the same as the case of a total PA grid number of 20 in section 3.2.1.1. The energy grid is of a step size of 1 eV and a range of 0.5-200.5 eV.

3.2.2.1 $F_{10.7}$ Values

Solar photon fluxes incident onto Mars vary dramatically during a solar cycle and even a Martian year. Hence, four Earth $F_{10.7}$ values, 50, 100, 150, and 200, are chosen as input for the Hinteregger model and after being scaled to Mars values by multiplying a factor of $1/r^2$ (r is the Mars-Sun distance in AU, 1.57 in this study), the modeled EUV fluxes against wavelength are shown in Figure 3.9a, highlighted in black, blue, green, and red, respectively. Despite the Hinteregger EUV flux's linear dependence on $F_{10.7}$, each wavelength has its own scaling factor. As a result, the increase of EUV flux varies for different wavelengths, as the four lines are "tighter together" in some wavelengths than others. This feature of the Hinteregger model translates into different responses of photoelectron fluxes for different energies.

To demonstrate, Figure 3.9b shows the energy spectra of omni-directional photoelectron flux for these four Earth $F_{10.7}$ inputs at 200 km altitude. The differences in flux between the lines are difficult to see, and so the normalized flux (by the fluxes with $F_{10.7}$ = 50) against $F_{10.7}$ values for several energies are shown in Figure 3.9c.

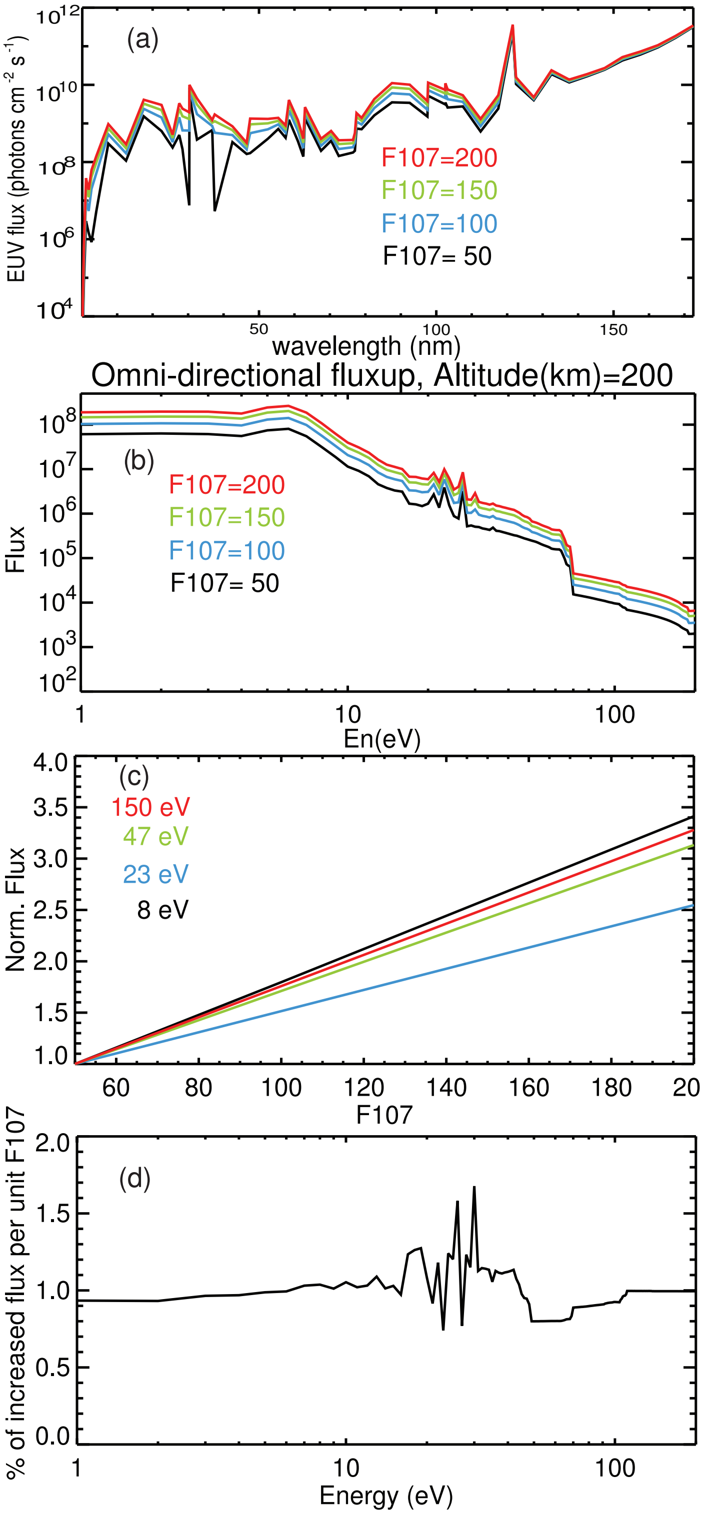
Omni-directional fluxup, Altitude(km)=200

Figure 3.9: (a) Modeled EUV fluxes against wavelength, and different F10.7 values at Earth are colored differently. (b) Omni-directional differential number flux (cm^{-2} s^{-1} eV^{-1} sr^{-1}) against energy at altitude 200 km. For both (a) and (b), colors mark different F10.7 cm inputs. (c) Normalized fluxes against $F_{10.7}$ values and four example energies are highlighted in different colors. (d) Percentage of increased fluxes per unit $F_{10.7}$ against energy.

From Figure 3.9c where different slopes are seen, the increase factors of fluxes, or the percentages of increased flux, per unit $F_{10.7}$ for all the energies are shown in Figure 3.9d. This percentage varies for different energies, being especially spiky in the energy range of 20-30 eV. This variation produced by the transport code in the photoelectron fluxes is consistent with the Hinteregger EUV flux changing for different ionizating photon wavelengths.

3.2.2.2 Thermal Electron/Plasma Density

Thermal electron/plasma density is directly related to the loss of photoelectrons due to Coulomb collisions. To examine this effect, the normal electron density from MTGCM, shown as the black line in Figure 3.2, is scaled by a factor of 0.1, 1, 10, and 100, and the resultant energy spectra are shown in Figure 3.10a - 3.10d, respectively.

When electron density increases (Figure 3.10c and 3.10d), the omni-directional fluxes at the top of the field line (colored in red) decrease more compared to the normal electron density (Figure 3.10b), especially at lower energies. It is due to the factor that the Coulomb collisional cross section is proportional to the inverse of squared energy ($1/E^2$). Also, the flux spikes in the 20-30 eV range are more degraded and barely seen at the top of the field line in Figure 3.10d.

When electron density decreases (Figure 3.10a), while the high-altitude flux drops are not as severe at the very low energies (below 10 eV), the results closely resemble the normal case. It hints that the loss due to Coulomb collisions plays a relatively minor role compared to other loss mechanisms, i.e. elastic and inelastic collisions with neutral particles, hence this reduced minor factor barely influences the final fluxes.

To quantitatively determine the photoelectron flux change caused by the different plasma densities, Figure 3.10e shows the normalized flux at the top of the magnetic field against the multiplication factor. For high energies, the photoelectron flux is barely affected due to the small Coulomb collision cross section. For really low energies

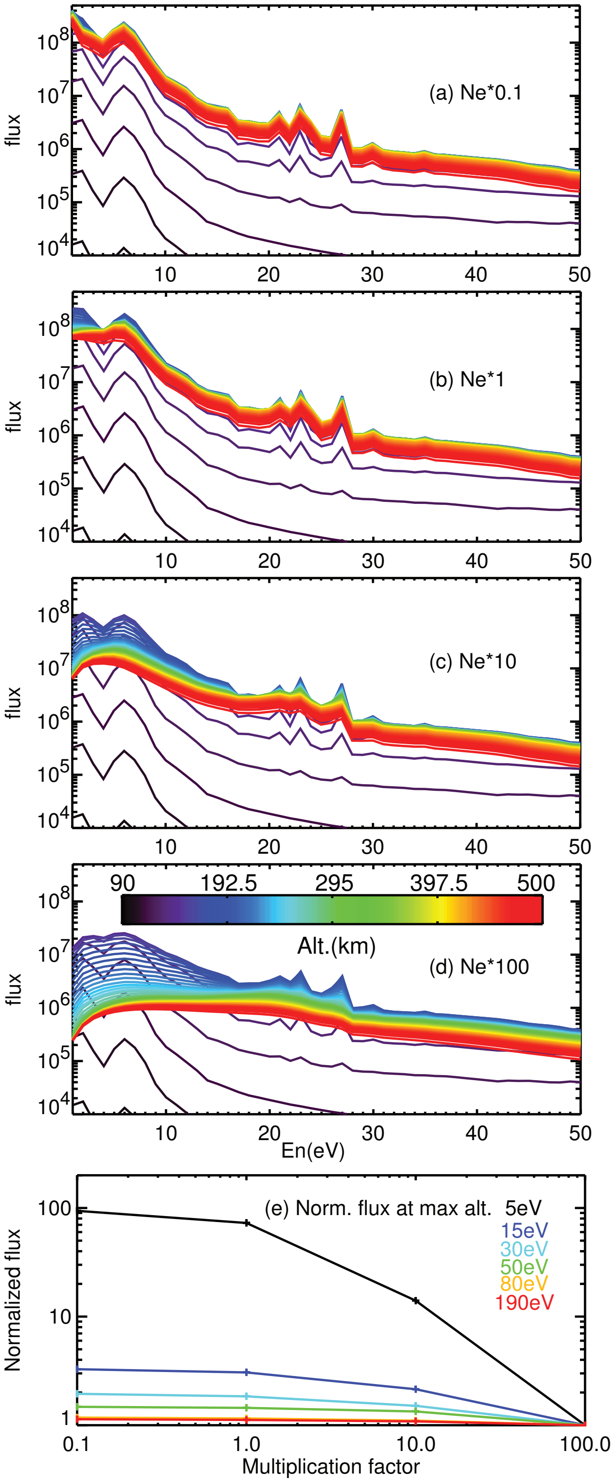

Figure 3.10: Omni-directional differential number flux (cm^{-2} s^{-1} eV^{-1} sr^{-1}) against energy at different altitudes, marked by different colors. Panel (b) is for normal thermal electron density as shown in Figure 3.2. Panel (a), (c) and (d) are for this density scaled by a factor of 0.1, 10, and 100, respectively. Panel (e) shows the normalized flux at the top of the magnetic field against the multiplication factor. Colors highlight different energies.

(e.g. 5 eV), photoelectron flux decreases almost linearly with the increase of the plasma density but barely changes with the decrease of the plasma density as the loss due to the Coulomb collision is small compared to other processes.

3.2.2.3 Neutral Densities

Neutral densities' effects on photoelectron fluxes are more complicated as they contribute to both the source and the loss. An easy way to validate the transport model's performance is to examine the electron flux peak altitude. According to Chapman theory (*Chapman*, 1931c,d), when neutral density increases, as the solar EUV flux is absorbed more in the upper atmosphere and the optical depth reaches 1 at a higher altitude, the altitude of the peak electron flux also increases.

The densities of five neutral species are scaled by a factor of 0.01, 0.1, 1, 10, and 100, results colored in black, blue, green, pink, and red in Figure 3.11, respectively. Each panel is the omni-directional flux against altitude for a particular energy. For all four panels, the peak altitude increases with elevated neutral densities. The peak fluxes tend to decrease a little as neutral densities increase but are mostly within 50% of each other. It might be partially due to the increased neutral temperature at the peak, as the neutral temperature increases with altitude in the Martian thermosphere, as shown in Figure 3.2 (the red line), and the peak altitudes for higher density cases increase as well. The resultant increased scale heights (H) lead to a decreased peak production rate ($\propto 1/H$) according to the Chapman theory (for example, see equation 9.23 in *Schunk and Nagy* (2000)). In addition, the flux decreases less from the peak to the top of the field line as the neutral density increases, providing an increased source at high altitudes.

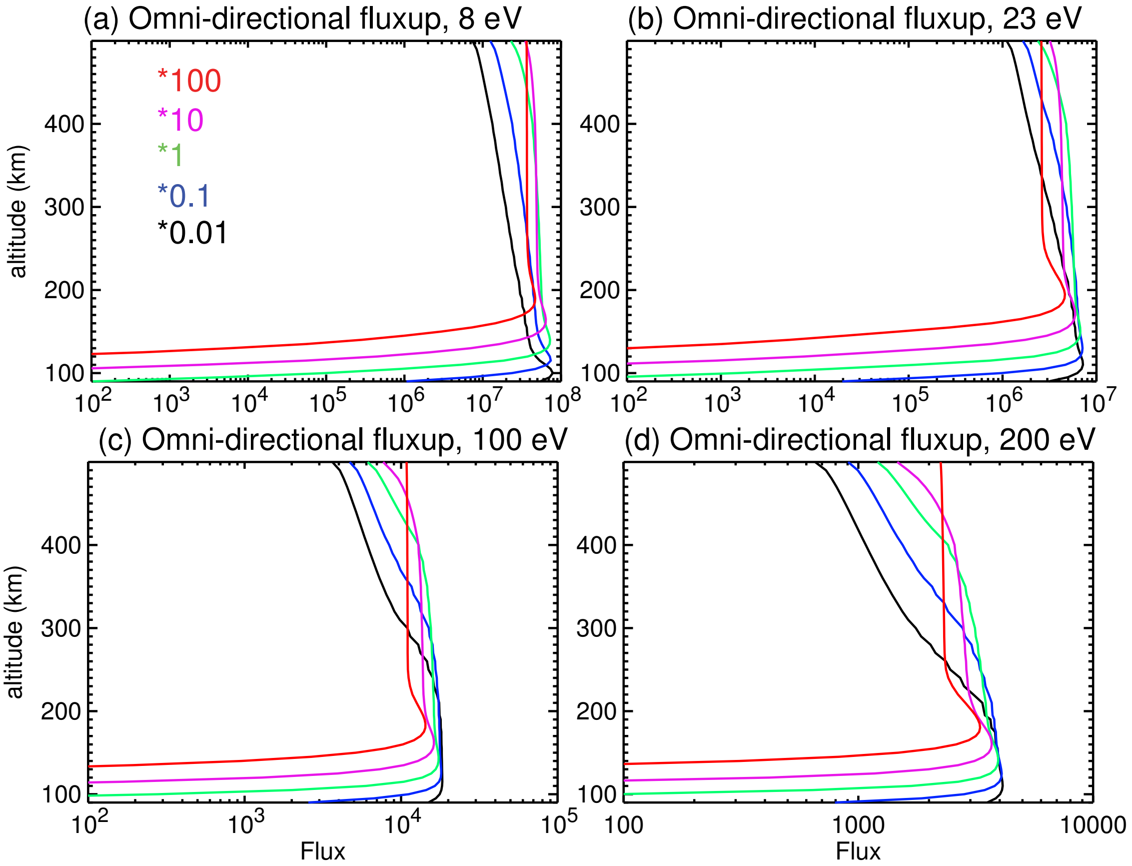

Figure 3.11: Omni-directional differential number flux (cm^{-2} s^{-1} eV^{-1} sr^{-1}) against altitude for different energies, (a) 8 eV, (b) 23 eV, (c) 100 eV, and (d) 200 eV. In each plot, different colors are for the results of different neutral densities. Green is for normal neutral densities as shown in Figure 3.2. Black, blue, pink, and red are for neutral densities of all species scaled by a factor of 0.01, 0.1, 10, and 100, respectively.

3.2.3 Data-Model Comparison

To further assess the STET model, the data-model comparison is performed here. An orbit of MGS on Nov. 7, 2005, 03:48:27-03:48:59, is chosen as the Sun, Earth and Mars aligned so that the solar flux can be directly scaled from Earth to Mars by their relative solar distances. The spacecraft was at local time 2 pm, south latitude $\sim 46°$, east longitude $\sim 190°$, solar zenith angle $\sim 37°$. The magnitude of magnetic field is around 200 nT and the magnetic elevation angle, angle relative to the planet surface, is from $0-30°$. For the model setup, the non-constant energy grid setup described in section 3.2.1.4 is used. Earth $F_{10.7}$ and the relative Sun-Earth and Sun-Mars distances are given accordingly. The two magnetic field configurations shown in Figure 3.3 are both tested here. For the short B field line, a total pitch angle number of 20 is used, while for the long B field line, the non-uniform setup with 25 pitch angle grid points, as described in section 3.2.1.3, is employed.

The data-model comparison of the omni-directional flux at MGS altitude (~400 km) is shown in Figure 3.12. The width of the solid red lines shows the energy resolution of the electron instrument and the red dots are the serial measurements from 03:48:27 to 03:48:59, 17 in total. The yellow line is the model run of Hinteregger 81 with the Solomon fix (*Solomon et al.*, 2001) for magnetic field line B2. Compared with the MGS observation, the model result matches with the data above 300 eV and is 2-4 times higher for energy below 200 eV. The Solomon fix is to multiply the EUV flux below 25 nm from Hinteregger 81 model by 4. Then, a model run of Hinteregger 81 without the Solomon fix for the short magnetic field line is shown in blue line in Figure 3.12. Now the modeled results matches well with the observation, within a factor of 2 below 200 eV. The disagreement at energy bin 61 eV, right around the large flux drop, is probably due to the spacecraft potential shift, yielding mixing electron fluxes of this bin with its neighbor bins and smearing the flux drop. In addition, another discrepancy between the model and the data is the flux spikes in 20-30 eV

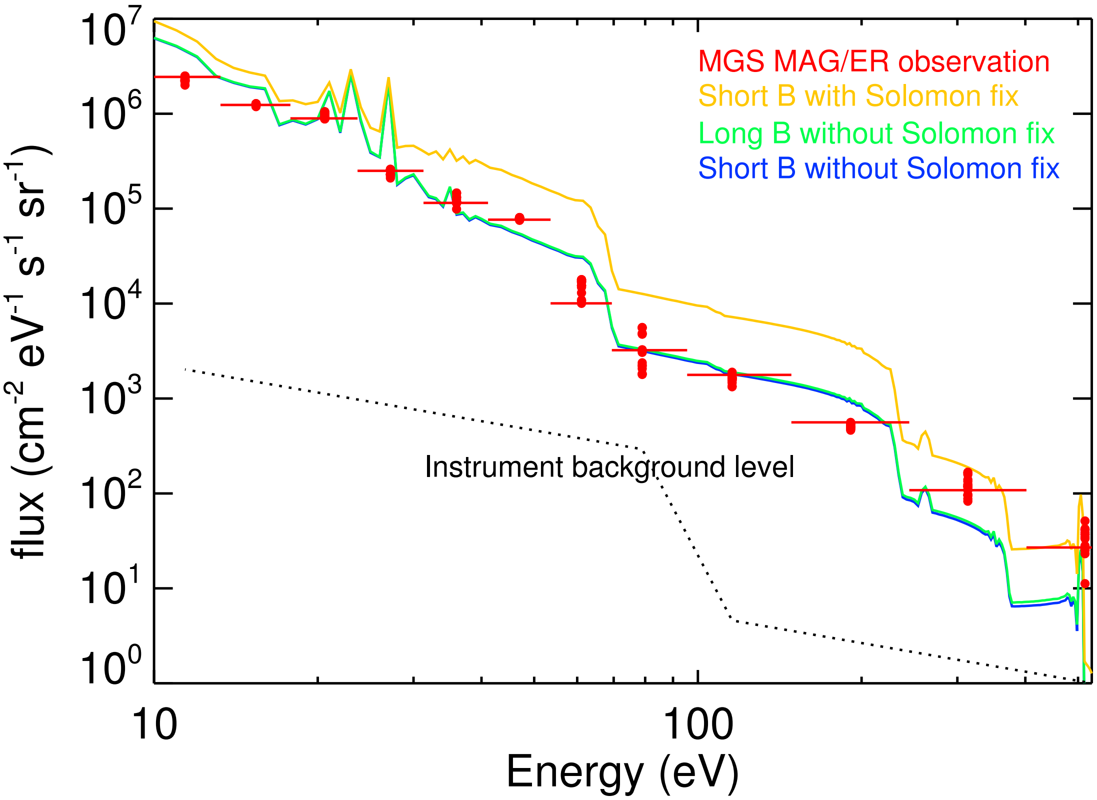

Figure 3.12: Omni-directional flux against energy. The width of the solid red lines shows the energy resolution of the electron instrument and the red dots are the serial measurements from 03:48:27 to 03:48:59, 17 in total. The black dashed line is the instrument background level flux. The solid lines are the model results with the short and long B field line in Figure 3.3. The blue and green lines are the model runs of Hinteregger 81 without the Solomon fix, for the short and long field line, respectively. The yellow line is the model run of Hinteregger 81 with the Solomon fix for the short B field line.

range, which are missing from the data. It may be caused by the coarse resolution ($\Delta E/E = 25\%$) of the instrument and/or the discrepancy between the modeled EUV fluxes and the actual values.

The model result, without the Solomon fix, with the long B field line, is also shown in Figure 3.3, highlighted in green. As can be seen in Figure 3.12, the magnetic field description had essentially no influence on the photoelectron omnidirectional flux values at 400 km altitude. While the magnetic field topology is important for electron transport and the details of the pitch angle distribution, Figure 3.12 shows that it is relatively unimportant for this pitch-angle averaged quantity. The disagreements between our model results and the observations are within a factor of two. Especially, solar EUV flux directly controls photoelectron fluxes and the EUV photon intensities from the Hinteregger-81 model may be off from the actual solar EUV by different factors at different wavelengths, which could introduce a significant different discrepancy at different energies. In addition, both neutral density and field line configuration discrepancies tend to introduce a systematic decrease/increase of fluxes for all energies. More detailed assessments of the factors controlling photoelectron fluxes at Mars will be the subject of future studies. Despite the fact that the two magnetic configurations are of different lengths, minimum and maximum ratios, the model results are almost identical, suggesting the high-altitude photoelectron omnidirectional fluxes are somewhat insensitive to the magnetic fields. However, as the two tested field lines are symmetric, an extremely asymmetric field line, such as an open field line, can lead to the decrease of omnidirectional flux by a factor less than three for transport dominant altitudes (e.g. *Mantas and Hanson*, 1979).

3.3 STET Model Development

Solar EUV photon fluxes directly control the photoelectron fluxes (e.g. *Banks and Nagy*, 1970). Measurements and models of the solar EUV and XUV fluxes are therefore vital to accurately obtain photoelectron fluxes. However, any one solar irradiance model is based on a limited set of observations and has caveats to its applicability and errors on its accuracy. For example, *Peterson et al.* (2012) compared the Earth observation and the modeled photoelectron spectra with five different solar irradiance models as the solar energy input and concluded that all the investigated models failed to capture the variability of solar irradiance on the solar rotation time scale. This limitation of observations is especially true at planets other than Earth, where solar irradiance measurements are few. Furthermore, most superthermal electron transport models only use a single solar irradiance model for the specification of this important input parameter. It is useful, then, to systematically examine the influence of using different solar irradiance flux models on the resulting superthermal electron distribution.

For our STET model, one of the mostly widely used solar irradiance modes, the Hinteregger-81 model (*Hinteregger et al.*, 1981), is currently incorporated to calculate solar irradiance. Hinteregger-81 is an empirical model based on the fitting of observations from the Atmospheric Explorer-E (AE-E) and several sounding rockets. However, *Woods et al.* (2005) found the discrepancy of a factor of a few between the modeled Hinteregger-81 solar fluxes and the observations from Thermosphere Ionosphere Mesosphere Energetics and Dynamics (TIMED) Solar Extreme Ultraviolet Experiment (SEE)(*Woods et al.*, 1998). Hence it is necessary to compare the performance of other solar irradiance models' to the Hinteregger-81 model, in the aspect of the resultant photoelectron fluxes. We have selected two recently developed solar irradiance models to implement into the STET model: the Flare Irradiance Spectral Model (FISM) (*Chamberlin et al.*, 2007, 2008) and the Heliospheric Environment Solar Spectral Radiation (HESSR) model (*Fontenla et al.*, 2009, 2014).

3.3.1 New Solar Irradiance Models

The FISM model, an empirical solar irradiance model that is based on more accurate measurements from several instruments on three different satellites (such as TIMED SEE for extreme ultraviolet irradiance data), makes use of six proxies for different wavelengths/bands, treats the solar cycle and solar rotational components separately, and also, in addition the daily component, includes the solar irradiance variations from both the impulsive and gradual phases of the solar flares.

The HESSR is a semi-empirical model of the Solar Spectral Irradiance (SSI) at planets and a derivative of the Solar extreme ultraviolet (EUV) Radiation Forecast

System (SERFS) model described by *Fontenla et al.* (2014), which was developed to model the Ultraviolet (UV) SSI at Earth. The SERFS model is based on the Solar Dynamics Observatory (SDO)/Atmospheric Imaging Assembly (AIA) images of the solar disk available since August 2010 that produce daily "masks" of the solar disk that identify a set of 11 chromospheric and coronal features directly observed on the disk. For application to other planets, i.e. in HESSR, maps of the features on the solar disk are derived from the current and previous solar disk masks. Using these maps, the solar features are projected to the planets viewing positions to produce daily projected masks at each planet. Then these projected masks are used in the same way as the Earth case to produce planetary UV SSI predictions. The resulting SSI can be produced at any desired resolution, but for practical purposes the planetary data used in this paper is re-binned into 1-nm bins. When observations are available from other viewpoints in the heliosphere, or helioseismology of the far-side, these data can be used to directly update the maps of features and thereby bring up to date the state of the solar disk viewed from other planets (*Fontenla et al.*, 2009).

For the HESSR model, the photon fluxes (available wavelength 0.05-160 nm, $http://www.galactitech.net/hessrdata/Mars/Spectra/$) are already in Mars values. For the other solar irradiance models, the modeled solar photon fluxes from both the Hinteregger-81 model and FISM (available wavelength 0-190 nm, $http://lasp.colorado.edu/lisird/fism/$) are currently Earth values, which are then scaled by the relative distances of the two planets from the Sun and interpolated according to the Mars-Sun-Earth angle, to obtain Mars values.

3.3.2 Implementation of New Solar EUV Models

To demonstrate the implementation of the two new solar EUV models, the STET model is set up as follows. The neutral densities, ionospheric density and temperature profiles based on MTGCM are shown in Figure 3.13a. The MTGCM run was at an

Ls of 90 degrees with an Earth $F_{10.7}$ of 100 sfu (1 sfu= 10^{-22} W/(m^2 Hz)) near the solar minimum and aphelion condition. The magnetic field line configuration is a symmetric field line, as shown in Figure 3.13b-3.13d. The distance step size of the field line is 5 km below 200 km to well resolve the ionosphere and 10 km above. A total of 20 pitch angle grid points for pitch angle $0-90°$ are used for electron fluxes flowing along the magnetic field direction and the same pitch angle setup for the opposite flowing electrons. In addition, a non-constant energy grid size is set up as follows: 1 eV for energy below 40 eV, 2 eV for 40-200 eV, and 4 eV for energy above 200 eV. All the runs for this part are steady-state by setting a large time step of 10^5 s, so that the time derivative term is mostly negligible. The simulation is considered to be converged as $|\psi - \psi_{last}|/\psi < 0.02$, where ψ and ψ_{last} are the electron flux at the current time step and the last time step at every location in the $E - s - \mu$ grid.

For this part, we have chosen July 13th, 2014 for the reference of the solar irradiance models. For the Hinteregger-81 model, the inputs are $F_{10.7} = 127$ sfu and 81-day average index $F_{10.7a} = 135$ sfu . As both the Hinteregger-81 model and the HESSR model predict daily solar photon fluxes, we only use the daily component of FISM for this part, rather than including the high-time-resolution flare component, to most appropriately compare the influence of three models' daily predictions on the photoelectron fluxes. In addition, there were only several very minor flares (class C) on July 13th, 2014 so that the daily component is an adequate representation of the total solar flux. Both FISM and HESSR use observations from July 13th, 2014 as inputs to drive the models.

The absorption and photoionization cross sections in the STET model are in the same resolution as the Hinteregger-81 model, 41 wavebands and 18 single spectral lines for strong emission lines, with a resolution of < 1 nm below 3.2 nm, then 1.8 nm for 3.2-5 nm and a resolution of 5 nm for the wavelength range $5-175$ nm (see more detailed resolution information in Table 1 of *Heroux and Hinteregger* (1978)). Both

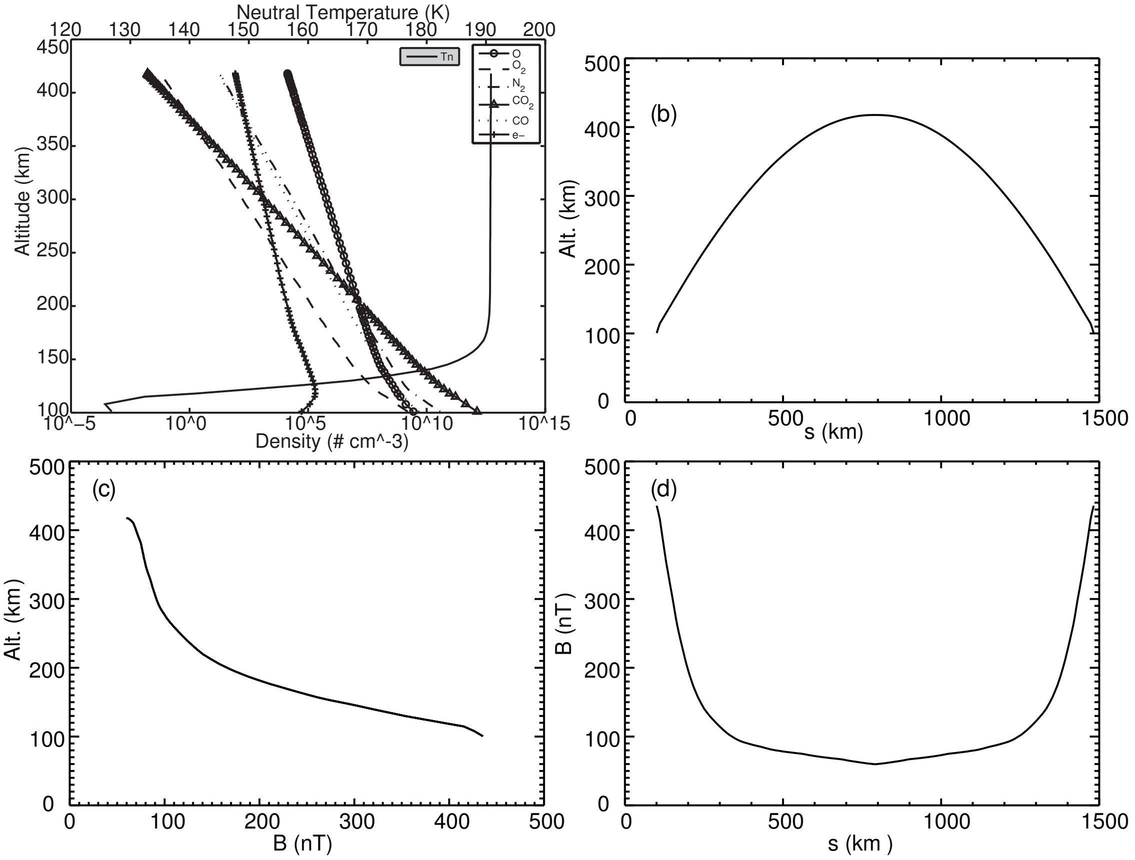

Figure 3.13: (a) Neutral densities, thermal electron density and neutral temperature of Mars to be used in the calculations that follow, against altitude. These values are from MTGCM for the altitude range of 100-240 km and linearly extrapolated from the logarithm of the two topmost values from MTGCM above 240 km; (b) B field line altitudes against distance s; (c) B field strength against altitude; (d) B field strength against distance s.

FISM and the HESSR model data used in this dissertation, however, are currently of a bin size of 1 nm. To avoid confusion, here we denote the resolution of the Hinteregger-81 model as “the uneven resolution”, in contrast to the 1 nm resolution of the two new solar irradiance models. Hence, we have constructed three ways to incorporate the two new models. The most straightforward way (method 1) is to integrate the solar photon fluxes from the two new models into the uneven resolution for long wavelengths and linearly interpolate for wavelengths below 3.2 nm, where the Hinteregger-81 model has finer resolution than 1 nm. Figure 3.14a shows the comparison of the solar photon fluxes from FISM (dark blue) and the HESSR model (red) in 1 nm resolution while the integrated versions of FISM (dark blue) and the HESSR model (red) in the uneven resolution are shown in Figure 3.14b, accompanied with the solar irradiance from the Hinteregger-81 model (black) as a comparison.

However, method 1 results in the loss of the finer wavelength resolution above 3.2 nm. Therefore, instead of integrating solar irradiance, the other two methods are to linearly interpolate the absorption and photoionization cross sections to 1 nm resolution. It is only suitable to implement this way when the cross sections are smooth. As shown in Figure 3.14c and 3.14d, both the absorption and photoionization cross sections, crosses for the uneven resolution and solid lines for the interpolated 1 nm resolution, are rather smooth below 70 nm but quite spiky above. Considering 70 nm ($\sim$18 eV in energy per photon) is about the wavelength threshold to photoionize neutrals, it is appropriate to interpolate the cross sections. The difference between the two methods lies in how to deal with the 18 single spectral lines, as indicated by the red/blue crosses in Figure 3.14a. The second method (method 2) is to first interpolate the cross sections for the 41 wavebands into 175 bins with 1-nm resolution. Then for those 18 1-nm bins that contain the single spectral lines, the cross sections obtained from the waveband interpolation will be replaced by the original cross sections of the corresponding single spectral lines.

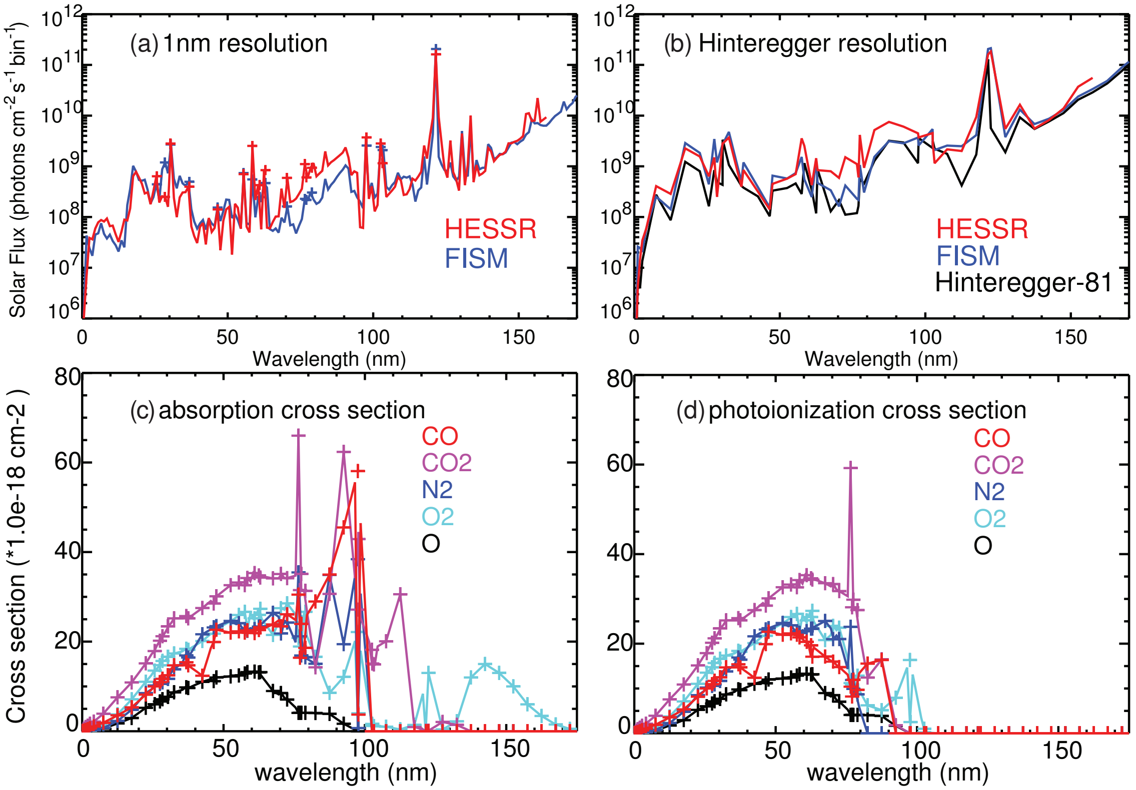

Figure 3.14: (a) Solar fluxes from FISM (blue) and HESSR model (red) against wavelength, in 1 nm resolution. The blue and red crosses indicate the wavelengths of the 18 single spectral lines. (b) Solar fluxes from Hinteregger-81 model (black), FISM (blue), and HESSR model (red) against wavelength, in the uneven resolution. Absorption cross section (c) and photoionization cross section (d) against wavelength; crosses for the uneven resolution and solid lines for the interpolated 1 nm resolution.

The third method (method 3) is to interpolate the cross sections for the 41 wavebands into 175 bins with 1-nm resolution and, instead of replacing, add the extra 18 single spectral lines. In other words, the third method has 18 more bins (with the same upper and lower bound for each bin) than does the method 2. The photon fluxes for the extra 18 single spectral lines are from the 1-nm bins that contain the 18 single spectral lines. The third method resembles the way the Hinteregger-81 model calculates the solar photon fluxes, adding extra photon fluxes from the single-spectral-line bins into the fluxes from the wavebands.

To briefly summarize, for both FISM and the HESSR model, there are two fundamental ways to incorporate them into the STET model: (1) integrating and interpolating the solar irradiance to fit the absorption and photoionization cross sections in uneven resolution (method 1); (2) interpolating the absorption and photoionization cross sections in 1 nm resolution (method 2 and method 3). Method 2 and method 3 differ in the treatment of the single spectral lines.

3.3.2.1 Flare Irradiance Spectral Model

The comparison of FISM implemented in these three methods is demonstrated in Figure 3.15. The upper panel of Figure 3.15 shows the omni-directional photoelectron fluxes against energy at 200 km, just above the collisional ionosphere. The solid line is for FISM in the uneven resolution, the dashed line for method 2 and the dotted line for method 3, the latter two in 1-nm resolution. All three energy spectra are mostly on top of each other. A noticeable difference between the two resolutions is the steeper drop of electron fluxes for the uneven resolution near 60-70 eV due to the coarser wavelength resolution above 3.2 nm. In contrast, the 1-nm resolution results in a broader decrease of fluxes from approximately 50 to 70 eV. A more quantitative comparison is shown in the lower panel of Figure 3.15 where the photoelectron fluxes generated by FISM using the absorption and photoionization cross sections at 1-nm resolution are ratioed relative to the fluxes of the uneven resolution FISM, by dividing the dashed and dotted lines in the upper panel by the solid line. The difference between the two resolutions is within a factor of 3. The discrepancy between method 2 and 3 is seen at energy below 40 eV. Without the extra single-spectral-line bins, the dashed line is off the solid line, i.e. in the uneven resolution, by a factor less than 2. The dotted line, however, is closer to the solid line, as both the method 1 and 3 have additional extra photon fluxes from the single-spectral-line bins. However, it is not yet clear if the additional fluxes from these single-spectral-line bins will result in overestimated photoelectron fluxes for the low energy range. In other words, it is inappropriate to conclude which method is better without a comprehensive data-model comparison study.

3.3.2.2 Heliospheric Environment Solar Spectral Radiation model

Similarly, Figure 3.16, in the same format as Figure 3.15, shows how the three methods used to incorporate the HESSR model affect the photoelectron energy spectra. Again, the resultant photoelectron fluxes from the three methods vary within a factor of around 4. The lower panel of Figure 3.16 mostly resembles the lower panel of Figure 3.15 below 100 eV. The noticeable feature for the HESSR model is that the second and third methods, (dashed and dotted lines), result in more variance from the first method above 100 eV, compared to the FISM case. It is due to the more dramatic decrease of the solar irradiance from 3 nm to 2 nm for the HESSR model, compared to FISM, as the HESSR model tends to predict much lower solar irradiance below 2 nm than FISM. As a result, the interpolation of the HESSR solar irradiance to the uneven resolution at short wavelengths brings more variance to the high-energy photoelectron fluxes.

As the only discrepancy between method 2 and 3 is below 40 eV, hereinafter we will only show the results of the method 2 to demonstrate cases of 1-nm resolution.

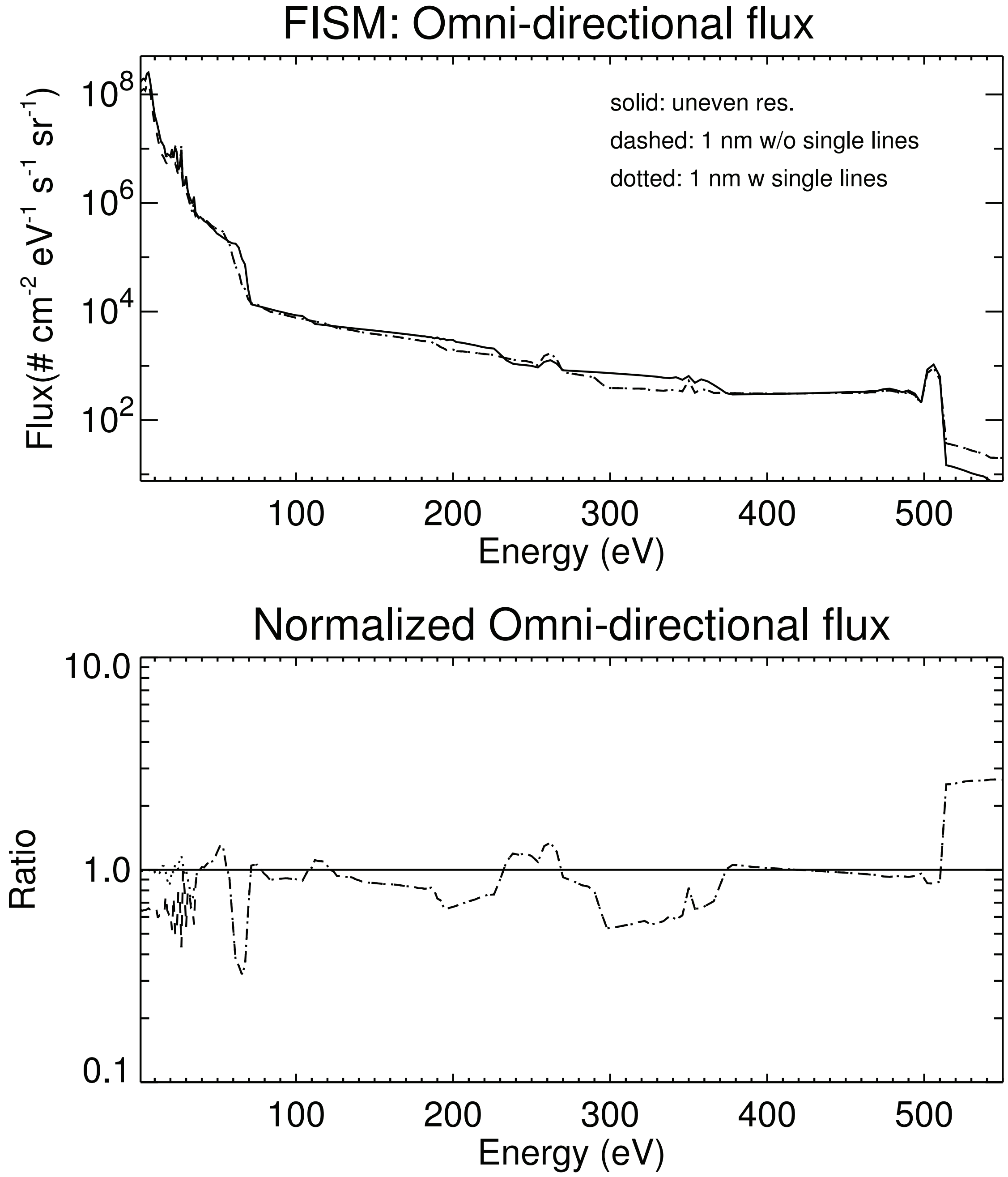

Figure 3.15: The upper panel is the omni-directional flux against energy. The three lines are for different ways to implement FISM, the solid line for method 1, integrating FISM photon fluxes to the uneven resolution, the dashed line for method 2, FISM and absorption and photoionization cross sections interpolated to 1 nm resolution, and the dotted line for method 3, FISM and absorption and photoionization cross sections interpolated to 1 nm resolution with additional single-spectral-line values. The lower panel is the relative omni-directional fluxes of three methods against energy, i.e., the dashed and dotted lines in the upper panel divided by the solid line.

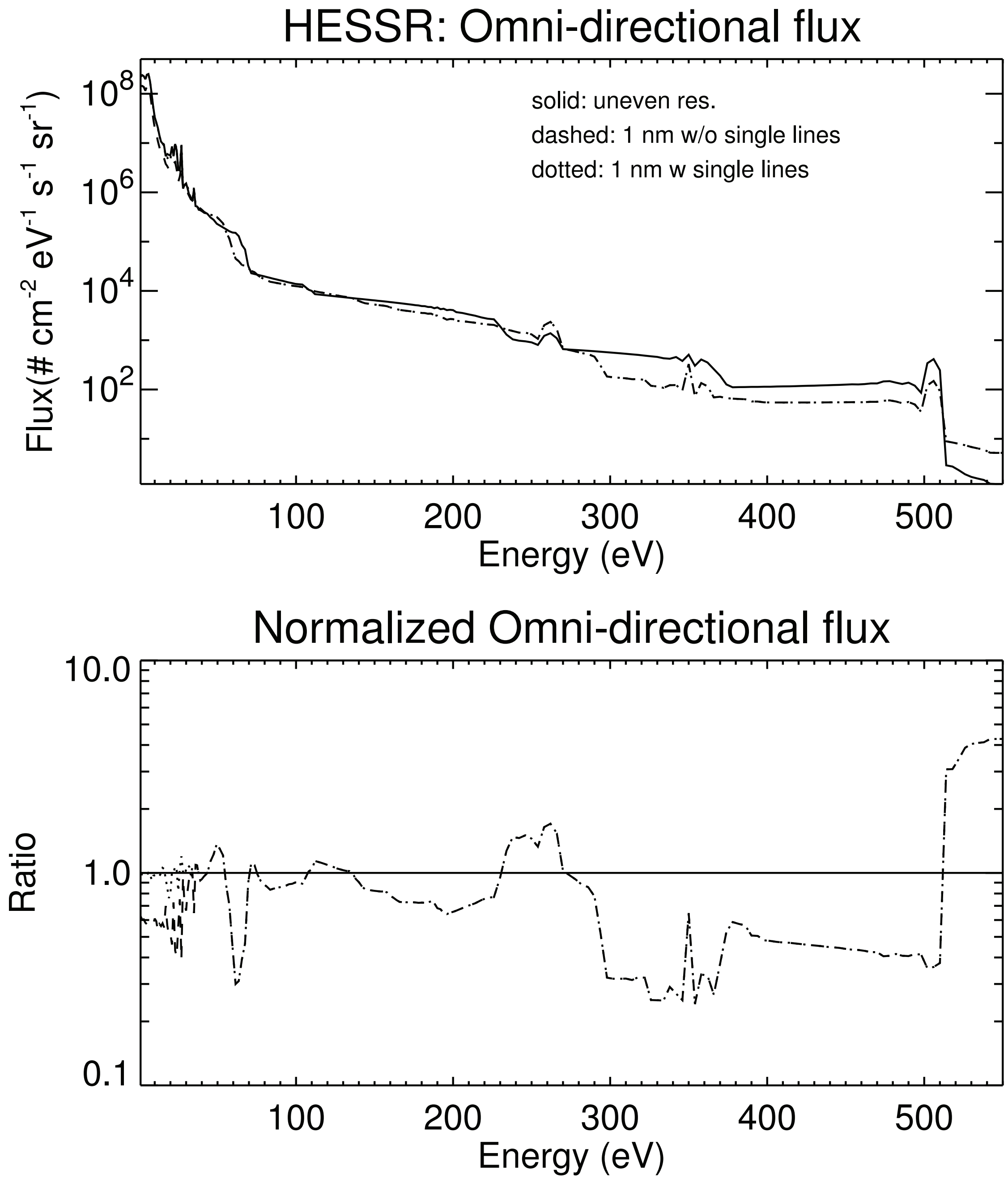

Figure 3.16: The same format as Figure 3.15. This figure shows the comparison of the three methods to implement the HESSR model.

3.3.3 Comparison of the Solar EUV Models

In this section, we will compare the photoelectron fluxes with different solar irradiance models as input, as shown in Figure 3.17. The left column demonstrates the comparison of the various models in the uneven resolution while the right column shows the results of FISM and the HESSR model with the model absorption and photoionization cross sections interpolated to 1-nm resolution, with the Hinteregger-81 model for comparison. Again, the upper panels are for omni-directional photoelectron fluxes against energy at 200 km and the lower panels for the fluxes relative to the Hinteregger-81 model case. In each panel, the Hinteregger-81 model case is in black, FISM in green, and the HESSR model in red.

3.3.3.1 Comparison of Photoelectron Fluxes

For the uneven resolution (left column of Figure 3.17), the results of FISM and the HESSR model generally agree well for the energy range 40-300 eV, within a factor of 2. Below 40 eV, though modeled photoelectron fluxes fluctuate dramatically, the photoelectron fluxes from the two newer solar irradiance models are generally within a factor of 2 as well. Above 300 eV, the resultant electron fluxes from the HESSR model are about half of that from FISM.

The right column of Figure 3.17, for absorption and photoionization cross sections being interpolated to 1-nm resolution, shows similar features described above. However, it is noticeable that the resultant photoelectron fluxes from the HESSR model is much lower than FISM, around 10-20 %, as the HESSR model tends to predict much lower solar irradiance below 2 nm than FISM. Also, the energy spectra resulting from the two new solar irradiance models, as shown in the right upper panel, decrease more smoothly from 50 eV to 300 eV, while for the Hinteregger-81 model case, the decrease is semi-staircase (likely due to the coarser wavelength resolution above 3.2 nm).

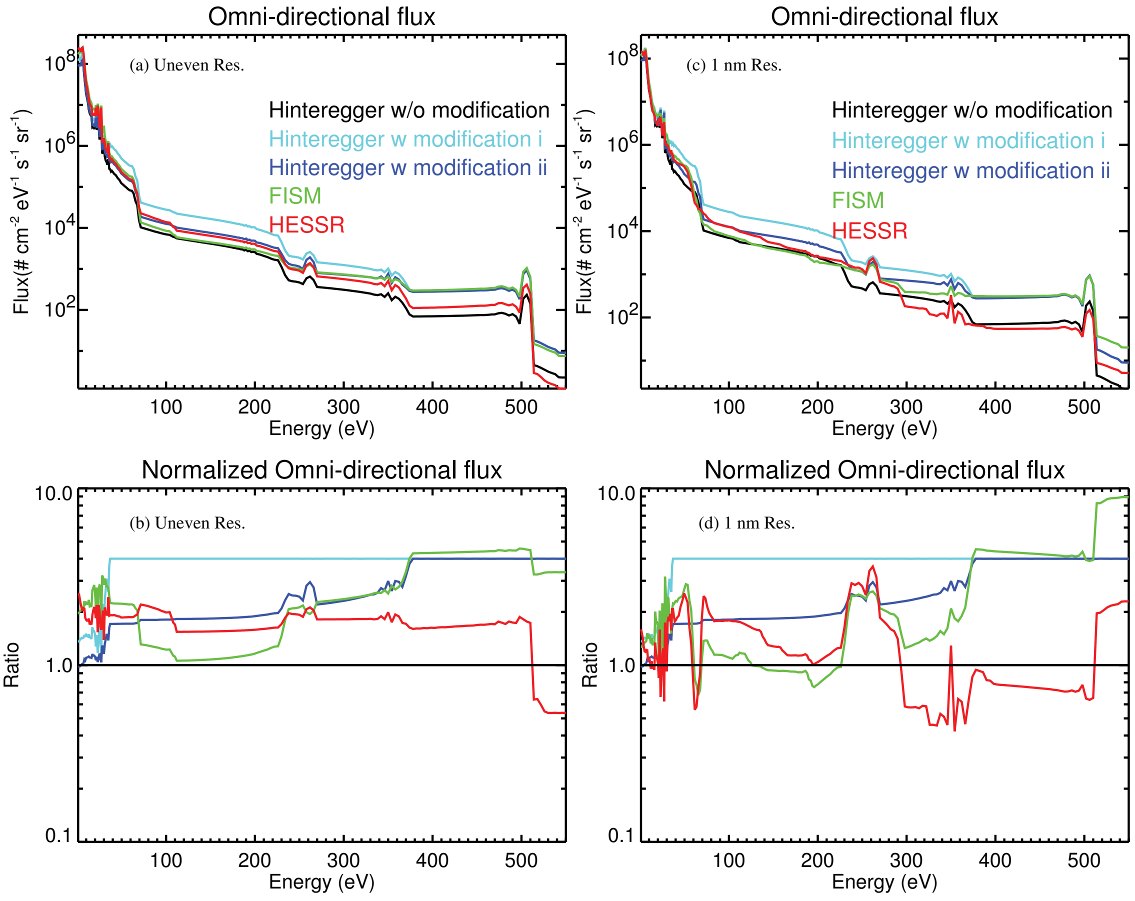

Figure 3.17: The upper two panels are the omni-directional flux with different EUV models against energy. The black line is for the Hinteregger-81 model without modification, aqua for Hinteregger-81 with the Solomon modification, blue for Hinteregger-81 with the new modification, green for FISM, red for HESSR model. The lower two panels are the relative omni-directional photoelectron fluxes against energy, i.e., other color lines divided by the black line in the upper panel. The left column is in the uneven resolution while the right column is for FISM and the HESSR model implemented with method 2.

3.3.3.2 Modifications to Hinteregger-81 Model

From Figure 3.17, it is easy to see that the Hinteregger-81 model leads to much lower photoelectron fluxes than the other two solar irradiance models, except for the HESSR model at high energy range. *Solomon et al.* (2001) concluded that the solar photon fluxes from the Hinteregger-81 model needed to be multiplied by a factor of 4 below 25 nm to match the observation. The Hinteregger-81 model with this modification is shown in aqua in Figure 3.17. While this modification makes the Hinteregger-81 model case match much better with FISM above 360 eV in the uneven resolution (left column), it results in higher photoelectron fluxes by a factor of around 2 from 40 eV to 360 eV than both FISM and HESSR cases. Section 3.2.3 also suggested that the correction of *Solomon et al.* (2001) seems to extend to longer wavelengths than necessary through their data-model comparison. The right column of Figure 3.17 shows this similar trend, better agreement with FISM above 230 eV but overshoot in the energy range of 40-230 eV compared to the two newer models.

Woods et al. (2005) found that the modeled solar photon fluxes from the Hinteregger-81 model was 50% higher in the 50-75 nm range than the SEE measurement from February 2002 to mid-2004 and that the observation was 70% higher than the modeled solar fluxes in the 5-25 nm range. Therefore, a simple new modification to the Hinteregger-81 model is to combine the findings from both studies, multiplying the modeled solar fluxes from the Hinteregger-81 model by 2/3 in the 50-75 nm range, by 1.7 in the 3.2-25 nm range, and by 4 below 3.2 nm. The choice of 3.2 nm cutoff instead of 5 nm is due to the better agreement with the other two models. The resultant photoelectron fluxes with this new modification are shown in blue in Figure 3.17 and agree quite well with the newer models for energies between 40 eV to 300 eV and with FISM above 300 eV. This new modification does lead to lower photoelectron fluxes below 40 eV than the Solomon modification and also the other two models.

3.3.4 Discussion of Incorporating New Solar Irradiance Models into STET

Both FISM and the HESSR model are improved solar spectral models which can be used to simulate the photoelectron fluxes at Mars. Our STET model currently includes the Hinteregger-81 model description of the photon fluxes. However, the Hinteregger-81 model contains a coarse wavelength resolution and we examine how the inclusion of the improved wavelength resolution of FISM and the HESSR model affects how the photoelectron fluxes predicted by STET would be altered.

In the previous sections, we have described how to incorporate FISM and the HESSR model into our STET model in detail. Due to the different wavelength resolutions of the absorption and photoionization cross sections and the two new solar irradiance models, three methods have been constructed to integrate the new models to STET. The first method is to simply integrate and linearly interpolate the FISM and the HESSR model into the uneven resolution, i.e. the Hinteregger-81 resolution. The second and third methods are to interpolate the cross sections, instead, and handle strong emission lines differently. The resultant omni-directional photoelectron fluxes of the three methods generally agree well with each other, varying within a factor of 3.

In this section we have also proposed a new modification for the Hinteregger-81 model. While *Solomon et al.* (2001) provided a good correction of the Hinteregger-81 model for short wavelengths, it does introduce higher photoelectron fluxes in the energy range 40-360 eV. This new modification combines the finding of *Solomon et al.* (2001) and *Woods et al.* (2005), leading to a better agreement with the other two models.

Finally, with the modifications, the resultant omni-directional fluxes of the three solar irradiance models, the Hinteregger-81 model, FISM, and the HESSR model, mostly vary within a factor of 2. However, the HESSR model does not include flares and therefore maybe somewhat lower than the daily averaged SSI at wavelengths below 2 nm, which leads to lower photoelectron fluxes above 300 eV. The variation among three models is decent enough to validate the three models but also leaves room to further discriminate which EUV model delivers the better performance. However, to determine which solar irradiance model prevails requires an extensive data-model comparison study. The Analyzer of Space Plasma and Energetic Atoms (ASPERA-3) experiment Electron Spectrometer (ELS) instrument (*Barabash et al.*, 2006) from Mars Express (MEx) provides a very fine resolution (dE/E=8%) for electron measurements at energies below 100 eV. These measurements could also be utilized to compare the solar irradiance models.

CHAPTER IV

Photoelectrons and Dust Storms

Trantham et al. (2011) concluded the local solar extreme ultraviolet (EUV) proxy as the main controlling factor of photoelectron fluxes at Mars, but the local EUV proxy was found to yield two distinct linear relations, suggesting some processes result in separating some photoelectron fluxes from others for the same solar irradiance level. The second elevated linear trend is due to the much higher photoelectron fluxes from late 2001 to early 2002, during which a global dust storm occurred. *Liemohn et al.* (2012) determined that the special enhancement of the photoelectron fluxes observed at 400 km was indeed a result of the global dust storm that occurred in late 2001. Also, the dust storms' influence on the photoelectron fluxes was long lived, roughly 7 Earth months. Yet both *Trantham et al.* (2011) and *Liemohn et al.* (2012) confined their studies to one single velocity space bin, 27 electron volts (eV) at pitch angle 80°-90°. In this chapter, we first examine dust storms' effects on all the available energy channels and pitch angles. Then we use the SuperThermal Electron Transport (STET) model to explore what kinds of atmosphere can lead to such photoelectron flux enhancements.

4.1 MGS Data Analysis

To investigate time-history effects of dust storms, time series of various quantities are shown in Figure 4.1. Figure 4.1a presents photoelectron fluxes of 36 eV at pitch angle $0^\circ - 10^\circ$ against time. The blue/red dots are the data values and the black vertical lines give the mean and 3-sigma uncertainty with a bin size of 0.1 Earth year (approximately 37 Earth days). The red dots are highlighted as the time period of the global dust storm in Mars Year (MY) 25 and exhibit the second linear dependence on the solar EUV proxy while the blue dots are for the rest of 'normal' time period. Here the 3-sigma uncertainty is used to exclude extremely high fluxes, along with the unusual high fluxes at the beginning of Year 1999 (approximately the first 73 days of Year 1999). Though consisting of a small amount of data points, these high fluxes can cause big drops of the Pearson correlation coefficients. To justify this exclusion, firstly, the energy spectra of the unusual high fluxes at the beginning of Year 1999 clearly show that these electrons are not photoelectrons. Secondly, these high fluxes can be magnetosheath fluxes. Thirdly, the solar EUV proxy might be more of a representative of average photoelectron fluxes. Finally, this study focuses on the two main linear trends dependence on the solar EUV proxy and these excluded fluxes are just a small portion of the data set. The exclusion of these fluxes should barely affect the findings of this study. Figure 3e is the local EUV proxy, i.e. F10.7 cm solar flux at Mars multiplying a solar zenith angle-dependent Chapman Function (*Trantham et al.*, 2011), against time. The very low values during southern summer (seen in the Figure 1c of *Liemohn et al.* (2012)), when the crustal fields were at LT 2 am but partially illuminated due to the tilt of the planet, are also excluded as the partially illuminated magnetic loops very likely straddle the terminator and therefore these fluxes may behave differently. Figure 4.1b - 4.1d are time-history dust opacity values against time. *Liemohn et al.* (2012) came up with two different methods to determine dust storms' long-term effects, time-history averages and maximums of dust opacities within a certain time window. In other words, for a data point, tracing back across a specified time length, either the averaged dust opacity or maximum within this window will be the new value. Here, time-history maximums are shown as examples and the window lengths are 7 Earth days, 154 Earth days and 354 Earth days, respectively. Figure 4.1f - 4.1h are the new controlling functions, calculated as the EUV proxy at Mars (Figure 4.1e) multiplying the left three corresponding time-history maximum dust opacities, against time. As said above, this inclusion of the time-history dust opacities serves as a modification to the dominant factor, solar EUV, of photoelectron fluxes. For instance, the multiplication of a high dust opacity may imply a denser neutral atmosphere at ionospheric altitudes and/or a higher collision rate due to a denser exosphere. Comparing Figures 4.1f - 4.1h with 4.1e shows that this adjustment sometimes exceeds an order of magnitude change in the controlling function values.

With the new controlling functions, the study of the relationship between dayside photoelectron fluxes and TES dust opacities is conducted in section 4.1.1. To further investigate the specialness of the global-scale dust storm at MY 25, two sets of modified dust opacities are also applied to the same method, with the results shown in section 4.1.2.

4.1.1 Relationship with TES Dust Opacities

Figure 4.2 shows the scatter plots of the fluxes of photoelectrons of different energies and different pitch angles (PA) against various controlling functions. The first three columns are photoelectrons of 515 eV, 116 eV, and 36 eV at PA $0° - 10°$, and the fourth shows 36 eV at PA $80° - 90°$. The x-axis for each row is EUV proxy, EUV proxy multiplying 7-day, 154-day and 364-day maximum time-history dust opacity. In each panel of Figure 4.2, all the data points are divided into 10 bins with equal number of data points inside each bin. Then the median values and quartiles (as

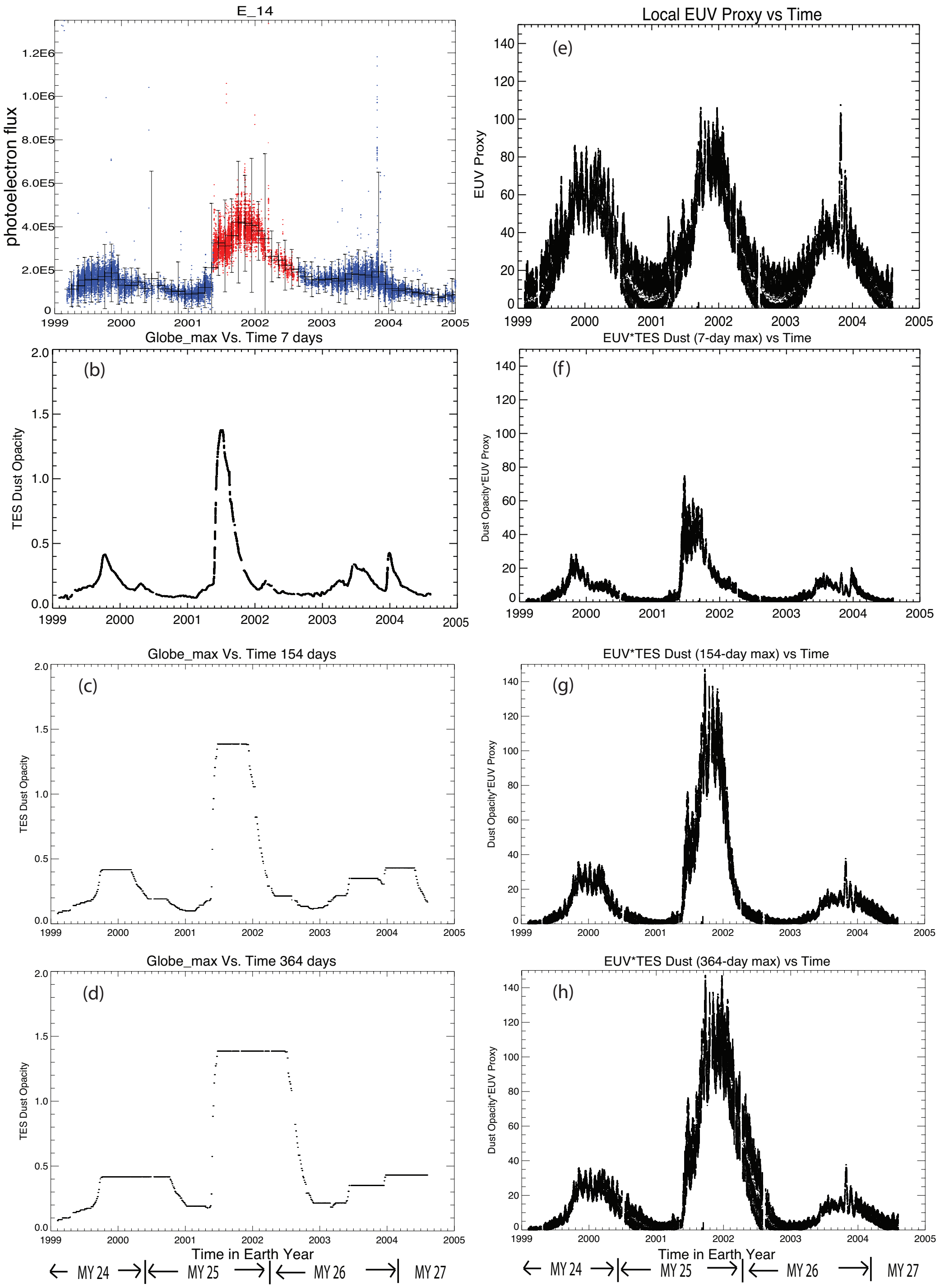

Figure 4.1: a) Photoelectron fluxes ($cm^{-2}s^{-1}ster^{-1}eV^{-1}$) at 36 eV and pitch angle $0° - 10°$ against time. The black vertical lines give the mean and 3-sigma uncertainty of all of the individual red/blue data points within a bin size of 0.1 Earth year. (b-d) 7, 154 and 354 Earth-day time-history dust opacity values against time, respectively. e) The local EUV proxy. (f-h) The new controlling functions, using the local EUV proxy at Mars (e) multiplied by the dust opacity values in b-d, against time.

error bars) for each bin are marked with the asterisk symbols, with a linear fit to these median values shown as a black line. The slope and intercept quantities to this fit, along with the Pearson correlation coefficients of all the data points in each plot, are also given in each panel. In addition, data points are highlighted in red and blue, the same as Figure 4.1a, with red designating the especially high flux interval from Earth year late 2001 to early 2002 (late MY 25 to early MY 26) while blue is used for the rest of the time.

The scatter plots of photoelectron fluxes against EUV proxy only (the first row) show a separation of photoelectron fluxes in the last three columns, the same feature as found in *Trantham et al.* (2011). In fact, this separation has been seen in 8 (×18 pitch angle bins) out of 12 energy bins with 4 energy channels as exceptions: 515 eV, 313 eV, 79 eV and 61 eV. For example, the top plot of the first column, 515 eV, does not show a clear separation. On the one hand, the results demonstrate that this double linear trend is not exclusive for only 27 eV photoelectrons at PA $80^\circ - 90^\circ$ (*Trantham et al.*, 2011) but is a common feature of the majority of energy and pitch angle bins. Especially, the fact that this feature exists in source cone pitch angles hints that the driving processes tend to happen at the source, i.e. the thermosphere/ionosphere, since photoelectrons in the trapped pitch angles are less likely to affect those in the source regions. An example of a different pitch angle, $80^\circ - 90^\circ$, is also shown in the last column. Usually, the scatter plots of pitch angle near 90° appear to be broader in flux than for field-aligned PA bins, which either can be a result of more data sampled at these particular pitch angles due to the design of the instrument or indicates some underlying physical processes. On the other hand, this feature is not found in every energy and pitch angle bin. In fact, the existence of these exceptions makes the question more complicated. While the possibility that this feature has an energy preference cannot be completely excluded, it is more likely that the exception of 79 eV and 61 eV is due to spacecraft potential. These two

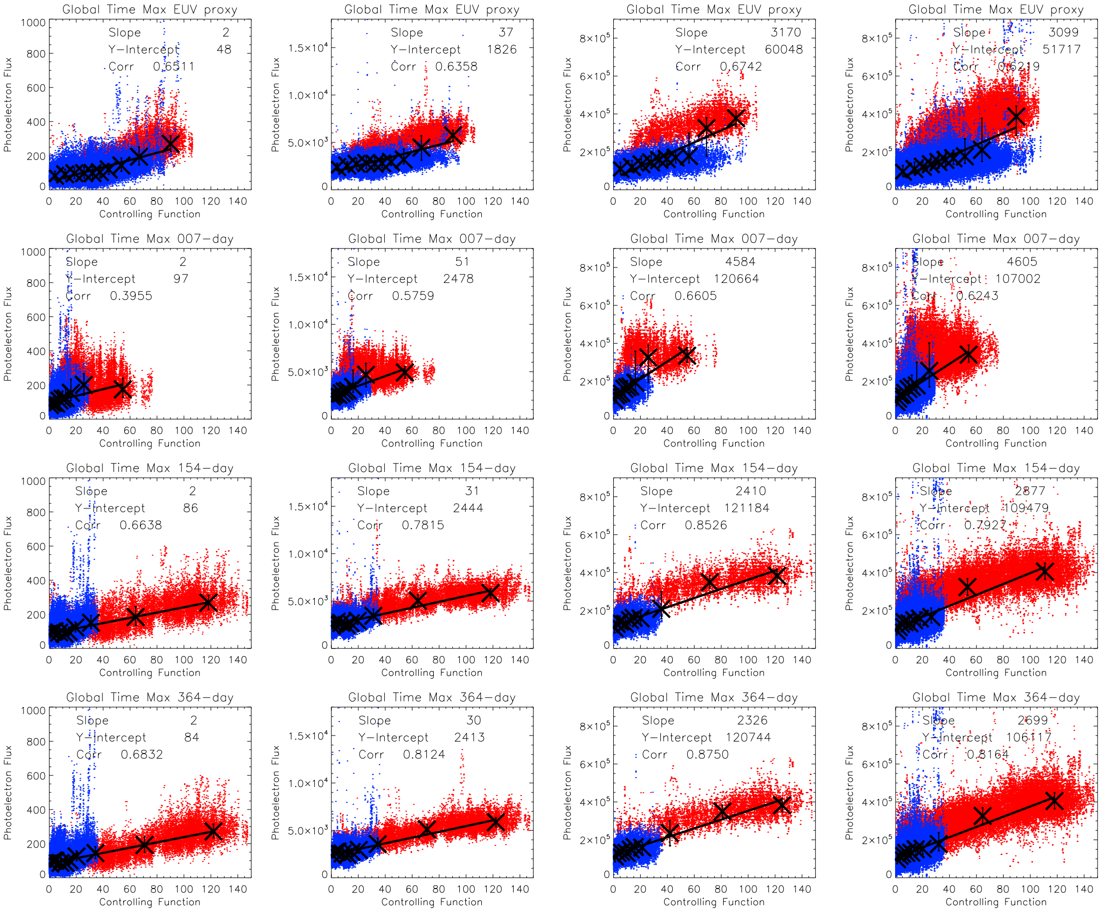

Figure 4.2: The four columns correspond to the scatter plots of the photoelectron fluxes ($cm^{-2}s^{-1}ster^{-1}eV^{-1}$) of 515 eV at $0°-10°$, 116 eV at $0°-10°$, 36 eV at $0°-10°$ and 36 eV at $80°-90°$, respectively, against different controlling functions. The x-axis for each row is: EUV proxy, EUV proxy multiplying 7-day, 154-day and 364-day time-history dust opacity, corresponding to Figure 4.1 e-h. The asterisk symbols in each panel mark the median values and quartiles (as error bars) for 10 bins with equal data points inside (with slope, intercept and correlation coefficient given in the upper). In addition, data points are highlighted in red and blue, the same as Figure 4.1a, with red for especially high flux from Earth year late 2001 to early 2002 while blue for the rest of time.

energy bins happen to be near the knee of the photoelectron energy spectrum (e.g. *Mitchell et al.*, 2001; *Liemohn et al.*, 2003), where there is an order or so of magnitude decrease of flux from 50 eV to 70 eV. The energy shift caused by spacecraft potential might cause the large variation of the fluxes of these two energies. As for the other two high energy channels that do not show the double-linear trend, 515 eV and 313 eV, it is probably because the driving factor of this feature does not favor these high energy photoelectrons.

The separation of the photoelectron population into two distinct linear trends with respect to the local EUV proxy suggests the existence of another controlling factor of photoelectrons. *Trantham et al.* (2011) investigated a few other possible candidates including solar wind pressure, the magnitude and elevation angle of magnetic field, as well as longitude and latitude (with one velocity space bin, 27 eV at PA $80° - 90°$) but concluded that these candidates have little control of photoelectrons. Our similar investigation on the rest of the energy and pitch angle bins seems to support this conclusion, as shown in the first row of Figure 4.2 for a few examples and checked for all others. However, *Liemohn et al.* (2012) provided another candidate, dust storms, and demonstrated that global dust storms may be responsible for the particularly high fluxes at Earth year 2002 by using a multiple of EUV and dust opacity as a new controlling function. Also, the correlation is the best with the use of a time-history of globally-averaged dust opacity value instead of the instantaneous value, which indicates a long-term influence from dust storms. However, this research also focuses on only one bin, 27 eV at PA $80° - 90°$.

The results above demonstrate that different energies may have different responses, hence it is necessary to investigate dust storms' influence on all energy and pitch angle bins. The same method as *Liemohn et al.* (2012) is applied to all usable bins. A few examples are also shown in Figure 4.2. The controlling function of rows 2 to 4 have multiplied three different time-history windows of dust opacity with local EUV proxy:

7 Earth days (one week), 154 Earth days (5 months) and 364 Earth days (1 year), respectively. The controlling functions against time are shown in Figure 4.1e - 4.1h, respectively. The second row sometimes has slightly better correlations compared to row 1 (such as 36 eV), but sometimes worse (such as 115 eV) and the separation has not yet disappeared. However, when the time-history window reaches 154 Earth days, the photoelectron fluxes against this controlling function are now one single linear trend, shown in row 3. As the window runs longer to 364 Earth days the last three columns in the 4th row now have an even better linear trend. Row 2 to 4 actually display the progress from two linear trends into a single one as the time-history window runs longer, if a separation is present in Row 1 (EUV proxy only). The multiplication of a 5-month window dust opacity is able to successfully merge the separations. Mathematically, the Pearson correlation coefficient (R) (shown in the upper left corner of each panel) has a ~ 0.1 increase for the last two rows, compared to the first two rows. This increase is statistically significant, given the number of data points included to calculate the correlation, which is hundreds of thousands.

Notice that for each column in Figure 4.2, the correlation coefficients of the 154-Earth-day time history window and 364-Earth-day window are almost the same, which indicates that R does not always rapidly increase as the time window increases. How R changes as a function of the time-history window is shown in Figure 4.3. The three columns are for three energy bins: 515 eV, 115 eV and 36 eV and each row for different pitch angle bins: PA $0° - 10°$, PA $80° - 90°$, PA $170° - 180°$, respectively. Notice that the y axes have different ranges for each plot. Two lines (red and blue) correspond to two methods to obtain the time-history dust opacity (the maximum and average within the window). A common feature of all the panels in Figure 4.3 (also seen in the rest of the pitch angle and energy bins not shown here) is that the correlation coefficient rapidly increases at first and then levels out for the rest of the time window.

However, in spite of the fact that rapid increases in the correlation are observed in all the energy and pitch angle bins as the time history window increases, it is important to compare with the correlation with solar EUV proxy only, denoted as "Orig Corr" in the right bottom corner of each panel. In fact, those energy and pitch angle bins that exhibited little to no separation of photoelectron fluxes in the scatter plots barely have any increase of correlation with window duration, especially in the trapped zone, such as 515 eV, PA $80^\circ - 90^\circ$. In this case, dust storms seem to have little effect on these energy channels. In contrast, the source region (pitch angle near 0° or 180°) of energy channels higher than 53 eV and all the pitch angles below 53 eV have shown a higher correlation than that of solar EUV proxy only. A few examples are shown in Figure 4.3. The increase is around 0.05 for 515 eV at both pitch angle bin $0^\circ - 10^\circ$ and $170^\circ - 180^\circ$ and 115 eV at PA $80^\circ - 90^\circ$. An increase of above 0.15 is seen in the source region of 115 eV and all three different pitch angles of 36 eV.

For those bins with higher correlation with inclusion of time-history dust opacities, the rapid increase of correlation stops at 120 Earth days (approximately 63° Ls) or longer, which implies that the influence of dust storms is most likely long-lasting. After this point in the window duration setting, the change of R is within 0.01 as the time-history window runs longer. This level-off implies the lack of sensitivity towards the exact length of this time-history window, pointed out by *Liemohn et al.* (2012). Also, because of the fact that the line shape of using the running average within a time-history window is similar to that of using the maximum value and that the latter usually has a similar or higher correlation than the former, especially for low energies, all the discussion below will be based on results of using this maximum value.

Two kinds of information can be extracted from Figure 4.3, the length of the time-history window and the improved correlation coefficients. For the former one, because of the insensitivity towards exact peak in the time-history window, the transition point, where R changes from a rapid increase to almost a constant, can be

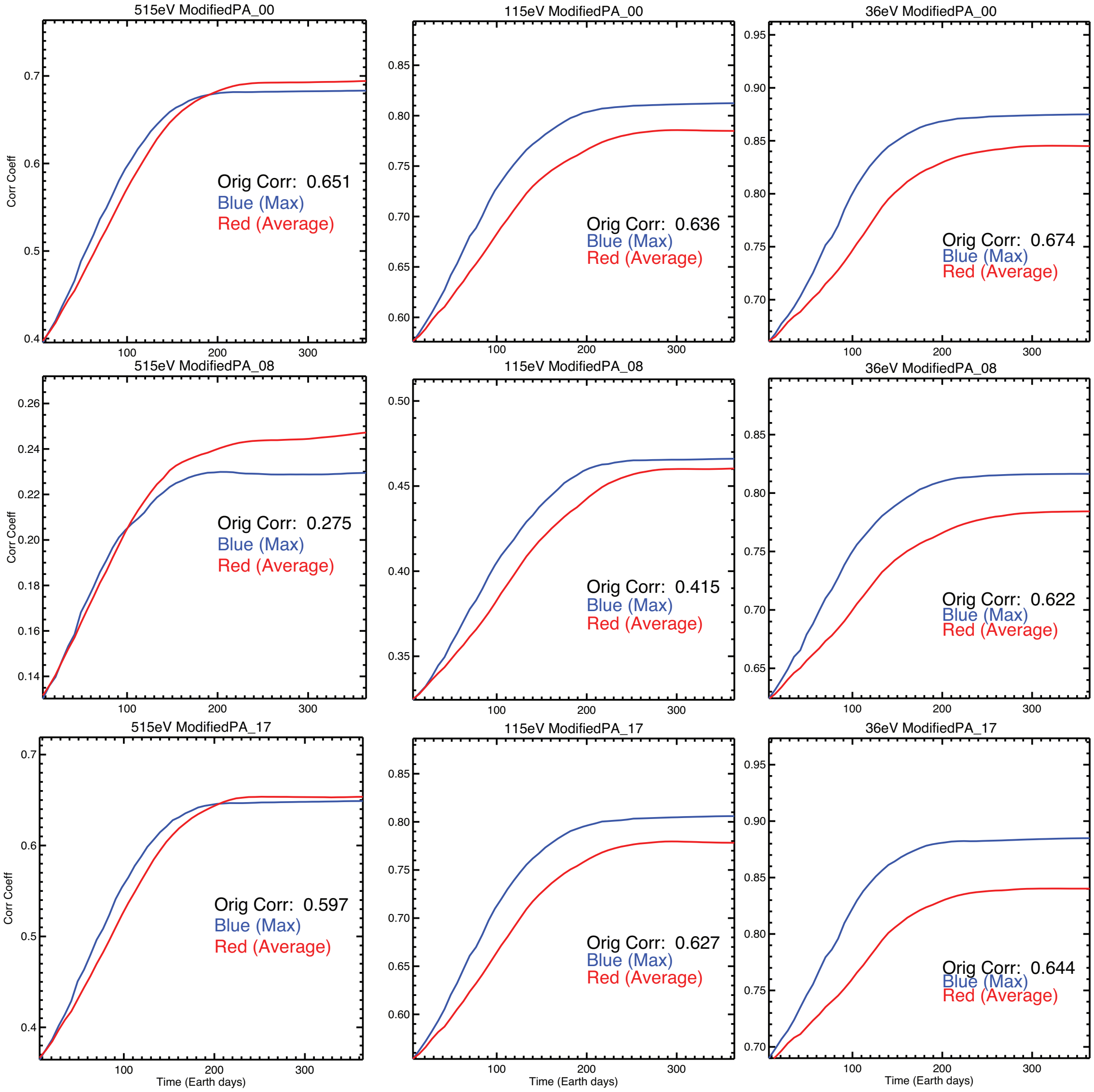

Figure 4.3: Correlation coefficient of photoelectron fluxes versus a controlling function (Figure 4.1 g), with red and blue curves corresponding to a running-average time-history dust opacity method and a maximum-value time-history dust opacity method. “Orig Corr” denotes the correlation without the inclusion of dust opacities. The three columns are for three energy bins: 515 eV, 115 eV and 36 eV and each row for different pitch angle bins: PA 0° – 10°, PA 80° – 90°, PA 170° – 180°, respectively. Notice that the y axes have different ranges for each plot.

considered as a reasonable representative of this time length. Here, two criteria are applied to determine this transition point. If dy is the subtraction of the maximum and minimum correlations, i.e. the correlation range of each panel of Figure 4.3, a transition point is such that its correlation is no more than 0.1*dy lower than the maximum correlation, defining a region near the maximum value, and also that its correlation is $\leq$ 0.05*dy larger than the previous point's correlation, to guarantee a very slow increase. In addition, since R is almost the same after this transition point, the correlation coefficient of this time point will be used as the improved correlation for the following discussion.

The correlation coefficients of all energy and pitch angle bins for both the case of the EUV proxy only and the case of including time-history dust opacities are given in Figure 4.4, in the upper and lower panel, respectively. In the upper panel, for energy greater than 53 eV, the correlations are mostly above 0.5 in the source region and lower in the trapped zone, especially low for all pitch angles of 79 eV, which is near the knee of the photoelectron energy spectrum. For energy lower than 53 eV, the correlations are generally higher than 0.6, and not obviously lower in the trapped zone.

There are two possible reasons for the slightly lower correlations at high energies. Firstly, high-energy photoelectrons are produced by shortwave photons, such as X-rays, while the EUV proxy used here, based on F10.7, is not a very good approximation for such shortwave solar flux. Secondly, the method used to account for the different angles of Mars and Earth are not able to capture all the solar flares and/or other short-lived solar activities. Another feature is that correlations of the trapped zone are lower for high energies. Notice that the measurement of MGS is at around 400 km, well above the source region of these examined photoelectrons (which is usually located below 200 km). Particles of pitch angles near 90° are mostly scattered into and reside at high altitudes. Their fluxes depend on not only solar

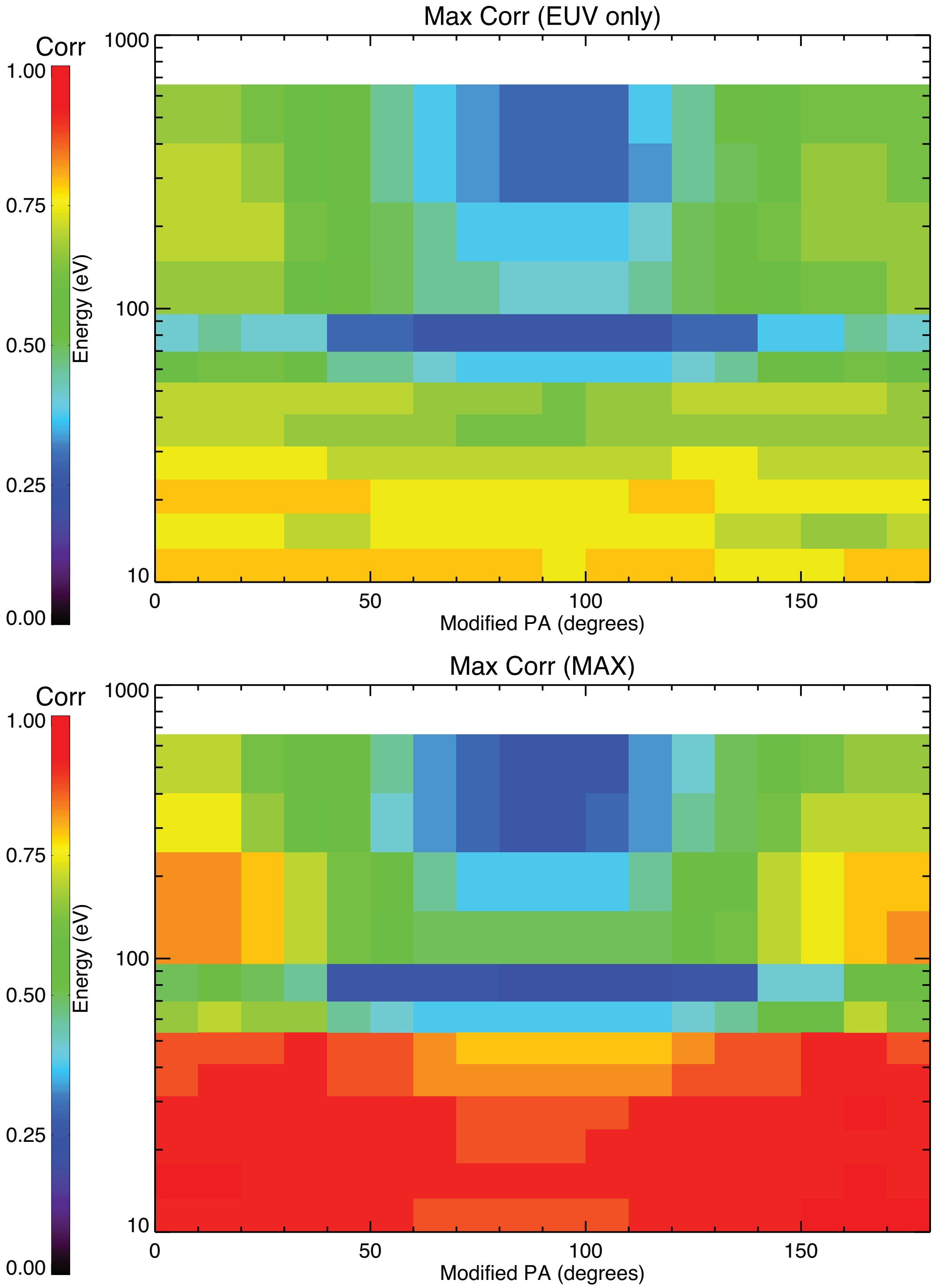

Figure 4.4: The correlation coefficients of the photoelectron fluxes versus a controlling function of all the energy and pitch angle bins. The controlling function of the upper panel is the local EUV proxy only while that of the lower panel is the local EUV proxy multiplied by the maximum-value time-history dust opacities.

radiation but also scattering. This extra controlling factor can lead to lower correlations. Especially, since the collision cross section is proportional to the inverse of energy square ($1/E^2$) (*Rutherford*, 1911; *Khazanov and Liemohn*, 1995), high-energy photoelectrons are harder to be scattered into the trapped zone. This may also be the reason for the different behaviors within the trapped zone for low and high energies. In addition, *Liemohn et al.* (2003) noted that observed high-energy photoelectron pitch angle distributions were more isotropic than at lower energies, indicating other scattering mechanisms could be dominant (e.g. wave-particle interactions).

After multiplying time-history dust opacities as new controlling functions, as shown in the lower panel of Figure 4.4, a similar pattern to the upper panel is found, but the correlation now is much higher in most bins. Especially, the number now is above 0.8 for the lower energies across all pitch angles. The obvious increases in the source region of high energies are also seen. However, as mentioned above, lower correlations than with the EUV proxy only are seen in the trapped zone of high energy channels.

As said above, it is important that the correlation after including the time-history dust opacities is higher than the correlation with the local EUV proxy only. To further demonstrate this criteria, the quantitative difference of the two panels of Figure 4.4 is shown in Figure 4.5, both the absolute and relative difference given in the two panels, respectively. For energy below 53 eV, the increase of correlation is mostly above 0.1, up to 0.25. Also, it appears that the downward fluxes experience a higher increase than do the upward fluxes while the trapped zone seems to be the lowest, again. For energy above 53 eV, the increase of correlations in the 115 eV and 190 eV channels, both displaying a double linear trend in the scatter plots, is seen across all the pitch angles, above 0.1 in the source region. For the 61 eV and 79 eV energy channels, there was barely flux separation seen in the scatter plots of electron fluxes against local EUV proxy but there is seen a correlation improvement in the source region,

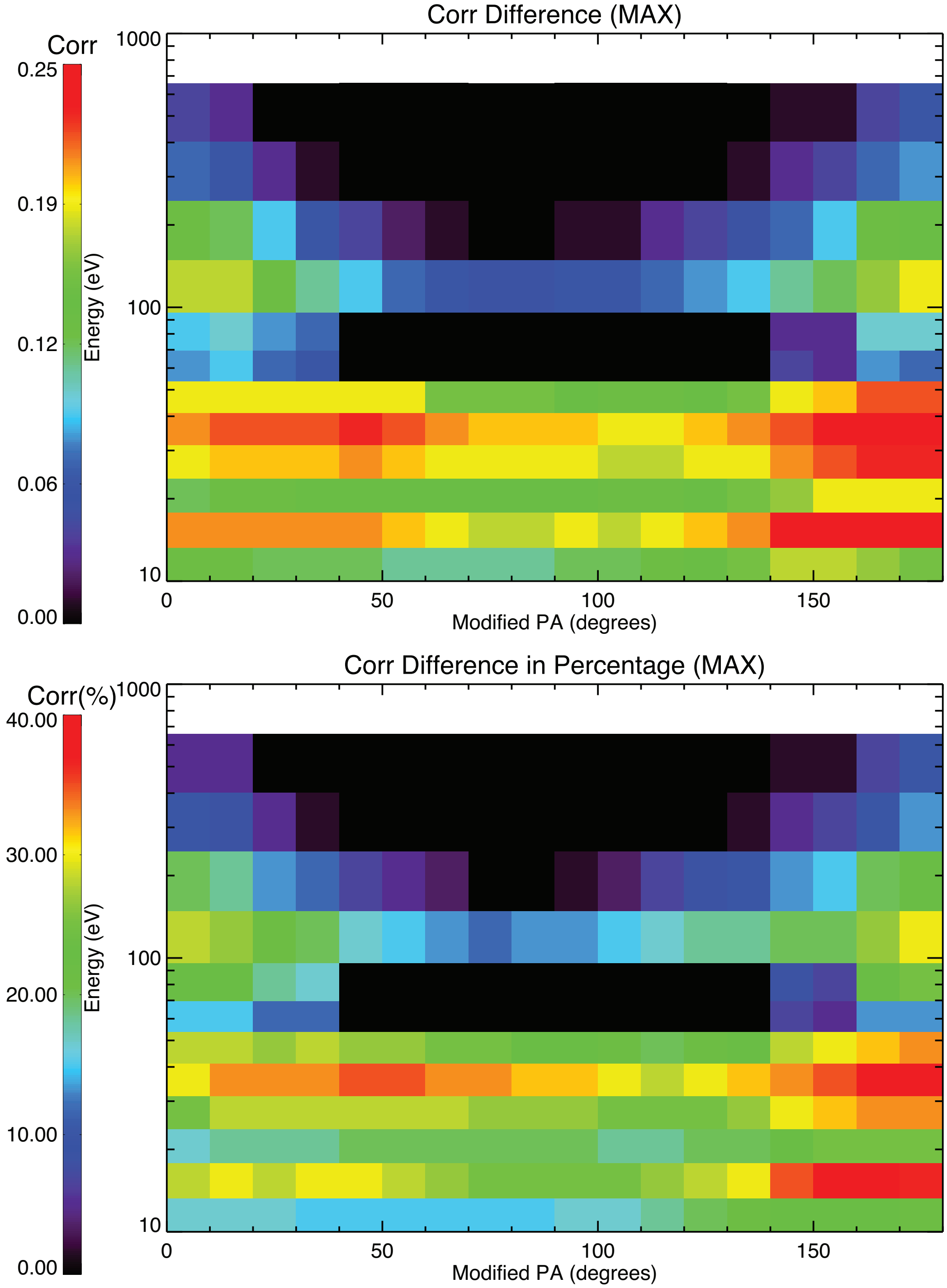

Figure 4.5: The absolute (upper) and relative (lower) correlation difference of the two panels of Figure 4.4. Note that the color scale for the upper panel is 0-0.2 while for the lower it is 0-40%.

as shown in Figure 4.4. It implies that the disappearance of the double linear trend in these two energy channels might be due to spacecraft potential effects that mix the very different flux intensities above and below the knee in these bins rather than some physical processes. Finally, the two highest examined energy channels, 313 eV and 515 eV, only have small increases (of less than 0.1) at a few source region bins. Over all, an increase of correlation in the source region is the common feature of high energies. While excluding two channels near the knee, it seems that the increase in the trapped zone is less and less when energy increases. The relative difference of the before/after including time-history dust opacities is also given in the lower panel of Figure 4.5. The pattern resembles the absolute difference plot. Mostly, the increase of correlation is around 20%. In all, it appears that, when there is a flux separation in the scatter plots like Figure 4.2, the correlation coefficient after including the time-history dust opacities will also more or less improve, such as for all the pitch angles of low energies and in the source region of high energies; on the contrary, when there is barely flux separation, little improvement is seen, like the trapped zone of high energies. The general improvement of correlations at all energies suggests that dust storms are responsible for the appearance of the second linear trend.

The fact that the maximum increase of correlation happens with ≥ 100 Earth-day time history dust opacities instead of instantaneous opacity values suggests a long-lasting effect of dust storms, as claimed by *Liemohn et al.* (2012). The exact time length of this long-lasting effect is also significant, shown in Figure 4.6, determined according to the method said above, upper and lower panels corresponding to the maximum value and running average methods, respectively. Also, notice that only for those bins with significant correlation improvement is the time-window length significant. For the maximum value case, this time length for low energies is around $140 - 160$ Earth days (approximately $70° - 84°$ Ls at Mars, given $1°$ Ls is about 1.9 Earth days on average at Mars) while for a few high energy bins where dust storms seem to play a role, the influence lasts longer, up to almost 190 Earth days (approximately 100° Ls at Mars). By comparing the upper panels of Figure 4.5 and Figure 4.6, an interesting feature is seen, for low energies, the history window seems longer where the increase of correlation is higher. For the running average case, the time length is around 210 Earth days (approximately 110° Ls at Mars) for most bins. Notice that the time-history length of the maximum value case is different from *Liemohn et al.* (2012) (which said 210 Earth days for both cases). It is because the method of determining this window length is different between the two studies. In fact, both studies have an agreement that the influence of dust storms is long-lasting instead of an instantaneous effect.

4.1.2 Relationship with Modified Dust Opacity Levels

The results above have shown that the conclusion of dust storms' long-living influence on photoelectrons applies to all energy and pitch angle bins below 53 eV and also the source region of higher energies. However, measured dust storms occurred on Mars in every southern spring from MY 24-27, as shown in Figure 4.1b. It is not yet clear whether all the dust storms affect the photoelectrons or whether the global-scale dust storm at MY 25 is special. Hence, two sets of modified dust opacity are made, by isolating the dust storm at MY 25 from the rest of the timeline. The first artificial dust opacity time series is the dust storm MY 25 opacity with a constant 0.2 for the rest of the time, colored as red in Figure 4.7 (denoted as high dust opacity) while the second new dust time series has the original low dust opacity everywhere but substitutes the large dust storm with a constant 0.2 level, colored black in Figure 4.8 (denoted as low dust opacity). The same time-history method has been applied to both sets and the results are shown in Figure 4.8: (a) and (b) corresponding to high dust opacity and (c) to low dust opacity.

Figure 4.8a shows an example of the plot of R against history-time window of 36

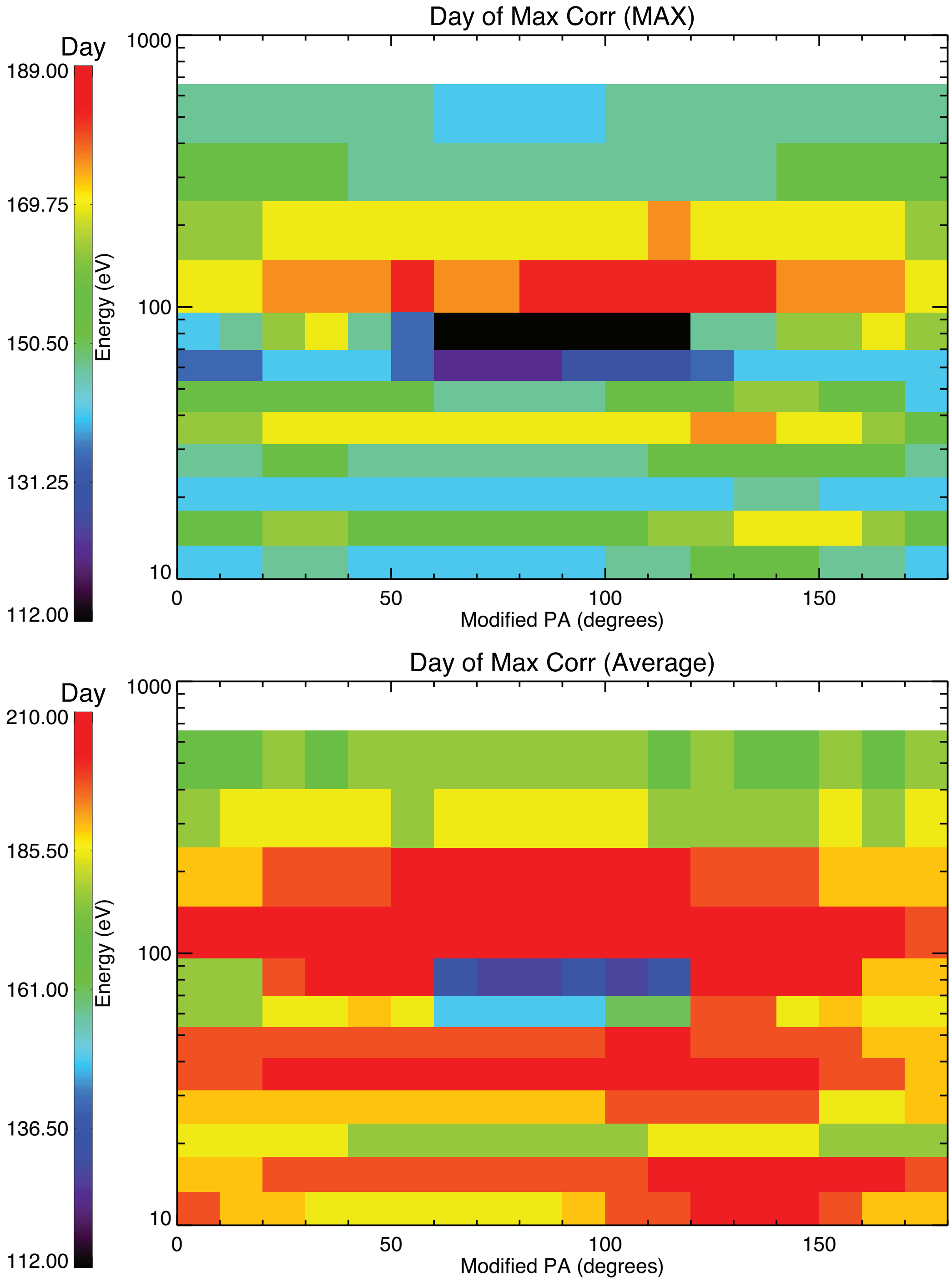

Figure 4.6: The window lengths of time-history dust opacities used to generate the correlation coefficients in the lower panel of Figure 4.4. The upper (lower) panel corresponds to a maximum-value (running-average) time-history dust opacity method. Note that the color scales of the two are different.

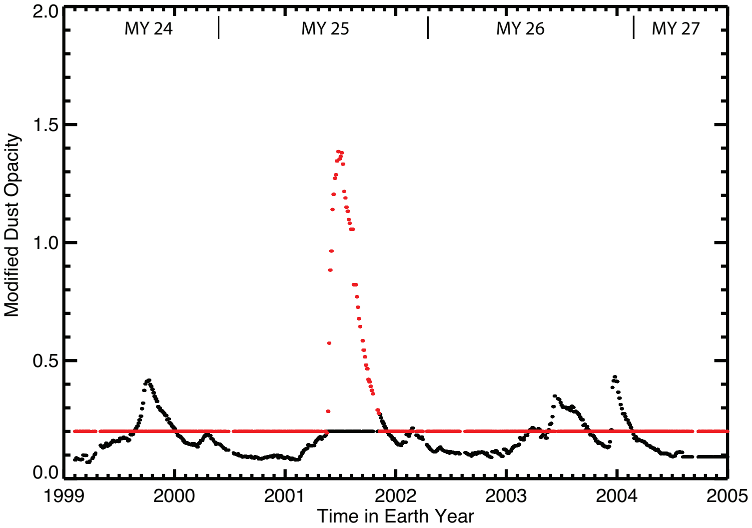

Figure 4.7: Two sets of modified dust opacities versus time. The red (black) line is for the high (low) dust case.

eV at pitch angle 0° – 10° and red/blue highlight the two methods of time-history dust opacity calculation, maximum and average. Similar to Figure 4.3, the correlation increases first and then levels off as the window length increases. In fact, the other line plots of this high dust opacity case resemble the real case. To illustrate this, the absolute difference of two sets of correlation coefficients, before and after including dust opacity, is given in Figure 4.8b. Compared with the upper panel of Figure 4.5, the two plots appear to be almost the same, with an increase of correlation seen in all the pitch angles of low energies and in the source region of high energies. This similarity between these two cases implies that the dust storm in MY 25 is entirely responsible for the improvement of correlation as well as the merging of the double linear trend in scatter plots.

To further investigate the influence of the unusually large dust storm, correlations for the low dust opacity case have also been conducted. One example of this low dust opacity case is exhibited in Figure 4.8c, the plot of R against time-history window for 36 eV at pitch angle 0° – 10° (as was shown in Figure 4.8a for the high dust

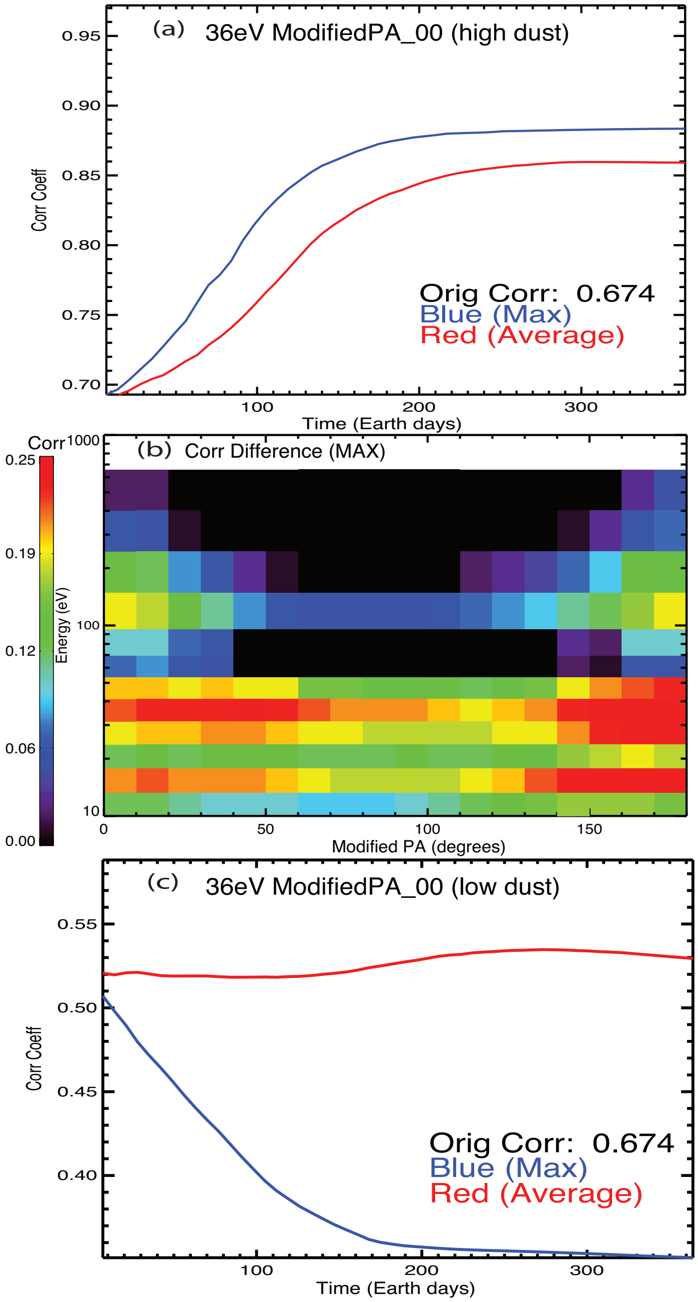

Figure 4.8: (a) Correlation coefficients of the fluxes of 36 eV photoelectrons at PA $0° - 10°$ versus the window length of the time-history dust opacities for the high dust case. Again, "Orig Corr" denotes the correlation without the inclusion of dust opacities. (b) The absolute correlation difference of all the energy and pitch angle bins between before and after including the time-history dust opacities for the high dust case. (c) Correlation coefficients of the fluxes of 36 eV photoelectrons at PA $0° - 10°$ versus the window length of the time-history dust opacities for the low dust case. Red (blue) curve in a and c highlights the running-average (maximum value) dust opacity method. Also notice the y axes have different ranges for the two plots.

case). The line shape no longer keeps increasing, but decreasing for the blue line. Also, the correlation coefficient with EUV proxy only is 0.67, given in the right lower corner, while the correlation after multiplying dust opacity is always lower than 0.55. Similarly, all the examined energy and pitch angle bins share the same feature that the inclusion of low dust opacity actually diminishes the correlation coefficients.

The opposite results for the two artificial dust opacity profiles strongly suggest not only that the dust storm in MY 25 is entirely responsible for the second linear trend in the scatter plots but also that the usual dust storms have little influence on photoelectrons. It appears that dust storms with high 9-micron dust optical depths (τ greater than some value between 0.5 and 1.4) can significantly change the Martian upper atmosphere. The question remains, what feature(s) of large dust storms give rise to this second linear trend in the scatter plots.

4.1.3 Discussion of Observed Photoelectron Fluxes and Dust Storms

The results presented above show that dust in the lower atmosphere has a long-lasting influence on high-altitude photoelectron fluxes. Note that photoelectrons will recombine and be lost to the neutral atmosphere on the nightside; thus such a long-lived effect of a dust storm must be due to the changes in the neutral atmosphere (*Liemohn et al.*, 2012). Two highly possible candidates of how dust storms affect the photoelectron fluxes are the change in the source, e.g. the perturbation of the neutral density below 400km, and/or high altitude scattering due to the density change at or above the altitude of MGS. With the inclusion of time-history dust opacities, a significant increase of correlation between photoelectron fluxes and the new controlling function is seen at all the low energy bins and more field-aligned high-energy bins but not the trapped zone of high energy channels. As mentioned in the methodology section, the source region pitch angles are more directly related to the source at the ionosphere while the trapped zone is more influenced by high-altitude scattering.

The increase of correlation happens at the source region of all energies, suggesting that the effects of dust storms more likely happen in the ionosphere. The different behaviors of trapped zones of different energy channels, again, can be caused by the fact that the collision cross section is proportional to the inverse of energy squared ($1/E^2$). Low-energy photoelectrons are more easily scattered into the trapped zone. In other words, the low-energy trapped zone is more sensitive to changes of sources than the high-energy trapped zone. In contrast, even if high-energy photoelectron fluxes in the ionosphere change due to dust storms, it might not be shown in the trapped zone at 400 km. In fact, before relating dust storms, the flux separation in the scatter plot of photoelectron flux against EUV proxy is found in both source and trapped pitch angles. It already implies that driving processes more likely happen in the source cone as the photoelectrons in the trapped pitch angles are less likely to affect those in the source regions.

Therefore, the results imply changes to the neutral densities in the thermosphere rather than the exosphere. According to Chapman production function (equation 9.21 in *Schunk and Nagy* (2009)), the peak production rate occurs at unit optical depth and is directly proportional to the neutral density at the bottom side of the thermosphere (equation 11.55 in *Schunk and Nagy* (2009)). The additional solar energy absorption of dust particles heats the lower atmosphere and therefore results in a larger scale height at low altitudes, which leads to an enhanced neutral density at the bottom of the thermosphere. This will then increase the peak production rate of photoelectrons. Note that ER measures the non-thermal primary photoelectrons (> 10 eV), as opposed to the thermal electrons that dominate the main peak and participate in the equilibrium that establishes the Chapman-like structure. The fluxes of non-thermal primary photoelectrons detected by ER are determined by the source but also the loss due to scattering.

The artificial opacity time series case has shown that only the dust storm at MY

25 is able to significantly affect photoelectron fluxes. It appears that dust storms with high 9-micron dust optical depths can significantly change the Martian upper atmosphere. In fact, although *Lillis et al.* (2010b) concluded that there was no clear trend between total electron content (TEC) in the Mars ionosphere and dust opacity, there was indeed a sudden increase of TEC at the end of MY 28, corresponding to the time period of a dust storm that reached a 9-micron dust optical depth of 1.0. The dust opacities are obtained from the Thermal Emission Imaging System (THEMIS) (e.g. *Smith*, 2009). Despite that the peak of dust opacity seemed broader than peaks of TEC, *Lillis et al.* (2010b) did not rule out the connection between the two, given no apparent change of other drivers. Our results imply that it is the changes in the ionosphere caused by the global-scale dust storm at MY 25 that greatly modified photoelectron fluxes at 400 km while this increase of TEC also shows the changes at ionospheric altitudes potentially caused by the global-scale dust storm at MY 28. However, it is not yet clear whether the influence of the global-scale dust storm at MY 28 on the ionosphere is long-lasting or not. Therefore, it is necessary to analyze the electron data from Mars Express ASPERA-3 ELS (e.g. *Barabash et al.*, 2006) and apply the similar method to investigate the time-history effects of the dust storm at MY 28 on electron fluxes. If it turns out that the MY 28 dust storm does not have an obvious and/or long-lasting effect on photoelectron fluxes and the ionosphere, it might imply that the MY 25 dust storm was special in some way and was a one-time event. And if the MY 28 dust storm does have an obvious and/or long-lasting influence, together with our results, it suggests that there exists a dust opacity threshold above which dust storms cause obvious and/or long-lasting changes in the ionosphere, or even higher altitudes like 400 km. Given the dust opacity values from Mars Year 24 to 28 (e.g. *Smith*, 2006, 2009; *Medvedev et al.*, 2011), this threshold might be roughly between a global-averaged 9-micron dust optical depth, τ, of 0.5 and 1.0. In other words, as long as dust storms become large enough, above this threshold, they

are able to affect the entire atmosphere to such an extent that the ionosphere and photoelectron fluxes are significantly affected.

Since we only investigated one case (MY 25 dust storm), it is hard to characterize the nature of the link between the dust storms and photoelectron fluxes and the ionosphere. The globally-averaged 9-micron dust optical depth threshold could lead to many possibilities for the underlying physics. For example, on one hand, the dust threshold could be related to the height where dust is still dense enough to significantly alter the upper atmosphere. On the other hand, global-scale dust storms might change the circulation or state of the lower atmosphere in ways that are transmitted to the upper atmosphere. It is also very possible that the two scenarios are connected. All these possibilities not only indicate the complex interactions between physical processes, but also demand further investigation of this issue.

Both *Liemohn et al.* (2012) and our study have shown that dust storms' influence tends to be long-lived, as long as about $140-160$ Earth days (approximately $70° - 84°$ Ls at Mars). This influence may be due to a long-lasting thermospheric density increase caused by dust storms. In fact, *Withers and Pratt* (2013) claimed a corrected decay time, approximately $80° - 120°$ Ls, of neutral density enhancement at altitudes of 130-160 km. The upper atmospheric changes by dust storms can also remain longer than the decay of the dust storms themselves, about 32° Ls, by analyzing the atmospheric densities at northern latitudes ($30° - 60°$N) from the MGS accelerometer responding to the Noachis dust storm (40°S, 20°E). In other words, the atmospheric densities remained elevated even though dust opacities dropped back to their pre-storm level. However, the correction to the neutral density decay time removes the effects of changing latitude and changing season, while the latter should be considered in our case since in reality density did decrease when the season advanced into winter. Hence, the fitted decay timescales (τ_{fit}), given in both Ls degrees and approximate Earth days, are examined again here, shown in Table 1 (values from Table 1 of *Withers*

Altitude (km)	Direction	Latitude (°N)	τ_{fit} (°)	τ_{fit} (Earth days)
130	Outbound	32.6-39.1	53.31±4.53	101.3±8.6
140	Outbound	32.2-36.4	59.65±3.95	113.3±7.5
150	Outbound	29.5-34.4	73.12±4.98	138.9±9.5
160	Outbound	27.5-32.6	82.98±6.50	157.7±12.6
130	Inbound	43.1-51.8	42.93±2.78	81.6±5.3
140	Inbound	44.2-54.5	39.64±1.72	75.3±3.3
150	Inbound	46.9-56.5	41.65±1.98	79.1±3.8
160	Inbound	49.0-58.3	50.94±3.24	96.8±6.2

Table 4.1: Atmospheric densities measured by the MGS accelerometer during the Noachis dust storm and related properties. The latitude range reported for each set of measurements corresponds from Ls = 224° to Ls = 260°. τ_{fit} is the decay timescale obtained by a direct exponential fit to the data, given in both Ls degrees and approximate Earth days. The uncertainties are 1σ. (Values from Table 1 of *Withers and Pratt* (2013))

and Pratt (2013)). Outbound measurements of latitudes from 30°N to 40°N, closer to the place where the dust storm originated, have longer fitted decay times, above 50° Ls and up to 80° Ls at the most equator-ward latitude (corresponding to $100 - 160$ Earth days), than the inbound measurements at latitudes greater than 40°N (where decay time is approximately $80 - 100$ Earth days). The fact that an 80° Ls decay of the upper atmospheric density responds to a dust storm with a peak localized 9-micron dust opacity $\tau \sim 0.75$ with a lower atmosphere decay time of 32° Ls hints that dust storms' effects on regional atmospheric densities can last longer than the dust storm itself. Our study shows that the time length of the long-lasting effects of the global dust storm with a peak globally-averaged 9-micron dust opacity $\tau \sim 1.5$ in MY 25, about $140 - 160$ Earth days, is roughly the same time length of the dust storm itself. In other words, the response of photoelectron fluxes lasts approximately twice as long as the dust storm, which matches the analysis above.

Another possibility is the influence of the two persistent high-altitude dust layers, centered at 20-30 km, high-altitude tropical dust maximum (HATDM), and 45-65 km, upper dust maximum (UDM) (*Guzewich et al.*, 2013). Given very few dust retrievals above 60 km, *Guzewich et al.* (2013) did not exclude the possibility of the UDM being located at altitudes higher than 60 km, especially during the MY 25 global dust storm. These two high-altitude dust layers may influence the neutral atmosphere, thus the photoelectron fluxes, at altitudes higher than we originally assumed. Even though dust storms contribute to these two dust layers, they are not usually the determinant factor. It is possible that a change in these two layers due to a dust storm lasts longer than the transient dust storm itself. The changes experienced by these two layers, especially the UDM, could be transmitted into the thermosphere/ionosphere. However, it is also important to notice that these two dust layers are a detail within the main column of dust and therefore less likely to be a candidate causing significant changes in the upper atmosphere.

In addition, *Forbes et al.* (2008) has shown that the MGS neutral densities at 400 km and exospheric temperatures are fit well (correlation coefficients of 0.96 and 0.99, respectively) with a Mars-adjusted F10.7 and an additional seasonal term, without any additional augmentation from a dust term. It suggests that dust storms do not cause a long-lasting effect on the exosphere. It may explain why there is no obvious improvement of correlation after adding time-history dust opacities at the trapped pitch angles, which is mainly affected by the state of the neutral exosphere.

One possible error of the results of high-energy photoelectron is to use an EUV proxy based on F10.7. Hence, another EUV proxy based on the Flare Irradiance Spectral Model (FISM) (*Chamberlin et al.*, 2007, 2008) with the same interpolation from Earth to Mars is employed to repeat the procedure above. The EUV irradiance is integrated over several bandwidths (0-10 nm, 0-50 nm and 50-100nm) to obtain the solar EUV fluxes. It turns out that all the results are nearly identical with the EUV proxy based on F10.7. It suggests that the difference between the proxy based on F10.7 and FISM is small and that the possible error from interpolation from Earth to Mars is more dominant. Regardless, even for high-energy photoelectrons, the correlation of their fluxes and these solar EUV proxies is greater than 0.5 for source pitch angles, decent enough to make the case.

Another possible error may result from the contamination of spacecraft secondary electrons at high-energy channels (*Furman and Pivi*, 2003). The contamination filter, excluding anode sections 5-12 facing the spacecraft, is also applied to high-energy channels. This new set of results are also nearly identical to those presented in section 3 (included in the supplemental figures accompanying this paper). It implies that the possible contamination at high-energy channels seems insignificant to our study.

4.1.4 Summary of Observed Photoelectron Fluxes and Dust Storms

A survey was conducted of the Mars Global Surveyor electron data across all the pitch angles (PAs) of 12 usable energy bins (11 eV−746 eV) for dayside photoelectron observations over regions of strong crustal fields. The results have shown that the unusual bimodal solar flux dependence of dayside photoelectron fluxes is seen in all the pitch angles of low energies ($\leq$ 53 eV) and some bins of higher energy channels but is not obvious in the rest of the high energy bins. By applying time-history dust opacities to obtain new controlling functions, the separations seen in the scatter plots are now merged into one linear trend. In addition, quantitatively, obvious correlation coefficient increases are also found at all pitch angles of energy channels lower than 53 eV and source regions of higher energy channels, even for 61 eV and 79 eV, two channels that are near the knee of the photoelectron energy spectrum.

The results not only confirm that dust storms' influence on photoelectron fluxes are long-lasting, about $140 - 160$ Earth days (approximately $70° - 84°$ Ls at Mars), but also imply that the changes caused by dust storms are most likely occurring in the source region, i.e. the thermosphere/ionosphere. Furthermore, the isolation of the global dust storm at MY 25 from the rest of the dust opacities shows that this global-scale dust storm is entirely responsible for photoelectron fluxes' second solar flux dependent trend. While it is possible that the MY 25 global dust storm was a one-time event, based on the results of this thesis and *Lillis et al.* (2010b), we hypothesize that, if the global-averaged 9-micron dust optical depth, τ, exceeds a threshold between 0.5 to 1.0, dust storms are more likely to cause significant and/or long-lasting changes in photoelectron fluxes and the ionosphere.

Two possible explanations as to why dust storms have such long-lived effects are also given. Firstly, the atmospheric density decay time could be much longer than the dust storm decay time. Such long-term elevated atmospheric densities can significantly increase the photoelectron fluxes at MGS altitude for a very long time. In addition, two high altitude dust layers, HATDM and UDM, might affect the thermosphere/ionosphere more than transient dust storms as they are located at higher altitudes and the changes of these two layers caused by dust storms might linger longer after dust storms subside.

4.2 Modeling

As mentioned in *Liemohn et al.* (2012), the dust storms' influences are long lived so that the changes mostly like originate from the neutral atmosphere as the ionosphere mostly depletes every day on the nightside at Mars. The basic idea is to use the neutral atmospheres in Figure 3.2 as the baseline, denoted as the "normal case", and then to test different artificial atmospheres to compare the resultant photoelectron fluxes at 400 km. In this section, we first show some examples of observations, then use the model to investigate candidate atmospheres that can replicate the observation.

4.2.1 Results

Figure 4.9 shows some examples of the photoelectron fluxes observed by the MGS MAG/ER instrument. The two clear linear trend dependences of the photoelectron fluxes on F10.7 cm values are seen. The median red and blue fluxes are fitted with

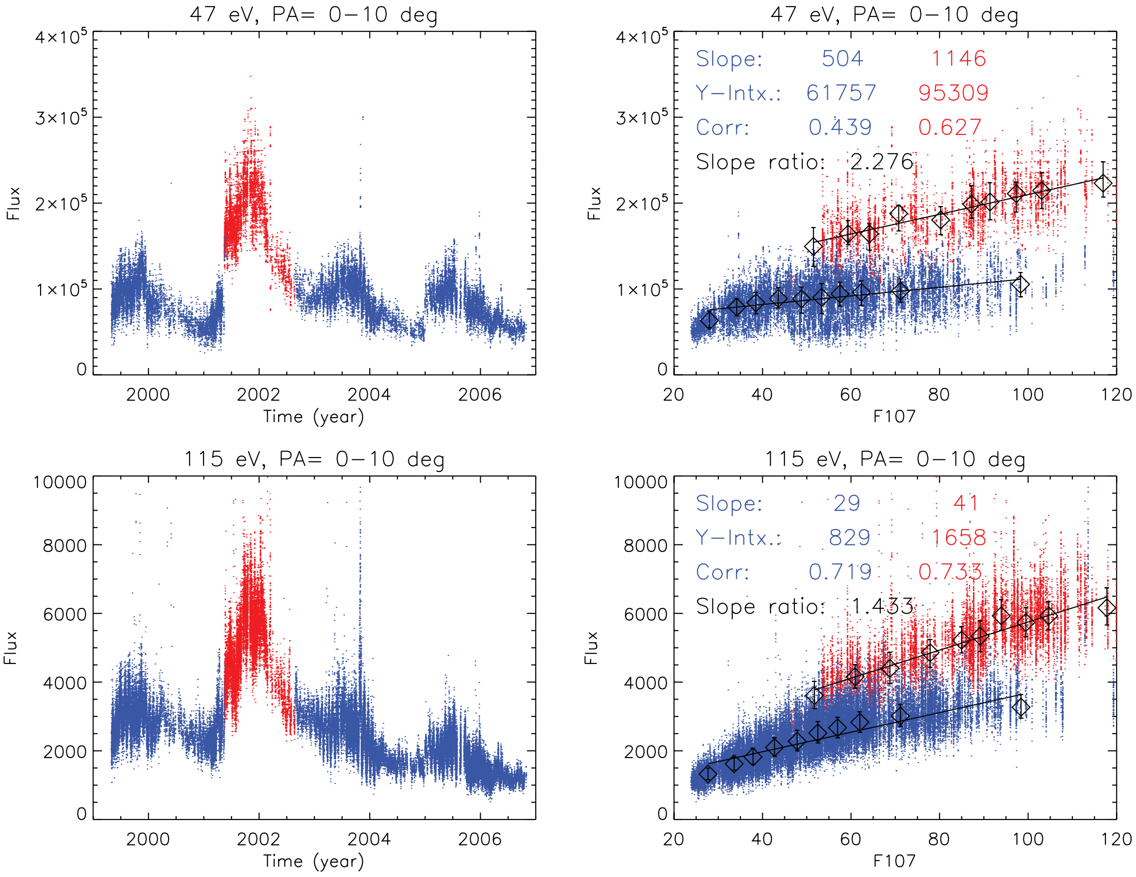

Figure 4.9: The photoelectron fluxes (# cm^{-2} eV^{-1} s^{-1} sr^{-1}) observed by MGS MAG/ER against time (the left column) and F10.7 cm values in sfu (the right column) for pitch angle $0° - 10°$ and the two rows are for 47 eV and 115 eV, respectively. The red highlights the extreme high photoelectron fluxes for a time period during which a global dust storm occurred. The rest of the "normal" photoelectron fluxes are colored in blue. For the right columns, the black diamond symbols show the median photoelectron fluxes and the error bars are quartile marks. The black solid lines are linear fits to the median fluxes. The fitted slopes and Y intersections are shown in the upper left corner. The ratios of the fitted slopes are also given. The correlations in blue and red are for the blue and red photoelectron fluxes and F10.7 cm values, respectively.

linear functions and the ratio of the fitted slopes is 2.276 for the 47 eV energy channel and 1.433 for the 115 eV channel at pitch angle 0°-10°. Generally, the slope ratio is around 1.5 for energies above 100 eV and $2-3$ for energies below 100 eV across all the pitch angles (not shown).

Assume that the neutral atmosphere in Figure 3.2 represents the normal case that produces the blue photoelectron fluxes in Figure 4.9, shown as the black lines in Figure 4.10a (only CO_2 and O density profiles are shown as examples). Now we test what artificial atmospheres can result in the red fluxes, i.e. significantly higher fluxes than the blue fluxes with the same F10.7 input. The first set of trials are to change the atmospheric densities by simply multiplying a factor (a factor of 5 for the green lines in Figure 4.10a), or only enhancing the neutral densities below a certain altitude (a factor of 10 below 200 km for the red lines in Figure 4.10a). The photoelectron fluxes resulting from these atmospheres are shown in Figure 4.10b-c. It is easy to see that, compared to the normal case (black lines), the resultant fluxes from these artificial atmospheres are lower than the normal case at pitch angle 0° but the same or higher at pitch angle 90°. In fact, various artificial atmospheres created through the aforementioned three methods that we have tested fail to enhance photoelectron fluxes at all the pitch angles.

Then, we investigate single-species-dominated atmospheres, which are given the total density of all species of the normal case, as shown in Figure 4.10d. Here we chose 115 eV as example because for MGS MAG/ER data, 115 eV energy channel is one of the most widely used energy channels (e.g. *Brain et al.*, 2007; *Lillis and Brain*, 2013). From Figures 4.10e and 4.10f, showing 115 eV the photoelectron fluxes at 0° and 90° pitch angles, only the CO_2 dominated atmosphere generates higher fluxes than the normal case. In contrast, the other single-species dominated atmospheres elicit the same or smaller photoelectron fluxes at all pitch angles. To examine all the energies, Figures 4.11a and 4.11b show the modeled omnidirectional photoelectron fluxes from

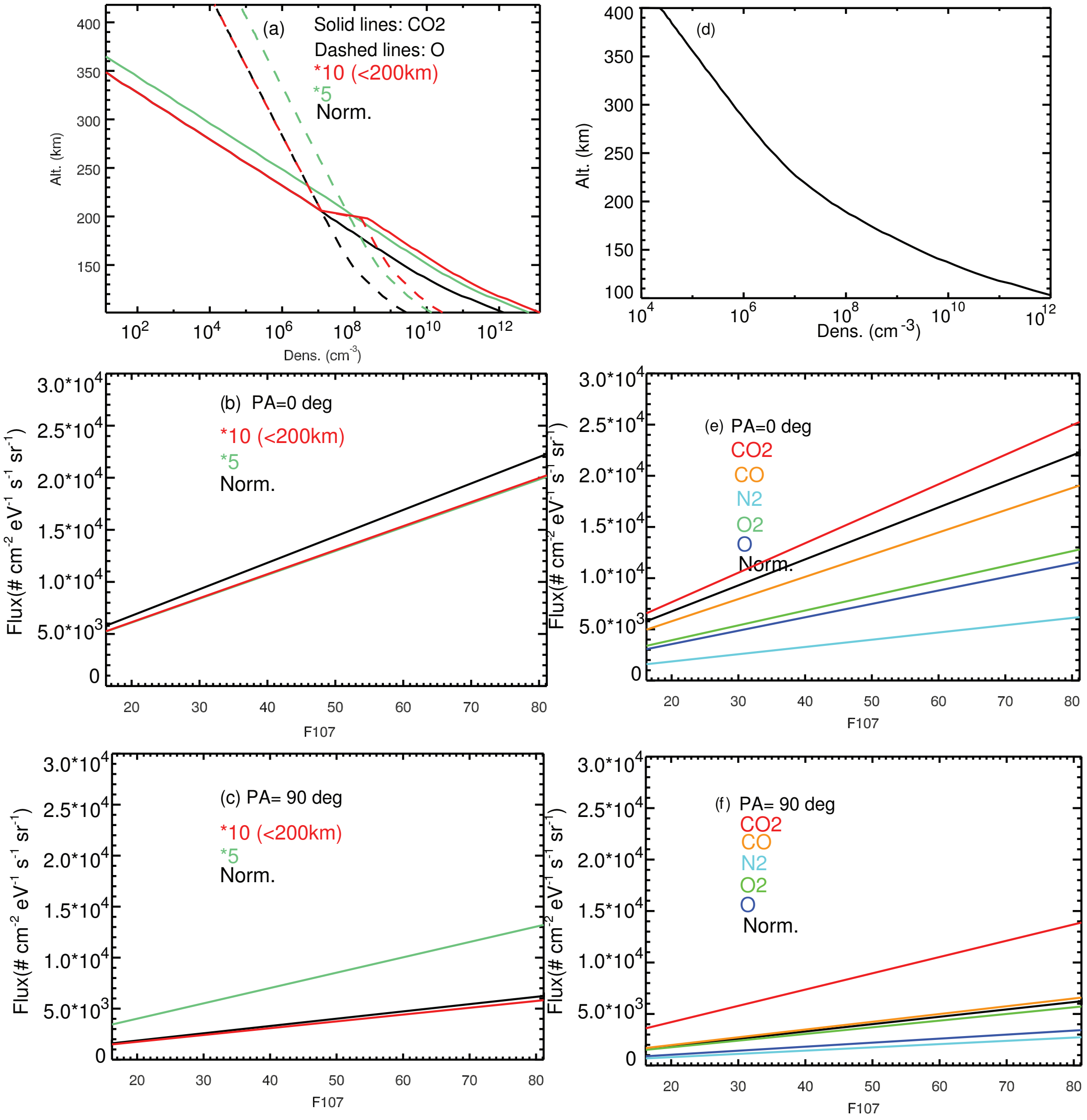

Figure 4.10: (a) Several artificial atmospheres, CO_2 (solid lines) and O (dashed lines) as examples. The resultant photoelectron differential number fluxes (# cm^{-2} eV^{-1} s^{-1} sr^{-1}) at 400 km against F10.7 cm values in sfu at pitch angles 0° (b) and 90° (c) for 115 eV. Different colors in (b-c) correspond to the density profile in (a) with the same color. (d) The density profile of each single-species-dominated atmosphere. The photoelectron differential number fluxes (# cm^{-2} eV^{-1} s^{-1} sr^{-1}) at 400 km resulting from single-species-dominated atmospheres, highlighted in different colors, as a function of F10.7 cm values at pitch angles 0° (e) and 90° (f) for 115 eV. The black lines in (e) and (f) are fluxes for the normal case, as a comparison.

each single-species-dominant atmosphere and the normalization of these fluxes by the normal case, with a Martian F10.7 of 86 sfu as input. As we can see, if O, CO, or N_2 dominates the density at all altitudes, the resultant omnidirectional photoelectron fluxes are about the same or lower than the normal case. On the other hand, for an O_2 dominated atmosphere, the photoelectron fluxes are enhanced by a factor around 2 below 70 eV but diminished at energies above. Only a CO_2 dominant atmosphere leads to higher photoelectron fluxes across all the energies and pitch angles.

Among all these tests, the resultant photoelectron fluxes at field-aligned pitch angles, so-called source cone pitch angles, are very insensitive to density changes but more controlled by the composition change, i.e. the proportion of each species' density out of the total density. According to *Banks and Nagy* (1970), for a single species atmosphere, the escaped photoelectron flux ψ_{escape} is expressed as:

$$\psi_{escape} = \frac{Q(E)\langle\cos\theta\rangle}{2\sigma_a}\left\{1 - R\left[1 - \frac{2\sigma_a}{Q(E)\langle\cos\theta\rangle}\psi^{-}(\infty)\right]\right\} \tag{4.1}$$

where Q(E) is the photoionization frequency and independent of density; $\langle\cos\theta\rangle$ is the averaged pitch angle distribution; σ_a is the inelastic cross section of collisions with neutrals; R is a factor that represents the portion of reflected electrons; and $\psi^{-}(\infty)$ is the downward photoelectron fluxes. Note that equation 4.1 is independent of the neutral atmospheric density, which cancels out between the numerator and the denominator terms. When $\psi_{escape}=\psi^{-}(\infty)$ is satisfied at a high altitude, such as the symmetric magnetic field with the same ionospheric source at each leg used in this study, Equation 4.1 is reduced to:

$$\psi_{escape} = \frac{Q(E)\langle\cos\theta\rangle}{2\sigma_a} \tag{4.2}$$

In Equation 4.2, ψ_{escape} is density independent and only controlled by species-related terms, including Q(E) and σ_a, where Q(E) is the product of the solar ir-

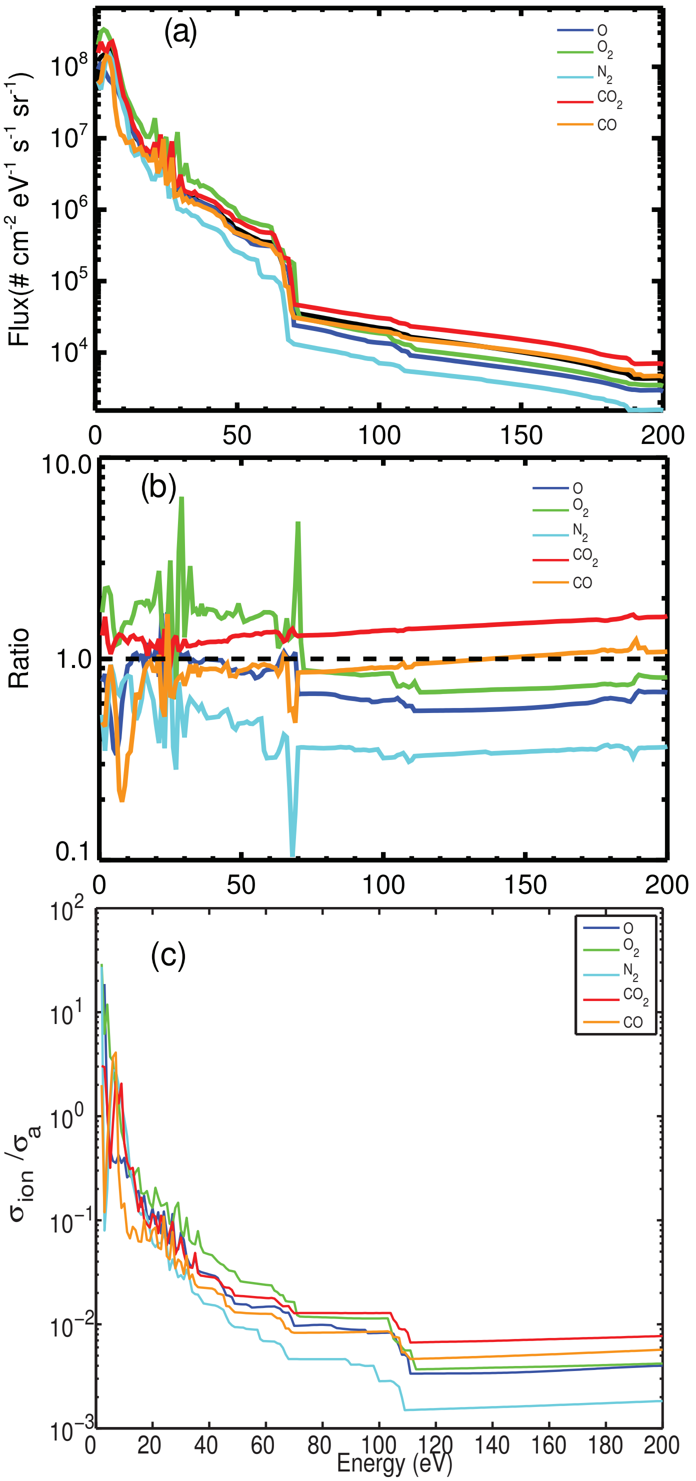

Figure 4.11: (a) The omnidirectional fluxes (# cm^{-2} eV^{-1} s^{-1} sr^{-1}) from single-species-dominated atmospheres, highlighted in different colors, against energy, with an Martian F10.7 of 86 sfu as input. The black line is for the normal case, as a comparison. (b) The omnidirectional fluxes normalized by the normal case. (c) The ratio of the photoionization cross section and the inelastic cross section for different species, highlighted in different colors.

radiance and the photoionization cross section. In other words, for a single species atmosphere, ψ_{escape} is proportional to the ratio of this species' photoionization cross section and inelastic cross section. This equation, however, is based on many assumptions, such as an isothermal atmosphere, ignoring the attenuation of the solar irradiance by the atmosphere at all altitudes. To verify it, we have plotted out the ratio of each species' photoionization cross section and inelastic collisional cross section, as shown in Figure 4.11c. Comparing Figure 4.11b and 4.11c, the normalized omnidirectional fluxes for the five single-species-dominated atmospheres are organized in the same order as the cross section ratio, which means our model results are consistent with the equations from *Banks and Nagy* (1970).

Therefore, the dust-altered atmosphere likely consists of higher proportions of species with a high photoionization and inelastic cross section ratio, compared to the normal atmosphere, which leads to the observed extremely high photoelectron fluxes. As this extreme photoelectron flux enhancement occurred to a wide range of energy and pitch angle, out of five species we have tested, CO_2 is the best candidate.

Nevertheless, Equation 4.2, which is derived from a two-stream model, does oversimplify the role that density plays in photoelectron fluxes. Taking the CO_2 dominated atmosphere as an example, we scaled the density (green line in Figure 4.12a) shown in Figure 4.10d by an extreme factor of 0.001 and of 1000, highlighted in blue and red in Figure 4.12a, respectively, with the normal case (black line) as a comparison. Note that in Figure 4.12b, the red, green and blue lines are all on top of each other and in Figure 4.12c, the blue line coincides with the x-axis. Despite the six orders of difference in CO_2 density, Figure 4.12b and 4.12c show that the resultant photoelectron fluxes are almost the same at pitch angle near 0° but significantly differ at more perpendicular pitch angles. On one hand, this experiment again demonstrates how insensitive to density the photoelectron fluxes at the source cone pitch angles are, like Equation 4.2 predicts. On the other hand, the higher

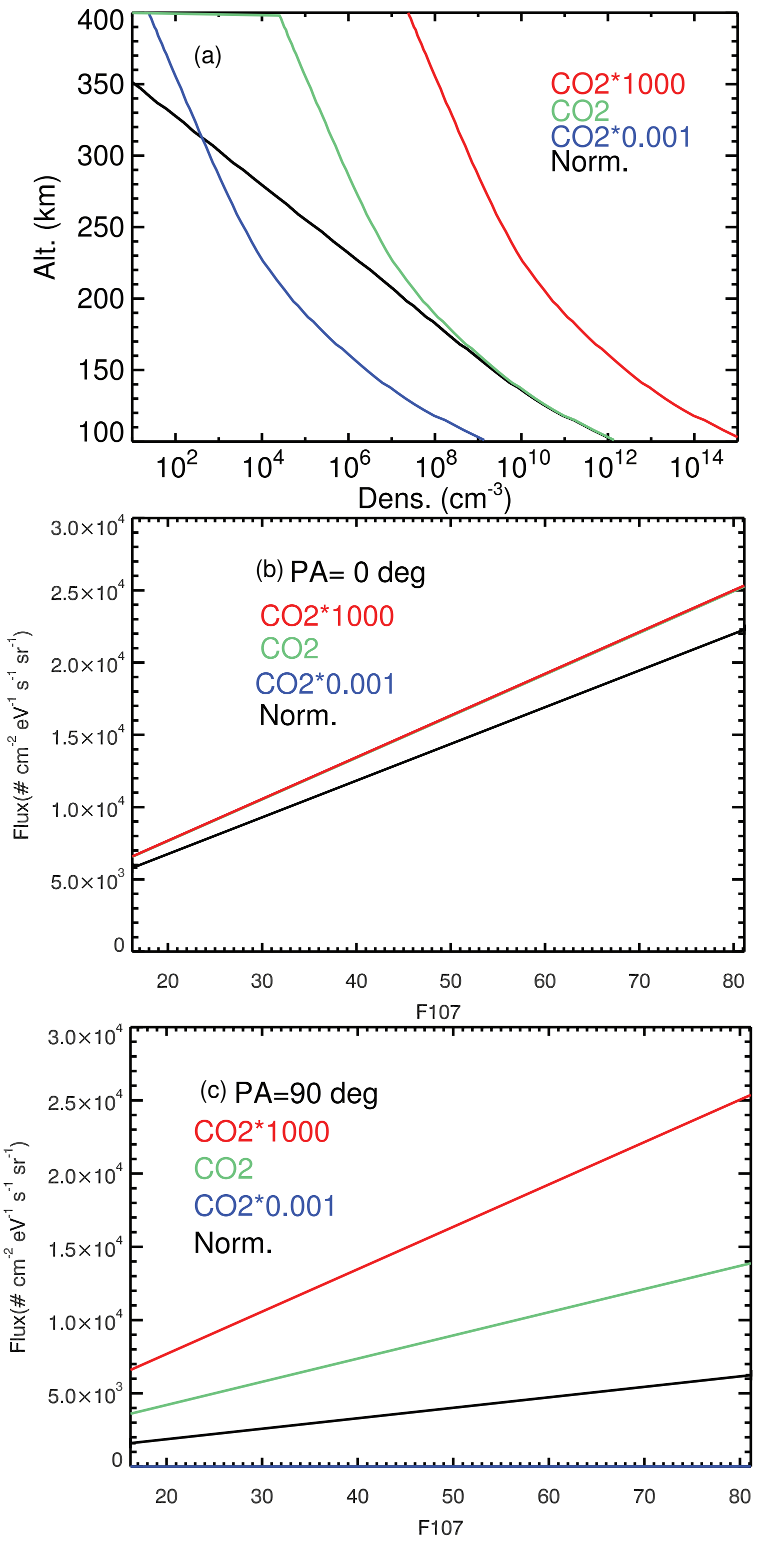

Figure 4.12: (a) Density profiles for the CO_2 dominated atmosphere, colored in red, green, and blue, and the black line is again for the normal case as a comparison. The resultant photoelectron differential number fluxes (# cm^{-2} eV^{-1} s^{-1} sr^{-1}) at 400 km against F10.7 cm values in sfu at pitch angles 0° (b) and 90° (c) for 115 eV. Different colors in (b-c) correspond to the density profile in (a) with the same color.

the density, the higher the photoelectron fluxes are at pitch angles near 90°. For a closed magnetic field with sources at lower altitudes of stronger magnetic strengths, to conserve the first adiabatic invariant, an electron' pitch angle becomes more field-aligned when it transports to higher altitudes as the magnetic strength decreases. As a result, photoelectrons have to be scattered into perpendicular pitch angles at high altitudes because they are not collisionlessly connected to the source region. When the CO_2 density increases, the high altitude sources become important, resulting in a wider source cone pitch angle range. With also increased collisions due to the density enhancement, photoelectrons are much easier to be scattered into perpendicular pitch angles. Thus, density is a determining factor of the photoelectron fluxes at perpendicular pitch angles.

4.2.2 Discussion of Simulation Efforts on High-Altitude Photoelectrons and Dust Storms

Studies have shown that the Martian global dust storm occurred in 2001 has a long-term influence on high-altitude photoelectron fluxes, most likely because the dust altered the neutral atmosphere in a significant way in terms of photoelectron production and loss (*Liemohn et al.*, 2012). This study provides a detailed investigation of the effects that thermospheric composition and density have on high-altitude photoelectron fluxes by using the STET model to determine candidate atmospheres that can replicate observations from the MGS MAG/ER instrument.

Various attempts to change all species as a whole fail to significantly increase the modeled photoelectron fluxes at all pitch angles. Instead, the single-species-dominant atmosphere leads to very different photoelectron fluxes at 400 km. This is because the fluxes at high altitudes, above the main source region of photoelectrons to be exact, at source pitch angles are very insensitive towards density but instead are determined by the neutral species' photoionization cross section and the inelastic cross section. It is actually quite understandable. A density enhancement means not only an increased source but also a higher loss due to collisions. For a single species atmosphere, the density in the source term is cancelled out by that in the loss term so that density does not matter in terms of photoelectron fluxes at source cone pitch angles. In the meanwhile, the source to loss ratio is determined by the ratio of the photoionization cross section and the inelastic cross section, characteristic quantities for each species. Therefore, for a multi-species atmosphere, to achieve the observed extra enhancement of photoelectron fluxes across a wide range of energy and pitch angle, the species with a larger ratio of the photoionization cross section and inelastic cross section, e.g. CO_2, needs to be preferentially increased as a proportion of the total density.

Through the examination of five species, the STET model results suggest that CO_2 is the only species here that can increase photoelectron fluxes at all energies. While O_2 is effective at increasing fluxes at lower energies, it is a very minor species of the Martian atmosphere, usually more than two orders of magnitude smaller than the dominant species below 400 km, and therefore unlikely contributes significantly to photoelectrons' productions and loses. Thus, CO_2 is the most reasonable candidate here. As dust absorbs the solar irradiance at low altitudes, the scale height increases due to the temperature increase. It can cause the altitude of the homopause to shift higher, therefore so does the altitude at which the dominant species changes from CO_2 to O. Thus far, CO_2 is known as the dominant species roughly below 200 km so it may seem confusing to ask for a CO_2 dominant atmosphere (*Nier and McElroy*, 1977). However, there exists a critical altitude range for photoelectrons (e.g. *Banks and Nagy*, 1970; *Butler and Stolarski*, 1978; *Mantas and Hanson*, 1979), only above which photoelectrons can transport to high altitudes, such as MGS mapping phase altitudes, and below which photoelectrons lose energy locally. The altitude range of this photoelectron exobase is from 160 km to 170 km for the baseline atmosphere used here. Thus, this study suggests that CO_2 is the dominant species above this altitude range, which is achievable. For example, the Mars-Global Ionosphere and Thermosphere Model (M-GITM) predicts that the crossing altitude from CO_2 dominating to O dominating the neutral density shifts from 190 km (for solar minimum, aphelion conditions) to ~250 km (for solar maximum, perihelion conditions) (*Bougher et al.*, 2015). With the extra heating to the atmosphere caused by the global dust storm, CO_2 can dominate a much larger altitude range than usual.

However, as Figure 4.10e and 4.10f suggests, the slope ratio of the photoelectron fluxes compared between the CO_2 dominant atmosphere and the normal case is always below 1.5 at field-aligned pitch angles, lower than the ratio (> 1.5) obtained from the observations. A possible explanation is that the baseline atmosphere used here might have a higher CO_2 concentration in the source altitudes of photoelectrons compared to the average Martian atmosphere. Martian neutral density measurements, especially composition measurements, are rather sparse. Because the high-altitude photoelectron fluxes are quite sensitive to composition changes, to more quantitatively match the observations requires a better quantification of the Martian upper atmosphere density profiles of the main species. The neutral composition measurements from the Neutral Gas and Ion Mass Spectrometer (NGIMS) instrument onboard Mars Atmosphere and Volatile EvolutioN (MAVEN) (*Jakosky et al.*, 2015) should provide profound insights to this issue. Despite the fact that the modeled photoelectron flux enhancement caused by a CO_2 dominant atmosphere is smaller compared to observations, this is the only solution among various tested artificial atmospheres that can qualitatively explain the observation. While there could be other explanations for the observations of enhanced photoelectrons during and after the very large dust storm of 2001, this study examined neutral atmosphere composition changes and found that only one possibility, enhanced CO_2, leads to increases high-altitude photoelectron fluxes at all energies and pitch angles.

Finally, even though total density makes little difference to photoelectron fluxes at source cone pitch angles, our model predicts that it significantly alters the high-altitude fluxes at perpendicular pitch angles. This finding also suggests the advantages of a multi-stream approach such as the STET model.

To briefly summarize, to simulate extremely high photoelectron fluxes observed by MGS during and after a global dust storm, instead of simply increasing the total density, the most effective way is to enlarge the proportion of species with higher photoionization cross section and inelastic cross section ratio. In this study, we provide one very likely candidate, CO_2. In other words, the global dust storm has likely led to CO_2 becoming the dominant species at a much larger altitude range than usual and for a much longer time than expected. We also do not exclude the possibility, however, of other mechanisms other than neutral atmosphere composition changes. On the other hand, as Equation 4.2 suggests, the high-altitude photoelectron fluxes depend on only a very few parameters and can be used to validate solar EUV models, such as the Flare Irradiance Spectral Model (FISM) (*Chamberlin et al.*, 2007, 2008) and the Heliospheric Environment Solar Spectral Radiation (HESSR) model (*Fontenla et al.*, 2009, 2014). In addition, it raises the point to monitor thermospheric composition changes through high-altitude photoelectron observations, which could be very useful, considering very limited planetary neutral density/composition measurements. Also, these findings and implications can be carefully applied or adapted to planets with significant vertical superthermal electron transport along magnetic fields, such as Earth, Saturn, and Jupiter.

CHAPTER V

Photoelectrons and Solar Zenith Angle

Electron transport can be significant when magnetic fields are present, such as over the Martian strong crustal field regions. Then, the high-altitude electron flux should be the integral of photoelectrons produced from all altitudes below. Because electron fluxes decrease exponentially with altitude, the photoelectron fluxes measured at high altitudes are supposed to be dominated by the production region at lower altitudes, where it is Chapman-like and has a strong solar zenith angle (SZA) dependence. At Mars, photoelectron fluxes over the crustal field regions were presumed to be SZA dependent. In this chapter, we examine the relationship of high-altitude photoelectron fluxes and solar zenith angle by analyzing the measured photoelectron fluxes from the magnetometer/electron reflectometer (MAG/ER) instrument on board Mars Global Surveyor, accompanied with further exploration with a superthermal electron transport model (STET).

5.1 SZA's Influence on Observed High-Altitude Photoelectron Fluxes

The relation between the observed high-altitude photoelectron fluxes and SZA is investigated through two methods. The first one is to compare the correlation of the photoelectron fluxes and the EUV proxy with or without SZA factored in. The other is to examine, for a particular solar irradiance level, indicated by F10.7 cm values, how the photoelectron fluxes change with SZA.

5.1.1 Correlation of Photoelectron Fluxes and EUV proxy

Trantham et al. (2011) investigated the main controlling factors of 27 eV photoelectron fluxes within pitch angles (PA) 80°-90° observed by MGS and concluded that their local EUV proxy is the best organizer of photoelectron fluxes. This local EUV proxy is the ratio of the solar irradiance proxy, denoted as 'I_0', and a Chapman function (*Smith and Smith*, 1972) to take into account SZA's effect, i.e. the attenuation of the solar irradiance because of a limb path. The solar irradiance at Mars is calculated according to the method described in *Mitchell et al.* (2001). The Chapman function, Ch(Rg, SZA), is a function of SZA and Rg=R/H, where R is the distance from the center of Mars and H is the scale height. This function resembles 1/cos(SZA) except for very high SZAs. The local EUV proxy is therefore $I = I_0/\mathrm{Ch}(\mathrm{Rg, SZA})$, which is the resultant solar irradiance spectrum from F10.7 cm solar flux measurements at Earth compiled by NOAA being scaled to Mars according to the planet-to-Sun distances as well as the Earth-Sun-Mars angle.

Notice that the photoelectron flux is proportional to I, in contrast to the thermal electron density predicted by Chapman theory correlated to $\sqrt{I}$. The square root operator originates from the assumption that for thermal plasma, the production rate balances with the recombination rate (main loss). Such equilibrium does not apply to superthermal electrons as the recombination loss is trivial compared to other losses such as collisions with neutral particles.

Figure 5.1 shows an example of photoelectron fluxes of the 115 eV energy channel (a widely used energy channel (e.g. *Brain et al.*, 2007; *Lillis and Brain*, 2013)) at PA 20°-30° as a function of time in Earth year (5.1a), the EUV local proxy I (5.1b), and F10.7 values (in sfu, I_0) only (5.1c). The photoelectron fluxes highlighted in yellow

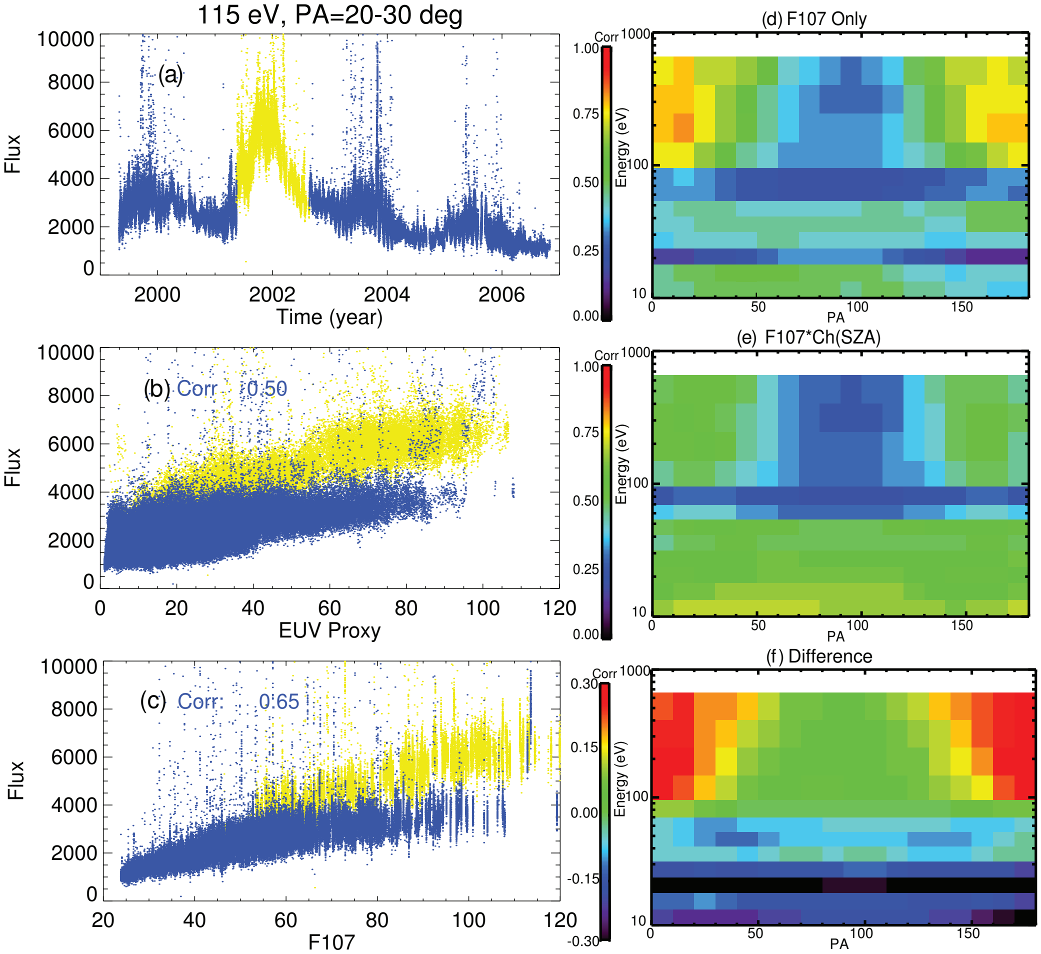

Figure 5.1: (a) The photoelectron fluxes (# cm^{-2} eV^{-1} s^{-1} sr^{-1}) of the energy channel 115 eV at pitch angle (PA) 20°-30° observed by MGS MAG/ER against time in Earth year. (b) The same photoelectron fluxes (# cm^{-2} eV^{-1} s^{-1} sr^{-1}) in (a) against EUV proxy, i.e. F10.7 ×Ch(Rg, SZA). (b) The same photoelectron fluxes (# cm^{-2} eV^{-1} s^{-1} sr^{-1}) in (a) against F10.7 only. In (b) and (c), the correlation of the blue fluxes and the EUV proxy and F10.7, respectively, is shown in the upper left corner. (d) The correlation of blue photoelectron fluxes and F10.7 only, as a function of PA and energy. (e) The Pearson correlation coefficient of blue photoelectron fluxes and the EUV proxy. (f) The difference of the correlation coefficient of (d) and (e) (d minus e).

are for a time period that a global dust storm occurred and are much higher than the rest of the fluxes, colored in blue, even with the same EUV proxy or F10.7 values, as shown in 5.1b and 5.1c. The specialness of these yellow fluxes has been investigated by *Liemohn et al.* (2012). Hence, here focuses only on the blue photoelectron fluxes. The correlations of these blue fluxes against the local EUV proxy and F10.7 values only are 0.5 and 0.65, as shown in Figure 5.1b and 5.1c, respectively. Such a 0.15 enhancement of correlation is statistically significant because the correlation is calculated from hundreds of thousands of data points. Therefore, the photoelectron flux correlates better with the solar irradiance without SZA factored in.

To examine the correlations for various energies and pitch angles, Figure 5.1d and 5.1e show the correlation of the blue photoelectron fluxes and the Mars-adjusted F10.7 values only and the local EUV proxy, respectively, as a function of energy and PA. Figure 5.1f shows the difference of Figure 5.1d and 5.1e. A general improvement of correlation, for more field-aligned pitch angles in particular, is seen for energy above 70 eV, up to 0.30, with SZA excluded. For energy below 70 eV, the exclusion of SZA leads to lower correlation. In other words, high-energy photoelectron fluxes observed by MGS tend to be not affected by SZA while SZA seems to partially control the low-energy fluxes.

5.1.2 Observed Photoelectron Fluxes against SZA

The other method is to directly examine how the photoelectron fluxes change with SZA. In Figure 5.2, an orbit on Oct. 16th, 2000 is chosen as an example. From top to bottom, each panel shows north latitude, east longitude, magnetic field strength, magnetic elevation angle (relative to the horizontal plane), SZA, and photoelectron fluxes at pitch angle $20^\circ - 30^\circ$ for four energy channels, 313 eV, 115 eV, 47 eV, and 20 eV, against time. As we can see, instead of decreasing dramatically as predicted by the Chapman function, the flux is rather constant for SZA $90^\circ - 60^\circ$. Quantitatively, the root mean square errors (RMSEs) to the mean electron flux and also to the best-fitted Chapman function are calculated and shown at the upper left and lower right corners, respectively. The RMSEs to the mean value are 2-3 times smaller than that to the Chapman function for all the energy channels. This implies that a straight-line fit is substantially better than the SZA-dependent Chapman function fit to these data. Then, in addition to this case study, we present another statistical examination of the relation between the photoelectron flux and SZA.

The blue fluxes in Figure 5.1a are divided into eight Mars-adjusted F10.7 levels and eight SZA bins. Then for the same F10.7 level, the median flux of each SZA bin is normalized by the maximum of these median fluxes. Normalized median photoelectron fluxes at pitch angles 20°-30° against SZA are shown in Figure 5.3. with different colors highlighting different F10.7 levels. The four rows, from top to bottom, are for energy channels 313 eV, 115 eV, 47 eV, and 20 eV, respectively. The left column shows the normalized median flux for each F10.7 level. For the right column, three F10.7 levels are selected, highlighted in different colors and line styles, and for each color, the three lines mark the quartile values for the normalized flux. The photoelectron fluxes vary within 80% from the maxima for energies above 30 eV for all the pitch angles, as shown in Figure 5.3a-5.3c. Only the energy channel below 30 eV is a more systematic flux decrease at high SZAs seen, e.g. in Figure 5.3d. Similarly, the calculated RMSEs to the mean flux are much smaller, by a factor of 2 to more than 10, than that to the fitted Chapman function, except for the 20 eV energy channel with F10.7 = 43 sfu.

Again, an independence of the photoelectron fluxes on SZA is seen for energy above 30 eV. In contrast, the photoelectron flux does decrease significantly with increasing SZA below 30 eV. This finding is consistent with the other method, even though the energy cutoff differs.

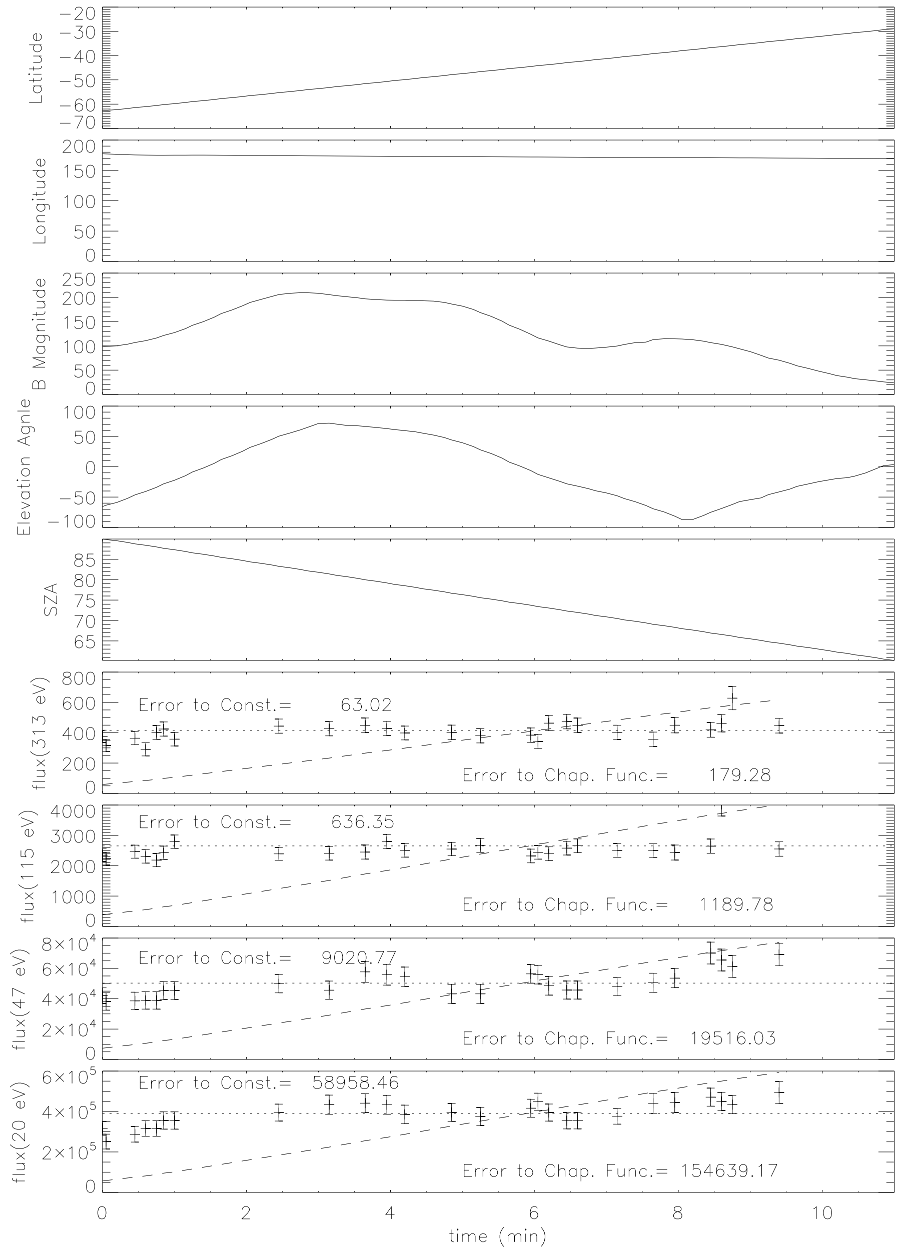

Figure 5.2: One orbit example: MGS data for Oct. 16th, 2000, the x-axis is the time in minute, starting from UT 17:27:50. From top to the bottom, shown are, MGS location over Mars in latitude (degree); MGS location over Mars in east longitude (degree); the magnitude of the magnetic fields (nT); the elevation angle of the magnetic fields (degree); MGS solar zenith angle (degree); differential number flux (# eV^{-1} cm^{-2} s^{-1} sr^{-1}) for 313 eV, 115 eV, 47 eV, and 20 eV four energy channels at PA $20° - 30°$, respectively. The dotted lines in the last four panels mark the mean flux and the dashed lines are for the best-fitted Chapman function. The standard errors to the mean photoelectron flux and the best-fitted Chapman function are shown at the upper left and lower right corners, respectively.

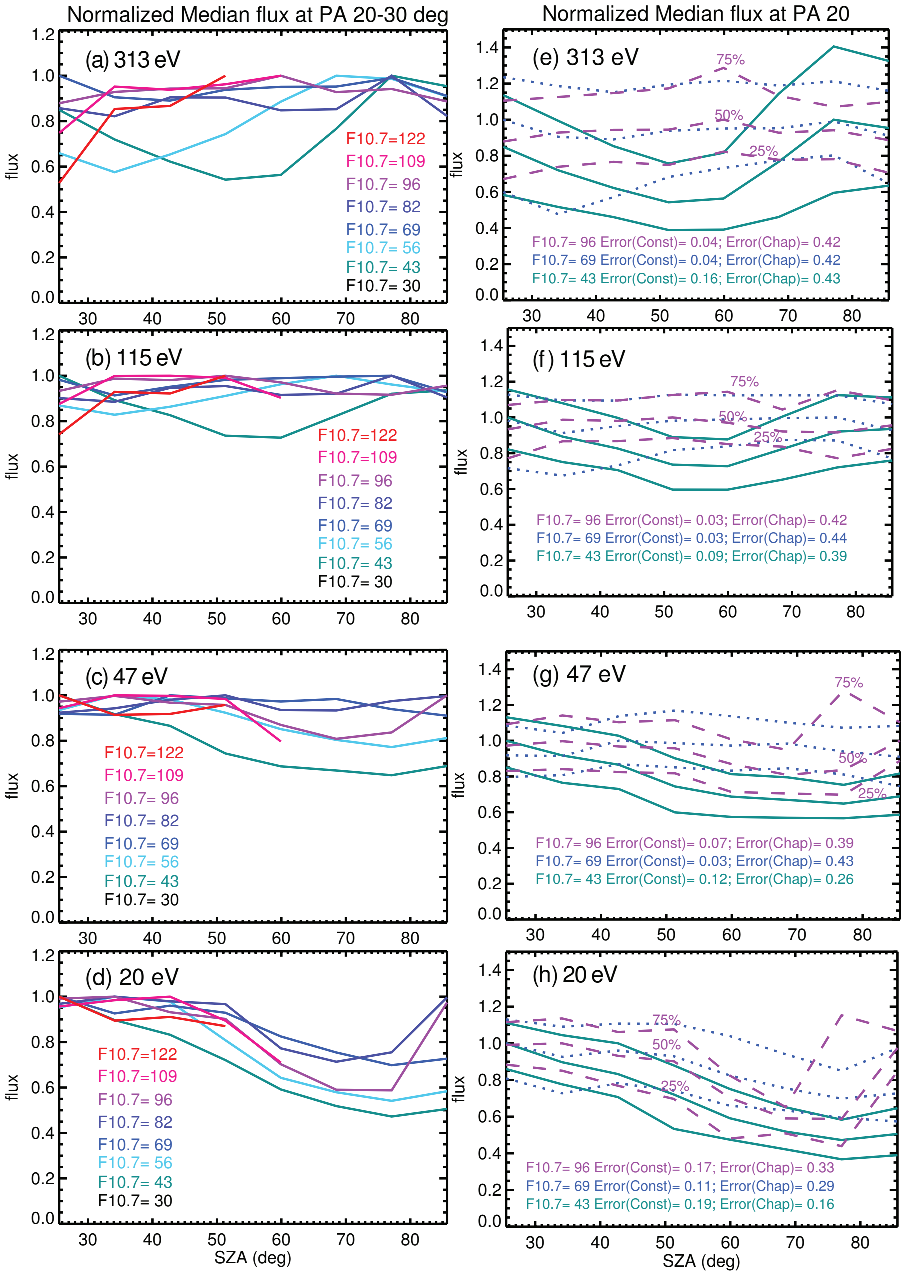

Figure 5.3: Normalized median photoelectron flux at pitch angles 20°-30° against SZA with colors showing different F10.7 levels. For each F10.7 level, the median fluxes are normalized by the maximum of all the SZA bins. The four rows, from top to bottom, are for energy channels 313 eV, 115 eV, 47 eV, and 20 eV, respectively. The left column shows the normalized median flux for each F10.7 level. For the right column, three F10.7 levels are selected, highlighted in different colors and line styles, and for each color, three lines mark the quartile values for normalized flux.

5.2 Simulations

Solar zenith angle affects the photoelectron fluxes in two ways. One is that the attenuation of the solar irradiance is larger with increasing SZA due to the slant path. The other is that the atmospheric densities and temperatures change with SZA. Hence, in this section, we will first use the same atmosphere (the atmosphere at SZA=0°, as shown in Figure 5.4) to simulate at ten SZAs, from 0° to 90°. Then, we will run STET with two extra atmospheres, at SZA=60° and at SZA=75°, as shown in Figure 5.4, to discuss how different atmospheres influence the results.

5.2.1 Superthermal Electron Exobase

The MGS observations are at 400 km and well above the main region of ionosphere. Various model efforts for different planets (e.g. *Banks and Nagy*, 1970; *Butler and Stolarski*, 1978; *Mantas and Hanson*, 1979) pointed out that there exists a critical altitude range for photoelectrons, only above which photoelectrons can transport/escape instead of losing energy locally. The measurements over the strong crustal fields from the MAG/ER instrument should be mainly the escaped population. To understand the relationship between these high-altitude electron samples and SZA, it is necessary to determine this altitude range.

Banks and Nagy (1970) define the photoelectron mean free path λ as:

$$\lambda = \frac{\langle \cos\theta \rangle \sin I}{n\sqrt{\sigma_a(\sigma_a + 2p_e\sigma_e)}}; \tag{5.1}$$

where $\langle \cos\theta \rangle$ is the averaged pitch angle distribution; I is the dip angle of the magnetic field line, relative to the horizontal plane; n is the neutral density; σ_a and σ_e are the inelastic and elastic collision cross sections with neutrals, respectively; p_e is the backscatter probability for the elastic collisions. When $\lambda \ll H$, where H is the scale height, there is no net transport and photoelectrons lose energy locally; while above

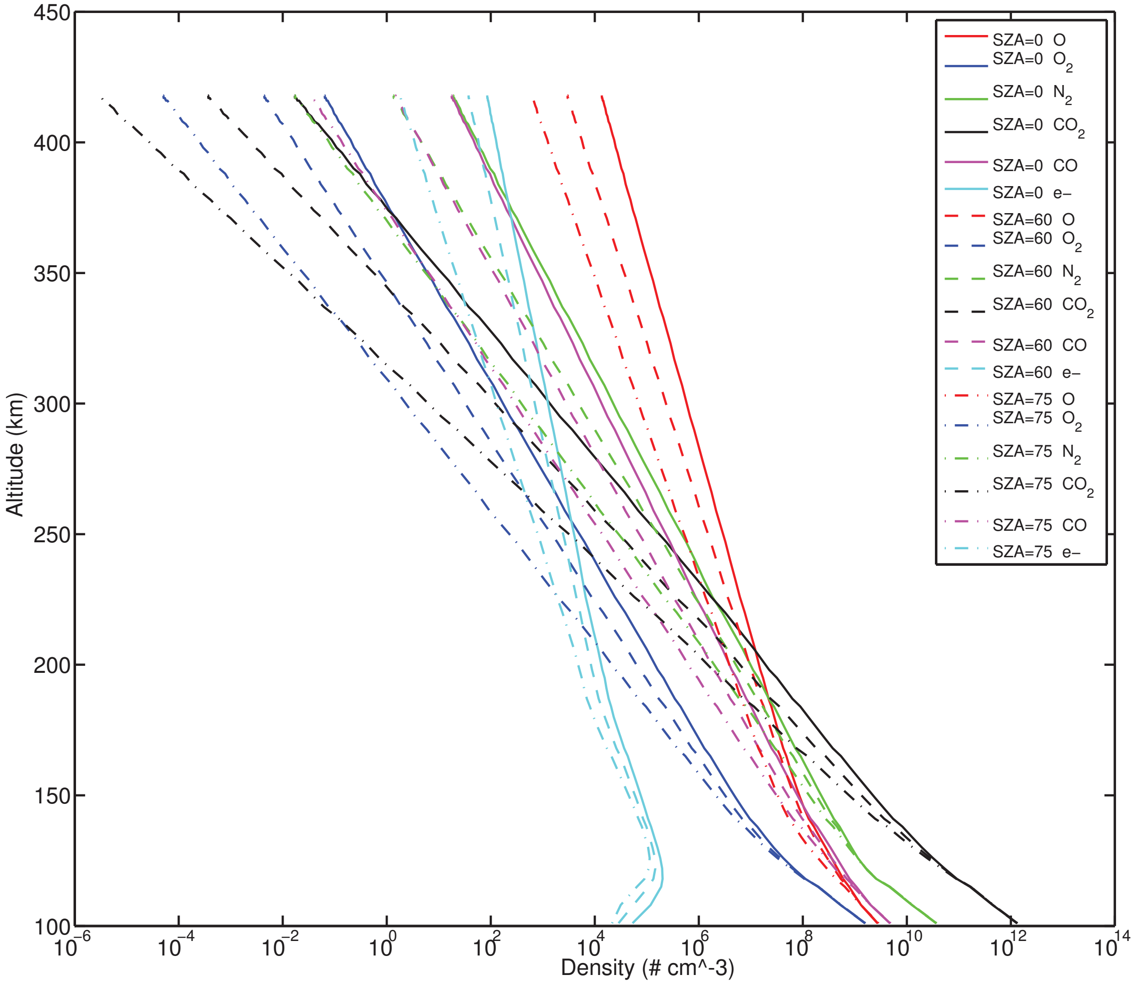

Figure 5.4: Neutral densities and thermal electron density of Mars from MTGCM against altitude at three SZAs: 0°, 60°, and 75°. Different colors are for different species' density profiles, red for O, blue for O_2, green for N_2, black for CO_2, purple for CO, and light blue for electron, while different line styles for different SZAs, solid for 0°, dashed for 60°, and dashed-dot-dot for 75°, respectively.

the altitude where $\lambda \simeq H$, the photoelectron transport becomes significant. Here, we generalize this formula to the multi-species case by changing the denominator in equation 5.1 to $\sum\limits_i n_i\sqrt{\sigma_{ai}(\sigma_{ai}+2p_{ei}\sigma_{ei})}$, where i indicates i_{th} neutral specie. For our calculation, I is near 90° below 200 km, and $\langle\cos\theta\rangle = 0.5$, as it ranges from 3/8 and 9/16 (*Banks and Nagy*, 1970). The photoelectron mean free path λ against altitude, along with the neutral scale height H (black dashed line), is shown in Figure 5.5a. The altitudes at which $\lambda = H$ for different energies range from 160 to 165 km for the MTGCM atmosphere at SZA=0° and from 150 to 155 km for the MTGCM atmosphere at SZA=75°. For convenience, we define the "photoelectron exobase" as the altitude of $\lambda = H$. However, it is important to note that it is not immediately collisionless above this exobase. Instead, there is a transition region where transport dominates but collisions still happen. The photoelectron exobase is at lower altitudes than the exobase of the neutral atmosphere, which is located above 200 km, because these high-energy electron' collision cross sections are much smaller than those for neutral-neutral particles.

Another approach to determine this photoelectron exobase is to calculate an "optical depth" τ for a superthermal electron moving downward from the top of the upper atmosphere:

$$\tau = \int\limits_{z(s)}^{z_{max}} \sum_j n_j p_j \sigma_j \,\mathrm{d}s \tag{5.2}$$

where σ_j can be the cross section of inelastic and elastic collisions with the j_{th} neutral species, as well as the Coulomb collision cross sections with electrons; n_j is the corresponding density; p_j is the backscatter probability for the elastic collision with neutrals and 1 for other collisions. Also, in equation 5.2, s is the distance along the field line. The electron-ion collision term is neglected as the effect is small compared to electron-neutral and electron-electron collisions. Note that τ is a unitless integral

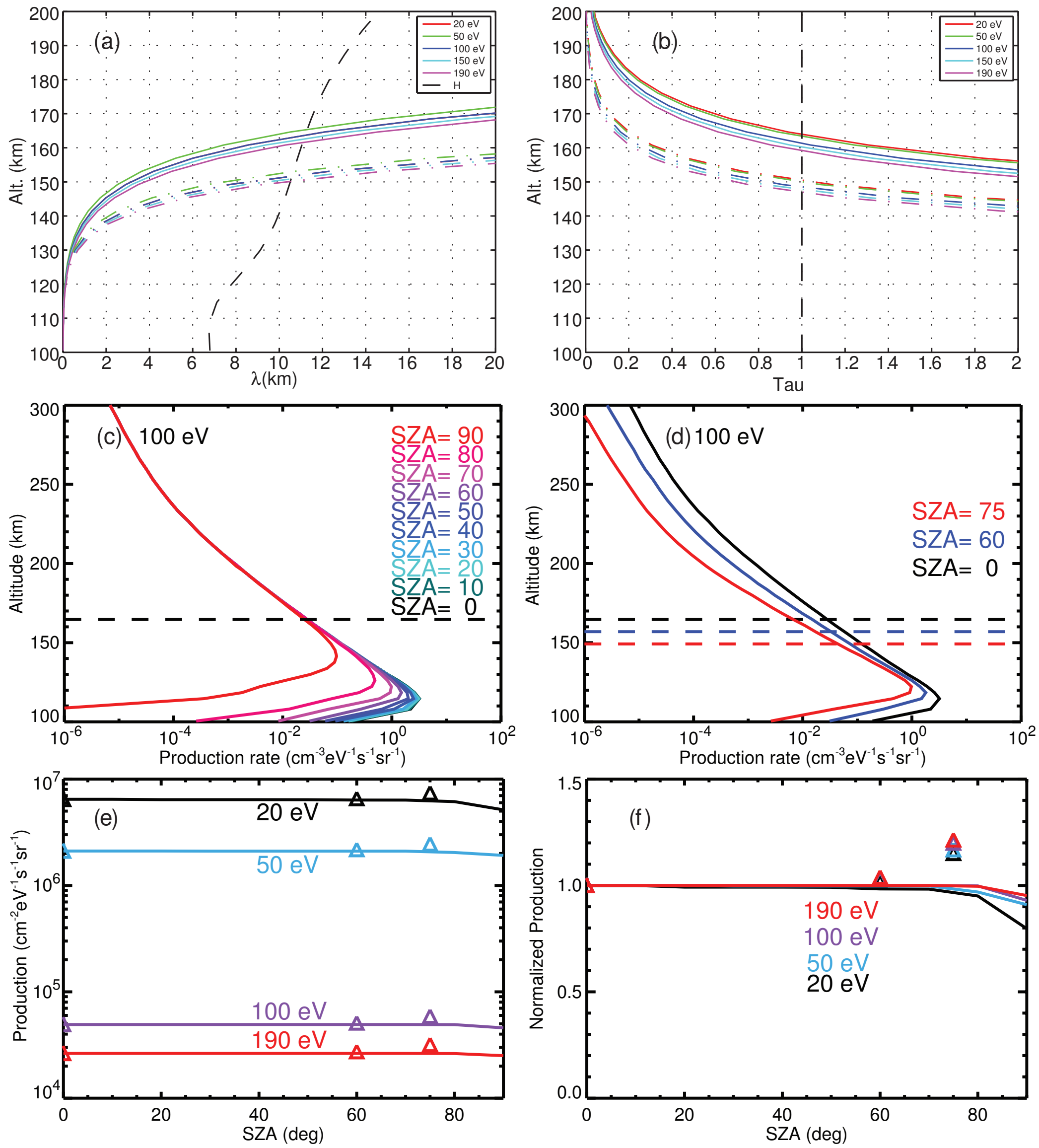

Figure 5.5: λ (a) and τ (b) against altitude. Different colors are for different energies. The solid lines are for the MTGCM atmosphere at SZA $= 0°$ and the dot-dashed lines for SZA=75°. The dashed black line in (a) is the scale height (H) against altitude. The dashed black line in (b) marks $\tau = 1$. (c) shows the photoelectron production rate (# cm^{-2} eV^{-1} s^{-1} sr^{-1}) from the same atmosphere, against altitude for 100 eV. Different colors highlight different SZAs. The horizontal dashed line marks the exobase. (d) shows the photoelectron production rate (# cm^{-3} eV^{-1} s^{-1} sr^{-1}) from the three MTGCM atmospheres (SZA=0°, 60°, 75°), against altitude for 100 eV. The dashed lines show the exobases for three atmospheres. (e) Integrated production rate (# cm^{-3} eV^{-1} s^{-1} sr^{-1}) above the exobase against SZA for different energies. The solid lines are for the ten runs with the same atmosphere and the symbols are for the three atmospheres. (f) Integrated production rate normalized by the production rate at SZA=0° against SZA for different energies, the same format as (e).

from the highest altitude z_{max} of the field line to a certain altitude $z(s)$ and stands for the probability of one photoelectron at $z(s)$ not able to transport from the top of field line to $z(s)$, or vice verse, from $z(s)$ to the top of the field line. In other words, only when $\tau \leq 1$, photoelectrons can be transported to high altitudes, otherwise they are lost locally or to nearby altitudes. Figure 5.5b shows τ of different energies against altitude. $\tau = 1$ happens at the 160-165 km altitude range for the MTGCM atmosphere at SZA=0° and at the 147-152 km range for the MTGCM atmosphere at SZA=75°, which is consistent with the previous method. Similarly, *Lillis et al.* (2008) determined that the scattering probability for 191 eV precipitating electrons at PA $< 24°$ reaches 1 at ~ 160 km, which also supports our finding.

The STET model was first run at ten SZAs, from 0° to 90°, with the same field line and the MTGCM atmosphere at SZA=0°. The calculated photoionization production rate against altitude at different SZAs for 100 eV is shown in Figure 5.5c. The peak production rate decreases and the peak altitude increases as SZA increases, as the Chapman theory predicted. However, above the photoelectron exobase, marked by the dashed black line, the production rates are about the same for all the SZAs. Then, we run the STET model at SZA=60° and 75 ° with the corresponding atmospheres from MTGCM. The photoionization rates against altitude for the three SZAs are shown in Figure 5.5d and the dashed lines are the calculated exobases. While the production rate decreases with increasing SZA, as expected, the exobase moves to lower altitudes, because the atmosphere is less dense.

To further demonstrate the effect of this photoelectron exobase, we integrated the photoionization production rate from the local exobase to the highest altitude z_{max} of the field line for each SZA, as shown in Figure 5.5e. The solid lines are for ten runs with the same atmosphere while the triangle symbols are for STET runs at different SZAs with the corresponding atmospheres. In addition, Figure 5.5f shows the normalization of this photoionization production rate integral against SZA, by the values at SZA=0°. For the ten runs with the same atmosphere, an almost constant photoionization production rate integral, with a slight decrease at high SZAs, is seen, while for the runs with different atmospheres, the production rate integral increases slightly at higher SZAs, as the exobase altitude decreases. In other words, in both sets of the simulations, with or without changing atmospheres, the photoionization production rate integral is fairly constant across all the SZAs.

5.2.2 Modeled Photoelectron Fluxes against SZA

As a result of the nearly constant production rate integral above the exobase for all the SZAs, Figures 5.6a-5.6d show the photoelectron fluxes at PA=0° at different altitudes against SZA for 20 eV, 50 eV, 100 eV, and 190 eV, respectively. Again, the solid lines are for ten runs with the same atmosphere and the triangle symbols for STET runs at different SZAs with the corresponding atmospheres.

For the runs with the same atmosphere, the photoelectron fluxes decrease as SZA increases at 130 km. For comparison, the dotted lines show the fluxes at 130 km divided by the Chapman function, Ch(Rg, SZA). The disagreement between the modeled fluxes at SZA=90° at 130 km (black solid line) and the Chapman function scaling is because this scaling is for peak densities but a particular altitude. For altitudes above 150 km, the photoelectron fluxes are almost constant across all SZAs, with a slight decrease at SZA=90°, resembling the production rate integral in Figure 5.5e and 5.5f. For the runs with different atmospheres, the fluxes are mostly constant with respect to SZA for all the altitudes, as the exobase altitude moves lower for higher SZA.

Therefore, the modeled photoelectron fluxes also show independence on the solar zenith angle due to the quite constant production rate integral above the exobase for all the SZAs. This model finding is consistent with the observations from section 5.1.

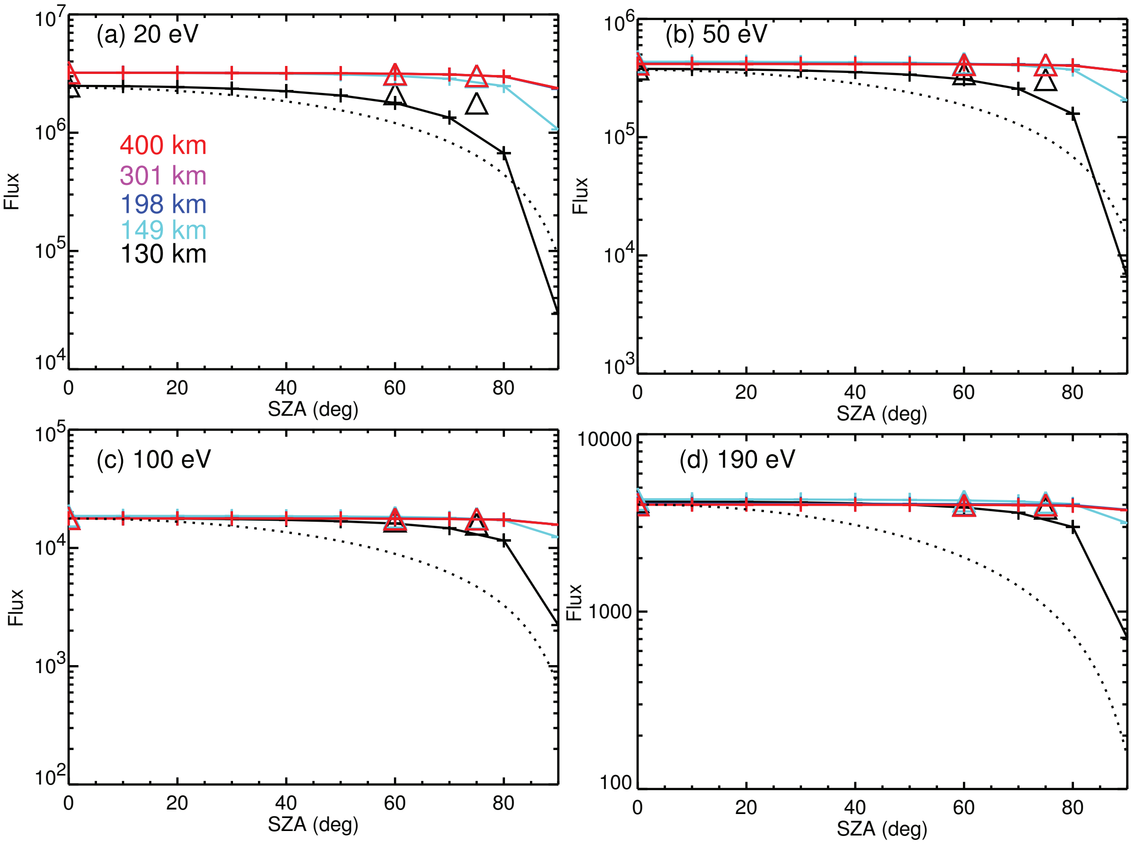

Figure 5.6: (a-d) The flux (# cm^{-2} eV^{-1} s^{-1} sr^{-1}) at PA 0 against SZA at different altitudes, highlighted in different colors, for 20 eV (a), 50 eV (b), 100 eV (c), and 190 eV (d), with the dotted line showing fluxes scaled by the Chapman function.

5.3 Discussion of High-Altitude Photoelectrons and SZA

Photoelectron fluxes over the strong crustal field regions at Mars were assumed to change with solar zenith angle because they are directly connected to the source region below 200 km altitude. If part of the photoelectrons produced at the peak altitude transport to high altitudes along closed magnetic fields, then the photoelectron fluxes should scale, though maybe not linearly, with the peak values. However, through our examination of the MGS MAG/ER data over the strong crustal fields, the high-altitude photoelectron fluxes are better organized solely by the solar irradiance, without SZA factored in, especially for the high energies. Furthermore, in addition to a case study as an example, the observed median photoelectron fluxes at different SZAs also change mostly within 80% of the maxima for the same Mars-adjusted F10.7 cm level. Plus, through the calculation of root mean square errors, the observed photoelectron flux is better described by a constant value against SZA rather than a Chapman function best-fitted curve, indicating an independence.

The STET model is able to replicate the independence of high-altitude photoelectron fluxes on SZA. Below the photoelectron exobase, while the peak fluxes vary roughly as the inverse of Ch(Rg, SZA), these photoelectrons are lost locally due to collisions. Only above this exobase, locally and freshly produced photoelectrons are able to transport to high altitudes. It was found that the photoelectron exobase is located between 145 and 165 km altitude, which is below the neutral atmosphere exobase because of the smaller collision cross section of these fast-moving particles. In addition, this value is in reasonable agreement with *Mantas and Hanson* (1979), who found that photoelectron transport starts to be significant in the 130-150 km altitude range. The analysis of the photoionization production rate from the simulation indicates that, above the photoelectron exobase, the production rate integral barely changes with SZA. As a result, high-altitude photoelectron fluxes are rather independent of the changing of the peak values when the peak altitude is several scale heights below the photoelectron exobase.

This result does not change when different atmospheres are used. In this study, we have tested three different atmospheres, taking into account the location difference. While the production rate changes with different atmospheres (Figure 5.5d), the production rate integral above the exobase, however, remains the same as the exobase varies in altitude for different atmospheres (Figure 5.5e and 5.5f). On the other hand, the observations are a collection of 7 years of data, spanning all the seasons and different solar irradiance strengths. The statistical approach of section 5.1.1 and 5.1.2 should average over the variations of the seasons and solar cycle changes. Also, the median fluxes are independent of SZA for all the observed F10.7 cm levels, which implies that this finding is applicable to different solar irradiance fluxes and that the atmospheres we used are appropriate and adequate.

Furthermore, take a closer examination of the observational results of high-energy photoelectrons in Figure 5.1f. The enhanced correlation is more prominent for more field-aligned pitch angles than perpendicular pitch angles. For pitch angles near 90°, the photoelectron fluxes observed at 400 km are mostly scattered into these pitch angles, as electrons' perpendicular velocities decrease with weakening magnetic strength, to conserve the first adiabatic invariant. In other words, these fluxes rely on not only the source but also the scattering processes at high altitudes, such as collisions with neutral particles or thermal electrons. This comparison of field-aligned and perpendicular pitch angles indicates a source change, consistent with our explanation. Also, the higher the energy, the more pitch angle bins show an increase in the correlation coefficient. The collision cross sections are lower with increasing energy and therefore photoelectron fluxes are less affected by collision processes but more controlled by the source changes.

The modeled low-energy photoelectron fluxes remain quite constant through all the SZAs, with a slight drop of fluxes at SZA$\sim 90^\circ$, at high altitudes. In contrast, the photoelectron fluxes observed by the MGS spacecraft show some dependence on SZA for low energies, even though the energy cutoff is different for the two approaches in section 5.1. From our model results, the peak altitudes are generally closer to the exobase for low energies than high energies (not shown). It is also suggested in Figure 5.5f, where the normalized production rate decreases more at high SZA for lower energies. It is possible that, in reality, the photoelectron exobase is systematically closer to the peak altitudes than what our model predicts. In such a case, the low-energy photoelectrons will be partially controlled by SZA. Another possibility of the discrepancy between the observation and the model results is that the sources and losses for low-energy photoelectrons are more complicated than the high energies. Cascading and secondary electrons are also important sources while the loss due to Coulomb collisions is more prominent at the low energy range. Therefore, the low-energy photoelectron fluxes depend on more parameters, such as the thermal electron density profile, so that it is harder to replicate by the simple model setup. Finally, the quality of the electron data for low energy channels from the MGS spacecraft might be not very good so that the findings of the low energy channels are questionable.

CHAPTER VI

Solar Wind Electron Precipitation

In this chapter, we take a statistical approach to identify solar-wind/magnetosheath electrons and ionospheric photoelectrons and determine the occurrence rate of dayside solar-wind/magnetosheath electron precipitation over strong crustal fields at Mars. In addition, we investigate the dependence of the occurrence rate on the magnetic elevation angle, as more vertical magnetic field lines have a higher chance to be open at MGS altitudes. The occurrence rate also depends on the solar zenith angle (SZA), as the normal solar wind dynamic pressure decreases from sub-solar point to terminator. Furthermore, although solar photon absorption is certainly the largest source of energy input to the Martian upper atmosphere, quantification of how superthermal electrons' energy input compares to solar input has not been done. This new approach also allows us to quantify the energy flux deposition of solar-wind/magnetosheath electrons into the dayside Martian upper atmosphere and compare it with solar flux input.

6.1 Occurrence Rate

6.1.1 Precipitating Solar Wind Electron Occurrence Rate Calculation

In order to obtain the ratio of the two populations and the cutoff to separate them, the bimodal distribution is treated as the addition of two Gaussian distributions. Even though some distributions of the left population, i.e. solar wind electrons, are not quite Gaussian-like, this Gaussian approximation is convenient and still reasonable. A new function that consists of two Gaussian functions is fitted to the bimodal distribution, with three to-be-fitted variables (the amplitude, the position of the peak, and the standard deviation) to each function, as shown in Figure 6.1. The basic idea of this fitting is to compute a non-linear least squares fit to this new function. The three columns of Figure 6.1 show the histogram plots of the flux ratios between the energy bins centered at 27 eV and 115 eV, 36 eV and 115 eV, 47 eV and 115 eV, respectively. Three energy pairs are examined here to show if their results are similar, therefore if this method delivers reliable performance. The four rows are for four pitch angles: $40° - 50°$, $80° - 90°$, $150° - 160°$ and $170° - 180°$. The red lines are the fits to the distributions. The red bars at the top of each panel of Figure 6.1 show the mean flux ratio, i.e. where the fitted curve peaks, and the standard deviation for each fitted Gaussian distribution. The far apart red bars for two distributions suggest that the bimodal distribution indeed consists of two populations.

Another significant and meaningful quantity that can be extracted from Figure 6.1 is the occurrence rate of the solar wind electrons' precipitation into the Martian upper atmosphere through cusps, which essentially is the percentage of the number of identified solar wind electron measurements out of the total measurements. Here, the ratio of the number of the measurements of the two populations is first calculated, given in the left upper corner of each plot in Figure 6.1. It is obtained by integrating each fitted Gaussian function from 0 to positive infinity (the negative part is neglected because of the lack of physical meaning) and then acquire the ratio of the two obtained integrals. Figure 6.2 shows how this ratio changes with pitch angle based on the distributions of three pairs of the flux ratios in Figure 6.1, highlighted by different colors. The three lines share the same trend: the plunging of the ratio at more field-aligned upward PAs, $0° - 40°$, due to the lack of solar wind electrons; then the near

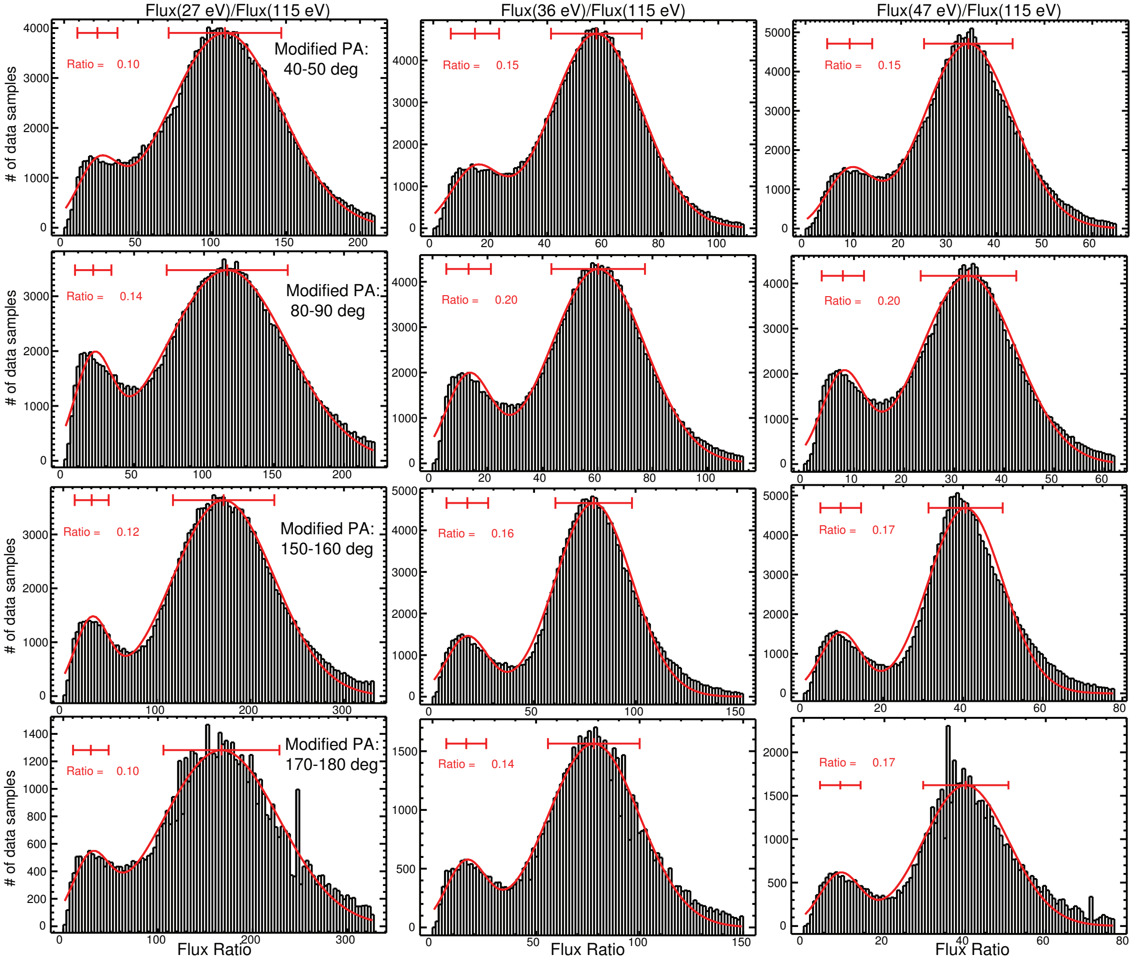

Figure 6.1: The three columns are the histogram plots of the flux ratios of three energy pair: 27 eV & 115 eV, 36 eV & 115 eV, and 47 eV & 115 eV. The four rows are for four pitch angles, from top to bottom: 40° – 50°, 80° – 90°, 150° – 160° and 170° – 180°. The red lines are fittings to each plot. Also, the sample ratio of the two populations are also shown at the upper left corner in each plot. In addition, the red bars at the top of each panel mark the flux ratio where the fitted Gaussian distribution peaks, along with the standard deviation of each Gaussian-like distribution.

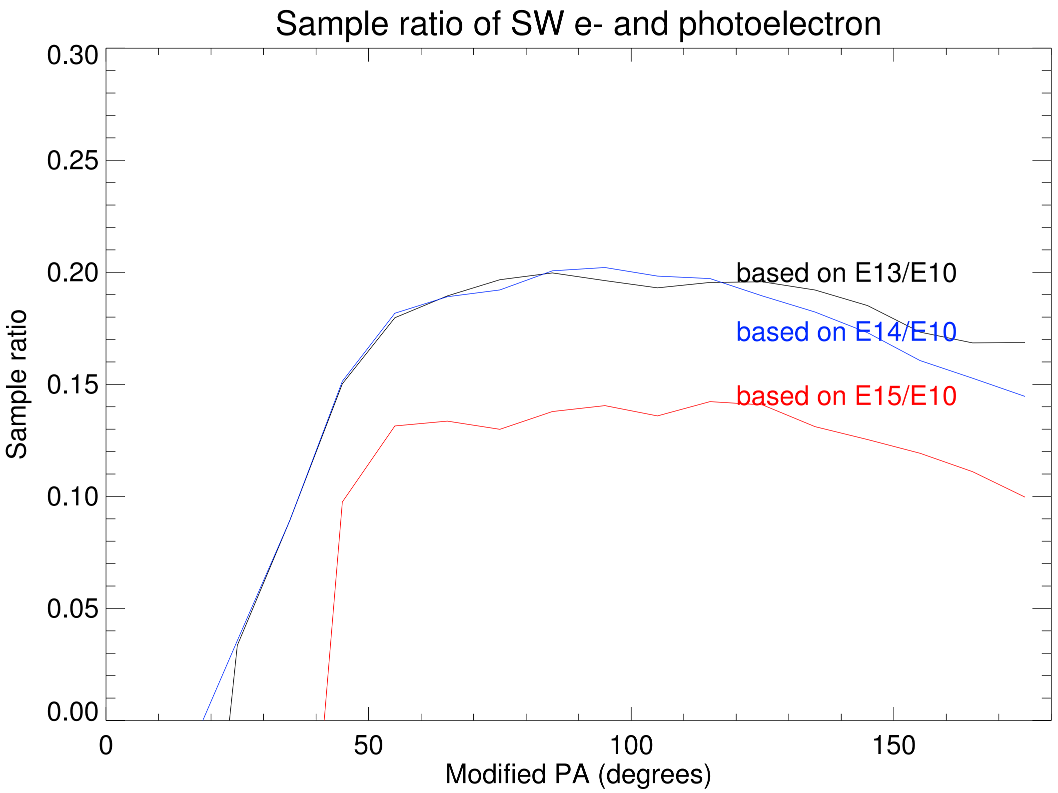

Figure 6.2: Sample ratio of the two populations against modified pitch angles. The three colors are for three energy pairs: 27 eV & 115 eV (red), 36 eV & 115 eV (blue), and 47 eV &115 eV (black).

constant value at PA $40° - 120°$; finally a slow decrease at the downward field-aligned PAs. For the first few upward pitch angle bins, the sample ratio is about 0.

The highest possibility of solar wind electron precipitation happens at pitch angle (PA) near 90°. There are two possible explanations. Firstly, It is possible that solar wind electrons are more likely to be found when the pitch angle distribution is only partially sampled. As said in the methodology section, the instrument has a 2D field of view (FOV) so that only part of the pitch angles, near 90°, are sampled when the magnetic field line is out of the plane of the instrument. As the data selected for this study are confined within a box of loop-structure strong crustal fields, the magnetic field (while not always true) is more likely north-south directed, thus in the plane of the instrument as Mars Global Surveyor (MGS) is flying northward in the dayside. The chance of magnetic field lines being twisted out of this plane due to the reconnection with the interplanetary magnetic field (IMF) is rather high as the IMF usually has an east-west component. As a result, partially sampled pitch angle distributions (PADs), centered at PA $\sim 90°$, may hint at a higher possibility of open magnetic field lines through which solar wind electrons can precipitate into the Martian atmosphere. Secondly, it seems that the measured pitch angle distribution of electron fluxes at the high-energy range at 2 pm is more isotropic than expected (e.g. *Liemohn et al.*, 2003; *Brain et al.*, 2007) over the strong crustal fields, which is actually identified as photoelectrons by *Brain et al.* (2007). The more isotropized pitch angle distribution of photoelectrons at 115 eV, compared to a classic source cone distribution, decreases the flux ratio for perpendicular pitch angles, due to a larger denominator, and increases the flux ratio for field-aligned pitch angles, due to a smaller denominator. As a result, photoelectrons are more easily miscounted as solar wind electron samples at perpendicular pitch angles due to the smaller flux ratio while the field-aligned pitch angles are not affected.

Despite the similarity of the three lines, while the ratios between solar wind electron samples and photoelectron samples derived from the distribution of the flux ratio of energy channels 36 eV & 115 eV (denoted as “E14/E10”, colored in blue, the second column of Figure 6.1) and 47 eV & 115 eV (denoted as “E13/E10”, colored in black, the third column of Figure 6.1) are on top of each other with a maximum value near 0.20, the red line, derived from the distribution of the flux ratio of 27 eV & 115 eV (denoted as “E15/E10”, the first column of Figure 6.1), has a ~ 0.05 offset from the other two, with a maximum around 0.15. The possible explanation of this discrepancy is as follows. The spiked fluxes in the 20-30 eV range (partially fall into the 27 eV energy channel), a typical feature of photoelectrons generated by the very intense He II 30.4 nm solar line, can be mixed with lower fluxes at nearby energies due to the energy shift caused by spacecraft potential. *Frahm et al.* (2006a) noted that

Mars Express (MEX) had a negative spacecraft potential when in the ionosphere, reducing the energy of the production spikes by 5 to 10 eV, which might be happening for MGS as well. A spacecraft potential shift would result in a broader flux distribution of photoelectrons in the 27 eV bin but not influence the other two energy channels nearly as much because the typical photoelectron spectrum is rather smooth from 30-60 eV. This broadening of photoelectron distribution at 27 eV (wider error bars for the photoelectron population, therefore larger overlapping areas of the two populations in the left column of Figure 6.1) makes it less distinguishable from the solar wind samples. Therefore, results from the 27 eV energy channel are relatively less trustworthy in this study. The following analysis focuses on one of the other two, the flux ratio of the energy channel pair 36 eV & 115 eV.

Based on the discussions above, it is easy to calculate that the occurrence rate of solar wind electrons in regions where the magnetic field elevation angle is above 45° is around 1/6. In addition, it seems that a flux ratio cut-off can be obtained from this bi-modal distribution to isolate solar wind electron samples or photoelectron samples for further use, such as studying the energy flux of each population. For each pair of flux ratios, we define this cutoff for each downward pitch angle bin such that the values from two fitted Gaussian distributions are equal and then use the minimum of these nine cutoffs as the solar wind electron cutoff and the maximum as the photoelectron cutoff. For the flux ratio of 36 eV and 115 eV, the cutoff for the solar wind electrons is 27, the dashed line as shown in Figure 2.6g, and the cutoff for the photoelectron is 35. For the flux ratio of 47 eV and 115 eV, the two numbers are 14 and 19. These numbers may be used to distinguish photoelectrons and solar wind electrons without examining the energy spectra for future studies.

6.1.2 Occurrence Rate's Dependence on Magnetic Elevation Angles

The occurrence rate of 1/6 is for a large variation of magnetic elevation angles. As mentioned above, the strong crustal magnetic field lines are more likely to be connected to the IMF (i.e. open) when the elevation angles are near 90°, thus yielding a larger chance for solar wind electron precipitation. How the occurrence rate changes against magnetic elevation angles is examined here.

The dataset is divided into nine magnetic elevation angle bins with a bin size of 5°. For each bin, similar to the previous section, the flux ratio distribution is obtained and then fitted with two Gaussian functions. From the fitting to the distributions, the sample ratio of the solar wind electron and the photoelectron can be determined. The sample number for each PA× Elevation Angle bin (a bin size of $10° \times 5°$) is shown in Figure 6.3a and the sample ratio in Figure 6.3b. As expected, Figure 6.3a shows large samples near PA 90°, then lower towards PA 0° and 180°. The sample number is about the same for all pitch angles as the elevation angle increases. When the elevation angle is near 90°, magnetic field lines have little horizontal component, thus are mostly in the plane of the instrument and all pitch angles are fully sampled for almost all of the measurements. One thing to notice is that the minimum sample number (colored in black) is 2670 instead of 0. The high sample ratio, up to 0.45, of the solar wind electrons concentrates at high elevation angle bins as shown in Figure 6.3b. For elevation angles lower than 60°, the sample ratio of solar wind electron to photoelectron is mostly below 0.2. Also, the sample ratio is higher again near PA 90° for low elevation angles. For high elevation angles, where most of the magnetic field lines are open, the sample ratio is higher for downward pitch angles. The observations for upward pitch angles consist of both photoelectrons and reflected solar wind electrons, while for downward pitch angles, the sample should be mostly solar wind electrons. In addition, the reflected solar wind electrons can be seen in the upward pitch angles as low as $20° - 50°$ (transition from blue to black in Figure 6.3b), indicating a loss cone width of about this size.

The fitting function does not perform well when solar wind electron samples are very small. For example, for elevation angle $45° - 50°$ and PA $40° - 50°$ in Figure 6.3b, the sample ratio (0.24) is unreasonably high for an upward pitch angle bin despite barely being able to see a second population. Also, some of the sample ratios are negative, such as elevation angle $45° - 50°$ and PA $170° - 180°$. It is because the fitting returns a negative amplitude to one of the two fitted Gaussian distributions. The negative sample ratios are set to 0 in Figure 6.3b.

From the discussion above, the occurrence rate of solar wind electron precipitation largely varies with magnetic elevation angles, lower than 10% for more horizontal magnetic field lines but as high as 1/3 for vertical field lines. This result is also consistent with Figure 11 of *Brain et al.* (2007). In between closed magnetic loops, the one-sided loss cone distribution, an indicator of solar wind electron precipitation as well as open magnetic field lines, is the dominant pitch angle distribution.

6.1.3 Occurrence Rate's Dependence on Solar Zenith Angles

Graphically, the occurrence rate of solar wind electron precipitation correlates with magnetic elevation angle because vertical magnetic field lines are more likely to be open. Physically, this rate can vary with the solar zenith angle (SZA) as solar wind normal pressure onto the planet is smaller with increasing SZA. In addition, the altitude of the Martian dayside electron density peak is also roughly proportional to a cosine function of SZA (e.g. *Hantsch and Bauer*, 1990; *Withers*, 2009; *Withers et al.*, 2014), which can be explained by Chapman theory (*Chapman*, 1931a,b). As a result, the magnetic pileup boundary (MPB) is closer to the planet near the sub-solar point and at higher altitudes at larger SZA (e.g. *Vignes et al.*, 2000; *Crider et al.*, 2002; *Nagy et al.*, 2004). With a higher downward-directed solar wind pressure, i.e. a smaller SZA, the IMF can erode more deeply into the Martian atmosphere and

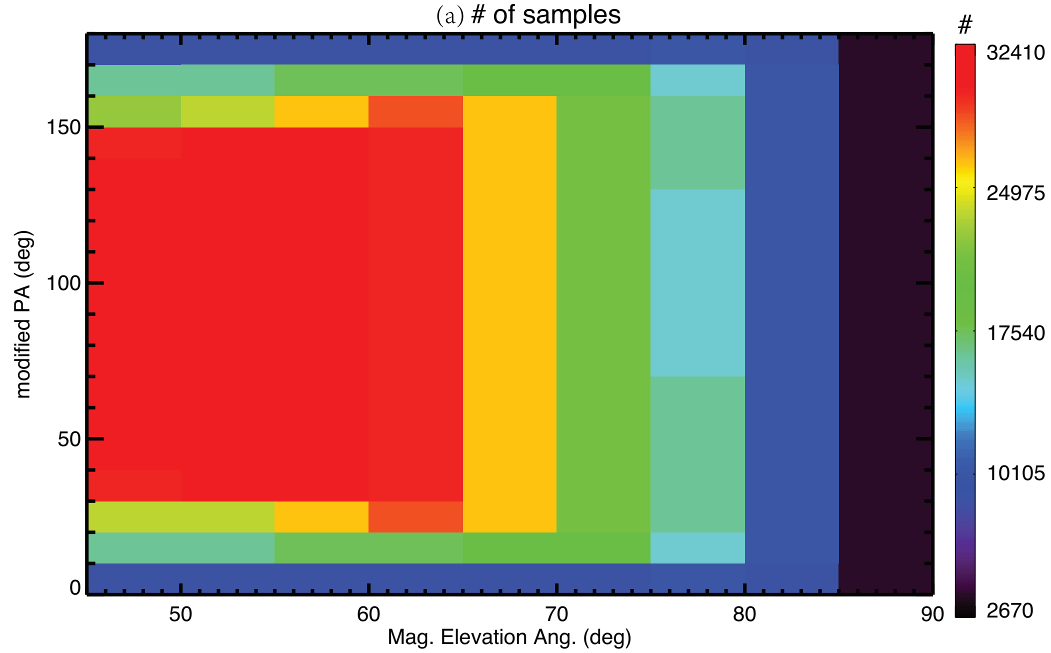

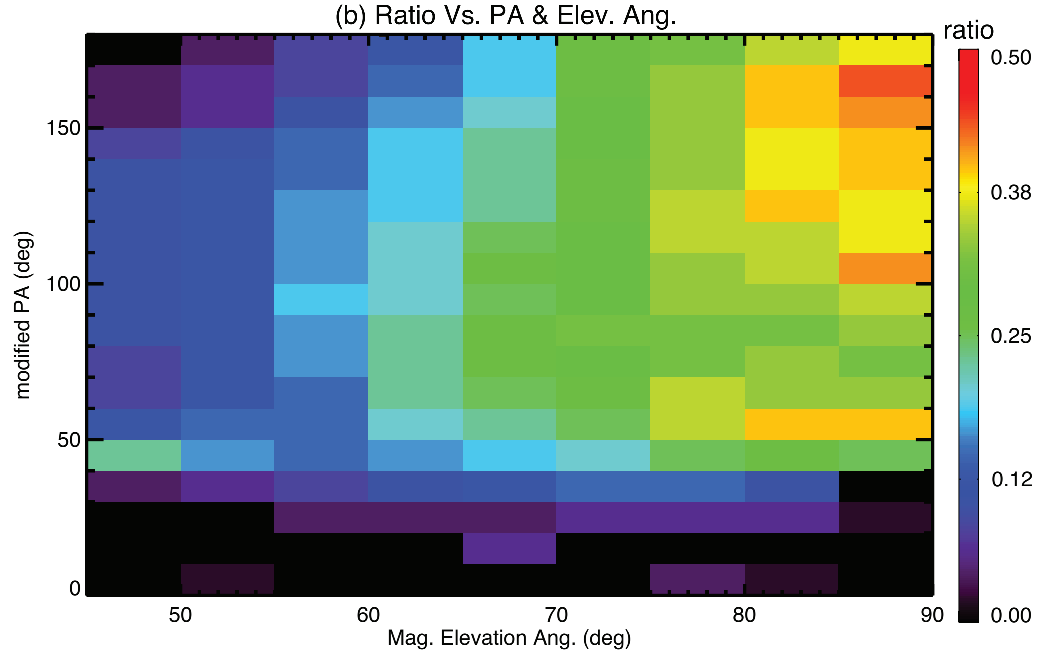

Figure 6.3: (a) The sample number for each pitch angle and magnetic elevation angle bin. (b) The sample ratio of the two populations for each pitch angle and magnetic elevation angle bin.

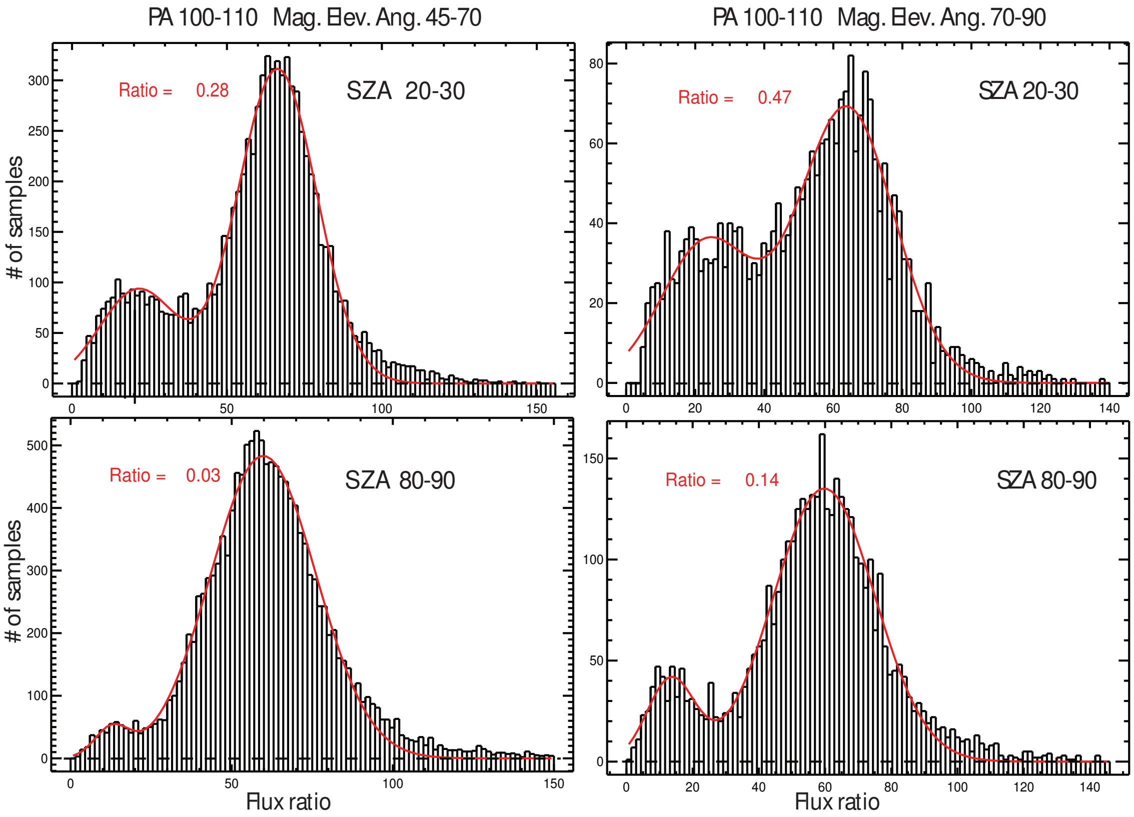

Figure 6.4: The distribution of flux ratio of energy pair 36 eV & 115 eV at different solar zenith angles (SZA) for modified PA 100° – 110°. The two figures in the left are for absolute magnetic elevation angle 45° – 70° and right for 70° – 90°; the upper row for SZA 20° – 30° and the lower for 80° – 90°. Similarly, the red lines are the fittings and the sample ratios of the two populations are shown at the upper left corner.

connect with strong crustal fields with the opposite component. To explore this relation, the dataset is divided into two magnetic elevation angle groups, absolute value within 45° – 70° and within 70° – 90°, and then into seven SZA bins of 10°. The minimum SZA is 20° because the measurements were made by MGS at 2 pm LT.

Figure 6.4 shows some histogram examples at PA 100° – 110°, the left column for absolute magnetic elevation angle 45° – 70° and right for 70° – 90°; the upper row for SZA 20° – 30° and the lower for 80° – 90°. Again, the distribution is bi-modal and the sample ratio derived from the fitting is bigger for large elevation angle by comparing the right column to the left column. For small SZAs (the upper two rows), the left population, i.e. the solar wind electrons, is of a larger proportion of the total sample than that for large SZAs (the bottom row), as shown as the sample ratios in the upper left corner of each panel. As expected, the occurrence rate of the solar wind electron precipitation is higher with smaller SZA.

To better examine all the pitch angles, Figure 6.5 shows the sample number (a and c) and sample ratio (b and d) for the two magnetic elevation angle groups, respectively. Because that dataset is confined in the geographic box as said in the methodology section, the high sample number concentrates in mid-SZA and PA $\sim 90°$. On one hand, for each group, the ratios in Figure 6.5d, where magnetic field lines are more vertical, are generally much higher than in Figure 6.5b, as expected. On the other hand, for both Figure 6.5b and d, one common feature is the higher ratio for smaller SZAs than larger SZAs. Also, the maximum ratio now increases to 0.7, which means a maximum occurrence rate of 41%. The pitch angle dependence can also be explained by the three possibilities described in section 1. Note that the few high ratios in PA $< 40°$ and SZA $20° - 30°$ are caused by the ill fittings.

Another common feature in Figure 6.5b and d is that the highest ratio surprisingly occurs at SZA $30° - 40°$ instead of $20° - 30°$. Although one would argue that it is caused by the small sample numbers for SZA $20° - 30°$, the comparison between the first and second row of Figure 6.4 seems to suggest some physical causes. Through the examination of the magnetic elevation angle against latitude, as shown in Figure 6.6, it is found that the magnetic loop of latitude $-30°$ to $-40°$, where most of the SZA $20° - 30°$ measurement comes from, has more random magnetic elevation angles than other latitudes. In other words, the magnetic field lines for SZA $20° - 30°$ might be of more random directions and less likely connect to the IMF.

From Figure 2.7, a seasonal change of low flux ratio population, i.e. solar wind electrons, is seen in the left column, being denser in the summer and sparser in the winter, as expected. This seasonal feature can be explained by the SZA dependence.

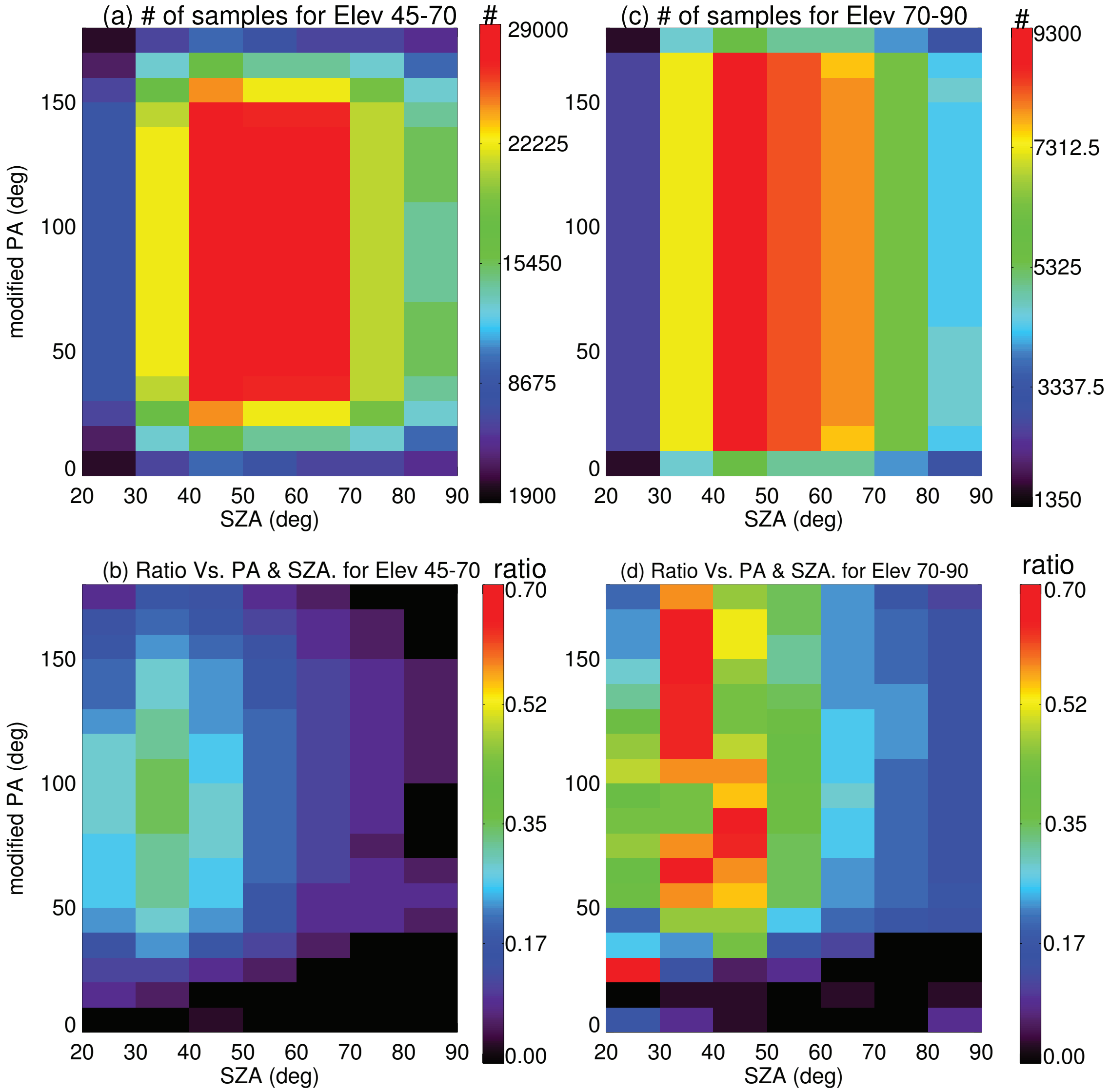

Figure 6.5: The upper two panels are the sample number for each pitch angle and magnetic elevation angle bin for absolute magnetic elevation angle $45° - 70°$ (a) and $70° - 90°$ (c). The lower two panels are the sample ratio of the two populations for each pitch angle and SZA bin for elevation angle $45° - 70°$ (b) and $70° - 90°$ (d).

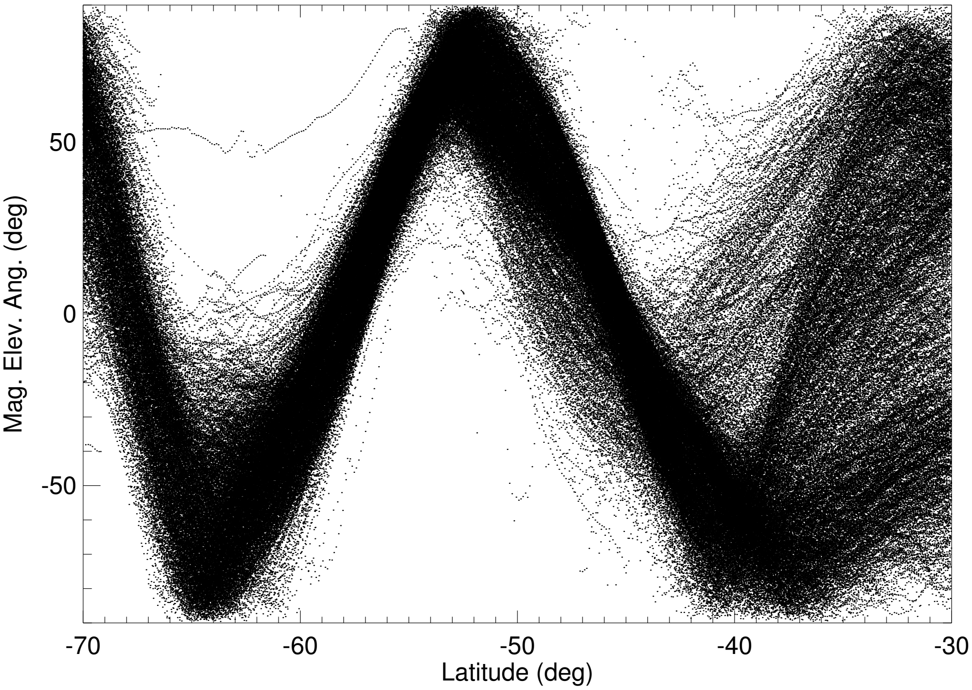

Figure 6.6: Magnetic elevation angle against latitude.

Because MGS is locked to 2 pm LT on the dayside and the tilt of Mars is around 25°, the alternating bar-like strong crustal fields, i.e. the geography box used to select data, are concentrated at low SZAs in the southern summer and high SZAs in the winter. It means that there is a higher chance to see solar wind electrons in the southern summer than winter. Generally speaking, even without locking a particular local time but just due to the tilt of Mars, the strong crustal fields can reach a lower SZA in the southern summer, leading to more solar wind electron precipitation. Furthermore, Mars is closer to the Sun during the southern summer, a higher dynamic pressure at the sub-solar point is also expected, likely causing more reconnection between the IMF and the crustal fields. All considered, a seasonal variation of solar wind electron precipitation is expected.

6.2 Energy Deposition

The identification of solar wind electrons, the occurrence rate and its dependence on the magnetic elevation angle and also solar zenith angle are discussed in the above sections. Another feature of these superthermal electrons is their energy deposition into the Martian atmosphere, which can cause localized heating, excitation and dissociation and ionization.

The first step is to isolate solar wind electron samples. As mentioned in section 3.2, the minimum flux ratio cutoff of nine downward PAs, $90° - 180°$, can be used to select solar wind electron precipitation events. To make this selection more strict, the minimum cutoffs of two energy pairs, 27 for 36 eV & 115 eV and 15 for 47 eV & 115 eV, are both applied. Due to the small samples at PA near 0° and 180°, as shown in Figure 6.3a, the cutoff criteria is applied to downward PA $90° - 170°$ and $90° - 180°$, separately. Even though the selected sample numbers of solar wind electron precipitation events for the two cases vary by a factor of two, (11374 and 5935, respectively), the results, such as the distributions and the number/energy fluxes, are actually quite similar. Hence, the results of the first case, filtered by only PA $90° - 170°$, are shown in Figure 6.7. The left column is for pitch-angle-averaged number flux distributions while the right column is for energy flux distributions. From top to bottom, each row is the downward, upward, and net (downward subtracting upward) flux, respectively. For the upward/reflected solar wind electron fluxes, the cutoff criteria is applied again to ensure excluding the photoelectrons. Also, the average (denoted as "mean"), median, and mode values are listed in each plot.

As shown in Figure 6.7, take the median values as examples, the precipitating solar wind electron number and energy fluxes are 1.02×10^8 $cm^{-2}s^{-1}$ and 3.24×10^9 $eV cm^{-2}s^{-1}$, respectively. However, $\sim 60\%$ of the incoming fluxes are reflected back to the MGS altitude by magnetic focusing and/or collisions, as shown in the second row. We have further investigated the reflection of solar wind electrons. Firstly, the

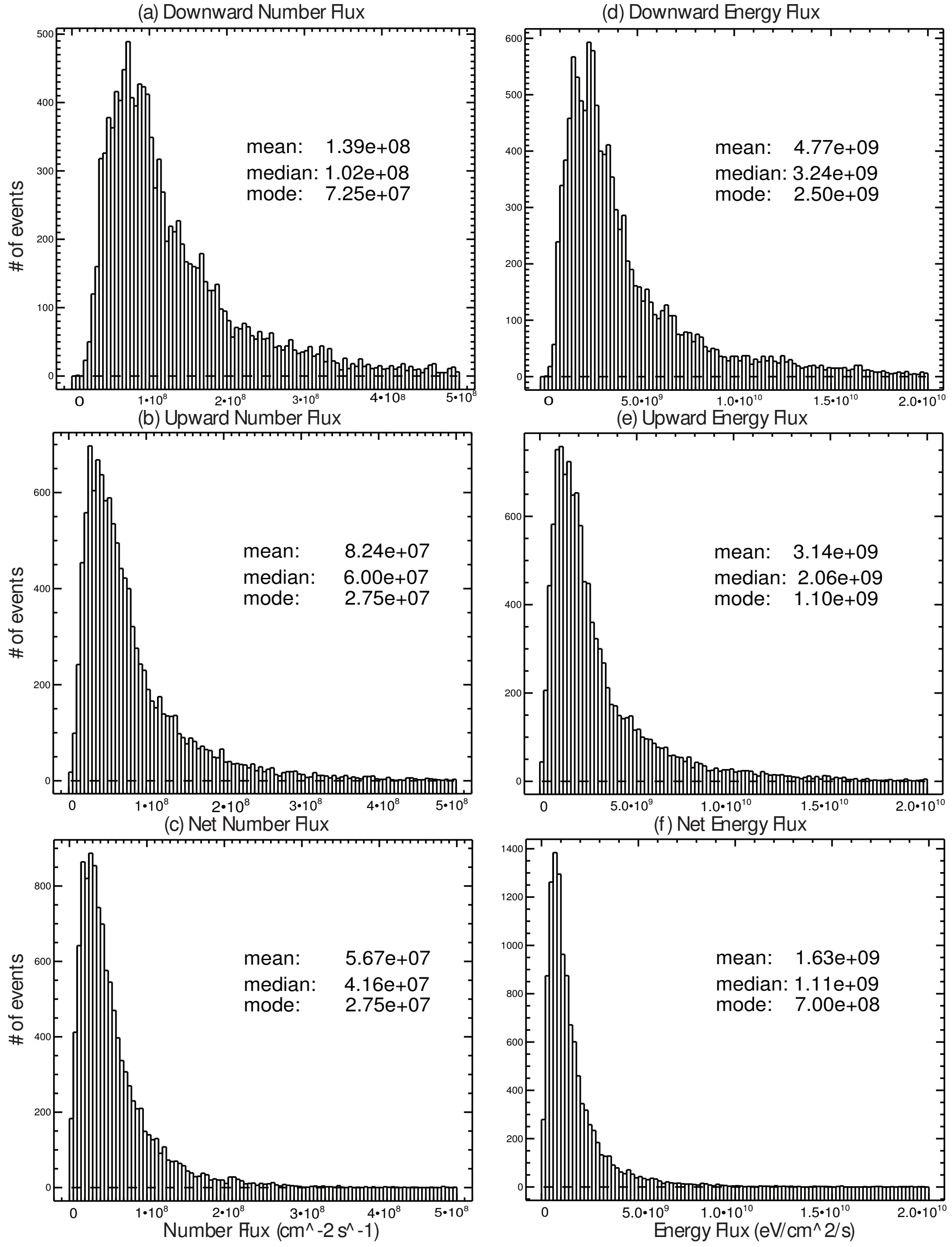

Figure 6.7: The distributions of solar wind electron fluxes: downward number fluxes (a), upward number fluxes (b), net number fluxes (c), downward energy fluxes (d), upward energy fluxes (e), net energy fluxes (f). The average, median and mode values of each distribution are also shown in the upper right corner.

percentage of the reflected out of the total solar wind electron samples varies with different upward pitch angles, $> 90\%$ for PA greater than $40°$ and $< 30\%$ for PA smaller than $20°$. In other words, more field-aligned solar wind electrons are of higher chance to deposit their energy into the upper atmosphere, as expected. Then, for electrons with energy lower than 100 eV, around 60% of the incoming energy flux is reflected while for energy above 100 eV, it is around 70%. On one hand, the reflection is about the same for these different energy ranges, which implies that the magnetic focusing is the dominant process. On the other hand, the high-energy electrons are more likely to be reflected, which maybe result from the lower collision cross sections ($\propto 1/E^2$). It also means that collisions play a relatively minor role in the reflection.

With so much energy reflected, the number/energy fluxes absorbed by the atmosphere down below 400 km are only the net part, a median value of 4.16×10^8 $cm^{-2}s^{-1}$ and 1.11×10^9 $eVcm^{-2}s^{-1}$ for the number and energy flux, respectively. To compare it with solar photon input, the solar flux based on the Flare Irradiance Spectral Model (FISM) (*Chamberlin et al.*, 2007, 2008) is calculated. The EUV irradiance is integrated from 1-100 nm and the resulting solar EUV flux is then scaled to Mars orbit, along with a time shift based on a point-by-point basis (assuming a 27-day solar rotation) to account for the different orbital positions of Earth and Mars, similar to the method used in *Mitchell et al.* (2001). The mean EUV flux from Jan. 1999 to Jan. 2007 (roughly the same time period of the MGS data set used in this study) is around 1.9×10^{-7} W/cm^2, or 1.2×10^{12} $eVcm^{-2}s^{-1}$. It means that the energy flux deposition of solar wind electrons into the Martian atmosphere is about 0.1% of the solar photon absorption. However, this 0.1% may need some adjustment. Firstly, unlike solar EUV fluxes that only vary within a factor of 2, the long tails in the flux distributions are seen in Figure 6.7 and under extreme cases, the energy input from solar wind electrons can be ten times larger. Also, the estimated solar EUV flux does not include the effect of solar zenith angles, which may drop by a factor of 2 at SZA greater than 60°.

This direct comparison between the energy input of these two sources seemingly suggests that the energy deposition of the solar wind electrons is insignificant. However, the deposition processes of these two energy sources are quite different. It is possible that solar wind electrons can cause significant changes locally. In fact, through a closer examination of the contribution of the net energy fluxes from electrons with energy lower and higher than 100 eV individually, the former is twice that of the energy flux deposition of the latter. Notice that low-energy electrons are more likely to cause heating at higher altitudes instead of ionization at lower altitudes. Therefore, it is possible that these solar wind electrons can efficiently heat the cusps. Further study of this energy deposition and possible influence on the upper atmosphere requires modeling.

One thing not addressed in the previous analysis is the possible contamination by spacecraft photoelectrons and other secondary electrons. The anode sectors (sector 5-12) of MGS ER more likely to detect these spacecraft electrons look towards zenith and along the spacecraft bus (*Mitchell et al.*, 2001). Since the dataset of this study is confined to more vertical magnetic fields lines, these contaminated sectors are converted into upward modified pitch angles while the downward modified pitch angles should be barely affected. Hence the possible contamination may not significantly influence most of the previous analysis. However, the reflected energy flux (in upward pitch angles) here might be overestimated because of the contamination. As a result, the different reflection of high- and low- energy electrons might be partly or even entirely due to the contamination. In addition, it also leads to an underestimation of solar wind electron energy deposition. The actual energy deposition should range from the net energy flux, $1.11 \times 10^9\ eVcm^{-2}s^{-1}$, to the downward energy flux (assuming all the upward energy fluxes are contaminations from spacecraft electrons), $3.24 \times 10^9\ eVcm^{-2}s^{-1}$. This upper bound of energy deposition also increases the percentage relevant to the solar input to 0.3% and more than 2% under extreme cases.

6.3 Discussion of Solar Wind Electron Precipitation

In this chapter, the “knee” feature near 60 eV in the photoelectron energy spectra is utilized to differentiate the solar wind/magnetosheath electrons from the ionospheric photoelectrons. The flux ratio of one energy channel lower than 60 eV and one higher, such as 36 eV and 115 eV, is calculated for the selected dataset, the nearly 8-year measurements of MGS MAG/ER over a specific dayside strong crustal field region. The distribution of the flux ratios is bi-modal, which implies the existence of a second population other than photoelectrons, i.e. the solar-wind/magnetosheath electrons.

Then a curve-fitting that consists of two Gaussian functions is applied, through which the occurrence rate of dayside solar wind electron precipitation through the cusps over the strong crustal fields is determined. For magnetic elevation angles greater than 45°, the occurrence rate is about 1/6. Furthermore, by dividing data into 9 magnetic elevation angle bins, the occurrence rate increases with the magnetic elevation angle, as expected. The maximum occurrence rate is 1/3, when the magnetic field lines are nearly vertical.

The results have shown that the occurrence rate is lower at larger solar zenith angles, probably resulting from the higher altitude of MPB due to a smaller normal solar wind dynamic pressure and also a flared away ionosphere near the terminator. A maximum occurrence rate of 40% is found, which suggests two things. Firstly, the reconnected/open magnetic fields are more likely near the sub-solar point. Secondly, even for vertical magnetic field lines with small SZA, the chance is surprisingly high that the magnetic field is still closed at 400 km. Due to the tilt and the orbital position of Mars, a seasonal variation of the precipitation is also expected and found. In other words, during the southern summer (winter), the solar wind precipitation occurs more (less) often. The occurrence rates presented here can roughly be approximated as how often the IMF is connected to strong crustal fields at 400 km. However, be aware that this rate may count in occasions when a draped field line moves to 400 km, even though this is very rare near the strong crustal fields (*Brain et al.*, 2005, 2007), and also the transit of solar-wind/magnetosheath electron samples on closed magnetic field lines when the reconnection between the IMF and strong crustal fields happens. In addition, this occurrence rate probably varies with altitude as the cusps expand in area with increasing altitude.

Open magnetic field lines also mean the particles and energy exchange between the Martian atmosphere and the solar wind. The energy flux input from solar wind electron precipitation is also investigated and is found to be roughly 0.1% up to 2% of the solar EUV flux input to the Martian atmosphere. However, this simple comparison does not take into account the effects of the solar zenith angle or the different deposition processes. The localized effects of the solar wind electrons might be significant. The energy deposition of the solar wind electrons, especially the heating rates, at different altitudes and SZAs can be further studied by modeling, such as the SuperThermal Electron Transport (STET) model (*Khazanov and Liemohn*, 1995; *Liemohn et al.*, 1997, 2003, 2006).

6.4 Superthermal Electron Precipitation on Martian Nightside

A mirroring study can be done when the strong crustal fields rotate to the nightside. Shane and Xu et al. (manuscript submitted) found that the photoelectron population still dominates the occurrence rate for solar zenith angles lower than 110°, which can be roughly considered as the terminator SZA for photoelectrons. When SZA $> 110°$, photoelectron occurrence rate firstly decreases at field-aligned pitch angles as electrons with more perpendicular pitch angles bounce at higher altitudes where fewer collisions happen. Then, photoelectrons deplete on more horizontal magnetic field lines, which tend to be shorter, and then the more vertical magnetic fields. On the other hand, solar wind electron precipitation is quite constant once past SZA $\sim 110^\circ$ in terms of occurrence rate. The energy deposition of post-terminator electrons happens mainly on more vertical magnetic fields with a median energy flux of $10^7 - 10^8$ eV cm^{-2} s^{-1}. Because this study is examining locations inside the strong crustal field regions, the majority of the precipitated electrons are magnetically reflected or scattered back out, with a maximum of fractional deposition rate around 0.16. Such energy deposition is found to be able to cause emission only less than 1% of the time but to be capable of supporting a nightside ionosphere patch with a column total electron content of 3.3×10^{14} m^{-2} and an averaged electron density of 1.6×10^4 cm^{-3}, which is agreeable with previous estimations (e.g. *Safaeinili et al.*, 2007; *Lillis et al.*, 2009).

CHAPTER VII

Preliminary Work With MAVEN

The National Aeronautics and Space Administration (NASA) dedicated the Mars Atmosphere and Volatile EvolutioN (MAVEN) mission, which was launched in September 2013, to determine the role that the loss of volatiles from the Mars' atmosphere to space has played through time, giving insight into the history of Mars atmosphere and climate, liquid water, and planetary habitability. The MAVEN mission (*Jakosky et al.*, 2015) provides a comprehensive set of plasma and magnetic field observations of Mars and also solar inputs to altitudes as low as ∼150 km (∼120-135 km during“deep dips”) and over a wide range of local times and solar zenith angles. With such a comprehensive dataset, more future work can be done to deepen our understanding of superthermal electrons and related topics at Mars. Here, we present some preliminary work with MAVEN measurements.

7.1 Nightside Photoelectron Observations

Crustal magnetic fields in the northern hemisphere of Mars are generally much weaker than those in the south (*Connerney et al.*, 2005). Over two large regions, Utopia Planitia and the Tharsis rise, the observed magnetic field at 400 km altitude is thought to be dominated by fields induced by the solar wind interaction, although the draping pattern is asymmetric and may be influenced by the presence of crustal sources far from the spacecraft (*Brain et al.*, 2006b). From 12/1/2014 to 2/15/2015, when MAVEN's periapsis was at high northern latitudes on the nightside, the Solar Wind Electron Analyzer (SWEA) observed ionospheric photoelectrons with energies from 3 to 500 eV at low altitudes (140-200 km) and high solar zenith angles (120-145 degrees) on 35% of the orbits.

One orbit (Orbit 520) is shown in Figure 7.1. From top to bottom, each panel shows solar zenith angle, altitude, ion energy spectrum and ion mass spectrum measured by the Suprathermal and Thermal Ion Composition (STATIC), magnetic field data measured by Magnetometer (MAG) in Mars-centered Solar Orbital (MSO) coordinates, normalized electron pitch angle distribution (111.2 - 140.3 eV) and electron energy spectrum measured by SWEA, against time. Soon after 08:02, the SWEA measurement shows electron depletion that lasts for about 5 minutes, which is thought to be due to localized closed magnetic fields. These closed loops prevent solar wind penetration and the planetary originated plasma that are bounded to these magnetic fields are also depleted because there are no significant sources but rather only continuous losses such as recombination and collisions when these fields rotate to nightside. From 08:07 to 08:12, when the spacecraft dips below $\sim$ 200 km, in addition to electron depletion, there are also continuous moderate to high electron fluxes observed. In particular, undeniable photoelectron signatures are seen for the time range 08:10:20-08:11:40. To demonstrate, Figure 7.2 is an example of pitch angle (PA) averaged electron energy spectrum at 08:10:44 when the spacecraft is at altitude 144 km and deep nightside (SZA$\sim$ 132°), black for PA $0-90°$ and the red line for PA $90°-180°$. The magnetic elevation angle, the angle relative to the horizontal plane, is 59°. For PA $90°-180°$ (red line), i.e. electrons flowing towards the planet, typical photoelectron features can be identified, including the peaks in the $20-30$ eV due to the very intense He II 30.4 nm solar emission and also the sharp decrease of electron flux near $50-70$ eV caused by the sudden drop in solar photons below

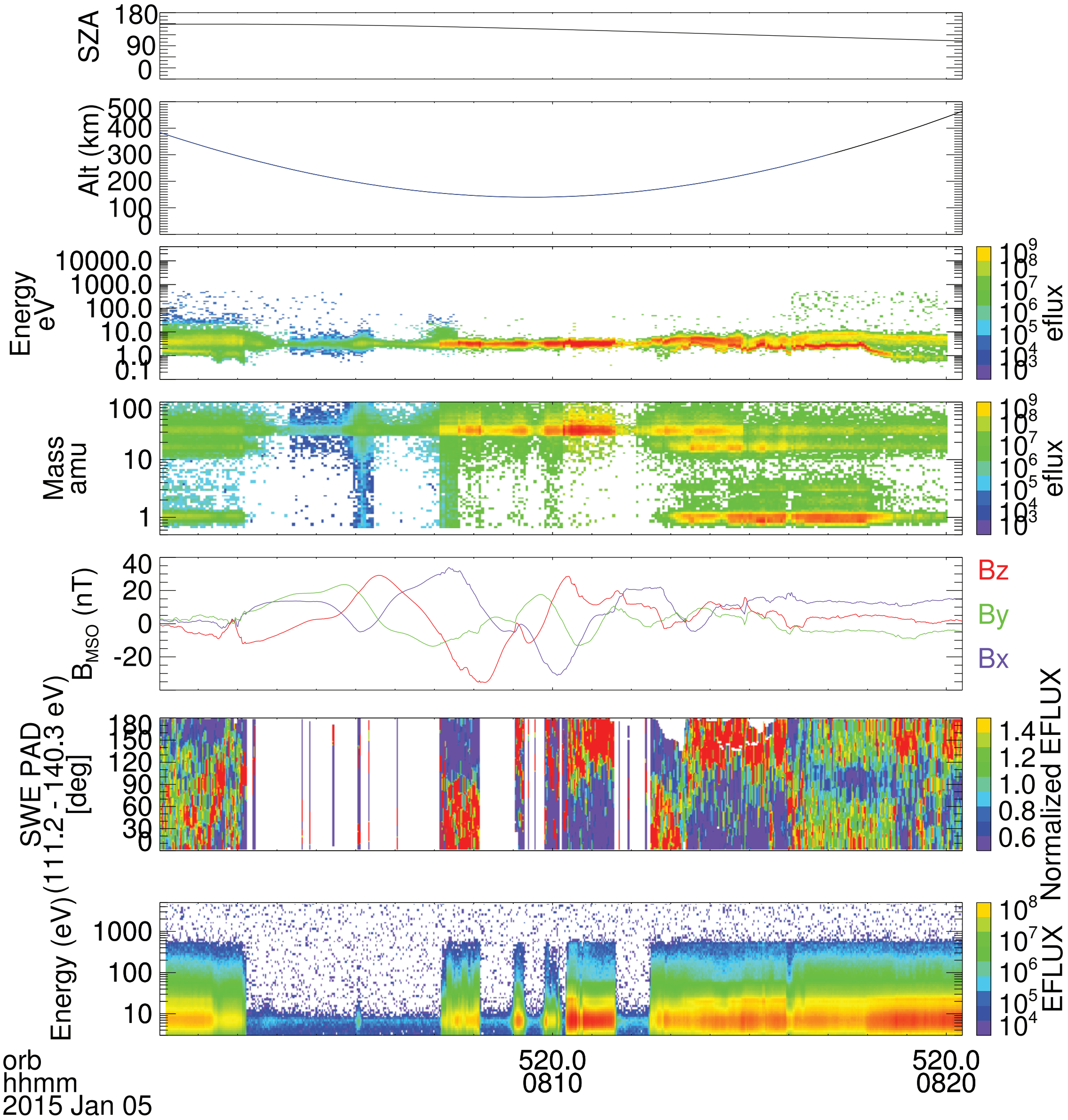

Figure 7.1: A MAVEN orbit example (Orbit 520) begins at universal time (UT) Jan. 5, 2015, 8:00:00. From top to bottom, solar zenith angle (degree), altitude (km), STATIC ion energy spectrum, STATIC ion mass spectrum, MAG magnetic field measurements in MSO coordinates, SWEA normalized electron pitch angle distribution (111.2 - 140.3 eV), SWEA electron energy spectrum. Both electron and ion energy fluxes are in units of eV s^{-1} cm^{-2} sr^{-1} eV^{-1}.

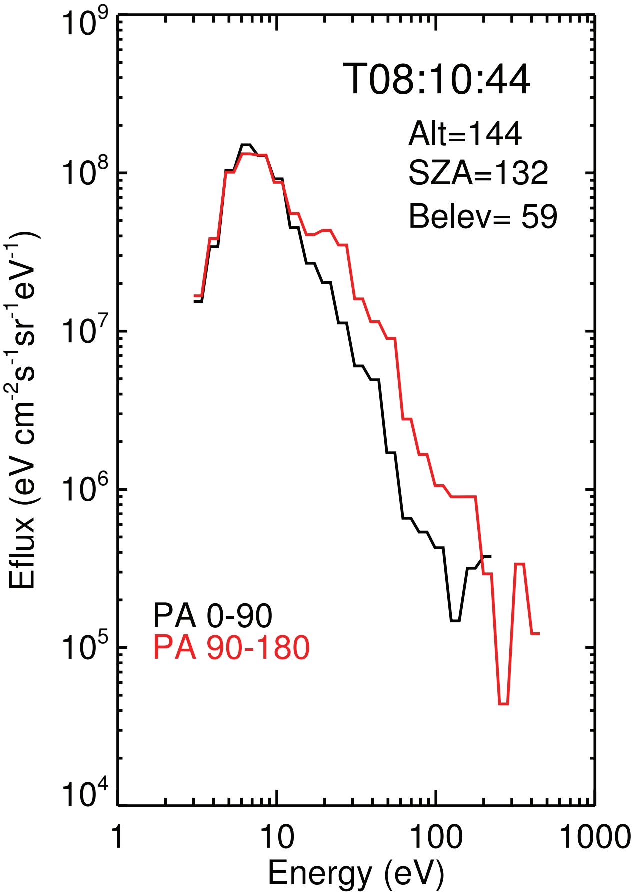

Figure 7.2: An example of low-altitude nightside photoelectron observation of the orbit 520, Jan. 5, 2015, 08:10:44, when MAVEN's periapsis in the northern hemisphere. The black line is for pitch angle $0-90°$ and the red line for pitch angle $90° - 180°$.

15 nm (e.g. *Mitchell et al.*, 2000; *Liemohn et al.*, 2003). For PA $0° - 90°$ (black line), the spectrum is smoother and arguably photoelectron-like with the flux decrease near $40 - 70$ eV. These electrons might be inflowing photoelectrons magnetically reflected or scattered back out.

Since this electron population is unambiguously produced in the dayside ionosphere, these observations demonstrate that the deep Martian nightside is at times magnetically connected to the sunlit hemisphere. We investigated the occurrence rate of ionospheric photoelectrons as a function of altitude, solar zenith angle, and magnetic field orientation, and found that photoelectrons are more likely to be observed

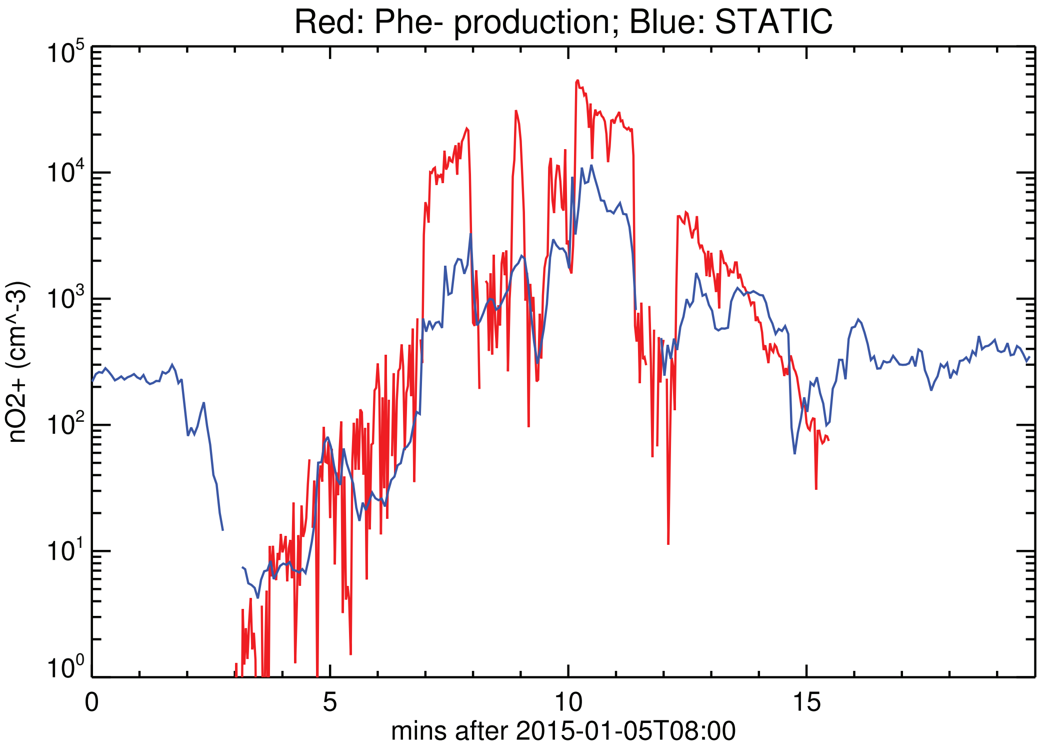

Figure 7.3: Observed O_2^+ density by STATIC of Orbit 520, colored in blue and calculated O_2^+ density through photoelectron impact ionization, colored in red.

at low altitudes and high solar zenith angles when the local field is more vertically oriented. This implies that the magnetic field extends to high altitudes between the night hemisphere, where photoelectrons are observed, and the source region in the dayside ionosphere, thus avoiding significant attenuation in transit. The BATS-R-US Mars multi-fluid MHD model (*Dong et al.*, 2014) suggests the presence of closed crustal magnetic field lines over the northern hemisphere that straddle the terminator and extend to high SZA. Simulations with the SuperThermal Electron Transport (STET) model show that photoelectron transport along such field lines can take place without significant attenuation. Closed crustal magnetic loops extending thousands of kilometers are common at low altitudes (below ∼200 km), even over the weakest crustal sources. Thus, there is probably no region on Mars with a purely ionospheric interaction with the solar wind.

7.2 Implications for the Nightside Ionosphere

The Martian nightside ionosphere is known to have low densities and be quite patchy. Precipitation of photoelectrons into the nightside atmosphere should cause ionization (e.g. *Lillis et al.*, 2009; *Fillingim et al.*, 2007; *Fillingim et al.*, 2010) and possibly auroral emissions (e.g. *Haider et al.*, 1992; *Seth et al.*, 2002; *Brain et al.*, 2006a) in localized regions. From Figure 7.1, it is easy to see that the ion energy flux corresponds with the electron energy flux well. The electron flux has a sharper cutoff than the ions because ions' collision frequency with neutral particles is much higher than electrons so that below 200 km the ions are much more diffusive than electrons. From 08:02 to 08:12, STATIC measures an ion population with 32 amu and 3 eV (due to the spacecraft speed), i.e. the thermal O_2^+. Based on such measurements, the O_2^+ density can be calculated, shown in the blue line in Figure 7.3. There are a few possible mechanisms that might be responsible for such a nightside ionosphere, such as the bulk thermal plasma transport from dayside to night, ion transport along a magnetic field due to ambipolar electric fields, and also electron precipitation. Here we test if the observed electron precipitation, especially photoelectron precipitation, is able to support such an ion density.

The main chemistry to produce O_2^+ on the Martian nightside is to first ionize CO_2 through electron impact ionization. The produced CO_2^+ ions then rapidly convert to O_2^+ through dissociative recombination. Assuming photochemical equilibrium and O_2^+ being the main ion species, according to Chapman theory (*Chapman*, 1931a,b), the electron number density can be calculated from the equation

$$n_e(z) = (P(z)/\alpha_{eff}(z))^{0.5} \tag{7.1}$$

where $P(z)$ is the ion production rate, and $\alpha_{eff}(z)$ is the effective recombination rate. Because of the fast chemical reactions between CO_2 and O, $\alpha_{eff}(z)$ is approximately the dissociative recombination rate of O_2^+ (e.g. *Sheehan and St-Maurice*, 2004):

$$\alpha_{eff}(z) = 1.95 \times 10^{-7}(300/T_e(z))^{0.7} \tag{7.2}$$

where $T_e(z)$ is the electron temperature. Assuming charge neutrality, then the O_2^+ density is equal to the calculated electron density. The outputs from the Mars Global Ionosphere-Thermosphere Model (M-GITM) (*Bougher et al.*, 2015) are used to determine the ion production rate. The neutral profiles and the electron temperature profile used are at latitude 67.5° and local midnight from a M-GITM run at solar longitude 270° and driven by an Earth F10.7 of 130 sfu. The ion production rate is the product of electron flux, electron impact ionization cross sections and CO_2 density. The calculated O_2^+ is shown as the red line in Figure 7.3.

As we can see, the observed and calculated O_2^+ densities have similar profiles. The calculated O_2^+ density due to the electron precipitation is also much higher than the STATIC measurements for the time range 08:07-08:12, which suggests that the observed electrons can totally support such a nightside ionosphere. As to why it is higher, these electrons are assumed to be lost locally instead of to an altitude range. This would be an overestimation.

7.3 Summary

To briefly summarize, this preliminary study with MAVEN measurements suggests that even in the Martian northern hemisphere, a region that is usually considered consisting of weak crustal sources, there are closed magnetic loops extending thousands of kilometers at low altitudes and straddling the terminator. Such a surprising magnetic connectivity to the dayside ionosphere also provides energetic electrons as energy and particle sources to the Martian nightside atmosphere. While photoelectron measurements are found in 35% of the orbits, the magnetic connectivity should be of a higher percentage of this number because some electron samples might be photoelectrons but too degraded, due to collisions, to be identified through features described above. Through simple calculations, it is concluded that these photoelectrons that precipitate to nightside are able to support the observed ion density. In all, this work exhibits a perfect example of the importance and usage of superthermal electrons: an excellent magnetic tracer and also redistributing energy over the Martian space environment.

CHAPTER VIII

Conclusions and Future Work

In this chapter, I will first recap three main studies of this dissertation and discuss their future work, especially with the Mars Atmosphere and Volatile EvolutioN (MAVEN) mission, and finally close this thesis with a summary and its broad impact.

8.1 Photoelectrons and Dust Storms

To study the relation between dust storms and photoelectron fluxes, we have conducted a survey of the Mars Global Surveyor (MGS) electron data across all the pitch angles of 12 usable energy bins (11-746 electron volts) for dayside photoelectron observations over regions of strong crustal fields. Studies have shown that the solar EUV flux is the main controlling factor but dust storms play an important role as well. Our study of different energies and pitch angles has shown that the unusual bimodal solar flux dependence is not a common feature but mainly found in low energies and a few bins of higher energy channels. By multiplying time-history dust opacity with a solar EUV proxy as a new controlling function, the statistically significant increase of the correlation of photoelectron flux against this function indicates that dust storms have a long-lasting influence on high-altitude photoelectron fluxes, especially at low energies and the pitch angle source regions of high energy channels. The correlation increases experienced by the pitch angle source regions of all examined energy channels suggest that dust storms' influence most likely happens in the thermosphere-ionosphere source region of the photoelectrons, rather than at exospheric altitudes at or above MGS. Furthermore, by isolating the global-scale dust storm in Mars Year 25 (2001) from the rest, the results suggest that this storm is entirely responsible for the second solar flux dependent trend. While not excluding the possibility of this phenomenon being a one-time event, we hypothesize that there is a threshold of dust opacity at which the low-altitude dust's influence on high-altitude photoelectron fluxes begins to be significant.

Then the SuperThermal Electron Transport (STET) model was used to investigate what kinds of atmosphere can replicate observations, especially focusing on the role that thermospheric composition and density play in high-altitude photoelectrons. It was found that high-altitude photoelectron fluxes at more field-aligned pitch angles are very sensitive to composition change and surprisingly independent of density. For more perpendicular pitch angles, both composition and density take part in determining photoelectron fluxes. This investigation suggests that the global dust storm altered the photoelectron fluxes via causing CO_2 to be the dominant species at a much larger altitude range than usual.

There are a few issues remaining unresolved. Firstly, to answer if the global dust storm in 2001 is a special event in terms of atmospheric response, it is important to investigate how the global dust storm at Mars Year (MY) 28 affects the photoelectron fluxes by analyzing the electron data from Mars Express Analyser of Space Plasma and Energetic Atoms (ASPERA)-3 electron spectrometer (ELS) (e.g. *Barabash et al.*, 2006), combined with the dust opacity values from Thermal Emission Imaging System (THEMIS) (e.g. *Smith*, 2009). However, the lack of a magnetometer on Mars Express complicates the interpretation of these measurements with respect to photoelectrons on closed magnetic loops. Then, it is still mysterious as to why dust storms have such long-living effects. More neutral atmosphere modeling and observations are needed to answer this question.

8.2 Photoelectrons and Solar Zenith Angle

Numerous studies have shown that ionospheric quantities depend on solar zenith angle (SZA), according to Chapman theory. One would assume that photoelectron fluxes are also SZA dependent, especially when transport along a magnetic field line is significant. However, Martian high-altitude ($\sim$ 400 km) superthermal electron observations from the magnetometer/electron reflectometer on board Mars Global Surveyor show that the photoelectron fluxes are better correlated with just the solar irradiance, without SZA factored in and that the median photoelectron fluxes are independent of SZA, especially for high energies. For low energies, the observed fluxes tend to be partially controlled by SZA. Such counterintuitive results are due to the existence of a photoelectron exobase, only above which the photoelectrons are able to transport and escape to high altitudes. In this study, two methods were used to determine the altitude range of this exobase, which varies between 145 km and 165 km depending on the atmosphere and SZA. Through our SuperThermal Electron Transport (STET) model, we found that the integral of the production rate above the photoelectron exobase, therefore the high-altitude photoelectron fluxes, is rather independent of SZA.

This finding has a few implications. Firstly, high-altitude photoelectrons are observed and modeled in the Martian tail (*Liemohn et al.*, 2006, 2007b; *Frahm et al.*, 2006b,a). *Frahm et al.* (2010) estimated a Martian photoelectron escape rate of $\sim 3 \times 10^{23} s^{-1}$, which was then compared with ion escape estimations. *Frahm et al.* (2010) and *Coates et al.* (2011) suggest that these escaping photoelectrons may at least partially contribute to Martian atmospheric loss. In particular, these photoelectrons can set up ambipolar electric fields that facilitate ion escape along open magnetic fields. Our study implies that such an effect is probably the same for open field lines at all SZAs. On the other hand, this study also discourages the possibility of relating escaping photoelectron fluxes on an open magnetic field to the footprint of this field line, as there is no SZA dependence and therefore the source region cannot be specifically identified. Furthermore, as shown in this study, the properties of photoelectrons above the photoelectron exobase can be quite counterintuitive and should be treated with extra care. In particular, with the new data from Mars Atmosphere and Volatile EvolutioN (MAVEN) (*Jakosky et al.*, 2015), it is critical to take into account the observation altitudes relative to this exobase to employ the correct analysis. Finally, such an independence relation between high-altitude photoelectron fluxes and SZA should be expected at planets for which vertical transport can be significant, such as Earth, but detailed data analysis is required.

8.3 Solar Wind Electron Precipitation

Measurements made by the magnetometer/electron reflectometer on board the Mars Global Surveyor spacecraft have shown spatially localized enhancements in electron fluxes over the strong crustal fields on both the dayside and night, which are used to identify the cusps in between the closed magnetic fields. This dissertation provided a comprehensive statistical study on the occurrence rate of dayside solar-wind/magnetosheath precipitation over the strong crustal fields. Also, the occurrence rate's dependence on the magnetic elevation angles and the solar zenith angle is presented. A seasonal variation of the precipitation is also expected and found, due to both the tilt and the orbital eccentricity of Mars. The maximum occurrence rate is 40%, when the solar zenith angles are small and the magnetic fields are nearly vertical. Finally, the energy flux deposition of the solar wind electrons was calculated as well, which is 0.1%−2% of solar extreme ultraviolet (EUV) flux input.

However, this simple comparison of energy input does not take into account the effects of the solar zenith angle or the different deposition processes. The localized effects of the solar wind electrons might be significant. *Gurnett et al.* (2005) and *Gurnett et al.* (2008) found that oblique echoes from Mars Advanced Radar for Subsurface and Ionosphere Sounding (MARSIS) onboard Mars Express arise from ionosphere bulges, which geographically coincide with Martian crustal field regions where field lines tend to be strong and vertical. These two studies also suggest that the bulges are likely due to solar wind electron precipitation, which causes heating to the ionosphere and therefore a larger plasma scale height. The energy deposition of the solar wind electrons, especially the heating rates, at different altitudes and SZAs can be further studied by modeling, such as the multi-stream superthermal electron transportation model (*Khazanov and Liemohn*, 1995; *Liemohn et al.*, 1997, 2003, 2006). Furthermore, the magnetic fields in the Martian northern hemisphere, where the crustal fields are weak, are more likely to be draped. The solar wind electrons may have access to the atmosphere through these draped fields lines and deposit their energy at some altitude range through collision with the neutral particles and/or ions. *Gan et al.* (1990) conducted a study on how the solar wind superthermal electrons affect the electron temperature near the ionopause on Venus. Their results suggested that except for solar EUV heating, the additional heating from the energy deposition of solar wind electron fluxes moving along the magnetic field lines was also needed to explain the high electron temperature in the magnetized upper ionosphere and in the mantle region on Venus. However, few studies have been conducted on the heating effect of solar wind electrons, which may deposit energy into the Martian upper atmosphere while moving along the draped magnetic field lines. Further investigations of this potential heat source are needed to have a better understanding of the Martian upper atmosphere.

8.4 Future Work With MAVEN

Observations from multiple instruments onboard MAVEN can be utilized to carry this thesis work to the next step. To name a few:

Firstly, the direct measurements at several wavelengths (0-7 nm, 171 nm, and 121.6 nm) from the instrument LPW/EUV will vastly improve our understanding of solar irradiance at Mars. Furthermore, the new superthermal electron data from SWEA can used to validate the solar irradiance models, such as the Hinteregger-81 model, Flare Irradiance Spectral Model (FISM) and the Heliospheric Environment Solar Spectral Radiation (HESSR) model.

Secondly, case studies of MGS dayside photoelectron data (e.g. *Liemohn et al.*, 2003; *Brain et al.*, 2007) have exhibited more isotropic pitch angle distributions than expected, especially compared to STET model results. It is necessary to convey a statistical study with MGS and MAVEN electron data on whether this dayside photoelectron isotropy is only occasionally present or more of a general case. Either way, the STET model can be used to investigate the physical processes behind this isotropy.

Also, in this thesis, it is confirmed that the global dust storm in late 2001 significantly altered the thermospheric composition, which caused the enhanced photoelectron fluxes observed by MGS. The neutral composition measurement from the Neutral Gas and Ion Mass Spectrometer (NGIMS) instrument (*Mahaffy et al.*, 2014) onboard Mars Atmosphere and Volatile EvolutioN (MAVEN) should shed light on what species is/are responsible. In particular, to more quantitatively match large photoelectron flux enhancement during the global dust storm seen in the MGS observation, it is important to quantify the crossing altitude from CO_2 dominating to O dominating and also the superthermal electron exobase. NGIMS data can be utilized to investigate how the two altitudes vary with solar conditions, seasons, and also dust storms.

Finally, it is very useful to conduct statistical studies on the occurrence rate of photoelectron transport to the Martian deep night and how this occurrence rate varies with solar wind parameters, with MAVEN measurements. Also, accompanied with STET modeling, it is possible to further quantify how the energy of these cross-terminator-transport photoelectrons deposit the Martian nightside.

8.5 Summary of Dissertation

Because of the complex magnetic topology of Mars, superthermal electrons, mainly including photoelectrons and solar wind electrons, are important to localized atmospheric dynamics as they can carry and rapidly transport energy from one place to another, especially to nightside. These electrons, in return, are also a reliable tool to deduce the Martian magnetic topology, which is critical to understand the electromagnetic dynamics of the Martian space environment. This dissertation has explored three aspects of superthermal electrons at Mars mainly by analyzing observations from Mars Global Surveyor and also simulations with the SuperThermal Electron Transport (STET) model.

- **How does full energy and pitch angle distribution of high-altitude photoelectrons respond to low-altitude dust storms? What is the physics governing this connection?**

  Upon discovering the long-lived influence of Martian dust storms on photoelectron fluxes, this dissertation determined that such an influence is common for a wide range of energy and pitch angles and originated from the thermosphere-ionosphere source region of the photoelectrons, rather than at exospheric altitudes at or above MGS (at ∼400 km). The global dust storm that occurred in late 2001 was also found to be unique in terms of the thermospheric response, compared to other smaller dust storms. Through simulations, we concluded that instead of simply increasing the neutral densities, composition changes were needed to replicate the observed photoelectron flux enhancement caused by the global dust storm. This investigation suggested that the global dust storm altered the photoelectron fluxes by causing CO_2 to be the dominant species at a much larger altitude range than usual.

- **Do the observed high-altitude photoelectron fluxes really depend on solar zenith angle?**

  When transport is significant, such as over the Martian strong crustal fields, the photoelectron flux had previously been thought to be solar zenith angle dependent. However, only photoelectrons produced above the superthermal electron exobase can transport to high altitudes. Due to the fact that the integral of production rate above this exobase is about the same for all the solar zenith angles, it was found, observationally and numerically/theoretically, that the high-altitude photoelectron fluxes are quite independent of solar zenith angle.

- **What is the occurrence rate of dayside solar wind/magnetosheath electron precipitation over strong crustal fields and also their energy deposition into the Martian atmosphere?**

  Half of the magnetic fields over the strong crustal field regions tend to be oppositely-directed with respect to interplanetary magnetic fields most of the time, thus they are more likely to be open here than elsewhere on the planet. Such open paths allow energy and particle exchange between solar wind and the Martian atmosphere. Based on the energy spectral (flux against energy) difference between photoelectrons and solar wind electrons, a statistical approach was taken to distinguish the two populations. This also makes it possible to quantify the occurrence rate of solar wind electron precipitation that can be as high as 40% at small solar zenith angles and near vertical magnetic field lines. On the other hand, the energy flux deposition of the solar wind electrons is around 0.1-2% of the solar EUV flux input.

This dissertation provides answers to those specific questions, but its impact extends beyond. To name a few, the investigation of low-altitude dust storms and high-altitude photoelectrons demonstrates the coupling between the lower atmosphere and thermosphere. Also, the high-altitude photoelectron flux depends on only a few parameters and can be used to validate solar EUV models, such as the Flare Irradiance Spectral Model (FISM) and the Heliospheric Environment Solar Spectral Radiation (HESSR) model, as well as to monitor the thermospheric composition changes. Furthermore, high-altitude photoelectron fluxes being independent of solar zenith angle implies similar ambipolar electron field setups for open field lines, thus similar polar-wind type ion escapes, all over the planet. In addition, the study of the solar wind precipitation and the preliminary work with MAVEN data are examples of superthermal electrons being important energy carriers and magnetic tracers. These electrons can be critical to localized dynamics and even to understand the large scale interaction between the solar wind and Mars. The superthermal electron measurements, as well as other neutral and plasma measurements from MAVEN, should greatly deepen our understanding of the Martian space environment. Finally, many of the findings and future work can be carefully applied or adapted to planets with significant vertical superthermal electron transport along magnetic fields, such as Earth, Jupiter, and Saturn.

BIBLIOGRAPHY

BIBLIOGRAPHY

Acuña, M., et al. (1992), Mars observer magnetic fields investigation, *Journal of Geophysical Research: Planets (1991–2012)*, *97*(E5), 7799–7814.

Acuña, M., et al. (1998), Magnetic field and plasma observations at mars: Initial results of the mars global surveyor mission, *Science*, *279*(5357), 1676–1680.

Baird, D. T., R. H. Tolson, S. Bougher, and B. Steers (2007), Zonal wind calculations from mars global surveyor accelerometer and rate data, *Journal of Spacecraft and Rockets*, *44*(6), 1180–1187.

Banks, P., and A. Nagy (1970), Concerning the influence of elastic scattering upon photoelectron transport and escape, *Journal of Geophysical Research*, *75*(10), 1902–1910.

Barabash, S., et al. (2006), The analyzer of space plasmas and energetic atoms (aspera-3) for the mars express mission, *Space Science Reviews*, *126*(1-4), 113–164.

Bell, J. M., S. W. Bougher, and J. R. Murphy (2007), Vertical dust mixing and the interannual variations in the mars thermosphere, *Journal of Geophysical Research: Planets (1991–2012)*, *112*(E12).

Bertaux, J.-L., F. Leblanc, O. Witasse, E. Quemerais, J. Lilensten, S. Stern, B. Sandel, and O. Korablev (2005), Discovery of an aurora on mars, *Nature*, *435*(7043), 790–794.

Bougher, S., J. Murphy, and R. Haberle (1997), Dust storm impacts on the mars upper atmosphere, *Advances in Space Research*, *19*(8), 1255–1260.

Bougher, S., G. Keating, R. Zurek, J. Murphy, R. Haberle, J. Hollingsworth, and R. Clancy (1999), Mars global surveyor aerobraking: Atmospheric trends and model interpretation, *Advances in Space Research*, *23*(11), 1887–1897.

Bougher, S., J. Bell, J. Murphy, M. Lopez-Valverde, and P. Withers (2006), Polar warming in the mars thermosphere: Seasonal variations owing to changing insolation and dust distributions, *Geophysical Research Letters*, *33*(2).

Bougher, S., D. Pawlowski, J. Bell, S. Nelli, T. McDunn, J. Murphy, M. Chizek, and A. Ridley (2015), Mars global ionosphere-thermosphere model: Solar cycle, seasonal, and diurnal variations of the mars upper atmosphere, *Journal of Geophysical Research: Planets*, *120*(2), 311–342.

Bougher, S. W., R. E. Dickinson, R. G. Roble, and E. C. Ridley (1988), Mars thermospheric general circulation model - Calculations for the arrival of PHOBOS at Mars, *Geophysical Research Letters*, *15*, 1511–514, doi:10.1029/GL015i013p01511.

Bougher, S. W., D. M. Hunten, and R. G. Roble (1994), CO2 cooling in terrestrial planet thermospheres, *Journal of Geophysical Research: Planets*, *99*, 14,609, doi: 10.1029/94JE01088.

Bougher, S. W., S. Engel, D. P. Hinson, and J. M. Forbes (2001), Mars Global Surveyor radio science electron density profiles : Neutral atmosphere implications, *Geophysical Research Letters*, *28*, 3091–3094, doi:10.1029/2001GL012884.

Bougher, S. W., S. Engel, D. Hinson, and J. Murphy (2004), Mgs radio science electron density profiles: Interannual variability and implications for the martian neutral atmosphere, *Journal of Geophysical Research: Planets (1991–2012)*, *109*(E3).

Brain, D., F. Bagenal, M. Acuña, and J. Connerney (2003), Martian magnetic morphology: Contributions from the solar wind and crust, *Journal of Geophysical Research: Space Physics (1978–2012)*, *108*(A12).

Brain, D., J. Halekas, R. Lillis, D. Mitchell, R. Lin, and D. Crider (2005), Variability of the altitude of the martian sheath, *Geophysical Research Letters*, *32*(18).

Brain, D., et al. (2006a), On the origin of aurora on mars, *Geophysical Research Letters*, *33*(1).

Brain, D., R. Lillis, D. Mitchell, J. Halekas, and R. Lin (2007), Electron pitch angle distributions as indicators of magnetic field topology near mars, *Journal of Geophysical Research: Space Physics (1978–2012)*, *112*(A9).

Brain, D., A. Baker, J. Briggs, J. Eastwood, J. Halekas, and T.-D. Phan (2010), Episodic detachment of martian crustal magnetic fields leading to bulk atmospheric plasma escape, *Geophysical Research Letters*, *37*(14).

Brain, D. A., D. L. Mitchell, and J. S. Halekas (2006b), The magnetic field draping direction at mars from april 1999 through august 2004, *Icarus*, *182*(2), 464–473.

Butler, D. M., and R. S. Stolarski (1978), Photoelectrons and electron temperatures in the venus ionosphere, *Journal of Geophysical Research: Space Physics (1978–2012)*, *83*(A5), 2057–2065.

Chamberlin, P. C., T. N. Woods, and F. G. Eparvier (2007), Flare irradiance spectral model (fism): Daily component algorithms and results, *Space Weather*, *5*(7), n/a–n/a, doi:10.1029/2007SW000316.

Chamberlin, P. C., T. N. Woods, and F. G. Eparvier (2008), Flare irradiance spectral model (fism): Flare component algorithms and results, *Space Weather*, *6*(5), n/a–n/a, doi:10.1029/2007SW000372.

Chapman, S. (1931a), The absorption and dissociative or ionizing effect of monochromatic radiation in an atmosphere on a rotating earth, *Proceedings of the Physical Society*, *43*, 26–45, doi:10.1088/0959-5309/43/1/305.

Chapman, S. (1931b), The absorption and dissociative or ionizing effect of monochromatic radiation in an atmosphere on a rotating earth part II. Grazing incidence, *Proceedings of the Physical Society*, *43*, 483–501, doi:10.1088/0959-5309/43/5/302.

Chapman, S. (1931c), The absorption and dissociative or ionizing effect of monochromatic radiation in an atmosphere on a rotating earth, *Proceedings of the Physical Society*, *43*, 26–45, doi:10.1088/0959-5309/43/1/305.

Chapman, S. (1931d), The absorption and dissociative or ionizing effect of monochromatic radiation in an atmosphere on a rotating earth part II. Grazing incidence, *Proceedings of the Physical Society*, *43*, 483–501, doi:10.1088/0959-5309/43/5/302.

Christensen, P. R., et al. (1992), Thermal emission spectrometer experiment: Mars observer mission, *Journal of Geophysical Research: Planets (1991–2012)*, *97*(E5), 7719–7734.

Christensen, P. R., et al. (2001), Mars global surveyor thermal emission spectrometer experiment: investigation description and surface science results, *Journal of Geophysical Research: Planets (1991–2012)*, *106*(E10), 23,823–23,871.

Clancy, R. T., M. J. Wolff, B. A. Whitney, B. A. Cantor, M. D. Smith, and T. H. McConnochie (2010), Extension of atmospheric dust loading to high altitudes during the 2001 mars dust storm: Mgs tes limb observations, *Icarus*, *207*(1), 98–109.

Coates, A. J., S. Tsang, A. Wellbrock, R. Frahm, J. Winningham, S. Barabash, R. Lundin, D. Young, and F. Crary (2011), Ionospheric photoelectrons: Comparing venus, earth, mars and titan, *Planetary and Space Science*, *59*(10), 1019–1027.

Connerney, J., M. Acuña, N. Ness, G. Kletetschka, D. Mitchell, R. Lin, and H. Reme (2005), Tectonic implications of mars crustal magnetism, *Proceedings of the national Academy of Sciences of the United States of America*, *102*(42), 14,970–14,975.

Crider, D., et al. (2000), Evidence of electron impact ionization in the magnetic pileup boundary of mars, *Geophysical Research Letters*, *27*(1), 45–48, doi:10.1029/1999GL003625.

Crider, D. H., et al. (2002), Observations of the latitude dependence of the location of the martian magnetic pileup boundary, *Geophysical Research Letters*, *29*, 1170, doi:10.1029/2001GL013860.

Dong, C., S. W. Bougher, Y. Ma, G. Toth, A. F. Nagy, and D. Najib (2014), Solar wind interaction with mars upper atmosphere: Results from the one-way coupling between the multifluid mhd model and the mtgcm model, *Geophysical Research Letters*, *41*(8), 2708–2715.

Dubinin, E., M. Fraenz, J. Woch, J. Winnigham, R. Frahm, R. Lundin, and S. Barabash (2008a), Suprathermal electron fluxes on the nightside of mars: Aspera-3 observations, *Planetary and Space Science*, *56*(6), 846 – 851, doi: http://dx.doi.org/10.1016/j.pss.2007.12.010, mars Express/Venus Express.

Dubinin, E. M., et al. (2008b), Access of solar wind electrons into the martian magnetosphere, *Annales Geophysicae*, *26*(11), 3511–3524, doi:10.5194/angeo-26-3511-2008.

England, S. L., and R. J. Lillis (2012), On the nature of the variability of the martian thermospheric mass density: Results from electron reflectometry with mars global surveyor, *Journal of Geophysical Research: Planets (1991–2012)*, *117*(E2).

Fillingim, M., L. Peticolas, R. Lillis, D. Brain, J. Halekas, D. Lummerzheim, and S. Bougher (2010), Localized ionization patches in the nighttime ionosphere of mars and their electrodynamic consequences, *Icarus*, *206*(1), 112–119.

Fillingim, M. O., et al. (2007), Model calculations of electron precipitation induced ionization patches on the nightside of Mars, *Geophysical Research Letters*, *34*, L12101, doi:10.1029/2007GL029986.

Fontenla, J. M., E. Quémerais, I. González Hernández, C. Lindsey, and M. Haberreiter (2009), Solar irradiance forecast and far-side imaging, *Advances in Space Research*, *44*, 457–464, doi:10.1016/j.asr.2009.04.010.

Fontenla, J. M., E. Landi, M. Snow, and T. Woods (2014), Far- and Extreme-UV Solar Spectral Irradiance and Radiance from Simplified Atmospheric Physical Models, *Solar Physics*, *289*, 515–544, doi:10.1007/s11207-013-0431-4.

Forbes, J. M., F. G. Lemoine, S. L. Bruinsma, M. D. Smith, and X. Zhang (2008), Solar flux variability of mars' exosphere densities and temperatures, *Geophysical Research Letters*, *35*(1).

Fox, J. L. (1991), Cross sections and reaction rates of relevance to aeronomy, *Reviews of Geophysics*, *29*, 1110–1131.

Fox, J. L., and A. Dalgarno (1979), Ionization, luminosity, and heating of the upper atmosphere of mars, *Journal of Geophysical Research: Space Physics (1978–2012)*, *84*(A12), 7315–7333.

Fox, J. L., and K. E. Yeager (2006), Morphology of the near-terminator Martian ionosphere: A comparison of models and data, *Journal of Geophysical Research (Space Physics)*, *111*, A10309, doi:10.1029/2006JA011697.

Fox, J. L., and K. E. Yeager (2009), MGS electron density profiles: Analysis of the peak magnitudes, *ICARUS*, *200*, 468–479, doi:10.1016/j.icarus.2008.12.002.

Frahm, R., et al. (2006a), Carbon dioxide photoelectron energy peaks at mars, *Icarus*, *182*(2), 371–382.

Frahm, R., et al. (2006b), Locations of atmospheric photoelectron energy peaks within the mars environment, *Space Science Reviews*, *126*(1-4), 389–402.

Frahm, R., et al. (2010), Estimation of the escape of photoelectrons from mars in 2004 liberated by the ionization of carbon dioxide and atomic oxygen, *Icarus*, *206*(1), 50–63.

Furman, M., and M. Pivi (2003), Simulation of secondary electron emission based on a phenomenological probabilistic model.

Gan, L., T. Cravens, and M. Horanyi (1990), Electrons in the ionopause boundary layer of venus, *Journal of Geophysical Research: Space Physics (1978–2012)*, *95*(A11), 19,023–19,035.

Gefan, G. D., and G. V. Khazanov (1990), Non-steady-state conditions of filling up the geomagnetic trap with superthermal electrons, *Annales Geophysicae*, *8*, 519–523.

Gierasch, P. J., and R. M. Goody (1972), The effect of dust on the temperature of the Martian atmosphere., *Journal of Atmospheric Sciences*, *29*, 400–402, doi:10.1175/1520-0469(1972)029¡0400:TEODOT¿2.0.CO;2.

Gombosi, T. I. (1998), *Physics of the space environment*, Cambridge University Press.

Gurnett, D. A., et al. (2005), Radar Soundings of the Ionosphere of Mars, *Science*, *310*, 1929–1933, doi:10.1126/science.1121868.

Gurnett, D. A., et al. (2008), An overview of radar soundings of the Martian ionosphere from the Mars Express spacecraft, *Advances in Space Research*, *41*, 1335–1346, doi:10.1016/j.asr.2007.01.062.

Guzewich, S. D., E. R. Talaat, A. D. Toigo, D. W. Waugh, and T. H. McConnochie (2013), High-altitude dust layers on mars: Observations with the thermal emission spectrometer, *Journal of Geophysical Research: Planets*.

Haberle, R. M., C. B. Leovy, and J. B. Pollack (1982), Some effects of global dust storms on the atmospheric circulation of mars, *Icarus*, *50*(2), 322–367.

Haider, S. A., J. Kim, A. F. Nagy, C. N. Keller, M. I. Verigin, K. I. Gringauz, N. M. Shutte, K. Szego, and P. Kiraly (1992), Calculated ionization rates, ion densities, and airglow emission rates due to precipitating electrons in the nightside ionosphere of Mars, *Journal of Geophysical Research (Space Physics)*, *97*, 10,637, doi:10.1029/92JA00317.

Haider, S. A., K. K. Mahajan, and E. Kallio (2011), Mars ionosphere: A review of experimental results and modeling studies, *Reviews of Geophysics*, *49*, RG4001, doi:10.1029/2011RG000357.

Hantsch, M., and S. Bauer (1990), Solar control of the mars ionosphere, *Planetary and Space Science*, *38*(4), 539–542.

Harnett, E. M., and R. M. Winglee (2005), Three-dimensional fluid simulations of plasma asymmetries in the martian magnetotail caused by the magnetic anomalies, *Journal of Geophysical Research: Space Physics*, *110*(A7), n/a–n/a, doi: 10.1029/2003JA010315.

Heroux, L., and H. Hinteregger (1978), Aeronomical reference spectrum for solar uv below 2000 å, *Journal of Geophysical Research: Space Physics (1978–2012)*, *83*(A11), 5305–5308.

Hinteregger, H. E., K. Fukui, and B. R. Gilson (1981), Observational, reference and model data on solar EUV, from measurements on AE-E, *Geophysical Research Letters*, *8*, 1147–1150, doi:10.1029/GL008i011p01147.

Jakosky, B. M., et al. (2015), The mars atmosphere and volatile evolution (maven) mission, *Space Science Reviews*, pp. 1–46.

Keating, G., et al. (1998), The structure of the upper atmosphere of mars: In situ accelerometer measurements from mars global surveyor, *Science*, *279*(5357), 1672–1676.

Khazanov, G., and M. Liemohn (1995), Nonsteady state ionosphere-plasmasphere coupling of superthermal electrons, *Journal of Geophysical Research*, *100*(A6), 9669–9681.

Khazanov, G. V. (1979), The kinetics of the electron plasma component of the upper atmosphere (in russian, english translation, national translation center, #80-50707, washington, d. c., 1980), *Moscow, Nauka.*

Khazanov, G. V., T. Neubert, and G. D. Gefan (1994), Unified theory of ionosphere-plasmasphere transport of suprathermal electrons, *IEEE Transactions on Plasma Science*, *22*, 187–198, doi:10.1109/27.279022.

Korablev, O., V. Krasnopolsky, A. Rodin, and E. Chassefiere (1993), Vertical structure of martian dust measured by solar infrared occultations from the phobos spacecraft, *Icarus*, *102*(1), 76–87.

Krymskii, A., T. Breus, N. Ness, M. Acuña, J. Connerney, D. Crider, D. Mitchell, and S. Bauer (2002), Structure of the magnetic field fluxes connected with crustal magnetization and topside ionosphere at mars, *Journal of Geophysical Research: Space Physics (1978–2012)*, *107*(A9), SIA–2.

Krymskii, A., T. Breus, N. Ness, D. Hinson, and D. Bojkov (2003), Effect of crustal magnetic fields on the near terminator ionosphere at mars: Comparison of in situ magnetic field measurements with the data of radio science experiments on board mars global surveyor, *Journal of Geophysical Research: Space Physics (1978–2012)*, *108*(A12).

Krymskii, A., N. Ness, D. Crider, T. Breus, M. Acuña, and D. Hinson (2004), Solar wind interaction with the ionosphere/atmosphere and crustal magnetic fields at mars: Mars global surveyor magnetometer/electron reflectometer, radio science, and accelerometer data, *Journal of Geophysical Research: Space Physics (1978–2012)*, *109*(A11).

Leblanc, F., et al. (2008), Observations of aurorae by SPICAM ultraviolet spectrograph on board Mars Express: Simultaneous ASPERA-3 and MARSIS measurements, *Journal of Geophysical Research (Space Physics)*, *113*, A08311, doi: 10.1029/2008JA013033.

Liemohn, M., G. Khazanov, T. Moore, and S. Guiter (1997), Self-consistent superthermal electron effects on plasmaspheric refilling, *Journal of Geophysical Research: Space Physics (1978–2012)*, *102*(A4), 7523–7536.

Liemohn, M., Y. Ma, A. Nagy, J. Kozyra, J. Winningham, R. Frahm, J. Sharber, S. Barabash, and R. Lundin (2007a), Numerical modeling of the magnetic topology near mars auroral observations, *Geophysical Research Letters*, *34*(24).

Liemohn, M. W. (1997), Self-consistent coupling of superthermal electrons with thermal plasma, Ph.D. thesis, UNIVERSITY OF MICHIGAN.

Liemohn, M. W., D. L. Mitchell, A. F. Nagy, J. L. Fox, T. W. Reimer, and Y. Ma (2003), Comparisons of electron fluxes measured in the crustal fields at mars by the mgs magnetometer/electron reflectometer instrument with a b field–dependent transport code, *Journal of Geophysical Research*, *108*(E12), 5134.

Liemohn, M. W., et al. (2006), Numerical interpretation of high-altitude photoelectron observations, *Icarus*, *182*(2), 383–395.

Liemohn, M. W., et al. (2007b), Mars global mhd predictions of magnetic connectivity between the dayside ionosphere and the magnetospheric flanks, in *The Mars Plasma Environment*, pp. 63–76, Springer.

Liemohn, M. W., A. Dupre, S. W. Bougher, M. Trantham, D. L. Mitchell, and M. D. Smith (2012), Time-history influence of global dust storms on the upper atmosphere at mars, *Geophysical Research Letters*, *39*(11).

Lillis, R. J., and D. A. Brain (2013), Nightside electron precipitation at mars: Geographic variability and dependence on solar wind conditions, *Journal of Geophysical Research: Space Physics*, *118*(6), 3546–3556.

Lillis, R. J., S. W. Bougher, D. L. Mitchell, D. A. Brain, R. P. Lin, and M. H. Acuña (2008), Continuous monitoring of nightside upper thermospheric mass densities in the martian southern hemisphere over 4 martian years using electron reflectometry, *Icarus*, *194*(2), 562–574.

Lillis, R. J., D. L. Mitchell, R. P. Lin, and M. H. Acuña (2008), Electron reflectometry in the martian atmosphere, *ICARUS*, *194*, 544–561, doi: 10.1016/j.icarus.2007.09.030.

Lillis, R. J., M. O. Fillingim, L. M. Peticolas, D. A. Brain, R. P. Lin, and S. W. Bougher (2009), Nightside ionosphere of Mars: Modeling the effects of crustal magnetic fields and electron pitch angle distributions on electron impact ionization, *Journal of Geophysical Research (Planets)*, *114*, E11009, doi: 10.1029/2009JE003379.

Lillis, R. J., S. W. Bougher, F. González-Galindo, F. Forget, M. D. Smith, and P. C. Chamberlin (2010a), Four martian years of nightside upper thermospheric mass densities derived from electron reflectometry: Method extension and comparison with gcm simulations, *Journal of Geophysical Research: Planets (1991–2012)*, *115*(E7).

Lillis, R. J., D. A. Brain, S. L. England, P. Withers, M. O. Fillingim, and A. Safaeinili (2010b), Total electron content in the mars ionosphere: Temporal studies and dependence on solar euv flux, *Journal of Geophysical Research: Space Physics (1978–2012)*, *115*(A11).

Ma, Y. J., X. Fang, A. F. Nagy, C. T. Russell, and G. Toth (2014), Martian ionospheric responses to dynamic pressure enhancements in the solar wind, *Journal of Geophysical Research: Space Physics*, *119*(2), 1272–1286, doi: 10.1002/2013JA019402.

Mahaffy, P. R., et al. (2014), The neutral gas and ion mass spectrometer on the mars atmosphere and volatile evolution mission, *Space Science Reviews*, pp. 1–25.

Mantas, G. P., and W. B. Hanson (1979), Photoelectron fluxes in the martian ionosphere, *Journal of Geophysical Research: Space Physics*, *84*(A2), 369–385, doi: 10.1029/JA084iA02p00369.

Medvedev, A. S., T. Kuroda, and P. Hartogh (2011), Influence of dust on the dynamics of the martian atmosphere above the first scale height, *Aeolian Research*, *3*(2), 145–156.

Medvedev, A. S., E. Yiğit, T. Kuroda, and P. Hartogh (2013), General circulation modeling of the martian upper atmosphere during global dust storms, *Journal of Geophysical Research: Planets*, *118*(10), 2234–2246.

Mitchell, D., R. Lin, H. Reme, D. Crider, P. Cloutier, J. Connerney, M. Acuña, and N. Ness (2000), Oxygen auger electrons observed in mars' ionosphere, *Geophysical research letters*, *27*(13), 1871–1874.

Mitchell, D., R. Lin, C. Mazelle, H. Reme, P. Cloutier, J. Connerney, M. Acuña, and N. Ness (2001), Probing mars' crustal magnetic field and ionosphere with the mgs electron reflectometer, *Journal of Geophysical Research: Planets (1991–2012)*, *106*(E10), 23,419–23,427.

Morgan, D. D., D. A. Gurnett, D. L. Kirchner, J. L. Fox, E. Nielsen, and J. J. Plaut (2008), Variation of the Martian ionospheric electron density from Mars Express radar soundings, *Journal of Geophysical Research (Space Physics)*, *113*, A09303, doi:10.1029/2008JA013313.

Nagy, A., et al. (2004), The plasma environment of mars, in *Mars Magnetism and Its Interaction with the Solar Wind*, pp. 33–114, Springer.

Nagy, A. F., and P. M. Banks (1970), Photoelectron fluxes in the ionosphere, *Journal of Geophysical Research: Space Physics*, *75*, 6260–6270, doi:10.1029/JA075i031p06260.

Nielsen, E., et al. (2007), Local plasma processes and enhanced electron densities in the lower ionosphere in magnetic cusp regions on mars, *Planetary and Space Science*, *55*(14), 2164–2172.

Nier, A., and M. B. McElroy (1977), Composition and structure of mars' upper atmosphere: Results from the neutral mass spectrometers on viking 1 and 2, *Journal of Geophysical Research*, *82*(28), 4341–4349.

Němec, F., D. D. Morgan, D. A. Gurnett, F. Duru, and V. Truhlík (2011), Dayside ionosphere of Mars: Empirical model based on data from the MARSIS instrument, *Journal of Geophysical Research (Planets)*, *116*, E07003, doi:10.1029/2010JE003789.

Peterson, W., T. Woods, J. Fontenla, P. Richards, P. Chamberlin, S. Solomon, W. Tobiska, and H. Warren (2012), Solar euv and xuv energy input to thermosphere on solar rotation time scales derived from photoelectron observations, *Journal of Geophysical Research: Space Physics (1978–2012)*, *117*(A5).

Rutherford, E. (1911), The scattering of α and β particles by matter and the structure of the atom, *Phil. Mag*, *21*(669), 1911.

Safaeinili, A., W. Kofman, J. Mouginot, Y. Gim, A. Herique, A. B. Ivanov, J. J. Plaut, and G. Picardi (2007), Estimation of the total electron content of the Martian ionosphere using radar sounder surface echoes, *Geophys. Res. Lett.*, *34*, L23204, doi:10.1029/2007GL032154.

Schunk, R., and A. Nagy (2000), Ionospheres: Physics, plasma physics, and chemistry, cambridge atmos, *Space Sci. Ser*, *59*.

Schunk, R., and A. Nagy (2009), Ionospheres.

Seth, S. P., S. A. Haider, and K. I. Oyama (2002), Photoelectron flux and nightglow emissions of 5577 and 6300 Å due to solar wind electron precipitation in Martian atmosphere, *Journal of Geophysical Research (Space Physics)*, *107*, 1324, doi:10.1029/2001JA000261.

Sheehan, C. H., and J.-P. St-Maurice (2004), Dissociative recombination of n2+, o2+, and no+: Rate coefficients for ground state and vibrationally excited ions, *Journal of Geophysical Research: Space Physics (1978–2012)*, *109*(A3).

Smith, F., and C. Smith (1972), Numerical evaluation of chapman's grazing incidence integral ch (x, χ), *Journal of Geophysical Research*, *77*(19), 3592–3597.

Smith, M. (2006), Tes atmospheric temperature, aerosol optical depth, and water vapor observations 1999-2004, *F. Forget, MA Lopez-Valverde, MC Desjean, JP Huot, F. Lefevre, S. Lebonnois, SR Lewis, E. Millour, PL Read & RJ Wilson, editeurs, Mars Atmosphere Modelling and Observations*, p. 211.

Smith, M. D. (2004), Interannual variability in tes atmospheric observations of mars during 1999–2003, *Icarus*, *167*(1), 148–165.

Smith, M. D. (2009), Themis observations of mars aerosol optical depth from 2002–2008, *Icarus*, *202*(2), 444–452.

Smith, M. D., B. J. Conrath, J. C. Pearl, and P. R. Christensen (2002), Thermal emission spectrometer observations of martian planet-encircling dust storm 2001a, *Icarus*, *157*(1), 259–263.

Solomon, S. C., S. M. Bailey, and T. N. Woods (2001), Effect of solar soft X-rays on the lower ionosphere, *Geophysical Research Letters*, *28*, 2149–2152, doi:10.1029/2001GL012866.

Sung, K., and J. L. Fox (2000), Electron impact cross sections for use in modeling the ionospheres/thermospheres of the earth and planets, *Eos Trans, AGU, 81(48), Fall Meet. Suppl., Abstract SA52A-11*.

Swartz, W. E., G. J. Bailey, and R. J. Moffett (1975), Electron heating resulting from interhemispherical transport of photoelectrons, *Planetary and Space Science*, *23*, 589–598, doi:10.1016/0032-0633(75)90099-9.

Tracadas, P. W., M. T. Zuber, D. E. Smith, and F. G. Lemoine (2001), Density structure of the upper thermosphere of mars from measurements of air drag on the mars global surveyor spacecraft, *Journal of geophysical research*, *106*(E10), 23,349–23.

Trantham, M., M. Liemohn, D. Mitchell, and J. Frank (2011), Photoelectrons on closed crustal field lines at mars, *Journal of Geophysical Research*, *116*(A7), A07,311.

Vignes, D., et al. (2000), The solar wind interaction with Mars: Locations and shapes of the bow shock and the magnetic pile-up boundary from the observations of the MAG/ER Experiment onboard Mars Global Surveyor, *Geophysical Research Letters*, *27*, 49–52, doi:10.1029/1999GL010703.

Wang, J.-S., and E. Nielsen (2003), Behavior of the martian dayside electron density peak during global dust storms, *Planetary and Space Science*, *51*(4), 329–338.

Withers, P. (2009), A review of observed variability in the dayside ionosphere of Mars, *Advances in Space Research*, *44*, 277–307, doi:10.1016/j.asr.2009.04.027.

Withers, P., and M. Mendillo (2005), Response of peak electron densities in the martian ionosphere to day-to-day changes in solar flux due to solar rotation, *Planetary and Space Science*, *53*, 1401–1418, doi:10.1016/j.pss.2005.07.010.

Withers, P., and R. Pratt (2013), An observational study of the response of the upper atmosphere of mars to lower atmospheric dust storms, *Icarus*.

Withers, P., M. Mendillo, H. Rishbeth, D. Hinson, and J. Arkani-Hamed (2005), Ionospheric characteristics above martian crustal magnetic anomalies, *Geophysical Research Letters*, *32*(16).

Withers, P., K. Fallows, and M. Matta (2014), Predictions of electron temperatures in the Mars ionosphere and their effects on electron densities, *Geophysical Research Letters*, *41*, 2681–2686, doi:10.1002/2014GL059683.

Woods, T. N., et al. (1998), Timed solar euv experiment, in *SPIE's International Symposium on Optical Science, Engineering, and Instrumentation*, pp. 180–191, International Society for Optics and Photonics.

Woods, T. N., F. G. Eparvier, S. M. Bailey, P. C. Chamberlin, J. Lean, G. J. Rottman, S. C. Solomon, W. K. Tobiska, and D. L. Woodraska (2005), Solar euv experiment (see): Mission overview and first results, *Journal of Geophysical Research: Space Physics (1978–2012)*, *110*(A1).

Zhang, M. H. G., J. G. Luhmann, and A. J. Kliore (1990), An observational study of the nightside ionospheres of Mars and Venus with radio occultation methods, *J. Geophys. Res.*, *95*, 17,095–17,102, doi:10.1029/JA095iA10p17095.

Zou, H., R. J. Lillis, J. S. Wang, and E. Nielsen (2011), Determination of seasonal variations in the martian neutral atmosphere from observations of ionospheric peak height, *Journal of Geophysical Research*, *116*(E9), E09,004.